The Motion of Bubbles in Hele-Shaw Cells

Daniel James Booth
Worcester College
University of Oxford

A thesis submitted for the degree of
Doctor of Philosophy

Trinity 2024

Acknowledgements

Firstly, I would like to thank my supervisors, Professors Ian Griffiths and Peter Howell, for their support, endless enthusiasm, and guidance. Their excellent advice has been invaluable to me and made me a much better mathematician.

Secondly, I would like to thank Howard Stone, Katie Wu, and Janine Nunes for the experiments they performed and for many helpful discussions. This thesis wouldn't be the same without their efforts.

I am grateful for the support of the Engineering and Physical Sciences Research Council (EPSRC) for funding my DPhil, grant reference number EP/V520202/1.

To the people of OCIAM for being my mathematical home for the last four years, and for the coffee, cake, and board games. Special thanks to James, Torin, Matty C., Arkady, Matthew S., Brady, Anna, Nick, Harry, Rohit, and Simon for making my time here great.

To my Dungeons and Dragons group for giving me much-needed weekly escapism and noodles.

Last but certainly not least to my family for their unwavering support over the many years, my nephew, Ollie, for never failing to make me smile, and my partner who has had to deal with me while I wrote this thesis. I could not have done it without you all.

Statement of Originality

The research presented in this thesis was performed in the Mathematical Institute at the University of Oxford between October 2020 and August 2024 under the supervision of Professors Ian Griffiths and Peter Howell.

This thesis describes my own work, except for the experiments in Chapters 1, 2, 3, 5, and Appendix B which were performed by Katie Wu (Princeton University). They have been appropriately credited within the text of this thesis.

The majority of the material in Chapter 2 and some of the material in Chapters 1 and 4 has been published in the *Journal of Fluid Mechanics* (Booth *et al.*, 2023). The remaining work in these chapters as well as Chapters 3, 5, 6 and 7 is original work.

Abstract

In this thesis, we present and analyse models for the motion of bubbles in a Hele-Shaw cell. We consider the experimentally relevant regime in which the bubbles are large enough that they are flattened against the top and bottom of the channel and assume pancake-like shapes, but are small enough to remain approximately circular when in plan view. We begin in Chapter 2 by considering the motion of a single bubble in a Hele-Shaw cell with a uniform background flow. The theoretical prediction for the bubble velocity is found to agree well with experiments. Including the effect of channel walls can either increase or decrease the bubble velocity depending on whether the bubble is travelling slower or faster than the background flow speed, respectively. Next, in Chapter 3 we consider the motion of two bubbles. We find that for two bubbles of different radii with the larger initially behind, in some cases the bubbles rotate around one another, while in others the bubbles collide. The motion of an arbitrary number of bubbles is considered in Chapter 4. We begin by developing a numerical method to solve the full model. Then, we derive approximate models, which significantly reduce the computational complexity while still retaining the qualitative behaviour of the full model. In Chapter 5, we return to the motion of a single bubble, now focusing on the bubble shape. We find that the aspect ratio of the bubble varies non-monotonically with its size, with it initially flattening in the direction of motion for small bubbles and elongating for large bubbles. We then consider the deformations of a pair of bubbles and find that, for two bubbles aligned with the uniform background flow, the one in front flattens, while the one behind elongates. In Chapter 6, we consider the propagation of a bubble in a Hele-Shaw cell with a non-uniform background flow. We find that the bubble centre travels along a streamline of the background flow although, unlike a tracer particle, the bubble does not travel at the same speed as the background flow. Using the same methodology, we derive approximate solutions for the motion of a bubble in more complicated domains including walls or obstacles. Finally, in Chapter 7 we consider the effect of surfactant on the motion of a bubble. Surfactants are commonly used in practice to stabilize the bubbles against coalesence. We find that a surfactant-laden bubble travels slower than a surfactant-free bubble under the same flow conditions.

Contents

List of Figures

Chapter 1

Introduction

1.1 Motivation

Many microfluidic experiments and devices involve generating bubbles and then transporting them along microfluidic channels (Huerre *et al.*, 2014; Anna, 2016; Gnyawali *et al.*, 2017). The bubbles are often large enough (compared with the channel height) to be pancake-shaped, i.e. flattened against the top and bottom walls of the channel (Zhu & Gallaire, 2016; Reichert *et al.*, 2018), but almost always small enough to remain approximately circular in plan view (see, e.g., Garstecki *et al.*, 2004; Beatus *et al.*, 2012; Shen *et al.*, 2014; Gnyawali *et al.*, 2017). In this thesis, we derive models for the motion of such bubbles in a Hele-Shaw cell and then use them to describe bubble propagation along a microfluidic channel.

The dynamics of bubbles in a Hele-Shaw cell is both a classical fluid dynamics problem (Taylor & Saffman, 1959; Saffman, 1959; Tanveer, 1986; Maxworthy, 1986) and a fundamental mathematical problem due to its connection to potential theory and complex analysis (Acheson, 1990; Howison, 1986, 1992; Cummings *et al.*, 1999; Gustafsson & Vasil'ev, 2006). In this thesis, we use a combination of analytic and numerical approaches to find new solutions to this well-studied problem. We compare our theoretical predictions with new experimental results by our collaborators at Princeton University (Katie Wu, Janine Nunes and Howard Stone). We show a schematic of the experimental setup in plan view in figure 1.1(a). In figure 1.1(b) we show an example experiment showcasing a two-bubble rollover, where the larger bubble catches the smaller one, and instead of colliding they rotate around one another leaving the larger bubble in front.

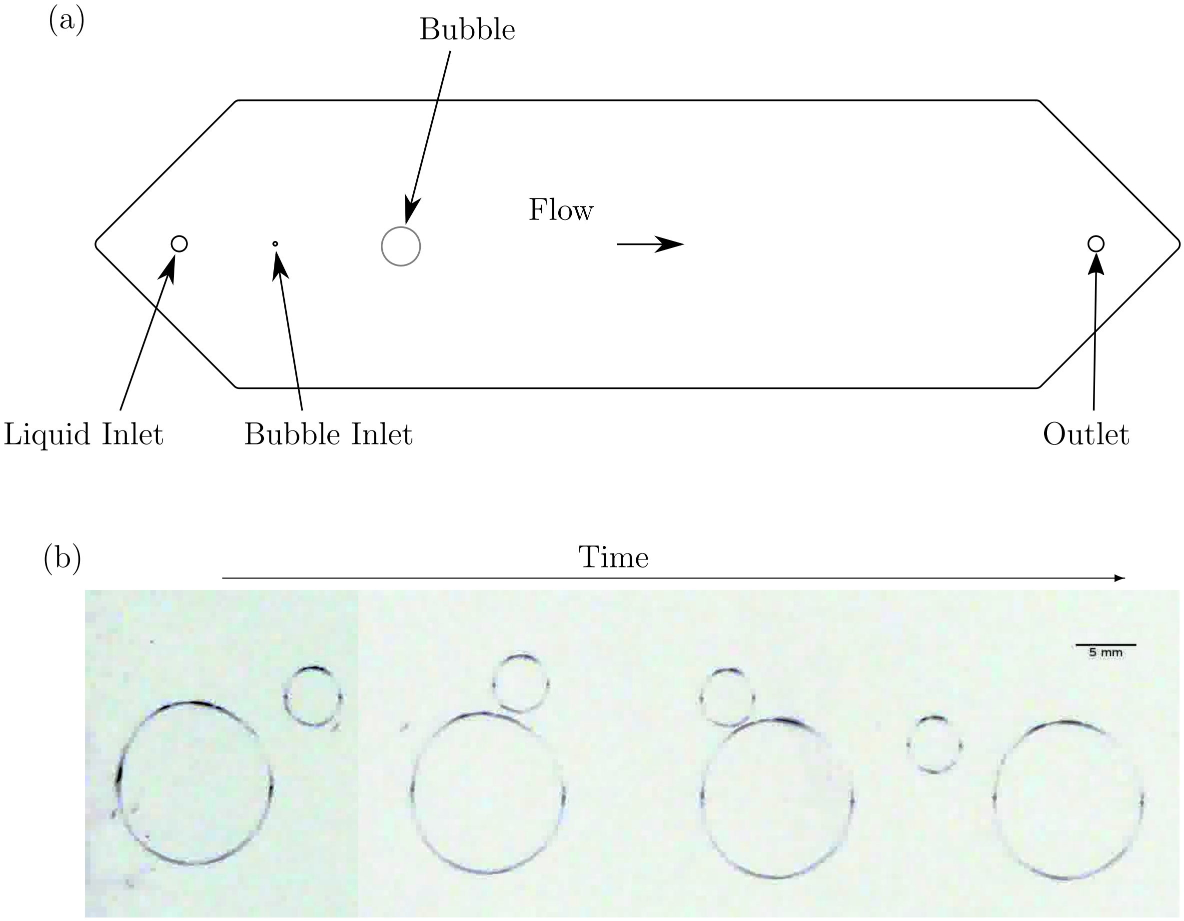

Figure 1.1: (a) Diagram of the Hele-Shaw cell including a bubble of typical size used by our collaborators at Princeton University. (b) Four snapshots of an experiment showcasing a two-bubble rollover. In these images, there is a uniform background flow from left to right.

1.2 Literature review

It was first shown by Taylor & Saffman (1959) that, in a regime where the Laplace pressure at the bubble interface is effectively constant, a circular bubble in a Hele-Shaw channel travels at twice the speed of the background flow. More generally they found that, for a specified channel width, outer liquid speed and bubble area, one can achieve an arbitrary bubble speed; selecting a particular speed then specifies the bubble shape.

Complex analysis lends itself to Hele-Shaw flow problems since the pressure in the fluid is modelled by Laplace's equation. For example, Crowdy (2009) used complex variable methods to study co-travelling multiple bubbles in an infinite Hele-Shaw cell. As in the Taylor–Saffman problem, this model does not involve surface tension and suffers from the same degeneracy. The degeneracy was resolved by Tanveer (1986), who used complex variable techniques to include surface tension in the Taylor–Saffman problem. In particular, Tanveer showed that, in the limit of large surface tension, the bubble shape is circular. A class of exact solutions for an infinite stream of groups of bubbles was derived by Vasconcelos (1994) by adapting the method of Tanveer. Green *et al.* (2017) numerically explored the effect of surface tension on the shape selection of one or two bubbles in a Hele-Shaw cell with a uniform background flow. They found that, for each fixed value of the dimensionless surface tension, there exists a countably infinite number of possible shapes, one of which is always a circular bubble travelling at twice the background velocity. This work was extended by Lustri *et al.* (2020) through the use of exponential asymptotics to solve the selection problem analytically in the limit as the dimensionless surface tension tends to zero.

The effects of varying the geometry of the Hele-Shaw cell have also been studied, both experimentally and numerically. For example, exotic stable bubble shapes can be obtained by introducing a rail along the centre-line of a Hele-Shaw channel (Gaillard *et al.*, 2021; Keeler *et al.*, 2019; Franco-Gómez *et al.*, 2018). Furthermore, Keeler *et al.* (2022) find stable configurations of two bubbles of different sizes that travel either along the same edge of the rail or along opposite edges.

In this thesis, unlike all of the above studies we include the effects of the thin liquid films above and below the bubble.

Bretherton (1961) studied an inviscid bubble moving through a viscous liquid in a capillary tube in the limit of small capillary number $\mathrm{Ca}_b = \hat{\mu}\hat{U}_b/\hat{\gamma}$, where $\hat{\mu}$ is the liquid viscosity, $\hat{U}_b$ is the bubble velocity, and $\hat{\gamma}$ is the liquid–air surface tension. Bretherton's analysis was formalised by Park & Homsy (1984) using matched asymptotic expansions, while applying the theory to two-phase flow in a Hele-Shaw cell. For our purposes, their main finding is that viscous flow in the thin liquid films between the bubble and the cell walls causes an additional pressure jump across the bubble–liquid interface, which is proportional to $\mathrm{Ca}_b^{2/3}$. This result was corroborated by Reinelt (1987), who further used numerical methods to extend the theory to $O(1)$ capillary numbers. Meiburg (1989) demonstrated numerically how Tanveer's solutions are modified by the inclusion of this additional pressure drop. The effective boundary condition used by Meiburg (1989) was improved by Burgess & Foster (1990), both to capture correctly the Bretherton pressure drop at the rear interface of a moving bubble, and to analyse inner regions where the liquid flow is approximately tangent to the bubble interface and the Park & Homsy (1984) model breaks down. Reichert *et al.* (2019) included the Bretherton pressure drop in their model for an isolated circular bubble in a Hele-Shaw cell with a uniform background flow. Reyssat (2014) also included the Bretherton drag force in his model for a bubble in a Hele-Shaw cell whose walls are slightly inclined to form a thin wedge, and observed that the bubble migrates out of the wedge to reduce its surface area.

Kopf-Sill & Homsy (1988) studied experimentally the velocities of variously shaped bubbles in a Hele-Shaw cell, in particular observing circular bubbles that travel more slowly than the background flow. However, Park *et al.* (1994) argued that this behaviour was due to the presence of surfactants, and their experiments showed circular bubbles moving more quickly than the background flow, though still less than twice as fast (the Taylor–Saffman limit). Similarly, Reichert *et al.* (2019) observed circular bubbles travelling faster than the outer liquid velocity but with a larger range of bubble velocities. Shen *et al.* (2014) investigated the motion of multiple droplets in a Hele-Shaw channel, observing behaviour including pair exchange, where a single droplet catches up to a pair of bubbles and then the leading bubble breaks away. Beatus *et al.* (2006, 2012) explored instabilities in a one-dimensional array of droplets, resulting in the formation of transverse and longitudinal waves. Their experimental observations were captured well by a model where the droplets are treated as dipoles, although in principle this approach is strictly valid only when the droplets are sufficiently well-separated.

It is common practice in many microfluidic experiments to include surfactants (Beatus *et al.*, 2006; Shen *et al.*, 2014; Anna, 2016) because surfactants stabilise bubbles against coalescence. Ratulowski & Chang (1990) extended the result of Bretherton to a finger of air propagating into a viscous fluid containing soluble surfactants. They proposed five different distinguished limits based on the convective, diffusive and kinetic timescales. Building on this work, Park (1992) considered the flow of a long bubble in a capillary tube and found that surfactants can rigidify the bubble's surface, and Maruvada & Park (1996) generalised the Taylor–Saffman solution to describe a rigid elliptical surfactant-laden bubble in a Hele-Shaw cell.

1.3 Overview

In Chapter 2 we derive a model for a bubble being swept along by a uniform flow in a Hele-Shaw cell, in a distinguished asymptotic limit where the Bretherton pressure drop is of the same order as the Hele-Shaw viscous forces. In this regime, the bubble remains approximately circular, as in many microbubble experiments. The pressure in the liquid is found by solving a Neumann boundary-value problem and the *a priori* unknown bubble velocity is determined by a net force balance on the bubble. The theoretically predicted bubble velocity is found to agree well with experimental results collected by our collaborator, Katie Wu (Princeton University). We then generalise this result to include the effects of cell boundaries.

Many microfluidic experiments involve the motion of more than one bubble. In Chapter 3 we extend our model to the motion of two bubbles in a Hele-Shaw cell in a uniform background flow. We derive analytical equations of motion using complex variable techniques. We find that, for two bubbles of different radii, a larger bubble can catch up with a smaller one. In some cases the bubbles rotate around each other, leaving the larger in front, while in other cases the bubbles collide, and we derive conditions to distinguish between the two cases.

For an arbitrary number of bubbles, a general analytic solution is no longer possible. In Chapter 4 we develop methodologies for simulating an arbitrary number of bubbles in a Hele-Shaw cell. We begin by developing a numerical framework to solve the full model, which we validate against the known two-bubble solution. In a train of three collinear identical bubbles moving along the centre-line of a Hele-Shaw channel, we find that the middle bubble moves either faster or slower than the outer two bubbles, forming what we refer to as a Hele-Shaw Newton's cradle.

It is common in the literature when modelling a large number of bubbles to assume that each bubble acts as if it is a dipole (see e.g. Beatus *et al.*, 2006; Shen *et al.*, 2014). We derive this result through the use of matched asymptotic expansions. We find that this method qualitatively reproduces the behaviour of the full model at a much reduced computational cost. We also derive a pairwise interaction model by using the analytical two-bubble solution and summing over each possible bubble pair. This improved model allows us to consider situations in which two bubbles become close to a greater accuracy than is provided by the dipole model.

In Chapter 5 we return to an isolated bubble in a Hele-Shaw cell with a uniform background flow, now focusing on the bubble shape. We observe that the bubble can either flatten or elongate in the direction of propagation, depending on the flow conditions. This behaviour is also captured in experimental observations by our collaborator, Katie Wu (Princeton University). We then examine the deformations of a pair of bubbles aligned with the direction of the flow. In the situation where the bubbles are the same size, we find that the bubble in front flattens in the direction of motion while the bubble behind elongates, resulting in the rear bubble travelling faster than the one in front.

We consider the propagation of a bubble in a non-uniform background flow in Chapter 6. We find that the bubble centre travels along a streamline of the background flow although, unlike a tracer particle, the bubble does not travel at the same speed as the background flow. We apply the model to common microfluidic components, such as a T-junction and injection sources and sinks. Using the same methodology, we derive approximate solutions for the motion of a bubble in more complicated domains including walls or obstacles. We validate the approximate approach with two test cases in which we can find the full solution analytically. First, we consider the effect of an impermeable wall on a bubble in a stagnation-point flow. Second, we consider the motion of a bubble around a circular obstacle. In both cases, the bubble deviates noticeably from the streamlines of the background flow only when it is very close to the wall or the obstacle.

As noted in §1.2 surfactants are widely used in microfluidic devices to stabilise bubbles against coalescence. In Chapter 7 we investigate how the addition of surfactants affects the governing equations for a bubble in a Hele-Shaw cell. Including surfactants changes the surface tension of the bubble interface and hence the pressure drop across it. We perform an asymptotic analysis similar to that conducted by Park & Homsy (1984) to determine how surfactant affects the Bretherton pressure drop. We find that a surfactant-laden bubble travels slower than a surfactant-free bubble experiencing the same flow conditions.

Finally, in Chapter 8 we end this thesis with a summary of the work and discuss avenues for further work.

Chapter 2

The motion of a single bubble in a Hele-Shaw cell

2.1 Introduction

In this chapter we derive a simple model for the motion of an approximately circular bubble in a Hele-Shaw cell, then use it to describe bubble propagation along a microfluidic channel modelled as a long Hele-Shaw cell with side walls.

We begin in §2.2 by deriving a model for a bubble being swept along by a uniform flow in a Hele-Shaw cell, in a distinguished asymptotic limit where the pressure drop due to the thin films above and below the bubble is of the same order as the Hele-Shaw viscous forces. In this regime, the bubble remains approximately circular, as in many microbubble experiments; the pressure in the surrounding liquid is found by solving a Neumann problem involving the *a priori* unknown bubble velocity, which is determined by a coupled net force balance on the bubble.

The effect of side walls on the bubble dynamics is considered in §2.3 and §2.4. An analytical solution is found for a single side wall using complex variable methods. For a general channel geometry we develop a numerical method to solve for the streamfunction of the flow around the bubble. We discover that the inclusion of side walls can either increase the bubble speed (in comparison to the speed of a bubble in an infinite medium) or decrease it, depending on the flow conditions.

2.2 Isolated bubble

2.2.1 Governing equations

We begin by considering an isolated bubble in a Hele-Shaw cell of thickness $\hat{h}$ parallel to the $(\hat{x}, \hat{y})$-plane. Under the lubrication approximation, in the limit where $\hat{h}$ is much

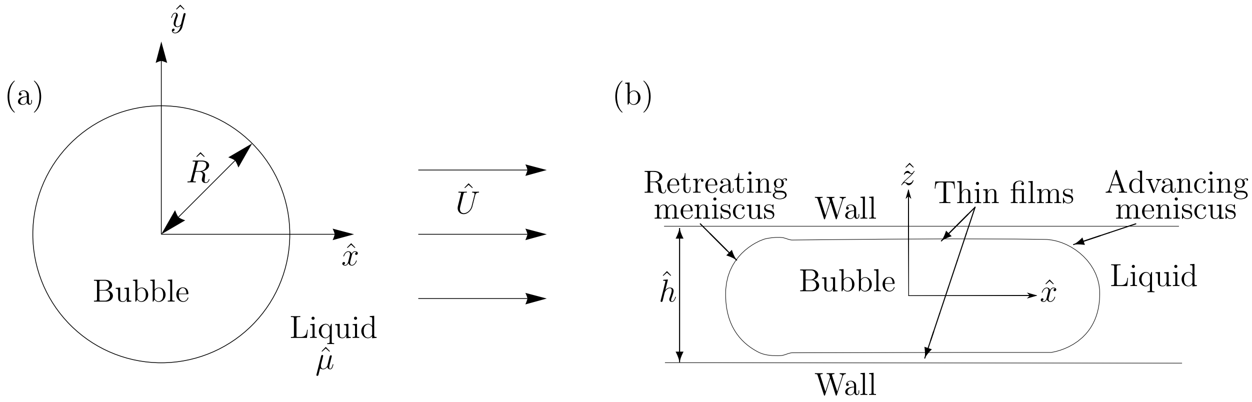

Figure 2.1: (a) Plan view of a bubble in a Hele-Shaw cell with a uniform background flow of speed $\hat{U}$. (b) Side view of the bubble.

smaller than the horizontal dimensions of the cell and the bubble, the flow away from the bubble is governed by the Hele-Shaw equations:

$$\hat{\boldsymbol{v}} = \frac{3}{2}\hat{\boldsymbol{u}}\left(1 - \frac{4\hat{z}^2}{\hat{h}^2}\right), \tag{2.1a}$$

$$\hat{\boldsymbol{\nabla}} \cdot \hat{\boldsymbol{u}} = 0, \tag{2.1b}$$

$$\hat{\boldsymbol{u}} = -\frac{\hat{h}^2}{12\hat{\mu}}\hat{\boldsymbol{\nabla}}\hat{p}. \tag{2.1c}$$

Here, $\hat{\boldsymbol{v}}(\hat{x}, \hat{y}, \hat{z})$ is the full fluid velocity profile, $\hat{\boldsymbol{u}}(\hat{x}, \hat{y})$ is the depth-averaged fluid velocity, $\hat{z} \in [-\hat{h}/2, \hat{h}/2]$ denotes the height coordinate, $\hat{p}(\hat{x}, \hat{y})$ is the leading-order pressure, and $\hat{\mu}$ is the fluid viscosity.

In this section we focus on the simple model problem of a single bubble in a large cell with a prescribed uniform background flow of speed $\hat{U}$ in the $\hat{x}$-direction, which gives us the far-field condition

$$\hat{\boldsymbol{u}} \to \hat{U}\boldsymbol{i} \quad \text{as} \quad \hat{x}^2 + \hat{y}^2 \to \infty, \tag{2.2}$$

where $\boldsymbol{i}$ is the unit vector in the $\hat{x}$-direction.

Looking down on the cell from above (figure 2.1(a)), the boundary of the bubble appears to be a closed curve in the $(\hat{x}, \hat{y})$-plane, on which we impose the effective boundary conditions (Meiburg, 1989)

$$\boldsymbol{n} \cdot \hat{\boldsymbol{u}} = \hat{U}_n, \tag{2.3a}$$

$$\hat{p}_b - \hat{p} = \frac{2\hat{\gamma}}{\hat{h}} + \frac{2\hat{\gamma}}{\hat{h}}\beta(\mathrm{Ca}_n)\mathrm{Ca}_n^{2/3} + \frac{\hat{\gamma}\pi}{4}\hat{\kappa}. \tag{2.3b}$$

Here, $\boldsymbol{n}$, $\hat{U}_n$ and $\hat{\kappa}$ are the outward-pointing normal, normal velocity and curvature of the apparent bubble boundary, respectively; $\hat{\gamma}$ is the surface-tension parameter, $\hat{p}_b$ is the uniform pressure inside the bubble, $\mathrm{Ca}_n = \hat{\mu}\hat{U}_n/\hat{\gamma}$ is the capillary number based on the normal velocity, and β is the Bretherton coefficient, whose value depends on whether the meniscus is advancing or retreating (Bretherton, 1961; Halpern & Jensen, 2002; Wong *et al.*, 1995):

$$\beta(\mathrm{Ca}_n) = \begin{cases} \beta_1 \approx 3.88 & \text{when } \mathrm{Ca}_n > 0, \\ \beta_2 \approx -1.13 & \text{when } \mathrm{Ca}_n < 0. \end{cases} \tag{2.4}$$

The first term on the right-hand side of equation (2.3b) is the capillary pressure difference due to the meniscus at the bubble boundary, whose leading-order radius of curvature is given by $\hat{h}/2$. The second term containing the capillary number is the correction to the pressure difference in the limit $\mathrm{Ca}_n \ll 1$, derived in Bretherton's original paper (Bretherton, 1961), due to the existence of the thin-film regions between the bubble and the walls of the cell (see figure 2.1(b)). The final term in (2.3b) captures the in-plane contribution to the curvature of the bubble interface, including the $\pi/4$ factor derived by Park & Homsy (1984). We will further discuss the underlying assumptions and validity of the boundary condition (2.3b) in §2.2.4.

2.2.2 Non-dimensionalisation

We non-dimensionalise the model (2.1)–(2.3), scaling lengths with a typical bubble radius, $\hat{R}$, and velocities with the far-field uniform flow speed, $\hat{U}$. We also scale $\hat{p}$ with $12\hat{\mu}\hat{U}\hat{R}/\hat{h}^2$, $\hat{p}_b$ with $2\hat{\gamma}/\hat{h}$ and $\hat{\kappa}$ with $1/\hat{R}$. This process yields the following dimensionless system (in which dimensionless variables are denoted without hats):

$$\begin{aligned} \nabla^2 p &= 0 && \text{in} \quad \Omega, && \text{(2.5a)} \\ p_b - \frac{3\mathrm{Ca}}{\epsilon} p &= 1 + \mathrm{Ca}^{2/3}\beta(U_n)U_n^{2/3} + \frac{\epsilon\pi}{4}\kappa && \text{on} \quad \partial\Omega_b, && \text{(2.5b)} \\ \boldsymbol{n}\cdot\boldsymbol{\nabla} p &= -U_n && \text{on} \quad \partial\Omega_b, && \text{(2.5c)} \\ p &\sim -x + o(1) && \text{as} \quad x^2+y^2 \to \infty, && \text{(2.5d)} \end{aligned}$$

where Ω is the fluid domain and $\partial\Omega_b$ is the apparent bubble–fluid boundary in the (x, y)-plane, whose normal velocity is U_n. The far-field condition (2.5d) (with no logarithmic contribution, so there are no fluid sources) enforces conservation of the bubble area and thus in principle allows the bubble pressure p_b to be determined as part of the solution.

The system (2.5) contains two dimensionless parameters, the aspect ratio and the capillary number, defined by

$$\epsilon = \frac{\hat{h}}{2\hat{R}}, \qquad \mathrm{Ca} = \frac{\hat{\mu}\hat{U}}{\hat{\gamma}}, \tag{2.6}$$

respectively. For the boundary-value problem (2.5) to be valid, both of these parameters must be small: the Hele-Shaw model relies on ϵ being small, while the boundary condition (2.3b) is an asymptotic approximation in the limit $\mathrm{Ca} \to 0$ (Park & Homsy, 1984). In the boundary condition (2.5b), the dominant balance depends on the relative size of these two small parameters.

In this chapter, we study flows in which the Hele-Shaw pressure is of the same order as the Bretherton drag term, and equation (2.5b) shows that this occurs when $\mathrm{Ca} = O(\epsilon^3)$. Expanding p_b and κ as asymptotic expansions in powers of ϵ in (2.5b) we then see that

$$p_{b_0} + \epsilon p_{b_1} + \epsilon^2 p_{b_2} - \underbrace{\frac{3\mathrm{Ca}}{\epsilon}p}_{O(\epsilon^2)} + O(\epsilon^3) \sim 1 + \frac{\epsilon\pi}{4}(\kappa_0 + \epsilon\kappa_1) + \underbrace{\beta \mathrm{Ca}^{2/3} U_n^{2/3}}_{O(\epsilon^2)} + O(\epsilon^3) \tag{2.7}$$

on $\partial\Omega_b$. At $O(1)$ we find that $p_{b_0} = 1$, indicating that the leading-order bubble pressure is determined by the capillary pressure jump across the meniscus. At $O(\epsilon)$ we obtain $\kappa_0 = 4p_{b_1}/\pi = \text{constant}$, which implies that the bubbles we are studying are circular to leading order in ϵ. By our choice of lengthscale $\hat{R}$ we can take the bubble here to have unit dimensionless radius.

Since the bubble remains (approximately) circular for all time, the normal velocity on the boundary is just given by $U_n = \boldsymbol{U}_b \cdot \boldsymbol{n}$, where $\boldsymbol{U}_b = (U_b, V_b)$ is the constant bubble velocity. In terms of plane polar coordinates (r, θ) based on the bubble centre, we therefore find that the pressure in the liquid satisfies the problem

$$\nabla^2 p = 0 \qquad \text{in} \quad r > 1, \tag{2.8a}$$

$$\frac{\partial p}{\partial r} = -\boldsymbol{U}_b \cdot \boldsymbol{n} = -U_b \cos\theta - V_b \sin\theta \qquad \text{on} \quad r = 1, \tag{2.8b}$$

$$p \sim -r\cos\theta + o(1) \qquad \text{as} \quad r \to \infty. \tag{2.8c}$$

If $\boldsymbol{U}_b$ were known, then p would be uniquely determined by (2.8). To find the bubble velocity, we return to the boundary condition (2.5b), which so far has been imposed up to $O(\epsilon)$. In principle the solvability condition at $O(\epsilon^2)$ determines $\boldsymbol{U}_b$ and closes the problem. As a shortcut to deriving this condition, we note that, for any smooth closed planar curve $\partial\Omega_b$ and with $\boldsymbol{k}$ denoting the unit vector in the z-direction,

$$\oint_{\partial\Omega_b} \boldsymbol{n}\,\mathrm{d}s = \oint_{\partial\Omega_b} \boldsymbol{k} \times \frac{\mathrm{d}\boldsymbol{r}}{\mathrm{d}s}\,\mathrm{d}s = \boldsymbol{0}, \qquad \oint_{\partial\Omega_b} \kappa\boldsymbol{n}\,\mathrm{d}s = \oint_{\partial\Omega_b} -\frac{\mathrm{d}^2\boldsymbol{r}}{\mathrm{d}s^2}\,\mathrm{d}s = \boldsymbol{0}, \tag{2.9}$$

by standard results from differential geometry (see, e.g., Kreyszig, 1959, Chapter 2). We therefore obtain from (2.5b) the constraint

$$\oint_{\partial\Omega_b} -p\boldsymbol{n}\,\mathrm{d}s = \frac{\epsilon}{3\mathrm{Ca}^{1/3}}\oint_{\partial\Omega_b}\beta(\boldsymbol{U}_b\cdot\boldsymbol{n})(\boldsymbol{U}_b\cdot\boldsymbol{n})^{2/3}\boldsymbol{n}\,\mathrm{d}s, \tag{2.10}$$

which may be interpreted as a force balance on the bubble.

To evaluate the integral on the right-hand side of (2.10), we now use the fact that, to leading order, the boundary $\partial\Omega_b$ is the unit circle, which we parameterise using

$$\boldsymbol{r}(s) = \frac{\boldsymbol{U}_b}{|\boldsymbol{U}_b|}\cos s + \frac{\boldsymbol{k}\times\boldsymbol{U}_b}{|\boldsymbol{U}_b|}\sin s. \tag{2.11a}$$

With β given by (2.4), we thus obtain

$$\begin{aligned}\oint_{\partial\Omega_b}\beta(\boldsymbol{U}_b\cdot\boldsymbol{n})(\boldsymbol{U}_b\cdot\boldsymbol{n})^{2/3}\boldsymbol{n}\,\mathrm{d}s &= \int_0^{2\pi}\frac{\beta(\cos s)|\cos s|^{2/3}}{|\boldsymbol{U}_b|^{1/3}}\left(\boldsymbol{U}_b\cos s + \boldsymbol{k}\times\boldsymbol{U}_b\sin s\right)\,\mathrm{d}s\\ &= (\beta_1-\beta_2)\,\frac{\sqrt{\pi}\Gamma(4/3)}{\Gamma(11/6)}\,\frac{\boldsymbol{U}_b}{|\boldsymbol{U}_b|^{1/3}},\end{aligned} \tag{2.11b}$$

where Γ denotes the Gamma function. Thus (2.10) reduces to the following condition for the bubble velocity:

$$\frac{\boldsymbol{U}_b}{|\boldsymbol{U}_b|^{1/3}} = \frac{\delta}{\pi}\oint_{r=1} -p\boldsymbol{n}\,\mathrm{d}s, \tag{2.12}$$

where we define the *Bretherton parameter*

$$\delta = \frac{3\sqrt{\pi}\Gamma(11/6)}{(\beta_1-\beta_2)\Gamma(4/3)}\,\frac{\mathrm{Ca}^{1/3}}{\epsilon} \approx 1.12\frac{\mathrm{Ca}^{1/3}}{\epsilon}. \tag{2.13}$$

By assumption, δ is $O(1)$ while ϵ and Ca are asymptotically small. The prefactor introduced in (2.13) is for later convenience, such that we observe a change in behaviour across $\delta = 1$.

2.2.3 Solution

The problem (2.8) for an isolated circular bubble in an infinite cell is easily solved to obtain the pressure

$$p = \left(\frac{U_b - 1}{r} - r\right)\cos\theta + \frac{V_b}{r}\sin\theta. \tag{2.14}$$

We can thus evaluate the integral on the right-hand side of the force balance (2.12) to obtain an equation for the bubble velocity, namely

$$\frac{\boldsymbol{U}_b}{|\boldsymbol{U}_b|^{1/3}} = \delta(2\boldsymbol{i} - \boldsymbol{U}_b). \tag{2.15}$$

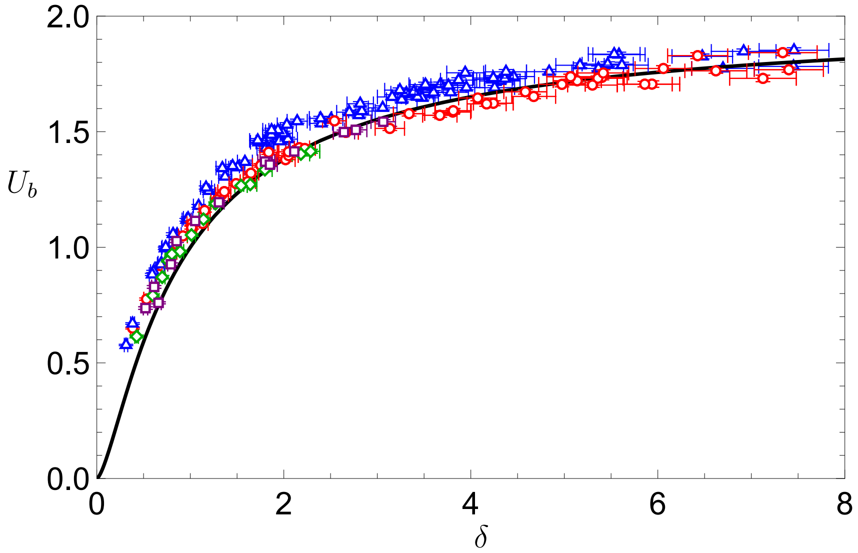

Figure 2.2: The ratio U_b of the bubble velocity to the outer fluid velocity as a function of the Bretherton parameter δ. The solid curve shows the model prediction (2.16). The points show experimental data (collected by Katie Wu, Princeton University): (red circle) $\mathrm{Ca} = 6.6 \times 10^{-4}$, (blue triangle) $\mathrm{Ca} = 3.3 \times 10^{-4}$, (green diamond) $\mathrm{Ca} = 4.1 \times 10^{-4}$, and (purple square) $\mathrm{Ca} = 6.1 \times 10^{-4}$ with the aspect ratio ϵ in the range 0.01–0.25.

It follows that the bubble moves parallel to the background flow, as expected, with $\boldsymbol{U}_b = U_b \boldsymbol{i}$, where U_b satisfies the algebraic equation

$$\frac{U_b^{2/3}}{2 - U_b} = \delta. \tag{2.16}$$

The equation (2.16) for the bubble speed is equivalent to that found in Reichert *et al.* (2019), using a laborious viscous dissipation argument[1]. We note that equation (2.16) may be transformed into a cubic and thus solved explicitly for U_b; however the resulting expression is unwieldy and not particularly illuminating.

From equation (2.16) we observe a transition in behaviour at $\delta = 1$: if $\delta < 1$ the bubble moves more slowly than the outer flow ($U_b < 1$) while if $\delta > 1$ the bubble moves faster than the outer flow ($U_b > 1$). The critical case where $U_b = 1$, so the bubble moves with the external flow, corresponds to the particular solution of the problem where $p \equiv -x$. We see that this solution satisfies (2.8) provided $(U_b, V_b) = (1, 0)$, and the force balance (2.12) is also satisfied provided $\delta = 1$.

---

[1] In Reichert *et al.* (2019) the constant of proportionality in (2.13) is found to be 1.20 rather than 1.12, due to inaccurate calculation of the integral and the Bretherton constants. Their method involves solution for the height of the thin liquid films above and below the bubble, followed by calculation of the viscous dissipation due to the thin films.

In figure 2.2, we plot the prediction (2.16) for the dimensionless bubble velocity U_b versus the Bretherton parameter δ, alongside results of experiments conducted by Katie Wu and our collaborators at Princeton University. We observe very good agreement between theory and experiments, including in the previously unstudied regime where $\delta < 1$. The experimental results support the predicted transition of the bubble speed from slower to faster than the outer flow as δ increases through 1.

We observe that U_b is an increasing function of δ; from (2.13) we see that δ is proportional to the bubble radius $\hat{R}$, which implies that larger bubbles should travel faster. As $\delta \to 0$, the Bretherton drag term dominates and $U_b \sim (2\delta)^{3/2}$. At the other extreme where $\delta \gg 1$, we recover the Taylor–Saffman result (Taylor & Saffman, 1959) of the bubble moving twice as fast as the outer flow. However, we note that the assumption of the bubble remaining approximately circular eventually fails if δ is too large. Specifically, we find from (2.5b) that variations in the curvature of the bubble boundary $\partial\Omega_k$ are of order $\delta^3\epsilon$. For the validity of our model we thus require $\delta \ll \epsilon^{-1/3}$. However as will be shown in Chapter 5 the assumption that the bubble is circular to leading order holds for a larger range of δ, specifically $\delta \ll \epsilon^{-1/2}$.

2.2.4 Validity of the model

We now discuss the validity of the boundary condition (2.3b). At the front interface of a moving bubble, the additional pressure drop (proportional to $\mathrm{Ca}_n^{2/3}$) may be derived by solving Bretherton's problem for a meniscus advancing with effective capillary number Ca_n (Bretherton, 1961). As noted by Reichert *et al.* (2019), this approach is invalid close to points where Ca_n changes sign. Burgess & Foster (1990) showed that the discontinuous term in (2.3b), involving the function β, is smoothed out in "lateral transition regions" (LTRs) where $\mathrm{Ca}_n = O(\epsilon^{3/5}\mathrm{Ca}^{1/5})$. In the distinguished limit studied here, Ca is assumed to be of order ϵ^3, and it follows that *the LTRs contribute corrections of order* $\epsilon^{6/5}$ *to the force balance* (2.10). Since other corrections of order ϵ have already been neglected, we conclude that these effects are indeed negligible in our model.

At a retreating meniscus, as well as the local value of Ca_n, the additional pressure drop depends also on the thickness of the liquid films between the bubble and the cell walls into which the interface is propagating. The liquid film thickness depends on Ca_n^+, the normal capillary number at the corresponding point on the front interface that deposited the thin films currently being consumed by the rear interface. In

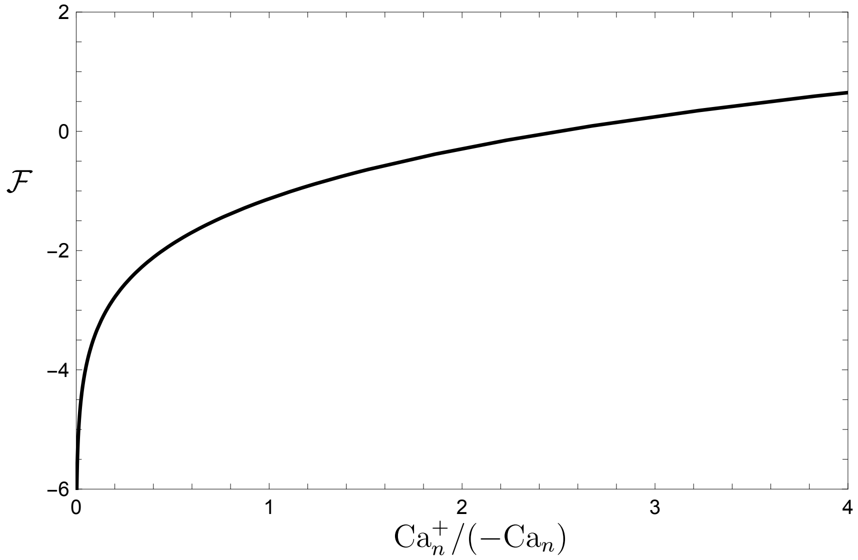

Figure 2.3: The function $\mathcal{F}(\mathrm{Ca}_n^+/(-\mathrm{Ca}_n))$ defined in (Burgess & Foster, 1990).

general, this dependence leads to a drag coefficient of the form

$$\beta(\mathrm{Ca}_n) = \mathcal{F}\left(\mathrm{Ca}_n^+/(-\mathrm{Ca}_n)\right) \tag{2.17}$$

when $\mathrm{Ca}_n < 0$. The function $\mathcal{F}$ has been calculated e.g. by Burgess & Foster (1990) and we plot the function in figure 2.3. For a circular bubble moving at constant velocity, we have $\mathrm{Ca}_n^+ \equiv -\mathrm{Ca}_n$, so $\beta(\mathrm{Ca}_n) = \mathcal{F}(1) = \beta_2$ whenever $\mathrm{Ca}_n < 0$, as in (2.4). For a non-circular bubble moving at constant velocity, the argument of the function $\mathcal{F}$ in (2.17) is equal to $\mathrm{Ca}_n^+/(-\mathrm{Ca}_n) = \cos\theta_+/(-\cos\theta_-)$, where $\theta_\pm$ are the angles the normal vectors make with the direction of motion at corresponding points on the front and rear bubble interfaces (Burgess & Foster, 1990), we show an example of this selection in figure 2.4.

The situation is more complicated when the motion is unsteady, even if the bubbles remain (approximately) circular, as assumed in this thesis. According to (2.17), the pressure drop across the rear meniscus depends on the normal velocity at the front meniscus at some previous time, and the force balance (2.10) thus produces an integral equation rather than an algebraic equation for the bubble velocity. This is the subject of further work.

2.3 Single bubble near a wall

Next we consider the case of a single bubble in a semi-infinite Hele-Shaw cell occupying the half-space $y > 0$ with an impermeable wall at $y = 0$ and a uniform

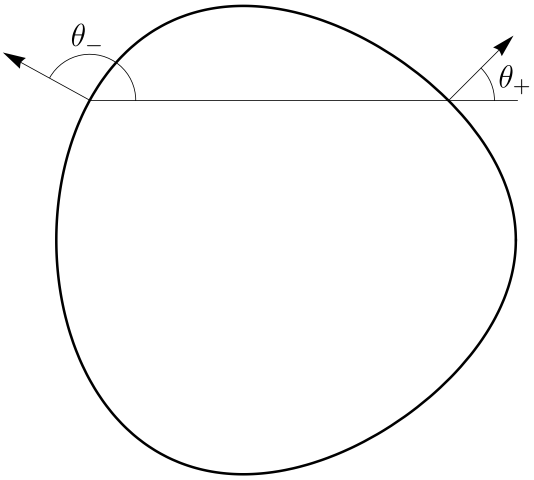

Figure 2.4: An example of the selection of $\mathrm{Ca}_n^+/(-\mathrm{Ca}_n) = \cos\theta_+/(-\cos\theta_-)$ for a non-circular bubble.

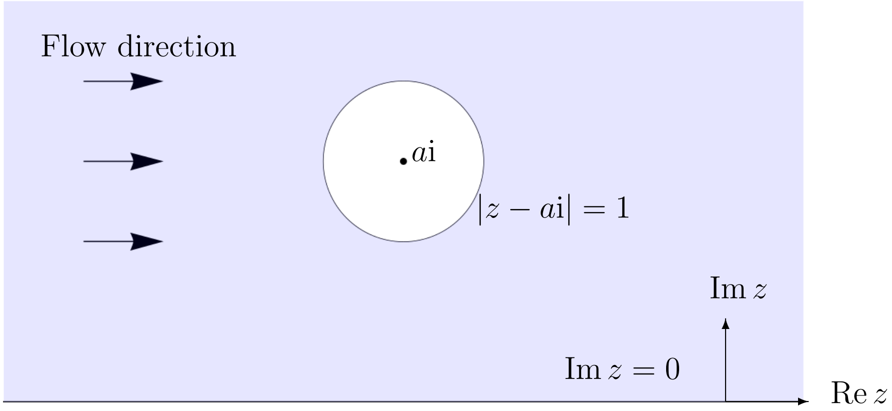

Figure 2.5: Plan view of a bubble in a semi-infinite Hele-Shaw cell.

flow $-\boldsymbol{\nabla} p \sim \boldsymbol{i}$ at infinity. The bubble is taken to have unit dimensionless radius with its centre a dimensionless distance $a > 1$ away from the boundary (see figure 2.5). The following analysis allows us to examine how proximity to a wall affects the velocity of the bubble, and also illustrates the application of complex variable methods to our model. This formulation is equivalent to the problem of two identical bubbles in an infinite cell with their centres separated by $2a$ and lined up perpendicular to the outer flow direction, with the wall representing the line of symmetry between them. The corresponding two-bubble problem was solved by Sarig *et al.* (2016) using bipolar coordinates rather than complex variables. We choose the bubble centre to be instantaneously at $z = x + \mathrm{i}y = a\mathrm{i}$, so that the domain of interest is $\Omega = \{z : \mathrm{Im}(z) > 0, |z - a\mathrm{i}| > 1\}$.

Since p satisfies Laplace's equation, we introduce a complex potential $w(z) = -p + \mathrm{i}\psi$, where ψ is the streamfunction. The problem is then to find a holomorphic function $w(z)$ in the region Ω such that

$$\operatorname{Im}[w(z)] = 0 \qquad \text{on} \quad \operatorname{Im} z = 0, \tag{2.18a}$$

$$\operatorname{Im}[w(z)] = q + \operatorname{Im}\left[\overline{\mathcal{U}}_b z\right] \qquad \text{on} \quad |z - a\mathrm{i}| = 1, \tag{2.18b}$$

$$w(z) \sim z \qquad \text{as} \quad z \to \infty. \tag{2.18c}$$

Both the complex bubble velocity $\mathcal{U}_b = U_b + \mathrm{i}V_b$ and the real constant q are *a priori* unknown; q represents the flux of liquid through the gap between the bubble and the wall (relative to the moving bubble). The over-bar denotes complex conjugation. Once we have solved for $w(z)$, the equation of motion (2.12) may be imposed by evaluating

$$\frac{1}{\mathrm{i}\pi} \oint_{\partial\Omega_b} w(z)\,\mathrm{d}z = -\mathcal{U}_b + \frac{1}{\pi} \oint_{\partial\Omega_b} p\mathrm{i}\,\mathrm{d}z = -\mathcal{U}_b + \frac{\mathcal{U}_b}{\delta\,|\mathcal{U}_b|^{1/3}}. \tag{2.19}$$

We proceed by conformally mapping Ω onto a concentric annulus, where the problem becomes solvable with standard techniques. Following the mapping

$$\zeta = f(z) = \frac{z - \mathrm{i}\sqrt{a^2-1}}{z + \mathrm{i}\sqrt{a^2-1}}, \tag{2.20}$$

the solution domain in the ζ-plane is $A = \{\zeta : X < |\zeta| < 1\}$, where

$$X = \ a - \sqrt{a^2 - 1}. \tag{2.21}$$

Writing the complex potential in the form $w(z) = z + W\big(f(z)\big)$, we find that $W(\zeta)$ is holomorphic on A and satisfies the boundary conditions (see figure 2.6)

$$\operatorname{Im}[W(\zeta)] = 0 \qquad \text{on} \quad |\zeta| = 1, \tag{2.22a}$$

$$\operatorname{Im}[W(\zeta)] = q - \operatorname{Im}\left[\alpha\left(\frac{1+\zeta}{1-\zeta}\right)\right] \qquad \text{on} \quad |\zeta| = X, \tag{2.22b}$$

where $\alpha = \big(1 - \overline{\mathcal{U}}_b\big)\,\mathrm{i}\sqrt{a^2-1}$.

Now we express $W(\zeta)$ as a Laurent expansion on A, i.e.

$$W(\zeta) = \sum_{n=-\infty}^{\infty} b_n \zeta^n. \tag{2.23}$$

We then use the boundary conditions (2.22) to calculate the coefficients b_n. On $|\zeta| = 1$ we have $\overline{\zeta} = 1/\zeta$ so (2.22a) may be rearranged to

$$\operatorname{Im}\big[W(\zeta)\big] = \operatorname{Im}[b_0] + \operatorname{Im}\left[\sum_{n=1}^{\infty} \left(b_n - \overline{b}_{-n}\right)\zeta^n\right] = 0. \tag{2.24}$$

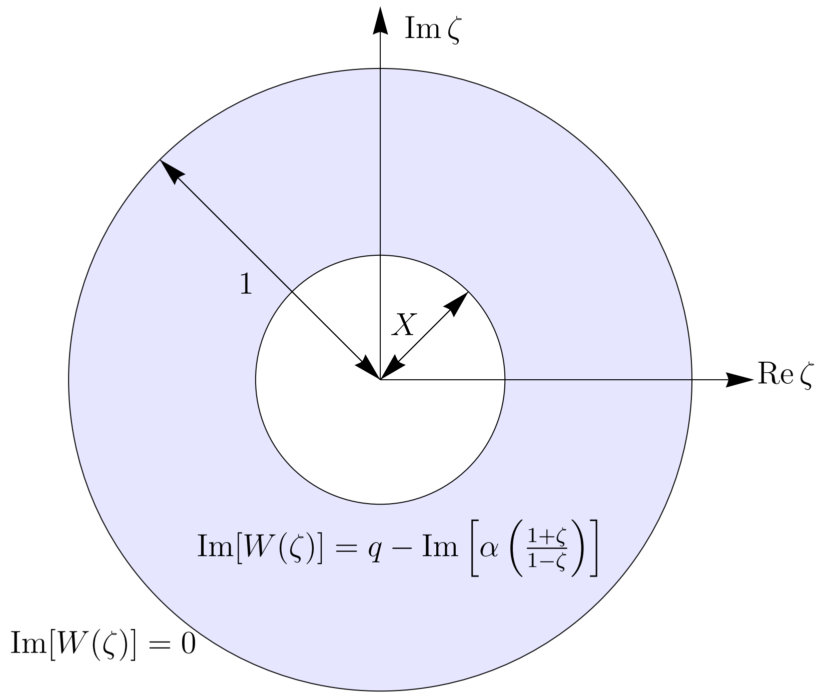

Figure 2.6: Schematic of the problem (2.22) in the ζ-plane.

It follows that

$$\overline{b}_{-n} = b_n \qquad (n \geq 1), \tag{2.25}$$

while b_0 is real and, without loss of generality, may be set to zero.

When we impose the boundary condition (2.22b) at $|\zeta| = X$, there is a singularity at $\zeta = 1$. We can remove this singularity by taking complex conjugates and using $\overline{\zeta} = X^2/\zeta$ to get

$$\begin{aligned}\mathrm{Im}\big[W(\zeta)\big] = q - \mathrm{Im}\left[\alpha\left(\frac{1+\zeta}{1-\zeta}\right)\right] &= q + \mathrm{Im}\left[\overline{\alpha}\frac{1+X^2/\zeta}{1-X^2/\zeta}\right] \\ &= q - \mathrm{Im}[\alpha] + 2\,\mathrm{Im}\left[\overline{\alpha}\sum_{n=1}^{\infty}\frac{X^{2n}}{\zeta^n}\right]\end{aligned} \tag{2.26}$$

on $|\zeta| = X$ (the series in square brackets now converges for $|\zeta| > X^2$). But also on $|\zeta| = X$ we have

$$\mathrm{Im}\big[W(\zeta)\big] = \mathrm{Im}\left[\sum_{n=1}^{\infty}\left(b_{-n} - X^{2n}\overline{b}_n\right)\zeta^{-n}\right]. \tag{2.27}$$

From (2.26) and (2.27) we find that the *a priori* unknown flux q is given by

$$q = \mathrm{Im}\,\alpha = (1 - U_b)\sqrt{a^2 - 1}, \tag{2.28}$$

and

$$b_n - \frac{\overline{b}_{-n}}{X^{2n}} = -2\alpha \qquad (n \geq 1). \tag{2.29}$$

Now solving (2.25) and (2.29) simultaneously we find

$$\overline{b}_{-n} = b_n = \frac{2\alpha X^{2n}}{1 - X^{2n}} \qquad (n \geq 1). \tag{2.30}$$

Thus we find that the complex potential $W(\zeta)$ in the ζ-plane is given by

$$W(\zeta) = \sum_{n=1}^{\infty} \frac{2X^{2n}}{1 - X^{2n}} (\alpha \zeta^n + \overline{\alpha} \zeta^{-n}). \tag{2.31}$$

We can thus calculate the integral on the left-hand side of equation (2.19) by transforming into the ζ-plane and then using Cauchy's Residue Theorem to obtain

$$\frac{1}{\mathrm{i}\pi} \oint_{\partial\Omega_b} w(z)\,\mathrm{d}z = \frac{2\sqrt{a^2 - 1}}{\pi} \oint_{|\zeta| = X} \frac{W(\zeta)}{(\zeta - 1)^2}\,\mathrm{d}\zeta = (1 - \mathcal{U}_b) F(a), \tag{2.32}$$

where

$$F(a) = 8\left(a^2 - 1\right) \sum_{n=1}^{\infty} \frac{n X^{2n}}{1 - X^{2n}}, \tag{2.33}$$

with X given as a function of a by (2.21). The formula (2.33) may be written in closed form as

$$F(a) = 2(a^2 - 1) \frac{\Psi'_{X^2}(1)}{\log^2 X}, \tag{2.34}$$

in which Ψ denotes the q-digamma function (Salem, 2012), defined by

$$\Psi_q(z) = \frac{1}{\Gamma_q(z)} \frac{\mathrm{d}\Gamma_q(z)}{\mathrm{d}z}, \tag{2.35}$$

where Γ_q is the q-gamma function (Askey, 1978); for more information on the q-digamma function and how to evaluate the sum (2.33) see Appendix A. As shown in figure 2.7, $F(a)$ is a decreasing function of a, with $F(1) = \pi^2/3$ and $F(a) \to 2$ as $a \to \infty$.

Comparing imaginary parts in equation (2.19) we find that $V_b = 0$, so the bubble moves parallel to the wall. Then equating real parts in equation (2.19), the bubble's velocity in the x-direction is found to satisfy the algebraic equation

$$\frac{U_b^{2/3}}{(1 - U_b) F(a) + U_b} = \delta. \tag{2.36}$$

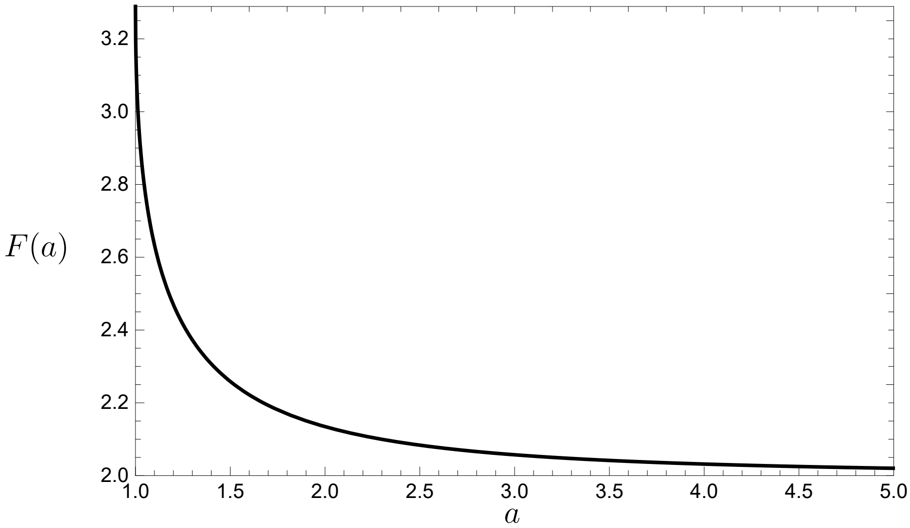

Figure 2.7: The function $F(a)$ defined by (2.34).

Once again (2.36) gives us a cubic that in principle can be solved explicitly for the dimensionless bubble velocity U_b. Rather than writing this complicated expression out explicitly, below we briefly examine the possible limiting cases.

First we observe that $U_b = 1$ when $\delta = 1$, so the bubble moves precisely with the external flow at this same critical value of the Bretherton parameter, regardless of the distance from the wall. As noted in §2.2.3, this special case corresponds to the particular solution where $p = -x$. For the extreme values of the Bretherton parameter δ, using (2.36) we derive the limits

$$U_b \to \frac{F(a)}{F(a)-1} < 2 \qquad \text{as} \quad \delta \to \infty, \tag{2.37a}$$

$$U_b \sim (\delta F(a))^{3/2} \qquad \text{as} \quad \delta \to 0. \tag{2.37b}$$

Taking the derivative of (2.36) with respect to δ we find

$$\frac{\partial U_b}{\partial \delta} = \frac{3U_b}{\delta\left[3\delta\big(F(a)-1\big)U_b^{1/3}+2\right]} > 0, \tag{2.38}$$

so U_b is a strictly increasing function of δ. It follows that $U_b > 1$ when $\delta > 1$ and *vice versa.*

As noted above, $F(a) \to 2$ as $a \to \infty$, so in this limit (2.36) reduces to the result (2.16) for a bubble in an infinite fluid medium, as expected. Similarly we can look at the limit $a \to 1$ in which the bubble touches the wall. Since $F(1) = \pi^2/3$, the bubble velocity tends to a non-zero value, which depends on the Bretherton parameter

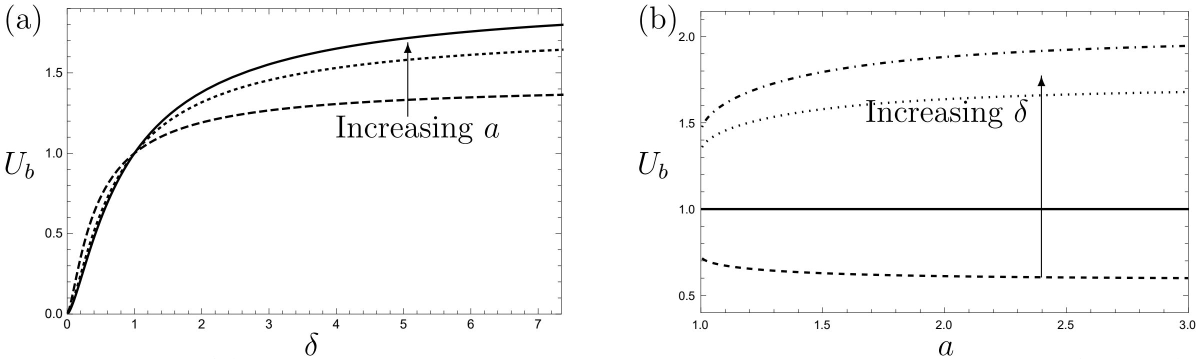

Figure 2.8: (a) Bubble velocity U_b versus Bretherton parameter δ for $a = 1$ (dashed), 1.5 (dotted) and ∞ (solid). (b) Bubble velocity U_b versus distance a from the wall for Bretherton parameter $\delta = 1/2$ (dotted), 1 (solid), 5 (dashed), $\delta = \infty$ (dot-dashed).

through the relation

$$\frac{3U_b^{2/3}}{\pi^2 - (\pi^2 - 3)U_b} = \delta. \tag{2.39}$$

For intermediate values of a, we find that

$$\frac{\partial U_b}{\partial a} = \left[\frac{-\delta F'(a)}{\delta(F(a) - 1) + \frac{2}{3}U_b^{-1/3}} \right] (U_b - 1), \tag{2.40}$$

in which the term in square brackets is positive. It follows that U_b is a decreasing function of a when $\delta < 1$, but an increasing function of a when $\delta > 1$.

The behaviour of the bubble velocity as the parameters a and δ are varied is shown in figure 2.8. As predicted, we observe that the presence of the wall either increases or decreases the bubble velocity, depending on whether $\delta < 1$ or $\delta > 1$, respectively. At the critical value of $\delta = 1$ we have $U_b = 1$ and the distance from the wall no longer matters.

At first glance it appears paradoxical that proximity to the wall may cause the bubble either to speed up or slow down, depending on the size of δ, but the behaviour may be explained as follows. By using the boundary condition (2.5c) and integrating by parts, the force balance (2.12) may be rewritten as

$$\boldsymbol{U}_b \left(1 + \frac{1}{\delta |\boldsymbol{U}_b|^{1/3}} \right) = \frac{1}{\pi} \oint_{\partial\Omega_b} \boldsymbol{u} \, \mathrm{d}s, \tag{2.41}$$

where $\boldsymbol{u} = (u, v)^{\mathrm{T}} = -\boldsymbol{\nabla} p$ is the dimensionless liquid velocity. For an isolated bubble, with the pressure given by (2.14), the integral on the right-hand side of (2.41) is easily calculated to be $2\boldsymbol{i}$, reproducing the equation of motion (2.15), and in general this term captures the influence of the outer flow on the bubble motion.

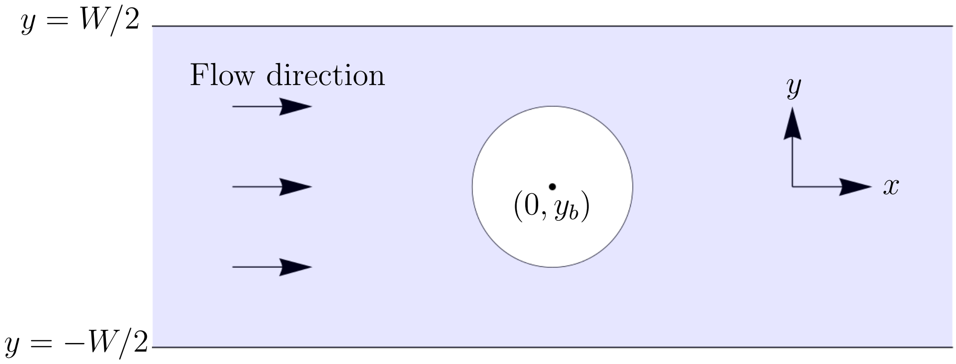

Figure 2.9: Plan view of a bubble in a Hele-Shaw channel of width W.

Now, what happens when a wall is introduced next to the moving bubble? From (2.28), we can calculate the average flow speed through the gap between the bubble and the wall (relative to the moving bubble) as

$$\frac{1}{a-1}\int_0^{a-1}(u-U_b)\,\mathrm{d}y = \frac{q}{a-1} = (1-U_b)\sqrt{\frac{a+1}{a-1}}. \tag{2.42}$$

First suppose the bubble is moving more slowly than the external flow, so $U_b < 1$. The right-hand side of equation (2.42) increases as the separation $a-1$ between the bubble and the wall decreases, measuring the flux of the liquid as it squeezes between the bubble and the wall. We find that the average velocity on the bubble surface thus increases and, according to (2.41), the bubble velocity also increases (relative to an isolated bubble). The horizontal component of the right-hand side of (2.41) may be calculated as

$$\frac{1}{\pi}\oint_{\partial\Omega_b} u\,\mathrm{d}s = 2 + (1-U_b)\big(F(a)-2\big), \tag{2.43}$$

which indeed increases as a decreases when $U_b < 1$.

On the other hand, if the bubble moves more quickly than the external flow ($U_b > 1$), then the liquid is squeezed backwards through the gap between the bubble and the wall so, by the same argument, the integral on the right-hand side of (2.41) and the bubble velocity should both decrease. This physical reasoning indeed agrees with the behaviour observed in figure 2.8. As noted above, the bubble travels faster or slower than the external flow depending on whether $\delta < 1$ or $\delta > 1$, respectively and the effect of proximity to the wall is accordingly either to speed up or to slow down the bubble.

2.4 Single bubble in a channel

Next we consider the motion of a single bubble of unit radius in a Hele-Shaw channel of width $W > 2$, between impermeable walls at $y = \pm W/2$ (see figure 2.9). We again impose a uniform flow with $p \sim -x$ at infinity and, without loss of generality, take the bubble centre to be instantaneously at $(x, y) = (0, y_b)$, where $|y_b| < W/2 - 1$. It may then be shown that p is an odd function of x, and it follows from (2.12) that $V_b = 0$. Thus a single bubble in a channel will continue moving parallel to the outer flow no matter where in the channel it is initially placed.

To facilitate numerical solution, we pose the problem in terms of the streamfunction ψ, which satisfies Dirichlet boundary-value problem:

$$\begin{aligned} \nabla^2\psi &= 0 && \text{in} \quad \Omega, && (2.44a) \\ \psi(x,y) &= \pm\frac{W}{2} && \text{at} \quad y = \pm\frac{W}{2}, && (2.44b) \\ \psi(x,y) &= q + U_b y && \text{at} \quad x^2 + (y - y_b)^2 = 1, && (2.44c) \\ \psi(x,y) &\to y && \text{as} \quad x \to \pm\infty. && (2.44d) \end{aligned}$$

The *a priori* unknown constant q is in principle determined by the constraint

$$\oint_{\partial\Omega_b} \frac{\partial\psi}{\partial n}\,\mathrm{d}s = 0, \tag{2.45}$$

which follows from single-valuedness of the pressure. The force balance (2.12), through the use of integration by parts and the Cauchy-Riemann equations, becomes

$$\frac{U_b^{2/3}}{\delta} = \frac{1}{\pi}\oint_{\partial\Omega_b} p\,\mathrm{d}y = -\frac{1}{\pi}\oint_{\partial\Omega_b}\left(x\frac{\partial\psi}{\partial x} + (y - y_b)\frac{\partial\psi}{\partial y}\right)\mathrm{d}x. \tag{2.46}$$

The streamfunction is decomposed as $\psi = U_b y + (1 - U_b)\psi_1 + q\psi_2$, where each ψ_k satisfies a normalised boundary-value problem that is independent of q and U_b:

$$\begin{aligned} \nabla^2\psi_1 &= 0 && \text{in} \quad \Omega, && (2.47a) \\ \psi_1 &= \pm\frac{W}{2} && \text{on} \quad y = \pm\frac{W}{2}, && (2.47b) \\ \psi_1 &= 0 && \text{on} \quad x^2 + (y - y_b)^2 = 1, && (2.47c) \\ \psi_1 &\to y && \text{as} \quad x \to \pm\infty. && (2.47d) \end{aligned}$$

$$\begin{aligned} \nabla^2\psi_2 &= 0 && \text{in} \quad \Omega, && (2.48a) \\ \psi_2 &= 0 && \text{on} \quad y = \pm\frac{W}{2}, && (2.48b) \\ \psi_2 &= 1 && \text{on} \quad x^2 + (y - y_b)^2 = 1, && (2.48c) \\ \psi_2 &\to 0 && \text{as} \quad x \to \pm\infty. && (2.48d) \end{aligned}$$

We solve for ψ_1 and ψ_2 using finite element methods and then compute the four integrals

$$I_k = \frac{1}{\pi}\oint_{\partial\Omega_b}\left(\frac{\partial\psi_k}{\partial x}\,\mathrm{d}y - \frac{\partial\psi_k}{\partial y}\,\mathrm{d}x\right), \tag{2.49a}$$

$$J_k = \frac{1}{\pi}\oint_{\partial\Omega_b}\left(x\frac{\partial\psi_k}{\partial x} + (y-y_b)\frac{\partial\psi_k}{\partial y}\right)\mathrm{d}x, \tag{2.49b}$$

($k = 1, 2$). The constraint (2.45) and the force balance (2.46) provide two algebraic equations for q and U_b. As in §2.3, the resulting equation of motion may be expressed in the form

$$\frac{U_b^{2/3}}{(1-U_b)F(W,y_b)+U_b} = \delta, \tag{2.50}$$

where now

$$F(W,y_b) = \frac{J_2 I_1}{I_2} - J_1. \tag{2.51}$$

For given values of W and y_b, the value of $F(W,y_b)$ can be computed once-and-for-all, following the procedure described above, and the dependence of U_b on δ is then determined by (2.50). An analogous approach is used to compute the numerical solutions with multiple bubbles in Chapter 4. To compute the numerical solutions we adopt a finite element approach using the in-built finite element package in Mathematica Wolfram Research (2024).

First we observe from (2.50) that $U_b = 1$ when $\delta = 1$. Again $\delta = 1$ is the critical value where the bubble moves with the external flow independently of the channel width, corresponding to the exact solution of the problem where $p = -x$. For the extreme values of the Bretherton parameter, δ, we derive the limits

$$U_b \to \frac{F(W,y_b)}{F(W,y_b)-1} \qquad \text{as} \quad \delta\to\infty, \tag{2.52a}$$

$$U_b \sim \left(\delta F(W,y_b)\right)^{3/2} \qquad \text{as} \quad \delta\to 0. \tag{2.52b}$$

Next, we consider a bubble travelling along the centre-line of the channel, with $y_b = 0$, in which case it is easy to see that q must also equal zero. Hence $F(W,0) = -J_1$, and the one remaining integral can in principle be calculated using a Schwarz–Christoffel mapping (Anselmo *et al.*, 2018) or approximation schemes described by Crowdy (2016); Love (1938), for example.

As shown in figure 2.10, $F(W,0)$ is a strictly positive decreasing function of W. Similarly to §2.3 we can calculate the derivative of the bubble velocity, U_b, with respect to δ as

$$\frac{\partial U_b}{\partial\delta} = \frac{3U_b}{\delta\left[3\delta\big(F(W,y_b)-1\big)U_b^{1/3}+2\right]} > 0, \tag{2.53}$$

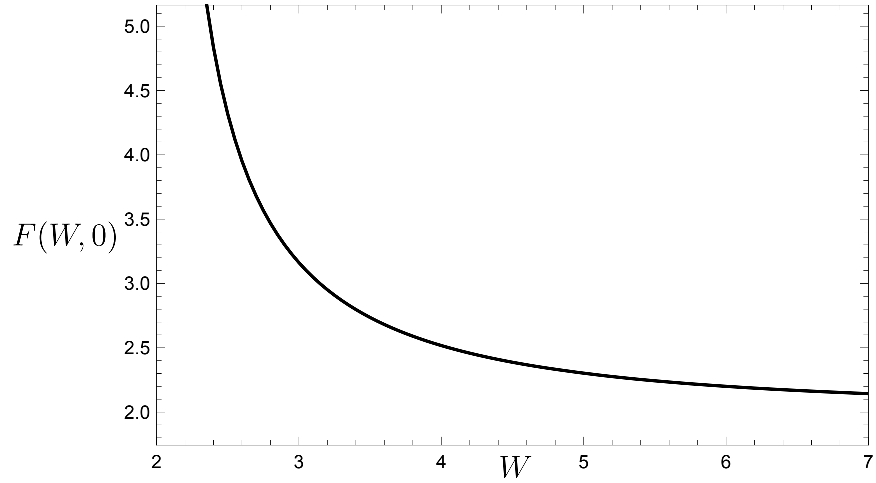

Figure 2.10: The function $F(W, 0)$, defined by (2.51)

so U_b is an increasing function of δ. It then follows that $U_b < 1$ for $\delta < 1$ and *vice versa*.

We find that for the extreme values of W, $F(W, 0) \to 2$ as $W \to \infty$ and $F(W, 0) \to \infty$ as $W \to 2$. In the first limit (2.50) reduces to (2.16), so if the walls are far away from the bubble we recover the result for a bubble in an infinite medium. The second limit implies that $U_b \to 1$ as $W \to 2$. This latter limit corresponds to the case when the bubble exactly fits the channel width and, by conservation of mass, must travel at the same speed as the outer flow. We may also calculate the derivative of the bubble velocity with respect to W which gives

$$\frac{\partial U_b}{\partial W} = \left[\frac{-\delta \frac{\partial F}{\partial W}(W, 0)}{\delta(F(W, 0) - 1) + \frac{2}{3} U_b^{-1/3}} \right] (U_b - 1). \tag{2.54}$$

Since the term in the square brackets is positive, U_b is a decreasing function of W for $\delta < 1$, but an increasing function for $\delta > 1$.

In figure 2.11 we examine the effects of varying the channel width W and Bretherton parameter δ. As expected we observe that U_b is an increasing function of δ and as $\delta \to \infty$ it tends to a value strictly less than the Taylor–Saffman value $U_b = 2$. As in §2.3, the bubble may be accelerated or retarded by the presence of walls, depending on whether $\delta < 1$ or $\delta > 1$, respectively. In the limit of large W, the solution approaches that for an isolated bubble, as expected, while the solutions all converge to $U_b = 1$ as $W \to 2$.

In figure 2.12 we study the effects of the bubble being off-centre in the channel by fixing $W = 4$ and varying y_b. Again we observe that proximity to a wall may either increase or decrease the bubble velocity, depending on whether $\delta < 1$ or $\delta > 1$,

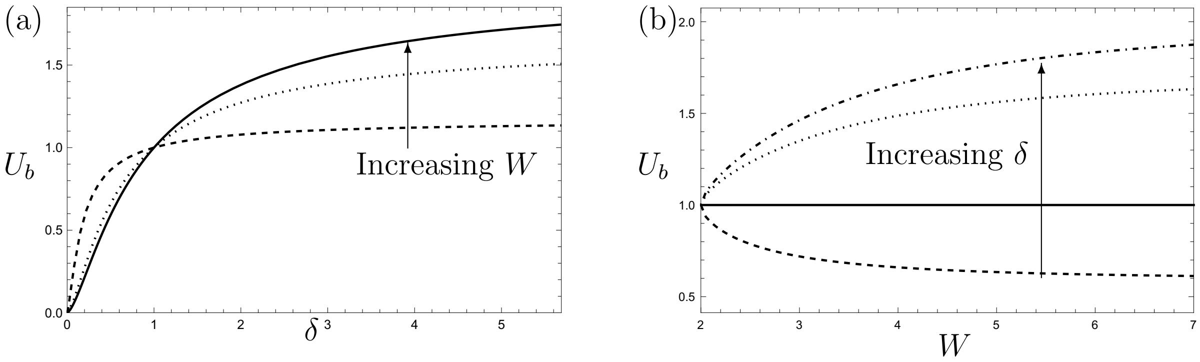

Figure 2.11: Velocity U_b of a bubble moving along the centre-line ($y_b = 0$) versus: (a) Bretherton parameter δ for $W = 2.2$ (dashed), 4 (dotted) and ∞ (solid); (b) channel width W, moving along the centre-line ($y_b = 0$) for Bretherton parameter $\delta = 1/2$ (dashed), 1 (solid), 5 (dotted) and ∞ (dot-dashed).

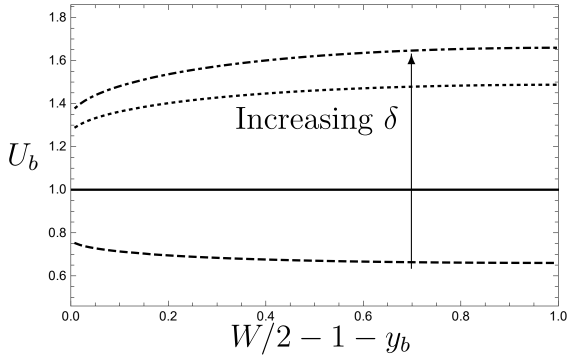

Figure 2.12: Bubble velocity U_b versus distance $W/2 - 1 - y_b$ from the top channel wall, with width $W = 4$ and offset $y_b \in [0, 1]$; Bretherton parameter $\delta = 1/2$ (dashed), 1 (solid), $\delta = 5$ (dotted), $\delta = \infty$ (dot-dashed).

respectively, with $\delta = 1$ the critical case where $U_b = 1$ for all y_b. As in §2.3, this behaviour is caused by the liquid flowing through the gaps between the bubble and the channel walls, which either increases or decreases the average velocity at the bubble surface in equation (2.41).

2.5 Conclusions

In this chapter we develop a model for the motion of a single bubble in a Hele-Shaw cell in the distinguished limit where the typical bubble aspect ratio ϵ and capillary number Ca satisfy $\mathrm{Ca}^{1/3} = O(\epsilon) \ll 1$. In this regime, the bubble remains approximately circular, and its velocity is determined by a net force balance.

For an isolated bubble in an infinite Hele-Shaw cell, the model may be solved analytically, and the qualitative behaviour depends on a dimensionless “Bretherton parameter", $\delta \propto \mathrm{Ca}^{1/3}/\epsilon$. The theoretically predicted bubble velocity agrees well with experimental data; these results also validate the prediction that the bubble moves faster than the fluid speed for $\delta > 1$ and slower for $\delta < 1$.

The inclusion of cell walls is found to increase the bubble velocity (from that of a bubble in an infinite medium) for $\delta < 1$, but to decrease the bubble velocity for $\delta > 1$ and to have no effect for $\delta = 1$, which is when the bubble travels with the background flow. Furthermore, the bubble speed is a decreasing function of the distance from the bubble to the wall for $\delta < 1$, whereas it is an increasing function for $\delta > 1$. The change in behaviour as δ is varied across $\delta = 1$, resonates throughout the results in this chapter and will also appear in Chapters 3 and 4 where we shall study the dynamics of multiple bubbles.

In Appendix B we show how one can generalise the results of this chapter to include buoyancy effects.

The results obtained here provide vital insight into the motion of a single bubble in a Hele-Shaw cell, in particular, the dependence on the dimensionless parameter, δ, which determines the qualitative behaviour of the system. In the next chapter, we will expand our analysis to study the interactions of two bubbles.

Chapter 3

The motion of two bubbles in a Hele-Shaw cell

3.1 Introduction

Many microfluidic experiments involve the flow of more than one bubble in a Hele-Shaw cell (Gnyawali *et al.*, 2017; Beatus *et al.*, 2006; Keeler *et al.*, 2022). In this chapter we derive and analyse a model for the propagation of two bubbles in a Hele-Shaw cell. This allows us to investigate bubble–bubble interactions analytically and to set the stage for methodologies to study a large number of bubbles.

We begin in §3.2 by writing down the governing equations for the flow of two bubbles in an infinite Hele-Shaw cell. In §3.3 we derive analytic equations of motion of the bubbles using complex variable techniques.

In §3.4 it is shown that the velocities of two identical bubbles in a uniform background flow are always equal, regardless of their initial positions. On the other hand in Chapter 2 we found that larger bubbles travel faster than smaller ones. In §3.5 we find that this result generalises for two bubbles so that a larger bubble can catch up with a smaller one. In some cases the bubbles rotate around each other, leaving the larger bubble in front, while in other cases the bubbles collide.

In §3.6 we analyse the limit in which the bubbles are very close to one another. In the case where the bubbles collide we suppose that, due to the high surface tension, the bubbles do not coalesce but instead exert a normal force on one another; the direction of this normal force determines whether they remain as a pair or separate.

In §3.7 we examine the other extreme limit, where the bubbles are far from one another, and find that the asymptotic approximations in this limit agree well with the behaviour predicted by the full model in §3.5 This approach is equivalent to the dipole models commonly used in the literature for the motion of bubbles in a Hele-Shaw cell (see for example, Beatus *et al.*, 2012; Shen *et al.*, 2014).

Finally in §3.8 we examine the possible trajectories for two bubbles of different radii, with the larger bubble initially far behind the smaller. The type of trajectory depends heavily on the flow conditions, resulting in two possible scenarios. The first is that the larger bubble collides with the smaller, they then rotate as a pair until aligned perpendicular to the flow at which point they separate and the larger bubble is free to travel faster. In the second case, instead of colliding the bubbles rotate past each other, leaving the larger bubble in front.

3.2 Governing Equations

We consider the flow of two bubbles in a Hele-Shaw cell in a uniform background flow of speed $\hat{U}$. We consider a dimensionless system in which we have scaled lengths with a typical bubble radius $\hat{R}$, which without loss of generality we take to be the smaller radius, velocities with the far-field uniform flow velocity $\hat{U}$, and the fluid pressure $\hat{p}$ with $12\hat{\mu}\hat{U}\hat{R}/\hat{h}^2$. Dimensionless quantities are represented without hats.

Suppose we have two bubbles at positions (x_1, y_1) and (x_2, y_2) in the (x, y)-plane with dimensionless radii R_1 and R_2, respectively. They experience a uniform velocity in the far-field of unit magnitude. We label the bubbles such that $R_1 = 1$ and $R_2 = R \geq 1$. As shown schematically in figure 3.1, the problem is instantaneously characterised by the length σ of the vector joining the smaller bubble centre to the larger bubble centre and the angle ϕ that it makes with the x-axis (which we take without loss of generality to be the background flow direction), as well as the radius ratio R.

Since the flow is governed by Laplace's equation we can formulate this as a problem for the complex potential $w(z) = -p + \mathrm{i}\psi$, where ψ is the streamfunction, and $z = x + \mathrm{i}y$. Then $w(z)$ is holomorphic in the region Ω outside the two bubbles and satisfies the boundary conditions

$$\mathrm{Im}[w(z)] = Q_1 + \mathrm{Im}\left[\overline{\mathcal{U}}_1 z\right] \qquad \text{on} \quad |z - z_1| = R_1 = 1, \tag{3.1a}$$

$$\mathrm{Im}[w(z)] = Q_2 + \mathrm{Im}\left[\overline{\mathcal{U}}_2 z\right] \qquad \text{on} \quad |z - z_2| = R_2 = R \geq 1, \tag{3.1b}$$

$$w(z) \sim z + o(1) \qquad \text{as} \quad z \to \infty, \tag{3.1c}$$

where $z_k = x_k + \mathrm{i}y_k$, $\mathcal{U}_k = U_k + \mathrm{i}V_k$ is the complex representation of the k^{th} bubble velocity, the Q_k are *a priori* unknown constants, and the over-bar denotes complex conjugation.

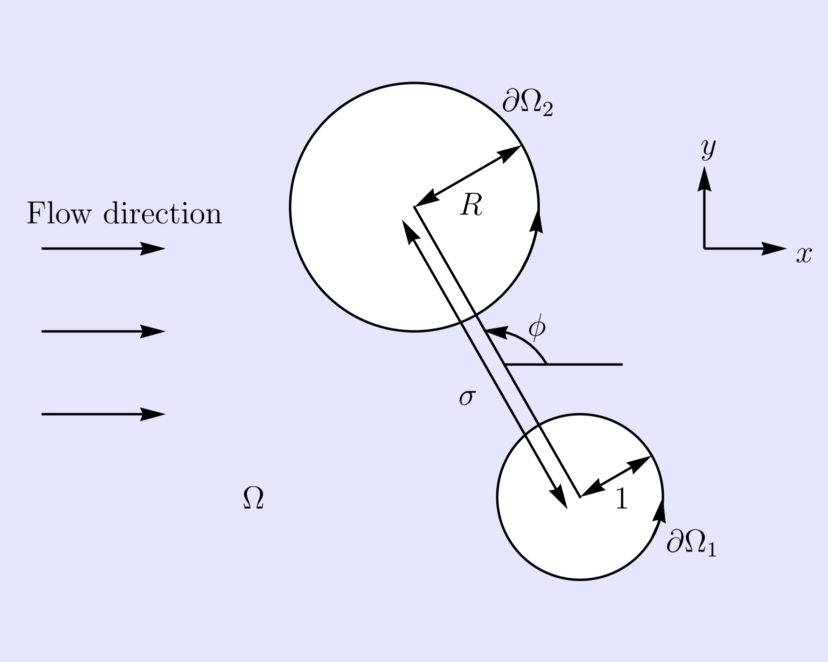

Figure 3.1: Schematic of the two-bubble problem.

Once we have solved for $w(z)$, to close the system we follow Chapter 2 §2.3, and perform an effective force balance on each bubble, which may be imposed by evaluating

$$\frac{1}{\mathrm{i}\pi}\oint_{\partial\Omega_1} w(z)\,\mathrm{d}z = -\mathcal{U}_1 + \frac{1}{\pi}\oint_{\partial\Omega_1} p\mathrm{i}\,\mathrm{d}z = -\mathcal{U}_1 + \frac{\mathcal{U}_1}{\delta\,|\mathcal{U}_1|^{1/3}}, \tag{3.2a}$$

$$\frac{1}{\mathrm{i}\pi}\oint_{\partial\Omega_2} w(z)\,\mathrm{d}z = -R^2\mathcal{U}_2 + \frac{1}{\pi}\oint_{\partial\Omega_2} p\mathrm{i}\,\mathrm{d}z = -R^2\mathcal{U}_2 + \frac{R\mathcal{U}_2}{\delta\,|\mathcal{U}_2|^{1/3}}. \tag{3.2b}$$

Here $\partial\Omega_k$ is the boundary of the k^{th} bubble given by $|z-z_k| = R_k$, and the Bretherton parameter, δ is given by (2.13).

The problem for the pressure field generated by two unequal bubbles was solved by Sarig *et al.* (2016) using a bipolar coordinate transformation, resulting in infinite series solutions for the interaction forces between the bubbles. Instead, using our complex variable formulation facilitates the evaluation of the integrals (3.2) in the force balance in closed form.

We expect the model (3.1)–(3.2) to break down when the distance between the bubble surfaces is comparable to the cell height (i.e. $\sigma - 1 - R = O(\epsilon)$). In this case, we expect that the three-dimensional effects of the bubble interfaces become important to the dynamics.

3.3 Solution for two bubbles of arbitrary radii

We begin by translating the coordinates so the bubble of unit radius is centred at the origin and rotating such that the bubbles centres lie on the real axis by defining $\tilde{z} = (z - z_1)\mathrm{e}^{-\mathrm{i}\phi} = g_1(z)$, where $\phi = \arg(z_2 - z_1)$. We then define $g_2(\tilde{z})$, a conformal map from $\tilde{\Omega}$, the solution domain in the $\tilde{z}$-plane, onto a concentric annulus, $A = \{\zeta : X \le |\zeta| \le 1\}$ (see figure 3.2 for a schematic overview of the conformal mapping procedure) given by

$$\zeta = g_2(\tilde{z}) = \frac{1 - a\tilde{z}}{\tilde{z} - a}, \tag{3.3}$$

where

$$a = \frac{\sigma^2 - R^2 + 1 - \sqrt{(\sigma^2 - R^2 + 1)^2 - 4\sigma^2}}{2\sigma}, \tag{3.4a}$$

$$X = a^2 + \frac{(R-1)a(a+1)(\sigma - R - 1)}{\sigma(\sigma - R - a)}. \tag{3.4b}$$

Note that $a^2 \le X < a < 1$. We then define $w(z) = z + W\left(g_2(g_1(z))\right)$, then $W(\zeta)$ is holomorphic on the annulus, A, and satisfies the conditions

$$\mathrm{Im}[W(\zeta)] = q_1 + \mathrm{Im}\left[\alpha_1\left(\frac{1 + a\zeta}{\zeta + a}\right)\right] \qquad \text{on} \quad |\zeta| = 1, \tag{3.5a}$$

$$\mathrm{Im}[W(\zeta)] = q_2 + \mathrm{Im}\left[\alpha_2\left(\frac{1 + a\zeta}{\zeta + a}\right)\right] \qquad \text{on} \quad |\zeta| = X, \tag{3.5b}$$

where $\alpha_k = (\overline{\mathcal{U}}_k - 1)\mathrm{e}^{\mathrm{i}\phi}$.

Now we express $W(\zeta)$ as a Laurent expansion on A, i.e.,

$$W(\zeta) = \sum_{n=-\infty}^{\infty} c_n \zeta^n, \tag{3.6}$$

and use the boundary conditions (3.5) to calculate the coefficients c_n. On $|\zeta| = 1$ we have $\overline{\zeta} = 1/\zeta$ so we can rewrite (3.6) as

$$\mathrm{Im}[W(\zeta)] = \mathrm{Im}[c_0] + \mathrm{Im}\left[\sum_{n=1}^{\infty}(c_n - \overline{c}_{-n})\zeta^n\right] \qquad \text{on} \quad |\zeta| = 1. \tag{3.7}$$

Boundary condition (3.5a) can be rearranged to

$$\begin{aligned} \mathrm{Im}[W(\zeta)] &= q_1 + \mathrm{Im}\left[\alpha_1\left(\frac{1 + a\zeta}{\zeta + a}\right)\right], \\ &= q_1 - \mathrm{Im}\left[\overline{\alpha_1}\left(\frac{\zeta + a}{1 + a\zeta}\right)\right], \\ &= q_1 - \mathrm{Im}[\overline{\alpha}_1 a] - \mathrm{Im}\left[\overline{\alpha}_1 \sum_{n=1}^{\infty}(1 - a^2)(-a)^{n-1}\zeta^n\right] \qquad \text{on} \quad |\zeta| = 1. \end{aligned} \tag{3.8}$$

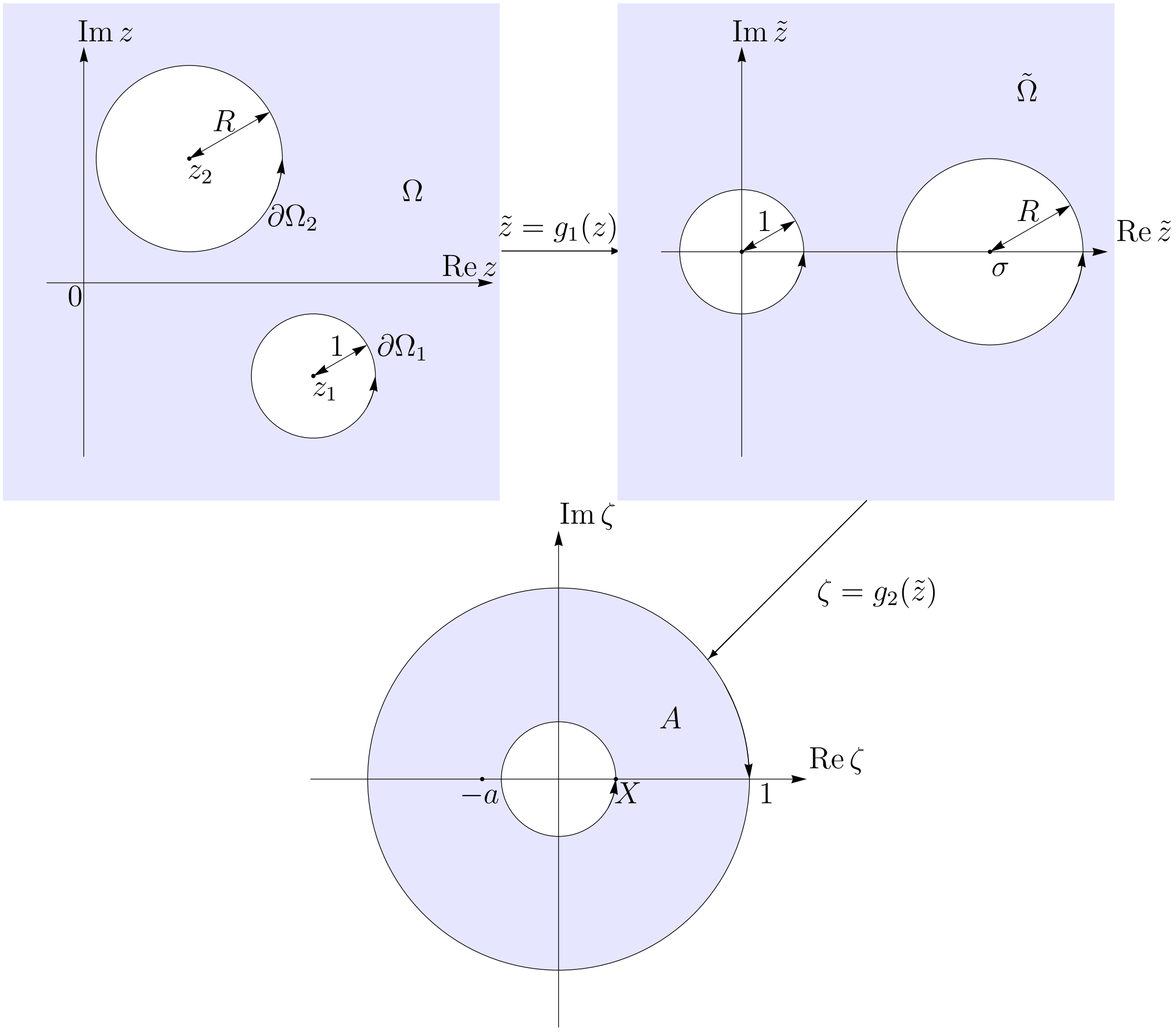

Figure 3.2: Schematic of the sequence of conformal maps from the fluid region Ω in the z-plane to the annulus $A = \{\zeta : X \leq |\zeta| \leq 1\}$ in the ζ-plane. The first is a rotation and a translation. The second is a Möbius transformation.

It then follows from (3.7) and (3.8) that

$$c_n - \overline{c}_{-n} = \frac{\overline{\alpha}_1(1-a^2)(-a)^n}{a} \quad (n \geq 1), \tag{3.9}$$

and, without loss of generality, we can choose $q_1 = \mathrm{Im}[\overline{\alpha}_1]a$, and choose $c_0 = 0$.

We progress similarly on $|\zeta| = X$, where now $\overline{\zeta} = X^2/\zeta$. The boundary condition (3.5b) can then be rewritten as

$$\begin{aligned} \mathrm{Im}[W(\zeta)] &= q_2 + \mathrm{Im}\left[\alpha_2\left(\frac{1+a\zeta}{\zeta+a}\right)\right] \\ &= q_2 - \mathrm{Im}\left[\overline{\alpha}_2\left(\frac{1+aX^2/\zeta}{X^2/\zeta+a}\right)\right] \\ &= q_2 - \mathrm{Im}\left[\frac{\overline{\alpha}_2}{a}\right] - \mathrm{Im}\left[\frac{\overline{\alpha}_2}{a}\sum_{n=1}^{\infty}(1-a^2)\left(\frac{-X^2}{a}\right)^n\zeta^{-n}\right] \quad \text{on} \quad |\zeta| = X. \end{aligned} \tag{3.10}$$

Similarly we can rewrite the Laurent expansion (3.6) as

$$\mathrm{Im}[W(\zeta)] = \mathrm{Im}\left[\sum_{n=1}^{\infty}(c_{-n} - X^{2n}\overline{c}_n)\zeta^{-n}\right] \qquad \text{on} \quad |\zeta| = X, \tag{3.11}$$

and it follows that

$$X^{2n}c_n - \overline{c}_{-n} = \frac{\alpha_2}{a}(1-a^2)\left(\frac{-X^2}{a}\right)^n, \tag{3.12}$$

and $q_2 = \mathrm{Im}(\overline{\alpha}_2/a)$. We simultaneously solve equations (3.9) and (3.12) to find that the complex potential $W(\zeta)$ is given by

$$\begin{aligned} W(\zeta) = \frac{(1-a^2)}{a}\sum_{n=1}^{\infty}\frac{X^n}{1-X^{2n}}\Bigg[&\left(\overline{\alpha}_1\left(\frac{-a}{X}\right)^n - \alpha_2\left(\frac{-X}{a}\right)^n\right)\zeta^n \\ &+ \left(\alpha_1(-aX)^n - \overline{\alpha}_2\left(\frac{-X}{a}\right)^n\right)\zeta^{-n}\Bigg]. \end{aligned} \tag{3.13}$$

The equations of motion for the bubbles can be found from (3.2) via

$$\frac{1}{\mathrm{i}\pi}\oint_{\partial\Omega_1} w(z)\,\mathrm{d}z = \frac{1}{\mathrm{i}\pi}\oint_{|\zeta|=1} W(\zeta)\frac{(1-a^2)\mathrm{e}^{\mathrm{i}\phi}}{(\zeta+a)^2}\,\mathrm{d}\zeta, \tag{3.14a}$$

$$-\frac{1}{\mathrm{i}\pi}\oint_{\partial\Omega_2} w(z)\,\mathrm{d}z = \frac{1}{\mathrm{i}\pi}\oint_{|\zeta|=X} W(\zeta)\frac{(1-a^2)\mathrm{e}^{\mathrm{i}\phi}}{(\zeta+a)^2}\,\mathrm{d}\zeta. \tag{3.14b}$$

The integral (3.14a) has poles at $\zeta = -a$ and 0, whereas (3.14b) only has a pole at $\zeta = 0$. The residue due to the pole at $\zeta = 0$ is the same for both integrals and can be calculated to give

$$\operatorname{Res}(\zeta = 0) = \frac{(1-a^2)^2}{a^2}\sum_{n=1}^{\infty}\frac{nX^{2n}}{1-X^{2n}}\left[\frac{\mathcal{U}_2 - 1}{a^{2n}} - (\overline{\mathcal{U}}_1 - 1)\mathrm{e}^{2\mathrm{i}\phi}\right]. \tag{3.15}$$

The residue at $\zeta = -a$ is given by

$$\begin{aligned}\operatorname{Res}(\zeta = -a) &= (1-a^2)\mathrm{e}^{\mathrm{i}\phi}\frac{\mathrm{d}}{\mathrm{d}\zeta}\left(W(\zeta)\right)\Big|_{\zeta=-a}\\ &= \frac{(1-a^2)^2}{a^2}\sum_{n=1}^{\infty}\frac{nX^{2n}}{1-X^{2n}}\left[(\overline{\mathcal{U}}_1 + \overline{\mathcal{U}}_2 - 2)\mathrm{e}^{2\mathrm{i}\phi} - (\mathcal{U}_1 - 1)\left(\frac{a}{X}\right)^{2n} - \frac{\mathcal{U}_2 - 1}{a^{2n}}\right]. \end{aligned}\tag{3.16}$$

Then, by Cauchy's Residue Theorem, we find

$$\frac{1}{\mathrm{i}\pi}\oint_{\partial\Omega_1} w(z)\,\mathrm{d}z = \frac{2(1-a^2)^2}{a^2}\sum_{n=1}^{\infty}\frac{nX^{2n}}{1-X^{2n}}\left[(\overline{\mathcal{U}}_2 - 1)\mathrm{e}^{2\mathrm{i}\phi} - (\mathcal{U}_1 - 1)\left(\frac{a}{X}\right)^{2n}\right], \tag{3.17a}$$

$$\frac{1}{\mathrm{i}\pi}\oint_{\partial\Omega_2} w(z)\,\mathrm{d}z = \frac{2(1-a^2)^2}{a^2}\sum_{n=1}^{\infty}\frac{nX^{2n}}{1-X^{2n}}\left[(\overline{\mathcal{U}}_1 - 1)\mathrm{e}^{2\mathrm{i}\phi} - \frac{\mathcal{U}_2 - 1}{a^{2n}}\right]. \tag{3.17b}$$

These series can be rewritten in the form

$$\frac{1}{\mathrm{i}\pi}\oint_{\partial\Omega_1} w(z)\,\mathrm{d}z = f_1(\sigma, R)(\overline{\mathcal{U}}_2 - 1)\mathrm{e}^{2\mathrm{i}\phi} - f_2(\sigma, R)(\mathcal{U}_1 - 1), \tag{3.18a}$$

$$\frac{1}{\mathrm{i}\pi}\oint_{\partial\Omega_2} w(z)\,\mathrm{d}z = f_1(\sigma, R)(\overline{\mathcal{U}}_1 - 1)\mathrm{e}^{2\mathrm{i}\phi} - f_3(\sigma, R)(\mathcal{U}_2 - 1), \tag{3.18b}$$

where

$$f_1(\sigma, R) = \frac{2(1-a^2)^2}{a^2}\sum_{n=1}^{\infty}\frac{nX^{2n}}{1-X^{2n}} = \frac{2(1-a^2)^2}{a^2}\frac{\Psi'_{X^2}(1)}{4\log^2 X}, \tag{3.19a}$$

$$f_2(\sigma, R) = \frac{2(1-a^2)^2}{a^2}\sum_{n=1}^{\infty}\frac{nX^{2n}}{1-X^{2n}}\left(\frac{a}{X}\right)^{2n} = \frac{2(1-a^2)^2}{a^2}\frac{\Psi'_{X^2}\left(\frac{\log a}{\log X}\right)}{4\log^2 X}, \tag{3.19b}$$

$$f_3(\sigma, R) = \frac{2(1-a^2)^2}{a^2}\sum_{n=1}^{\infty}\frac{nX^{2n}}{1-X^{2n}}\left(\frac{1}{a}\right)^{2n} = \frac{2(1-a^2)^2}{a^2}\frac{\Psi'_{X^2}\left(\frac{\log(X/a)}{\log X}\right)}{4\log^2 X}, \tag{3.19c}$$

where a and X are functions of σ and R, given by (3.4a) and (3.4b), respectively, and Ψ is the q-digamma function (Salem, 2012) (see Appendix A for more information on the derivation of the results (3.19)). Note that these formulae provide closed forms for the infinite series solutions derived by Sarig *et al.* (2016).

The equations of motion for the bubbles are given by (3.2), which reduces to

$$f_1(\sigma,R)(\overline{\mathcal{U}}_2-1)\mathrm{e}^{2\mathrm{i}\phi}-f_2(\sigma,R)(\mathcal{U}_1-1)=-\mathcal{U}_1+\frac{\mathcal{U}_1}{\delta\,|\mathcal{U}_1|^{1/3}},\tag{3.20a}$$

$$f_1(\sigma,R)(\overline{\mathcal{U}}_1-1)\mathrm{e}^{2\mathrm{i}\phi}-f_3(\sigma,R)(\mathcal{U}_2-1)=-R^2\mathcal{U}_2+\frac{R\mathcal{U}_2}{\delta\,|\mathcal{U}_2|^{1/3}}.\tag{3.20b}$$

For general R, both σ and ϕ vary with time, t. At each instant, the system (3.20) is solved for $\mathcal{U}_k$ ($k=1,\,2$), and the bubble positions $z_k=x_k+\mathrm{i}y_k$ are then updated using

$$\frac{\mathrm{d}z_k}{\mathrm{d}t}=\mathcal{U}_k,\tag{3.21}$$

where time is non-dimensionalised with the advective timescale $\hat{R}/\hat{U}$.

For fixed σ and R, the equations (3.20) are invariant under the transformation $\phi\mapsto\pm\pi-\phi$, $V_k\mapsto -V_k$, and $U_k\mapsto U_k$. This symmetry implies that the velocities in the x-direction, U_k, are symmetric and the velocities in the y-direction, V_k, are anti-symmetric across $\phi=\pm\pi/2$. It follows that, if the flow direction is reversed, the bubbles travel backwards along the trajectories just traversed, as expected in Stokes flow.

3.4 Two identical bubbles

If the bubbles are identical then $R=1$, so (3.4b) implies that $X=a^2$ and equations (3.20) are equivalent. It then follows that $\mathcal{U}_1=\mathcal{U}_2\equiv\mathcal{U}_p$, so the two bubbles move at the same velocity, and the values of σ and ϕ remain fixed for all time.

If in addition we set $\phi=0$, then the bubble pair move in a line in the direction of the background flow at constant speed $\mathcal{U}_p=U_p\in\mathbb{R}$ determined by either of (3.20a) or (3.20b) and given by

$$\frac{U_p^{2/3}}{f_2(\sigma,R)-f_1(\sigma,R)+(1+f_1(\sigma,R)-f_2(\sigma,R))U_p}=\delta.\tag{3.22}$$

In figure 3.3 we observe that $U_p<U_b$ when $\delta<1$ and $U_p>U_b$ when $\delta>1$, where U_b is the corresponding isolated bubble velocity determined by equation (2.16), i.e.,

$$\frac{U_b^{2/3}}{2-U_b}=\delta.\tag{3.23}$$

As the separation of the bubbles, $\sigma\to\infty$ we find that the bubble pair velocity $U_p\to U_b$ the isolated bubble velocity as we expect. This result will be verified via an asymptotic expansion in §3.7.

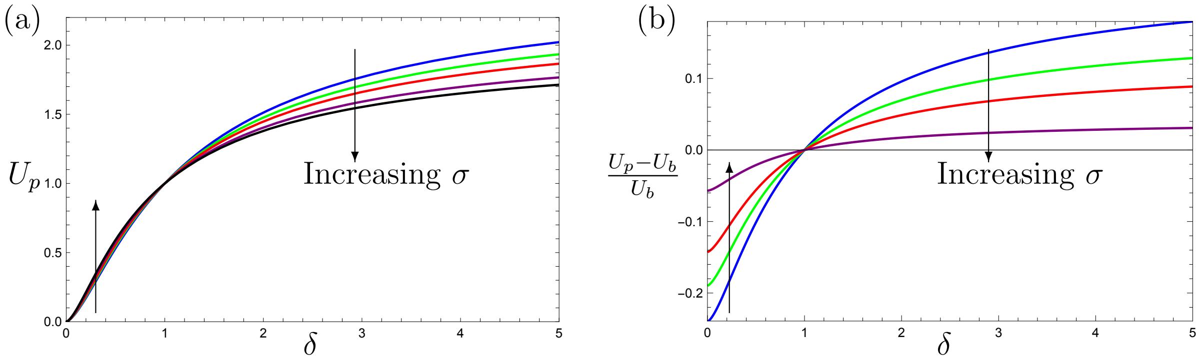

Figure 3.3: Aligned ($\phi = 0$) bubble pair velocity, U_p (3.22), as a function of Bretherton parameter, δ, for fixed bubble separations, $\sigma = 2.1$ (blue), 2.5 (green) 3 (red), 5 (purple), ∞ (black). (b) The ratio $(U_p - U_b)/U_b$ as a function of Bretherton parameter, δ, for fixed bubble separations, $\sigma = 2.1$ (blue), 2.5 (green) 3 (red), 5 (purple).

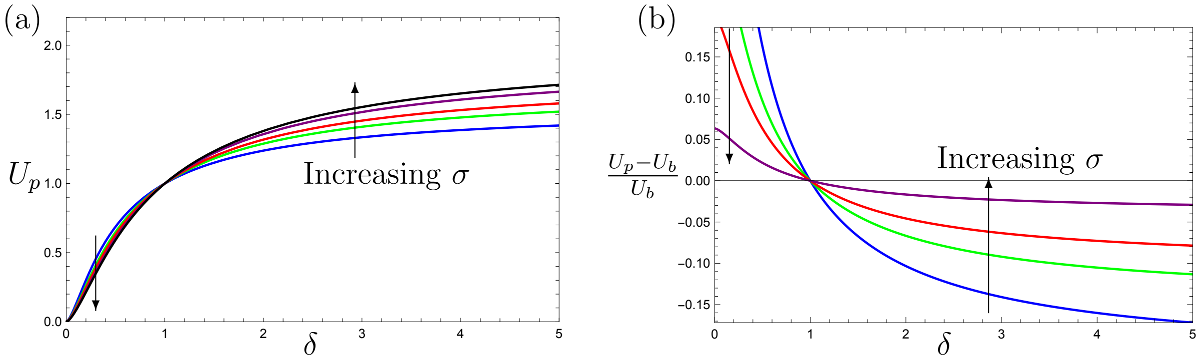

Figure 3.4: (a) Perpendicular ($\phi = \pi/2$) bubble pair velocity, U_p (3.24), as a function of Bretherton parameter, δ, for fixed bubble separations, $\sigma = 2.1$ (blue), 2.5 (green) 3 (red), 5 (purple), ∞ (black) (b) The ratio $(U_p - U_b)/U_b$ as a function of Bretherton parameter, δ, for fixed bubble separations, $\sigma = 2.1$ (blue), 2.5 (green) 3 (red), 5 (purple).

If we set $\phi = \pi/2$ then we find that the bubbles move side-by-side in the direction of the background-flow direction at a velocity, U_p, given by

$$\frac{U_p^{2/3}}{f_1(\sigma, R) + f_2(\sigma, R) + (1 - f_1(\sigma, R) - f_2(\sigma, R))U_p} = \delta. \tag{3.24}$$

In figure 3.4 we observe that, when the bubbles are aligned perpendicularly to the background flow direction, $U_p > U_b$ for $\delta < 1$ and $U_p < U_b$ for $\delta > 1$ in contrast with the case where the bubbles are aligned with the flow. This configuration is equivalent to the bubble near a wall studied in Chapter 2, via the method of images.

For $\phi \in (-\pi/2, \pi/2)\backslash\{0\}$ (by symmetry, ϕ in this range covers all other possible configurations) from (3.20) we find that $V_p \neq 0$. Thus the bubble pair will drift in the y-direction if neither aligned with nor perpendicular to the flow. In figure 3.5 we plot the x- and y-direction bubble velocities as ϕ is varied for two illustrative values

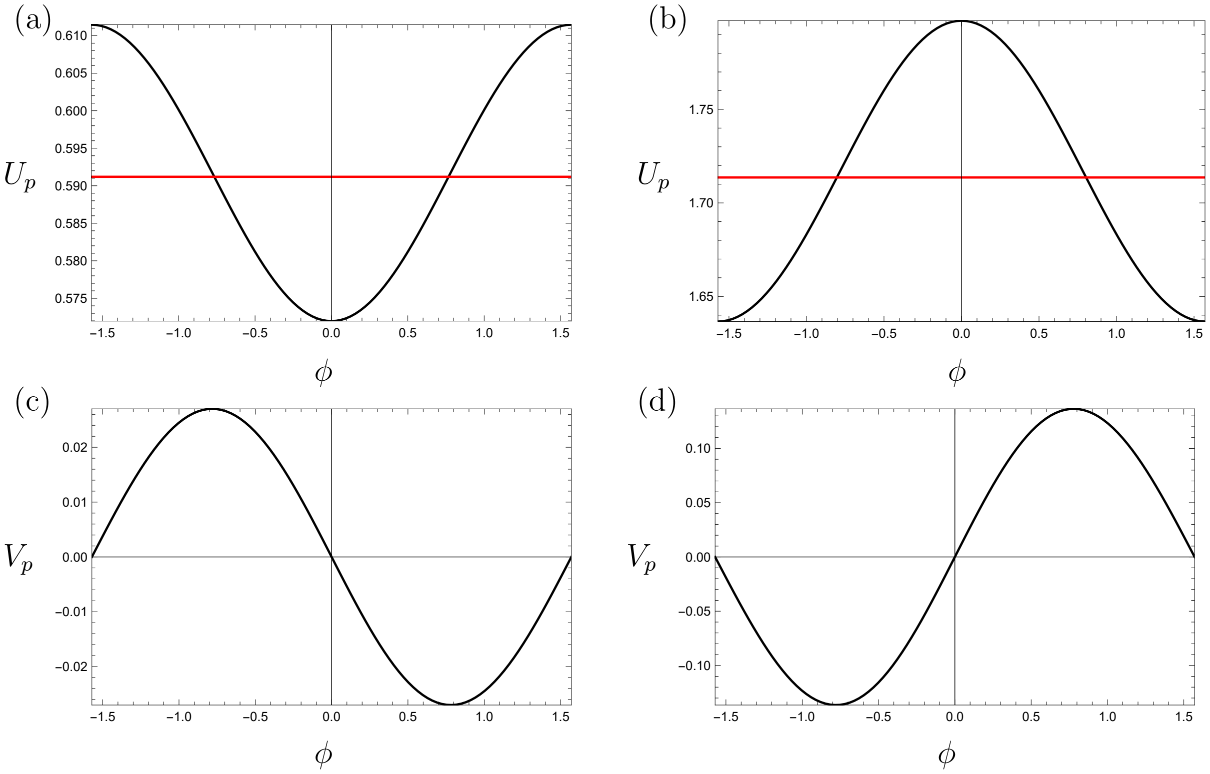

Figure 3.5: Top: The bubble pair velocity in x-direction, U_p, as a function of angle, ϕ for (a) $\delta = 0.5$, (b) $\delta = 5$. The red line indicates the single bubble velocity, U_b, for the same value of δ. Bottom: The bubble pair velocity in y-direction, V_p, as a function of angle, ϕ for (c) $\delta = 0.5$. (d) $\delta = 5$.

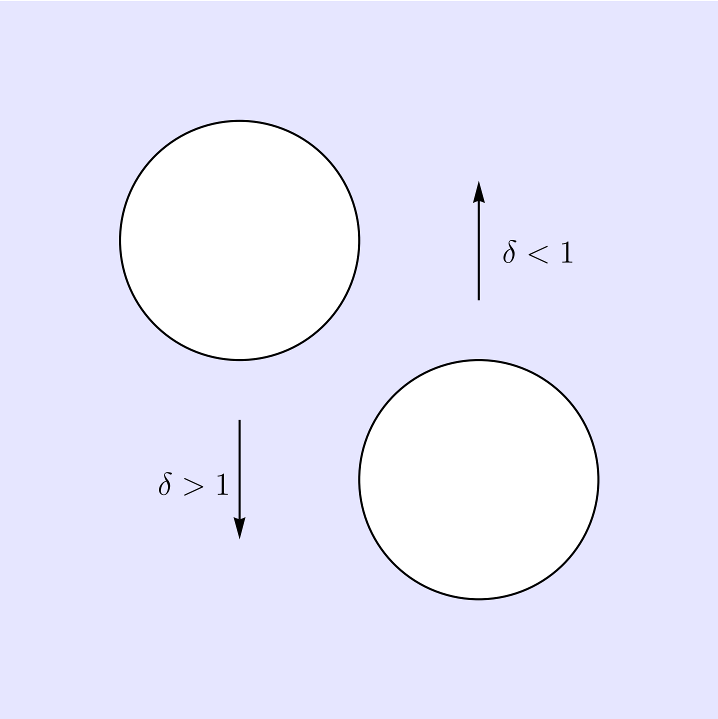

Figure 3.6: Schematic of the y-direction drift for non-aligned, non-perpendicular bubbles. Direction of the drift is shown by the arrows

of δ: (a and c) for $\delta < 1$ and (b and d) for $\delta > 1$. We observe that for $\phi \in (-\pi/2, 0)$ the bubble pair has a drift in the positive y-direction for $\delta < 1$ but in the negative y-direction for $\delta > 1$, and *vice versa* for $\phi \in (0, \pi/2)$. Similarly we find that the x-direction bubble pair velocity $U_p < U_b$ in the range $\phi \in (-\pi/4, \pi/4)$ for $\delta < 1$ and $U_p > U_b$ for $\delta > 1$ and *vice versa* for $\phi \in (-\pi/2, -\pi/4) \cup (\pi/4, \pi/2)$. Again we observe this change in behaviour as we pass through $\delta = 1$. In figure 3.6 we show the direction of the drift schematically for $\phi = -\pi/4$, the bubble pair drift in the positive y-direction for $\delta < 1$ and *vice versa* for $\delta > 1$. Shen *et al.* (2014) conducted experiments on identical pairs of bubbles with surfactants and found that bubbles that are slower than the background velocity behave the same as our $\delta < 1$ regime as the angle between the bubbles is varied. A quantitative comparison cannot be made at this time due to the inclusion of surfactants; in Chapter 7 we will analyse how to modify the model to include surfactant effects.

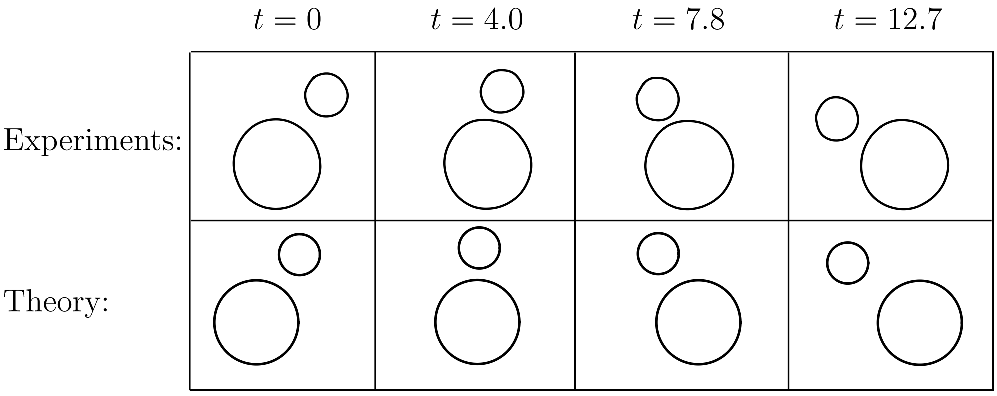

Figure 3.7: (top) Experimental images showcasing a two-bubble rollover with $\delta = 1.17$ and $R = 2.05$; (bottom) simulations of the dynamical system (3.21) shown at different dimensionless times $t = \hat{t}\hat{U}/\hat{R}$. The background flow is from left to right. In the experiment $\epsilon = 0.081$, and $\mathrm{Ca} = 6.1 \times 10^{-4}$.

3.5 Bubbles of different radii

3.5.1 Observed behaviour

We now relax the condition of equal bubble radii. We consider situations where the larger bubble is initially behind the smaller one and has an offset in the y-direction, such that $x_1 > x_2$ and $|y_1 - y_2| > 0$. Thus the bubbles would collide if they only moved parallel to the background flow. However, for a range of starting positions, we find that the nonlinear interaction between the bubbles allows them to avoid collision by rotating around one another, so that the larger bubble manoeuvres to the front and can now freely move faster than the smaller bubble.

In figure 3.7 we show experimental images (taken by Katie Wu, Princeton University) demonstrating this rollover effect, with $\delta = 1.17$ and $R = 2.05$. This value of δ is achieved in the experiments with $\epsilon = 0.081$, and $\mathrm{Ca} = 6.1 \times 10^{-4}$. The larger bubble catches up with the smaller one, which evades contact by rolling over the larger one. In the lower plots, we demonstrate good qualitative agreement with solutions of the dynamical system (3.21) for the same parameter values and initial conditions.

In figure 3.8 we compare the experimental and theoretical results for the (x, y)-positions of the bubble centres, for the same experiment as shown in figure 3.7. We observe that the motion of the larger bubble is barely affected by the interaction and that the smaller bubble moves in the y-direction, thus avoiding contact with the larger one as it passes by.

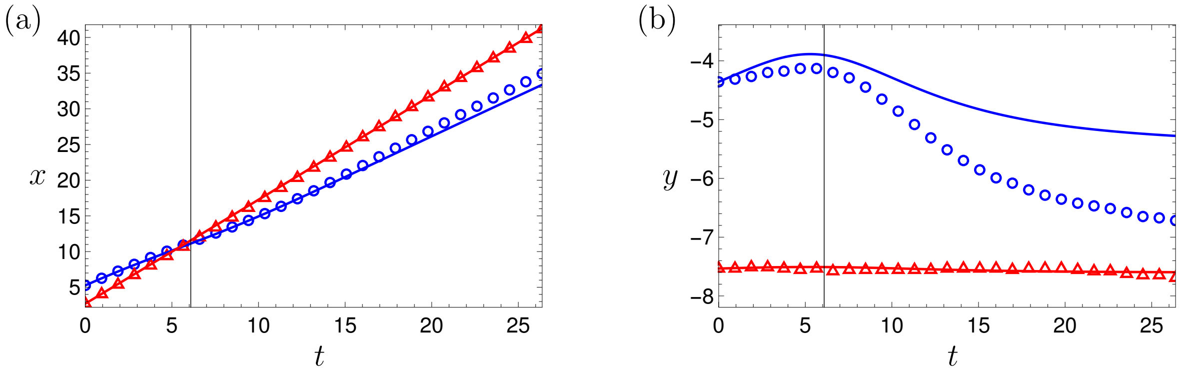

Figure 3.8: The trajectories of the bubble centres (x, y) (a and b, respectively) versus dimensionless time t for $\delta = 1.17$ and $R = 2.05$. The bubble of unit radius is shown in blue and the bubble of radius $R = 2.05$ is shown in red. Theoretical results are solid lines and experimental data are points. In the experiment $\epsilon = 0.081$, and $\mathrm{Ca} = 6.1 \times 10^{-4}$.

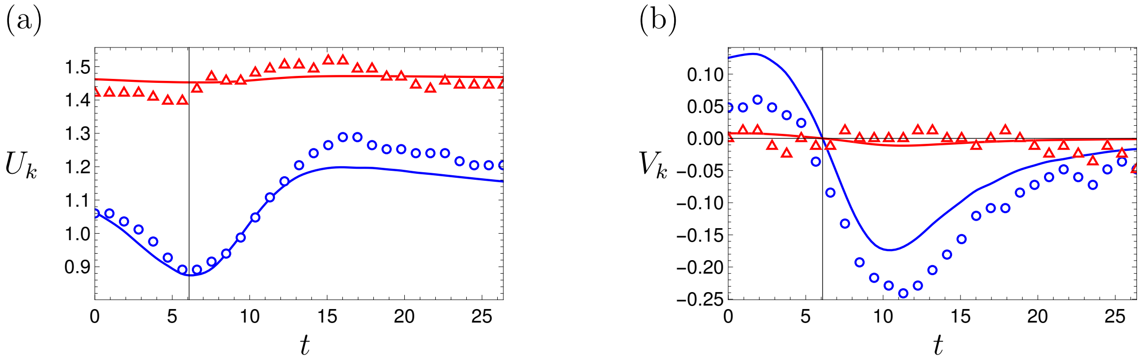

Figure 3.9: The instantaneous bubble velocity (U_k, V_k) ((a) and (b), respectively) versus dimensionless time t for $\delta = 1.17$ and $R = 2.05$. The bubble of unit radius is shown in blue and the bubble of radius R is shown in red. Solid lines show theoretically determined trajectories and points show experimental data. In each plot, the time at which $x_1 = x_2$ is shown with a vertical line. In the experiment $\epsilon = 0.081$, and $\mathrm{Ca} = 6.1 \times 10^{-4}$.

The instantaneous bubble velocities (U_k, V_k), are plotted in figure 3.9. The time at which the pair of bubbles is aligned perpendicularly (i.e. $x_1 = x_2$) to the background flow coincides with when the x-direction velocity of the smaller bubble reaches a minimum and when $V_1 = V_2 = 0$. We observe reasonable agreement between theory and experiment. The small discrepancies between the theoretical and experimental velocities can accumulate over time and lead to noticeable differences between the theoretical and experimental bubble trajectories, as shown in figure 3.8.

Finally, in figure 3.10 we plot the trajectories calculated using (3.20) of the centre of the larger bubble relative to that of the smaller one (i.e. $z_2 - z_1$). Any trajectory entering the shaded grey region $|z_1 - z_2| \leq 1 + R$ corresponds to a collision between the bubbles. Points extracted from the trajectories of bubbles in experiments are

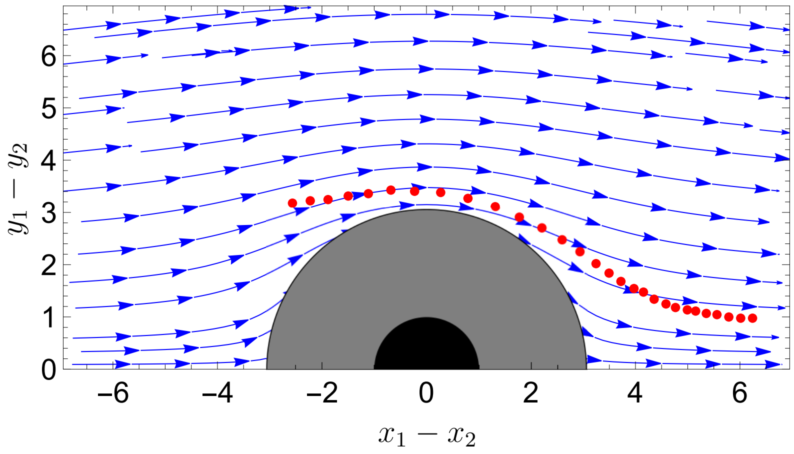

Figure 3.10: Trajectories for the two-bubble dynamical system (3.21) in the reference frame of the smaller bubble, with (a) $\delta = 1.17$ and $R = 2.05$, (b) $\delta = 0.90$ and $R = 2.32$. The blue vectors show the predicted trajectories of the centre of the larger bubble relative to the smaller one, and the red points show the experimentally measured bubble positions. Error bars are comparable to the size of the markers and are thus omitted. Any trajectories entering the solid grey region $|z_2 - z_1| \leq (1+R)$ are such that the two bubbles will collide. The solid black region $|z_2 - z_1| \leq 1$ represents the smaller bubble. In the experiment $\epsilon = 0.081$, and $\mathrm{Ca} = 6.1 \times 10^{-4}$.

superimposed on the theoretically determined trajectories. We observe that in experiments, the smaller bubble initially follows a streamline (or trajectory), and then departs from that streamline when the two bubbles are close. This departure is likely due to interactions between the bubbles that are not included in the model. Finally, as the bubbles separate, the smaller bubble once again closely follows a streamline. However, this is a different streamline than the one on which the bubble started.

While the x positions are well captured by the theory, there is a significant disagreement between the predicted and observed y positions of the smaller bubble following the rollover. In the experiments, the smaller bubble trails behind the larger bubble such that the distances between their centres in both the x- and y-directions are smaller than the theory predicts. This process breaks the fore-aft symmetry that is predicted by (3.20), and indeed which is expected in Stokes flow. However, it should be noted that there are perturbations to the bubble shape due to the background flow that are fore-aft asymmetric due to the differences between the advancing and retreating menisci (see Chapter 2 §2.2.4). Other possible reasons for this symmetry breaking include small inertial effects and imperfections in the geometry of the Hele-Shaw cell (see, for example, Gaillard *et al.*, 2021). Non-uniform distribution of contaminants over the bubble surface might also be a contributing factor, as described by Park *et al.*

(1994), though these effects are expected to be negligible in systems of air bubbles in silicone oil, as used in the experiments. We note that the process of the bubbles approaching and interacting occurs rather slowly, which may allow apparently small effects to accumulate and have a significant influence over time.

By analysing the dynamical system (3.21), we can predict when or if the bubble rollover effect will occur. At each instant of time, the system (3.20) determines $\mathcal{U}_1$ and $\mathcal{U}_2$ as functions of σ and ϕ. We can then update σ and ϕ using $\mathcal{U}_2-\mathcal{U}_1 = \left(\dot{\sigma} + \mathrm{i}\sigma\dot{\phi}\right) \mathrm{e}^{\mathrm{i}\phi}$ (where the dot represents differentiation with respect to t). In figure 3.11 we plot the phase space showing the resulting trajectories of the larger bubble relative to the smaller one, i.e. $z_2 - z_1 = -\sigma \mathrm{e}^{\mathrm{i}\phi}$. In this figure, we take $R = 2$ for illustration, and the shaded disc shows the region $|z_1 - z_2| \leq (1 + R)$, corresponding to the intersection between the bubbles. The rollover effect occurs on any trajectory that starts from $x_1 > x_2$ with $|y_1 - y_2| > 0$ and that does not enter the solid grey region, and the likelihood of observing the effect is strongly dependent on the value of δ. In figure 3.11(a) we show a case where δ is large, and all suitable initial conditions (such that they satisfy the above inequalities) will give rise to the rollover effect. In this case, the bubbles repel each other so strongly that collision between the bubbles is impossible. On the other hand, in figure 3.11(b) we show that a smaller value of δ leads to much weaker interaction between the bubbles, so the trajectories remain almost parallel to the flow. In this case, the rollover effect can occur only for a very narrow band of initial conditions, and instead, we are much more likely to observe the bubbles colliding with each other.

In figure 3.11 there are trajectories entering the grey region, these suggest that the bubbles do collide in finite time. We prove this claim in §3.6.

In the next subsection, we derive conditions under which one will always observe the bubbles rotating around one another, instead of colliding.

3.5.2 Do the bubbles collide?

3.5.2.1 Conditions for a bubble collision

In §3.5 we found that the bubbles can avoid colliding by rolling over one another. By analysing the dynamical system (3.21), we can predict when or if the bubble rollover effect will occur. At each instant in time, (3.20) determines $\mathcal{U}_1$ and $\mathcal{U}_2$ as functions of σ and ϕ. We can then update σ and ϕ using $\mathcal{U}_2 - \mathcal{U}_1 = \left(\dot{\sigma} + \mathrm{i}\sigma\dot{\phi}\right) \mathrm{e}^{\mathrm{i}\phi}$ (where the dot represents differentiation with respect to t). In figure 3.11, we plot the phase

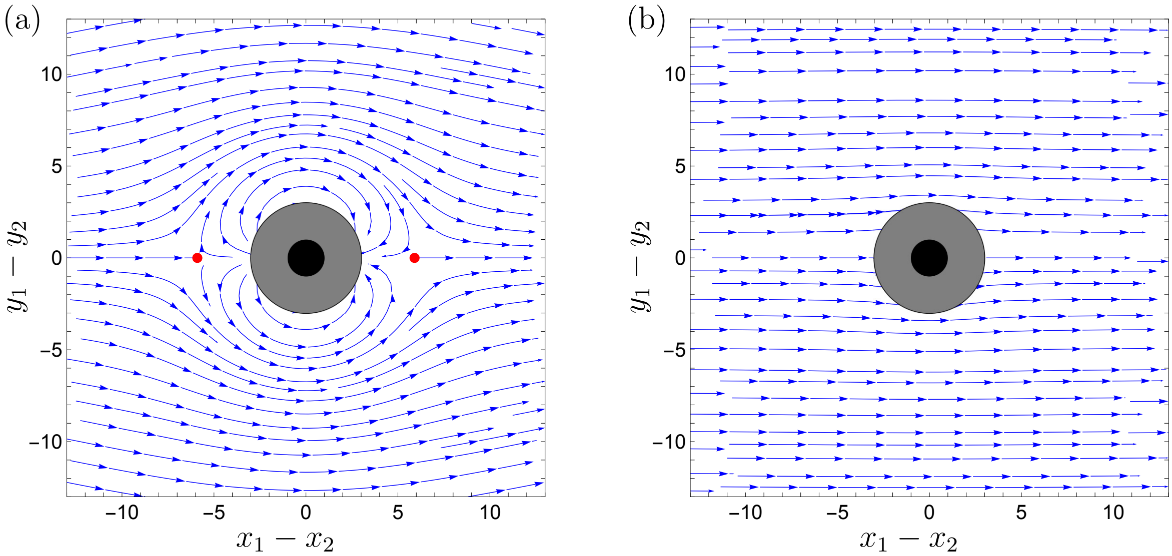

Figure 3.11: Trajectories for the two-bubble dynamical system (3.21) in the reference frame of the smaller bubble, with $R = 2$ and (a) $\delta = 5$, (b) $\delta = 1/2$. Any trajectories entering the solid grey region $|z_2 - z_1| \leq (1 + R)$ are such that the two bubbles will collide. Stationary points are shown in red. The solid black region $|z_2 - z_1| \leq 1$ represents the smaller bubble.

space showing the resulting trajectories of the larger bubble relative to the smaller one, i.e., $z_2 - z_1 = \sigma e^{i\phi}$. In this figure, we take $R = 2$ for illustration. The solid grey region, $1 < |z_2 - z_1| \leq (1 + R)$, corresponds to the region of intersection between the bubbles. The rollover effect occurs on any trajectory that starts from $x_1 - x_2 \gg 1$ with $0 < |y_2 - y_1| < 1 + R$ and that does not enter the solid grey region, and the likelihood of observing the effect depends strongly on the value of δ. In figure 3.11(a), we show a case where δ is large, and all suitable initial conditions satisfying the inequalities stated above will give rise to the rollover effect. In this case, the bubbles repel each other so strongly that collision between the bubbles is impossible. On the other hand, in figure 3.11(b), we show that a smaller value of δ leads to much weaker interaction between the bubbles, such that the trajectories remain almost parallel to the flow. In this case, the rollover effect can occur only for a very narrow band of initial conditions, and we are much more likely to observe the bubbles colliding with each other.

In this section, we consider conditions under which the bubbles will collide. First, we observe that there are stationary points (saddle points, located at $\phi = 0$ and $\phi = \pi$, shown in red) in figure 3.11(a) but not in figure 3.11(b). The existence of such stationary points implies that two aligned bubbles (i.e., with $y_1 = y_2$) will never collide. Furthermore, we find that, in figure 3.11(a), the trajectories on the surface $|z_2 - z_1| = 1 + R$ with $x_2 > x_1$ (the larger bubble in front) are directed inwards (into the solid grey region) and for $x_2 < x_1$ are directed outwards. In this case, bubbles may only collide if they are initially close to each other with $|y_1 - y_2| > 0$ or the larger one is ahead of the smaller one, $x_2 > x_1$ initially; in any case, the larger bubble is ahead of the smaller one when the collision occurs. The reverse is true in figure 3.11(b), in which the surface $|z_2 - z_1| = 1 + R$ is entirely outside of the separatrix connecting the two stationary points.

Motivated by these observations, we examine the following two conditions on the flow:

1. The stationary points of the dynamical system (3.21) in the reference frame of the smaller bubble are in the region $|z_2 - z_1| \geq 1 + R$.

2. In a neighbourhood of $x_1 = x_2$, the trajectories point *into* the region $|z_2 - z_1| \leq 1 + R$ for $x_2 > x_1$ and *out of* the region $|z_2 - z_1| \leq 1 + R$ for $x_2 < x_1$.

In §3.5.2.2 and §3.5.2.3, for each condition $k \in \{1, 2\}$, we will find a critical minimum value of $\delta = \delta_k$. Then, for $\delta < \delta_1$, we argue that there is always a range of initial conditions with $x_1 - x_2 \gg 1$ and $|y_2 - y_1| < 1 + R$ such that the bubbles collide (including the case $y_2 = y_1$ where the bubbles are aligned). On the other hand, for $\delta > \delta_2$, it is impossible for bubbles that start far apart to collide.

Note that there exists a third critical value of $\delta = \delta_c$ satisfying $\delta_1 \leq \delta_c \leq \delta_2$, at which the separatrix connecting the two stationary points is tangent to $|z_2 - z_1| = 1 + R$. This critical value provides a sharp bound on δ above which collision between two initially well separated bubbles is impossible. However, δ_c is extremely delicate to compute numerically as it depends on the global properties of the flow.

3.5.2.2 Condition 1: stationary points

If this condition is satisfied, then two aligned bubbles will never collide. By analysing (3.20), we can find the stationary points by solving for $\mathcal{U}_1 = \mathcal{U}_2 \equiv \mathcal{U}$ and for $(\sigma, \phi) \equiv (\sigma_s, \phi_s)$ at a fixed δ. Since each f_k in (3.19) is real, by symmetry we find that $\mathcal{U} = U \in \mathbb{R}$ and $\phi_s = 0$ or π. We focus on the case $\phi_s = 0$ since by symmetry the stationary points are at $(\pm\sigma_s, 0)$. Thus, for given δ and R we find U and σ_s by solving the nonlinear algebraic equations

$$\big(f_1(\sigma_s,R)-f_2(\sigma_s,R)\big)(U-1)=-U+\frac{U^{2/3}}{\delta}, \tag{3.25a}$$

$$\big(f_1(\sigma_s,R)-f_3(\sigma_s,R)\big)(U-1)=-R^2U+\frac{RU^{2/3}}{\delta} \tag{3.25b}$$

numerically, using Newton's method.

The position of the stationary point, σ_s, is plotted as a function of the Bretherton parameter, δ, in figure 3.12. The black dashed curve shows where $\sigma_s = 1 + R$. For each fixed value of R we observe that, for suitably small δ, there are no stationary points in the region $|z_2 - z_1| \geq 1 + R$. As δ is increased, there exists a first value $\delta = \delta_1(R)$ at which a stationary point appears at $\sigma_s = 1 + R$. Then, for $\delta > \delta_1$, σ_s is a monotonically increasing function of δ.

We can find $\delta_1(R)$ by substituting $\sigma_s = 1 + R$ in (3.25) and solving for U and δ_1; the details of this calculation may be found in Appendix C. We plot δ_1 as a function of the bubble radius ratio, R, in figure 3.13. We observe that δ_1 is a monotonically decreasing function of R, which means that for larger values of R the stationary points are present for smaller values of δ. We also observe that, as $R \to 1^+$, $\delta_1(R)$ tends to a finite value that is approximately 2.37.

In figure 3.14(a), we plot the phase space showing the resulting trajectories of the larger bubble relative to the smaller bubble with $R = 2$ for $\delta = \delta_1(2)$. We observe that the stationary points of the system occur on the real axis at $\sigma_s = 1 + R$ (shown by red points); however there are still trajectories that enter the solid grey region $|z_2 - z_1| \leq 1 + R$. Hence the bubbles can still collide.

3.5.2.3 Condition 2: normal velocity

Condition 2 concerns the sign of the normal relative velocity of the two bubbles in a neighbourhood of the two points where $z_2 - z_1 = \pm \mathrm{i}(1 + R)$. When this condition is satisfied, the only trajectories that result in a collision of the bubbles are ones in which the bubbles are initially close to one another, and collisions always occur when the larger bubble is ahead of the smaller bubble. If the larger bubble is initially behind the smaller one, the bubbles will rotate around one another before colliding. We define the normal velocity by $U_n = (\boldsymbol{U}_2 - \boldsymbol{U}_1) \cdot \boldsymbol{n}$, where here $\boldsymbol{n}$ is the outward unit normal of the smaller bubble at the point where the bubbles are touching. When the separatrix encapsulates the region $|z_2 - z_1| \leq 1 + R$, we have $U_n > 0$ for $x_2 < x_1$, meaning the bubbles separate when the larger bubble is behind, and $U_n < 0$ for $x_2 > x_1$, meaning

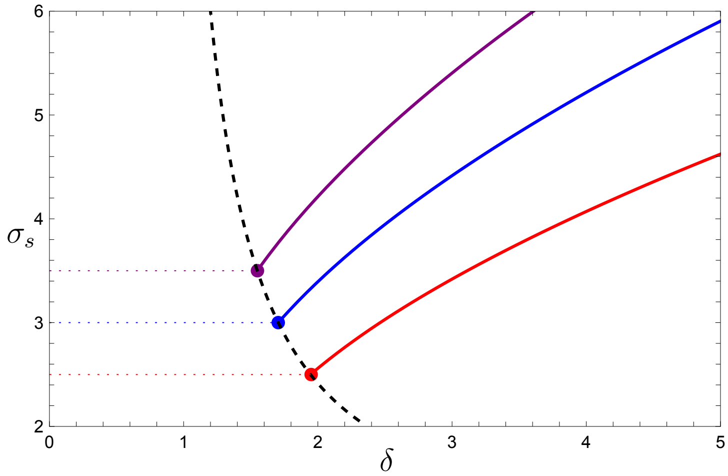

Figure 3.12: Position of the stationary point, σ_s, as a function of Bretherton parameter, δ, for $R = 1.5$ (red), 2 (blue), 2.5 (purple). The dashed black curve shows where $\sigma_s = 1 + R$.

the bubbles collide when the larger bubble is ahead. For condition 2, we find the value of δ at which U_n is stationary at $x_1 = x_2$, i.e., $\partial U_n/\partial\phi = 0$ at $\sigma = 1 + R$, $\phi = \pm\pi/2$. The details of the calculation can be found in Appendix C.

We plot δ_2 as a function of the bubble radius ratio, R, in figure 3.13. We observe that $\delta_2(R)$ is a monotonically decreasing function of R. We also observe that as $R \to 1^+$, $\delta_2(R)$ tends to a finite value $\delta^* \approx 3.10$. For all R, we have $\delta_2(R) > \delta_1(R)$, as expected, and we know that the critical value $\delta_c(R)$ lies somewhere between these two curves. In figure 3.14(b), we plot the phase space showing the resulting trajectories of the larger bubble relative to the smaller bubble with $R = 2$ for $\delta = \delta_2(2)$. We observe that the separatrix fully encloses the region $|z_2 - z_1| < 1 + R$ and hence it is impossible for the bubbles to collide whenever they start far apart. Hence, we find that for any value of R, if $\delta \geq \delta^* \approx 3.10$ (we note that this is not a sharp bound), then any trajectory with the larger bubble initially far behind will result in the bubbles rolling over one another instead of colliding.

3.6 Small separation limit

3.6.1 Asymptotic expansions

Now we will consider the extreme limit where the bubbles are almost touching. This limit is important as we have seen in §3.5 that bubbles can apparently collide in finite time, and thus we need to understand the behaviour as the bubbles become arbitrarily close. We note that, as mentioned in §3.2, we expect the model (3.1)–(3.2)

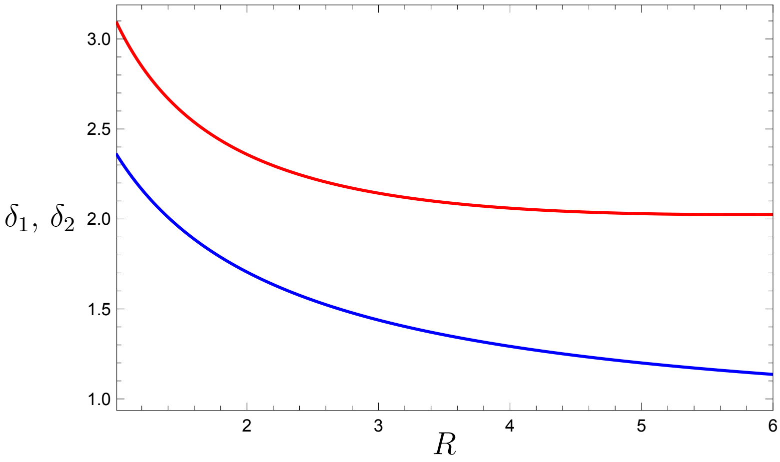

Figure 3.13: δ_1 (blue) and δ_2 (red) as a function of R.

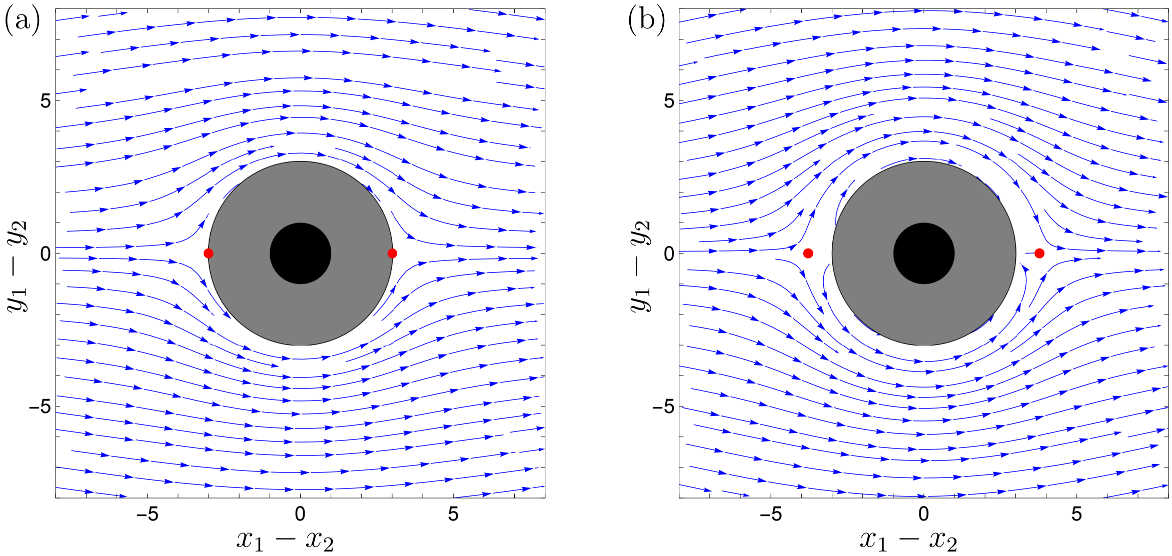

Figure 3.14: Trajectories for the two-bubble dynamical system (3.21) in the frame of the smaller bubble, with $R = 2$ and (a) $\delta = \delta_1(2)$, at which the stationary points (shown as red points) lie on the surface $|z_2 - z_1| = 1 + R$, (b) $\delta = \delta_2(2)$, above which the separatrix encloses the region $|z_2 - z_1| < 1 + R$ (solid grey fill). The solid black region $|z_2 - z_1| \leq 1$ represents the smaller bubble.

to break down when the bubbles are close, however in this section we analyse the small separation limit within the Hele-Shaw model. In the small separation limit, $\sigma \to 1 + R$, we find that

$$X^2 = 1 - \nu, \tag{3.26a}$$

$$a^2 \sim 1 - \alpha\nu + O(\nu^2), \tag{3.26b}$$

where $\alpha = R/(1+R)$ and

$$\nu = 2\sqrt{\frac{2(1+R)}{R}}\sqrt{\sigma - 1 - R} + O(\sigma - 1 - R) \ll 1. \tag{3.27}$$

We now apply the approximations (3.26) to the sums (3.19). In the first we have

$$\begin{aligned} f_1 &= \frac{2(1-a^2)^2}{a^2}\sum_{n=1}^{\infty}\frac{nX^{2n}}{1-X^{2n}}, \\ &\sim (2\alpha^2\nu^2 + O(\nu^4))\sum_{n=1}^{\infty}\frac{n(1-\nu)^n}{1-(1-\nu)^n}. \end{aligned} \tag{3.28}$$

The sum may be approximated by an integral using Euler-Maclaurin summation (Abramowitz & Stegun, 1968)

$$\sum_{n=1}^{\infty} f(n;\nu) \sim \int_1^{\infty} f(x;\nu)\,\mathrm{d}x + \frac{f(1;\nu) + f(\infty;\nu)}{2} + \text{h.o.t.}, \tag{3.29}$$

where h.o.t. is an abbreviation of higher order terms. Applying this result to our sum we find

$$\begin{aligned} \sum_{n=1}^{\infty}\frac{n(1-\nu)^n}{1-(1-\nu)^n} &\sim \int_1^{\infty}\frac{x(1-\nu)^x}{1-(1-\nu)^x}\,\mathrm{d}x + \frac{(1-\nu)}{2(1-(1-\nu))} + O(1), \\ &\sim \frac{1}{\nu^2}\int_0^{\infty}\frac{s(1-\nu)^{s/\nu}}{1-(1-\nu)^{s/\nu}}\,\mathrm{d}s - \int_0^1\frac{x(1-\nu)^x}{1-(1-\nu)^x}\,\mathrm{d}x + \frac{1}{2\nu} + O(1). \end{aligned} \tag{3.30}$$

Now we let $\nu \to 0$ giving

$$\sum_{n=1}^{\infty}\frac{n(1-\nu)^n}{1-(1-\nu)^n} \sim \frac{1}{\nu^2}\int_0^{\infty}\frac{s\mathrm{e}^{-s}}{1-\mathrm{e}^{-s}}\,\mathrm{d}s - \frac{1}{\nu}\int_0^1(1-x\nu)\,\mathrm{d}x + \frac{1}{2\nu} + O(1). \tag{3.31}$$

Hence to $O(\nu^2)$ we find that

$$f_1 \sim \frac{2R^2}{(1+R)^2}\left(\frac{\pi^2}{6} - \frac{1}{2}\nu\right) + O(\nu^2). \tag{3.32}$$

We now use (3.27) to show the explicit dependence on σ and R, i.e.,

$$f_1 \sim \frac{\pi^2 R^2}{3(1+R)^2} - \left(\frac{2R}{1+R}\right)^{3/2} \sqrt{\sigma - 1 - R} + O(\sigma - 1 - R). \tag{3.33}$$

We follow a similar methodology to find the leading-order behaviour of f_2 and f_3, namely

$$\begin{aligned} f_2 &\sim \frac{2R^2}{(1+R)^2}\left(\mathcal{Z}\left(2, \frac{R}{1+R}\right) - \frac{1}{2}\nu\right) + O(\nu^2), \\ &\sim \frac{2R^2}{(1+R)^2}\mathcal{Z}\left(2, \frac{R}{1+R}\right) - \left(\frac{2R}{1+R}\right)^{3/2} \sqrt{\sigma - 1 - R} + O(\sigma - 1 - R), \end{aligned} \tag{3.34}$$

and

$$\begin{aligned} f_3 &\sim \frac{2R^2}{(1+R)^2}\left(\mathcal{Z}\left(2, \frac{1}{1+R}\right) - \frac{1}{2}\nu\right) + O(\nu^2), \\ &\sim \frac{2R^2}{(1+R)^2}\mathcal{Z}\left(2, \frac{1}{1+R}\right) - \left(\frac{2R}{1+R}\right)^{3/2} \sqrt{\sigma - 1 - R} + O(\sigma - 1 - R), \end{aligned} \tag{3.35}$$

where $\mathcal{Z}(s, b)$ is the Hurwitz zeta-function (Kanemitsu *et al.*, 2000), given by

$$\mathcal{Z}(s, b) = \sum_{n=0}^{\infty} \frac{1}{(n+b)^s}. \tag{3.36}$$

In figure 3.15 we plot, in blue, these approximations as functions of σ, for an illustrative value of $R = 2$.

To find the bubble velocities, we expand $\mathcal{U}_k$ for $k \in \{1, 2\}$ in powers of ν as

$$\mathcal{U}_k \sim \mathcal{U}_k^{(0)} + \nu \mathcal{U}_k^{(1)} + O(\nu^2). \tag{3.37}$$

The leading-order expansion of (3.20) is given by

$$\frac{2R^2}{(1+R)^2}\left(\frac{\pi^2}{6}(\overline{\mathcal{U}}_2^{(0)} - 1)\mathrm{e}^{2\mathrm{i}\phi} - \mathcal{Z}\left(2, \frac{R}{1+R}\right)(\mathcal{U}_1^{(0)} - 1)\right) = -\mathcal{U}_1^{(0)} + \frac{\mathcal{U}_1^{(0)}}{\delta\left|\mathcal{U}_1^{(0)}\right|^{1/3}}, \tag{3.38a}$$

$$\frac{2R^2}{(1+R)^2}\left(\frac{\pi^2}{6}(\overline{\mathcal{U}}_1^{(0)} - 1)\mathrm{e}^{2\mathrm{i}\phi} - \mathcal{Z}\left(2, \frac{1}{1+R}\right)(\mathcal{U}_2^{(0)} - 1)\right) = -R^2\mathcal{U}_2^{(0)} + \frac{R\mathcal{U}_2^{(0)}}{\delta\left|\mathcal{U}_2^{(0)}\right|^{1/3}}. \tag{3.38b}$$

This is the limit of the equations when the bubbles are touching. Whether they remain in contact then depends on the sign of $\mathrm{Re}[(\mathcal{U}_1^{(0)} - \mathcal{U}_2^{(0)})\mathrm{e}^{-\mathrm{i}\phi}]$. If they do then we must study the dynamics of the bubbles when they are touching. Due to the large surface tension, we assume the bubbles do not coalesce but stay circular and apply a normal reaction force on each other. We shall explore this regime in §3.6.3.

We can continue the small-separation approximation to find the $O(\nu)$ correction to the velocities, which satisfy

$$\begin{aligned}\frac{R^2}{(1+R)^2}&\left(\left(\frac{\pi^2}{3}\overline{\mathcal{U}_2^{(1)}}-\overline{\mathcal{U}_2^{(0)}}\right)\mathrm{e}^{2\mathrm{i}\phi}-2\mathcal{Z}\left(2,\frac{R}{1+R}\right)\mathcal{U}_1^{(1)}+\mathcal{U}_1^{(0)}\right)\\ &=-\mathcal{U}_1^{(1)}+\frac{1}{\delta}\left(\frac{\mathcal{U}_1^{(1)}}{|\mathcal{U}_1^{(0)}|^{1/3}}-\frac{\mathrm{Re}\left[\mathcal{U}_1^{(0)}\overline{\mathcal{U}_1^{(1)}}\right]}{3\overline{\mathcal{U}_1^{(0)}}|\mathcal{U}_1^{(0)}|^{1/3}}\right),\end{aligned} \tag{3.39a}$$

$$\begin{aligned}\frac{R^2}{(1+R)^2}&\left(\left(\frac{\pi^2}{3}\overline{\mathcal{U}_1^{(1)}}-\overline{\mathcal{U}_1^{(0)}}\right)\mathrm{e}^{2\mathrm{i}\phi}-2\mathcal{Z}\left(2,\frac{1}{1+R}\right)\mathcal{U}_2^{(1)}+\mathcal{U}_2^{(0)}\right)\\ &=-R^2\mathcal{U}_2^{(1)}+\frac{R}{\delta}\left(\frac{\mathcal{U}_2^{(1)}}{|\mathcal{U}_2^{(0)}|^{1/3}}-\frac{\mathrm{Re}\left[\mathcal{U}_2^{(0)}\overline{\mathcal{U}_2^{(1)}}\right]}{3\overline{\mathcal{U}_2^{(0)}}|\mathcal{U}_2^{(0)}|^{1/3}}\right).\end{aligned} \tag{3.39b}$$

Though this system may look cumbersome, it is linear in $\{\mathcal{U}_1^{(1)},\mathcal{U}_2^{(1)}\}$, which makes it easily solvable. In figure 3.16 we compare the small-separation approximation (3.38)–(3.39) with the analytic solution (3.20). We find that we accurately match the behaviour seen in the analytic solution when the bubbles are very close together. However the accuracy of this approximation drops off very quickly as the bubble separation is increased.

3.6.2 Do the bubbles collide in finite time?

In figure 3.11(b), we observe trajectories that enter the solid grey region $|z_2 - z_1| \leq 1 + R$, which suggests that the bubbles collide. To show that a collision occurs in finite time, we calculate the relative normal velocity U_n of the two bubbles in in the limit when they are touching as $\sigma \to 1+R$, given by (3.38). If $U_n < 0$, the bubbles collide in finite time if they start sufficiently close. We plot U_n as a function of ϕ in figure 3.17(a) for $R = 2$ and various values of δ. Figure 3.17(b) shows a schematic of the two bubbles touching with the definitions of $\boldsymbol{n}$ and ϕ.

We find three possible regimes:

(*i*) If $\delta \geq \delta_c$ (see §3.5.2), then when a trajectory starts inside the separatrix with a non-zero offset in the y-direction, it will result in a collision in finite time (see figure 3.11(a)).

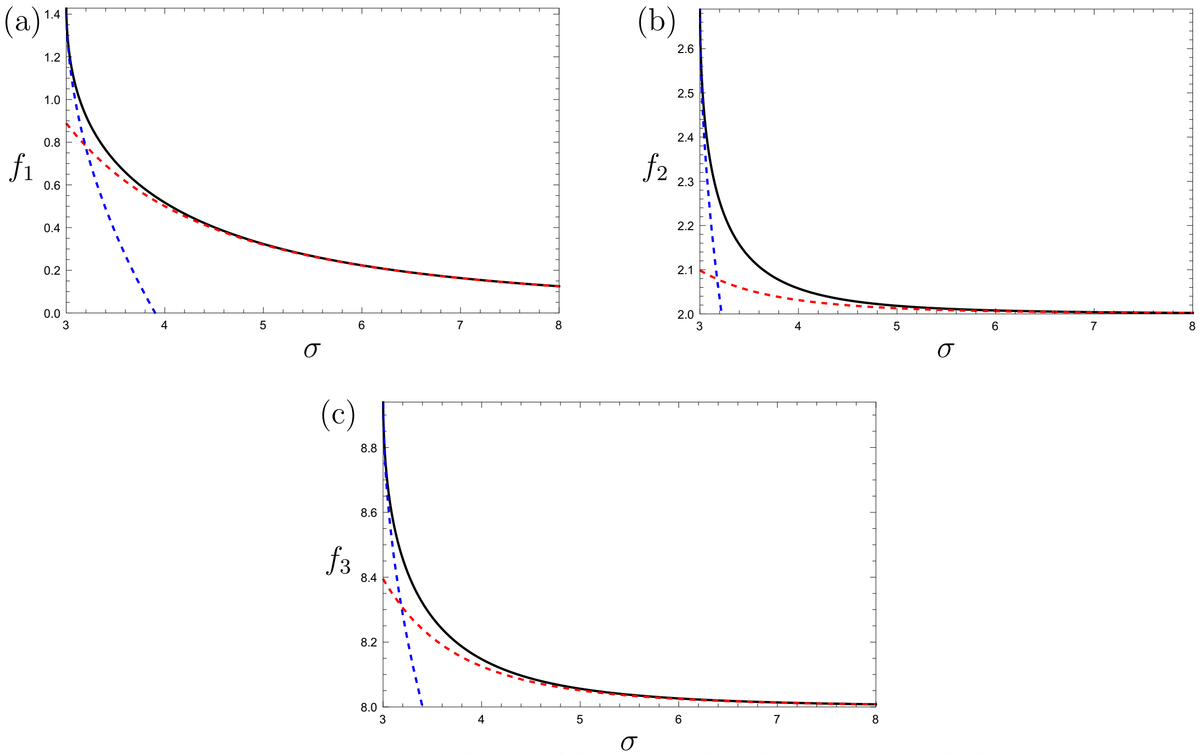

Figure 3.15: The functions $f_1(\sigma, R)$ (a), $f_2(\sigma, R)$ (b) and $f_3(\sigma, R)$ (c), versus σ for fixed $R = 2$. The red curves show the large separation asymptotic results (3.52) and the blue curves show the small separation asymptotic results (3.32), (3.34) and (3.35).

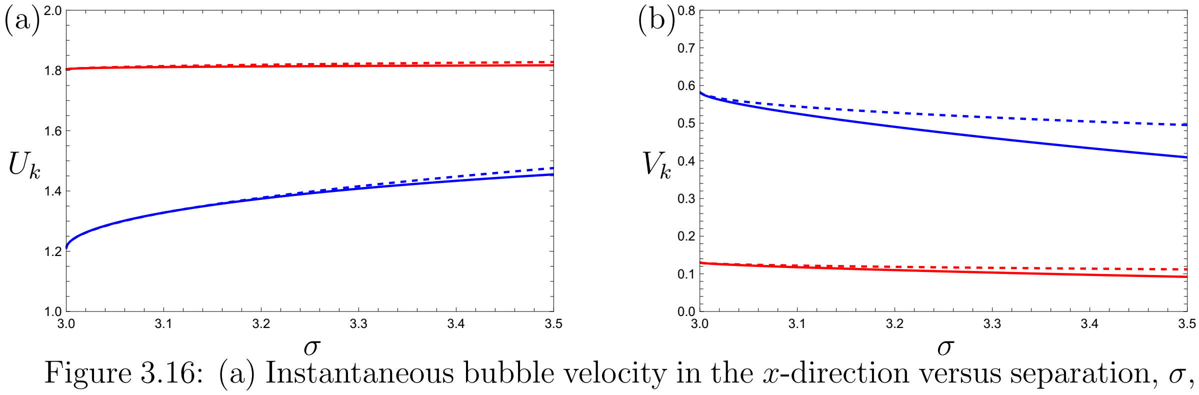

Figure 3.16: (a) Instantaneous bubble velocity in the x-direction versus separation, σ, for the smaller bubble U_1 (blue) and the larger bubble U_2 (red), with $R = 2$, $\phi = \pi/3$ and $\delta = 5$. (b) Instantaneous bubble velocity in the y-direction versus separation, σ, for the smaller bubble V_1 (blue) and the larger bubble V_2 (red), with $R = 2$, and $\delta = 5$. The full solution of (3.20) is shown by the solid curves and the small separation solutions (3.38)–(3.39) are shown by the dashed curves.

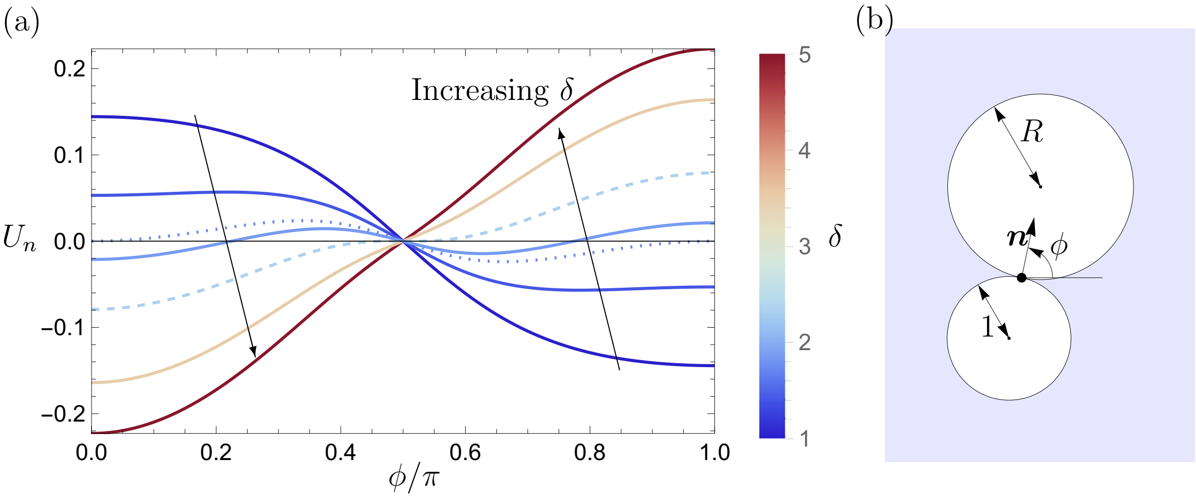

Figure 3.17: (a) The relative normal velocity, U_n, of the two bubbles as a function of the polar angle, ϕ, for a fixed $R = 2$ and δ shown by the colour bar. The dotted and dashed curves show U_n as a function of ϕ at $\delta = \delta_1(2)$, and $\delta = \delta_2(2)$, respectively (see §3.5.2). (b) Schematic of two bubbles touching showing the definitions of $\boldsymbol{n}$ and ϕ.

(*ii*) If $\delta_1 < \delta < \delta_c$, we are in an intermediate regime where $U_n > 0$ for parts of both $\phi \in (0, \pi/2)$ and $\phi \in (\pi/2, \pi)$ and the separatrix does not completely enclose $|z_2 - z_1| \leq 1 + R$. In this regime, the stationary points of (3.21) are in the region $|z_2 - z_1| > 1 + R$. Hence, there exist trajectories with the larger bubble beginning far behind the smaller one ($x_1 - x_2 \gg 1$) that result in collision in finite time.

(*iii*) If $\delta \leq \delta_1$, we have $U_n < 0$ for $\phi \in (\pi/2, \pi)$. Thus, in configurations where the larger bubble is behind the smaller one ($x_1 > x_2$), they collide in finite time provided that the initial value of $|y_1 - y_2|$ is not too large. Example trajectories of this kind are observed in figure 3.11(b).

It should be noted that we would expect our model to break down in the moments preceding the collision because the squeezing and drainage of liquid out from between the bubbles significantly influences bubble dynamics (see, for example, Crabtree & Bridgwater, 1971; Chauhan & Kumar, 2020). Furthermore, when the distance between the bubble interfaces is on the order of the gap height, we expect additional three-dimensional effects to become important.

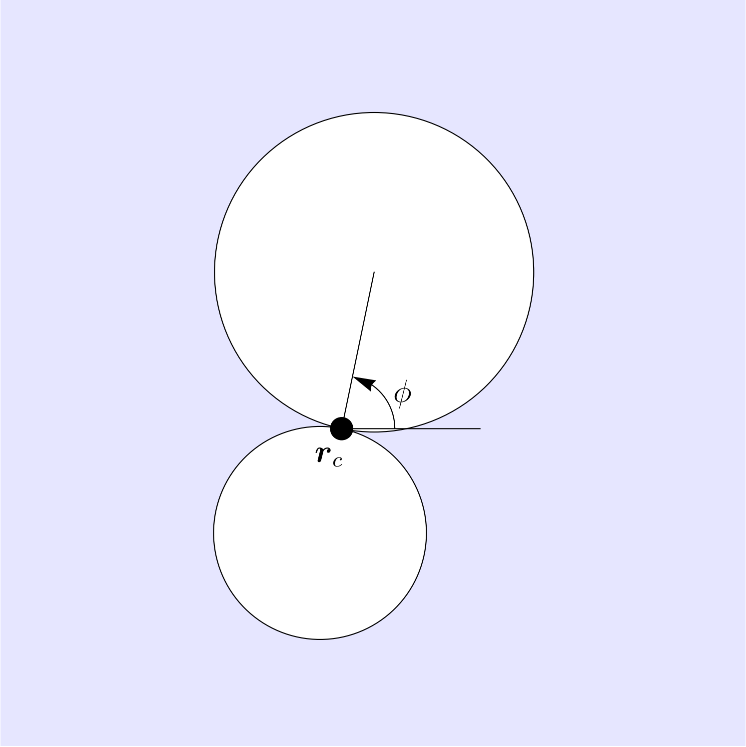

Figure 3.18: Schematic of two touching bubbles.

3.6.3 Touching bubbles

3.6.3.1 Force and moment balance

We have seen that, in finite time, two bubbles of different radii can collide and form a bubble pair. Assuming due to the high surface tension the bubbles do not coalesce, the bubble pair can then be modelled as a single entity. We can determine whether the bubbles stay together or separate depending on the sign of the mutual reaction force between the bubbles. To determine the rotational velocity we now need to consider a moment balance on the bubble pair as well as a force balance.

We denote the point of contact between the two bubbles by $\boldsymbol{r}_{\mathrm{c}}(t)$ and the angle between the line joining the bubble centres and the x-direction by $\phi(t)$. The position and orientation of the bubble pair is determined by three scalars: ϕ and the two components of $\boldsymbol{r}_{\mathrm{c}}$ (see figure 3.18). The centres of the two bubbles are given by

$$\boldsymbol{r}_1(t) = \boldsymbol{r}_{\mathrm{c}}(t) - R_1\boldsymbol{d}(t), \qquad \boldsymbol{r}_2(t) = \boldsymbol{r}_{\mathrm{c}}(t) + R_2\boldsymbol{d}(t), \tag{3.40}$$

where

$$\boldsymbol{d}(t) = \begin{pmatrix} \cos\phi(t) \\ \sin\phi(t) \end{pmatrix}. \tag{3.41}$$

As before, without loss of generality we can set $R_1 = 1$ and $R_2 = R \geq 1$.

The total hydrodynamic force on each bubble is given by

$$\boldsymbol{f}_k(t) = \oint_{|\boldsymbol{r}-\boldsymbol{r}_k|=R_k} -\Pi\,\boldsymbol{n}\,\mathrm{d}s = -\frac{1}{R_k}\oint_{|\boldsymbol{r}-\boldsymbol{r}_k|=R_k} \Pi\,(\boldsymbol{r}-\boldsymbol{r}_k)\,\mathrm{d}s, \tag{3.42}$$

where $\boldsymbol{n}$ is the unit normal to the bubble surface, s is an element of arclength, and Π is a modified pressure, which includes the "Bretherton" contribution from the meniscus, and is given by

$$\Pi = p + \frac{\epsilon}{3\mathrm{Ca}^{1/3}}\,\beta(U_n)U_n^{2/3}. \tag{3.43}$$

A net force balance on the system requires

$$\boldsymbol{f}_1 + \boldsymbol{f}_2 = \boldsymbol{0}. \tag{3.44}$$

The corresponding moments (about the contact point) are given by

$$\boldsymbol{m}_k(t) = -\oint_{|\boldsymbol{r}-\boldsymbol{r}_k|=R_k} \Pi\,(\boldsymbol{r}-\boldsymbol{r}_c)\times\boldsymbol{n}\,\mathrm{d}s, \tag{3.45}$$

and the net moment balance on the system reads

$$\boldsymbol{m}_1 + \boldsymbol{m}_2 = \boldsymbol{0}. \tag{3.46}$$

The expression (3.45) can be simplified as follows. With $k=1$, for example, we have

$$\boldsymbol{m}_1(t) = -\frac{1}{R_1}\oint_{|\boldsymbol{r}-\boldsymbol{r}_1|=R_1} \Pi\,(\boldsymbol{r}-\boldsymbol{r}_1+R_1\boldsymbol{d})\times(\boldsymbol{r}-\boldsymbol{r}_1)\,\mathrm{d}s, \tag{3.47}$$

which may be simplified to

$$\boldsymbol{m}_1 = -R_1\boldsymbol{d}\times\boldsymbol{f}_1. \tag{3.48a}$$

Similarly for $k=2$ we find

$$\boldsymbol{m}_2 = R_2\boldsymbol{d}\times\boldsymbol{f}_2. \tag{3.48b}$$

We suppose that the mutual reaction force at the contact point (of magnitude F_N, say) acts purely in the normal direction, i.e.

$$\boldsymbol{f}_1 = F_N\boldsymbol{d}, \qquad\qquad \boldsymbol{f}_2 = -F_N\boldsymbol{d}. \tag{3.49}$$

Then the force balance (3.44) is satisfied, and the moments $\boldsymbol{m}_j$ are equal to zero, so the moment balance (3.46) is also satisfied identically. The reaction force assumption (3.49) provides four scalar equations which, in principle, allow us to determine the velocities $\dot{\boldsymbol{r}}_c$ and $\dot{\phi}$ as well as the additional unknown F_N. As long as $F_N > 0$ the bubbles remain stuck together as a pair, and they drift apart whenever $F_N < 0$.

3.6.3.2 Complex variable formulation

To be consistent with our previous work in this chapter we now convert (3.49) into complex variables. We combine (3.49) with our leading-order equations (3.38) to give the governing equations

$$\frac{2R^2\pi}{(1+R)^2}\left(\frac{\pi^2}{6}\left(\overline{\mathcal{U}_2}-1\right)\mathrm{e}^{2\mathrm{i}\phi}-\mathcal{Z}\left(2,\frac{R}{1+R}\right)\left(\mathcal{U}_1-1\right)\right)+\pi\mathcal{U}_1-\frac{\pi\mathcal{U}_1}{\delta\left|\mathcal{U}_1\right|^{1/3}}=F_N\mathrm{e}^{\mathrm{i}\phi}, \tag{3.50a}$$

$$\frac{2R^2\pi}{(1+R)^2}\left(\frac{\pi^2}{6}\left(\overline{\mathcal{U}_1}-1\right)\mathrm{e}^{2\mathrm{i}\phi}-\mathcal{Z}\left(2,\frac{1}{1+R}\right)\left(\mathcal{U}_2-1\right)\right)+\pi R^2\mathcal{U}_2-\frac{\pi R\mathcal{U}_2}{\delta\left|\mathcal{U}_2\right|^{1/3}}=-F_N\mathrm{e}^{\mathrm{i}\phi}, \tag{3.50b}$$

for the bubble pair, where

$$\mathcal{U}_k=\dot{z}_c+(-1)^k\mathrm{i}R_k\dot{\phi}\,\mathrm{e}^{\mathrm{i}\phi}, \tag{3.50c}$$

for $k\in\{1,2\}$, where $R_1=1$, $R_2=R$ and $z_c=x_c+\mathrm{i}y_c$. By taking the real and imaginary parts of (3.50) we have a system of four equations for our four unknowns $\{\dot{x}_c,\dot{y}_c,\dot{\phi},F_N\}$.

Note that in the specific case $R=1$ the expressions on the left-hand sides of (3.50a) and (3.50b) are equal and thus $F_N=0$. When the bubbles have equal radii, they travel at the same velocity and never separate.

3.6.3.3 Results

The normal force, F_N is plotted as a function of ϕ in figure 3.19 with $R=2$ and various values of δ. The solutions where $F_N>0$ are shown as solid lines with the direction of rotation shown by the arrows. The solutions where $F_N<0$ are shown by dashed lines and indicate when the bubbles separate.

We find three possible regimes:

1. If $\delta\geq\delta_2$ (see blue curve in figure 3.19), where δ_2 is the critical value of the Bretherton parameter (see §3.5.2), then $F_N>0$ for $\phi\in(0,\pi/2)$, and $F_N<0$ for $\phi\in(\pi/2,\pi)$. For $\phi\in(0,\pi/2)$, when the larger bubble is ahead, we find that the bubble pair will rotate towards $\phi=0$, where the larger bubble is in front, and stay a bubble pair for all time. In the other case $\phi\in(\pi/2,\pi)$, where the larger bubble is now behind, the bubble pair will separate, in agreement with the streamlines in figure 3.11(a) where for $\phi\in(\pi/2,\pi)$ the trajectories are directed away from the shaded region, $|z_1-z_2|\leq 1+R$. After separating,

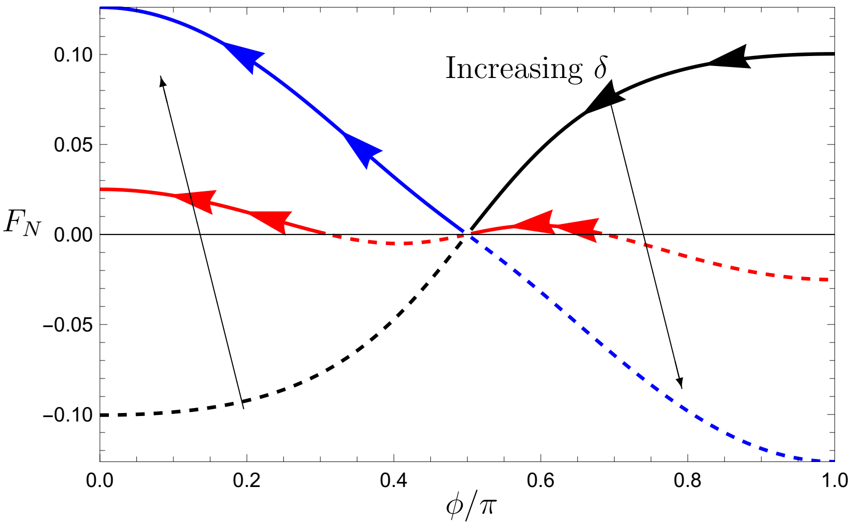

Figure 3.19: The normal force, F_N, as a function of the angle, ϕ, for a fixed $R = 2$ and $\delta = 5$ (blue), 2 (red), 1 (black). The curves are solid when $F_N > 0$ and dashed when $F_N < 0$. The arrows on the solid curves denote the direction of rotation of the bubble pair.

the bubbles will follow one of the trajectories away from $|z_1 - z_2| \leq 1 + R$. However, following this trajectory the bubbles will collide again in the region $\phi \in (0, \pi/2)$, rotate until $\phi = 0$, and then stay as a pair for all time, with the smaller bubble behind the larger.

2. For $\delta_1 < \delta < \delta_2$, where δ_1 is the first value of δ such that the stationary points of (3.21) lie on $|z_1 - z_2| = 1 + R$ (see §3.5.2), we have an intermediate regime (see red curve in figure 3.19) where $F_N > 0$ for parts of both $(0, \pi/2)$ and $(\pi/2, \pi)$. This behaviour occurs because, while the stationary points of the trajectories are in the region $|z_1 - z_2| \geq 1 + R$, they are not far enough away from $|z_1 - z_2| = 1 + R$ such that $U_n = (\boldsymbol{U}_1 - \boldsymbol{U}_2) \cdot \boldsymbol{n} > 0$ for all $\phi \in (0, \pi/2)$.

3. For $\delta \leq \delta_1$, we have $F_N < 0$ for $\phi \in (0, \pi/2)$, and $F_N > 0$ for $\phi \in (\pi/2, \pi)$ (see black curve in figure 3.19). Hence we observe that, if the larger bubble is ahead ($\phi \in (0, \pi/2)$) then the bubble pair separates. However if the larger bubble is behind ($\phi \in (\pi/2, \pi)$), then the bubble pair will rotate towards $\phi = \pi/2$, at which point they will separate from one another. This behaviour is consistent with the streamlines shown in figure 3.11(b).

3.7 Large separation limit

3.7.1 Asymptotic expansions

A common simplification used when studying the motion of multiple bubbles in a Hele-Shaw cell is effectively to consider well-separated bubbles and thus use a dipole approximation. In the literature these dipole methods are often supplemented with a linear drag law (see for example, Shen *et al.*, 2014; Beatus *et al.*, 2006, 2012). It was shown by Green (2018) that the two-bubble pressure field found by Sarig *et al.* (2016) reduces to the dipole approximation used by Beatus *et al.* (2006) in the well-separated limit with a linear drag law. Here we shall look at the limit as $\sigma \to \infty$ in (3.20) to derive a dipole method for the two-bubble model with the nonlinear drag law proposed in this thesis.

First we expand (3.4a) and (3.4b) in powers of $1/\sigma$ to get

$$a \sim \frac{1}{\sigma} + \frac{R^2}{\sigma^3} + O\left(\frac{1}{\sigma^5}\right), \tag{3.51a}$$

$$X \sim \frac{R}{\sigma^2} + \frac{R(1+R^2)}{\sigma^4} + O\left(\frac{1}{\sigma^5}\right). \tag{3.51b}$$

From these expressions we can find the expansions of (3.19), namely

$$f_1 \sim \frac{2R^2}{\sigma^2} + O\left(\frac{1}{\sigma^5}\right), \tag{3.52a}$$

$$f_2 \sim 2 + \frac{2R^2}{\sigma^4} + O\left(\frac{1}{\sigma^5}\right), \tag{3.52b}$$

$$f_3 \sim 2R^2 + \frac{2R^4}{\sigma^4} + O\left(\frac{1}{\sigma^5}\right). \tag{3.52c}$$

These approximations are plotted as red dashed curves in figure 3.15. We find that the approximations hold provided the bubbles are at least about a radius of the smaller bubble apart (measured edge to edge).

Finally, to derive the dipole approximation, we expand $\mathcal{U}_k$ in powers of $1/\sigma^2$, since only even powers of $1/\sigma$ appear in (3.52), i.e.,

$$\mathcal{U}_k \sim \mathcal{U}_k^{(0)} + \frac{1}{\sigma^2}\mathcal{U}_k^{(2)} + \cdots . \tag{3.53}$$

Substituting this expansion into the equations of motion (3.20), we find at leading order

$$-2(\mathcal{U}_1^{(0)} - 1) = -\mathcal{U}_1^{(0)} + \frac{\mathcal{U}_1^{(0)}}{\delta \left|\mathcal{U}_1^{(0)}\right|^{1/3}}, \tag{3.54a}$$

$$-2R^2(\mathcal{U}_2^{(0)} - 1) = -R^2\mathcal{U}_2^{(0)} + \frac{R\mathcal{U}_2^{(0)}}{\delta \left|\mathcal{U}_2^{(0)}\right|^{1/3}}, \tag{3.54b}$$

which are simply the equations of motion for an isolated bubble (of size 1 or R) in an infinite medium (2.15) written in complex variables. To leading order, the bubbles move as if they are in isolation, so $\mathcal{U}_k^{(0)} = U_k^{(0)} \in \mathbb{R}$.

At $O(1/\sigma^2)$ in (3.20a) we find

$$\begin{aligned} 2R^2\left(U_2^{(0)} - 1\right)\mathrm{e}^{2\mathrm{i}\phi} - 2\mathcal{U}_1^{(2)} &= -\mathcal{U}_1^{(2)} + \frac{1}{\delta\left(U_1^{(0)}\right)^{1/3}}\left(\mathcal{U}_1^{(2)} - \frac{1}{3}\operatorname{Re}\left[\mathcal{U}_1^{(2)}\right]\right), \\ &= -\mathcal{U}_1^{(2)} + \frac{2 - U_1^{(0)}}{U_1^{(0)}}\left(\mathcal{U}_1^{(2)} - \frac{1}{3}\operatorname{Re}\left[\mathcal{U}_1^{(2)}\right]\right), \end{aligned} \tag{3.55}$$

with a similar expression for (3.20b). Writing $\mathcal{U}_1^{(2)} = U_1^{(2)} + \mathrm{i}V_1^{(2)}$ and taking real and imaginary parts of (3.55) we find

$$U_1^{(2)} = -\frac{6U_1^{(0)}\left(1 - U_2^{(0)}\right)R^2}{4 + U_1^{(0)}}\cos 2\phi, \tag{3.56a}$$

$$V_1^{(2)} = -U_1^{(0)}\left(1 - U_2^{(0)}\right)R^2\sin 2\phi. \tag{3.56b}$$

Similarly for (3.20b) we find

$$U_2^{(2)} = -\frac{6U_2^{(0)}\left(1 - U_1^{(0)}\right)}{4 + U_2}\cos 2\phi, \tag{3.57a}$$

$$V_2^{(2)} = -U_2^{(0)}\left(1 - U_1^{(0)}\right)\sin 2\phi. \tag{3.57b}$$

In figure 3.20 we compare the bubble velocities given by the large-separation approximation (3.54)–(3.57) with the analytic solution (3.20). We observe that the approximation matches the analytic solution very closely for large σ. However, in the limit $\sigma \to 1 + R$, the approximation falls short and does not accurately capture the bubble velocities in the x-direction, U_k (see figure 3.20(a)). On the other hand, the approximation very closely matches the analytic solution for the velocities in the y-direction, V_k, despite the large-separation assumption.

Since the large-separation approximation matches the dynamics of the two-bubble system so well, even when the bubbles are not especially far apart, in the next subsection we derive a dynamical system using these results.

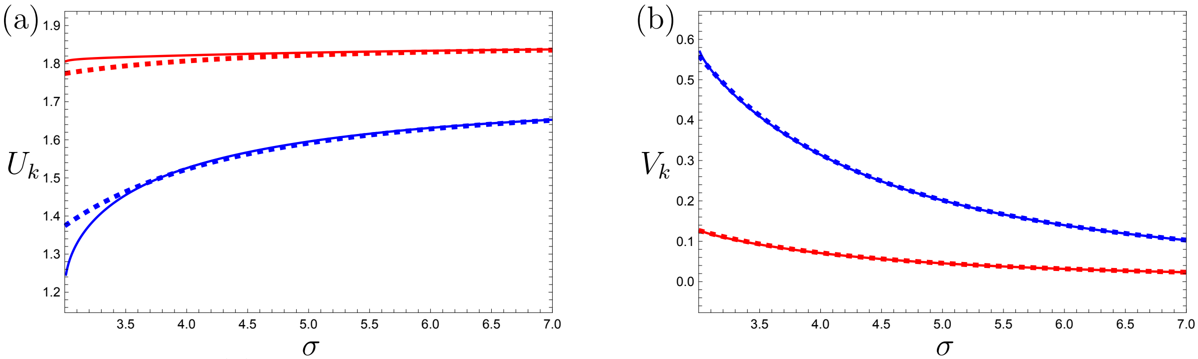

Figure 3.20: (a) Instantaneous bubble velocity in x-direction versus separation, σ, for the smaller bubble U_1 (blue) and the larger bubble U_2 (red), with $R = 2$, $\phi = \pi/3$ and $\delta = 5$. (b) Instantaneous bubble velocity in y-direction versus separation, σ, for the smaller bubble V_1 (blue) and the larger bubble V_2 (red), with $R = 2$, $\phi = \pi/3$ and $\delta = 5$. The analytic solutions (3.20) are shown by the solid curves and the large separation solutions (3.54)–(3.57) are shown by the dashed curves.

3.7.2 The dipole method

We will now use the results (3.54)–(3.57) to create a dynamical system for the bubble positions similar to (3.21) for the large separation limit. This approach is commonly referred to as a “dipole method” because it is equivalent to assuming each bubble acts as a dipole of strength $\left(1 - U_k^{(0)}\right) R_k^2$ centred at the bubble centre. This gives the system

$$\frac{\mathrm{d}x_1}{\mathrm{d}t} = U_1^{(0)} \left(1 - \frac{6\left(1 - U_2^{(0)}\right) R^2}{\sigma^2 \left(4 + U_1^{(0)}\right)} \cos 2\phi \right), \tag{3.58a}$$

$$\frac{\mathrm{d}y_1}{\mathrm{d}t} = -\frac{U_1^{(0)} \left(1 - U_2^{(0)}\right) R^2}{\sigma^2} \sin 2\phi, \tag{3.58b}$$

$$\frac{\mathrm{d}x_2}{\mathrm{d}t} = U_2^{(0)} \left(1 - \frac{6\left(1 - U_1^{(0)}\right)}{\sigma^2 \left(4 + U_2^{(0)}\right)} \cos 2\phi \right), \tag{3.58c}$$

$$\frac{\mathrm{d}y_2}{\mathrm{d}t} = -\frac{U_2^{(0)} \left(1 - U_1^{(0)}\right)}{\sigma^2} \sin 2\phi. \tag{3.58d}$$

Rewriting σ and ϕ to obtain an explicit system for (x_k, y_k) we obtain

$$\frac{\mathrm{d}x_1}{\mathrm{d}t} = U_1^{(0)} \left(1 - \frac{6\left(1 - U_2^{(0)}\right) R^2}{\left(4 + U_1^{(0)}\right)} \frac{(x_1 - x_2)^2 - (y_1 - y_2)^2}{((x_1 - x_2)^2 + (y_1 - y_2)^2)^2} \right), \tag{3.59a}$$

$$\frac{\mathrm{d}y_1}{\mathrm{d}t} = -U_1^{(0)} \left(1 - U_2^{(0)}\right) R^2 \frac{2(x_1 - x_2)(y_1 - y_2)}{((x_1 - x_2)^2 + (y_1 - y_2)^2)^2}, \tag{3.59b}$$

$$\frac{\mathrm{d}x_2}{\mathrm{d}t} = U_2^{(0)} \left(1 - \frac{6\left(1 - U_1^{(0)}\right)}{\left(4 + U_2^{(0)}\right)} \frac{(x_1 - x_2)^2 - (y_1 - y_2)^2}{((x_1 - x_2)^2 + (y_1 - y_2)^2)^2} \right), \tag{3.59c}$$

$$\frac{\mathrm{d}y_2}{\mathrm{d}t} = -U_2^{(0)} \left(1 - U_1^{(0)}\right) \frac{2(x_1 - x_2)(y_1 - y_2)}{((x_1 - x_2)^2 + (y_1 - y_2)^2)^2}, \tag{3.59d}$$

This set of equations for the bubble-centre positions (x_k, y_k) is significantly easier to solve than (3.21). However, the real power of the dipole method comes to fruition when we consider more than two bubbles, in Chapter 4.

We move into the frame of reference of the larger bubble, by defining $\mathcal{X} = x_1 - x_2$ and $\mathcal{Y} = y_1 - y_2$, which are governed by the dynamical system

$$\frac{\mathrm{d}\mathcal{X}}{\mathrm{d}t} = -A + B_1 \frac{\mathcal{X}^2 - \mathcal{Y}^2}{(\mathcal{X}^2 + \mathcal{Y}^2)^2}, \tag{3.60a}$$

$$\frac{\mathrm{d}\mathcal{Y}}{\mathrm{d}t} = 2B_2 \frac{\mathcal{X}\mathcal{Y}}{(\mathcal{X}^2 + \mathcal{Y}^2)^2}, \tag{3.60b}$$

where

$$A = U_2^{(0)} - U_1^{(0)}, \tag{3.61a}$$

$$B_1 = \frac{6U_2^{(0)}\left(1 - U_1^{(0)}\right)}{4 + U_2^{(0)}} - \frac{6U_1^{(0)}\left(1 - U_2^{(0)}\right) R^2}{4 + U_1^{(0)}}, \tag{3.61b}$$

$$B_2 = U_2^{(0)}\left(1 - U_1^{(0)}\right) - U_1^{(0)}\left(1 - U_2^{(0)}\right) R^2. \tag{3.61c}$$

Recall that U_1 and U_2 are determined in terms of R and δ by (3.54) In figure 3.21 we plot the phase space of (3.60) showing the trajectories of the smaller bubble relative to the larger. These phase planes show the same qualitative behaviour as seen for the full system in figure 3.11.

The stationary points of the system (3.60) are readily found to be at

$$\mathcal{X} = \pm s_p = \pm\sqrt{\frac{B_1}{A}}, \qquad \mathcal{Y} = 0. \tag{3.62a,b}$$

Note that for physically relevant stationary points we require that $s_p = \sqrt{B_1/A} \geq 1 + R$. In figure 3.22 we plot the position of the stationary point as a function of δ, alongside

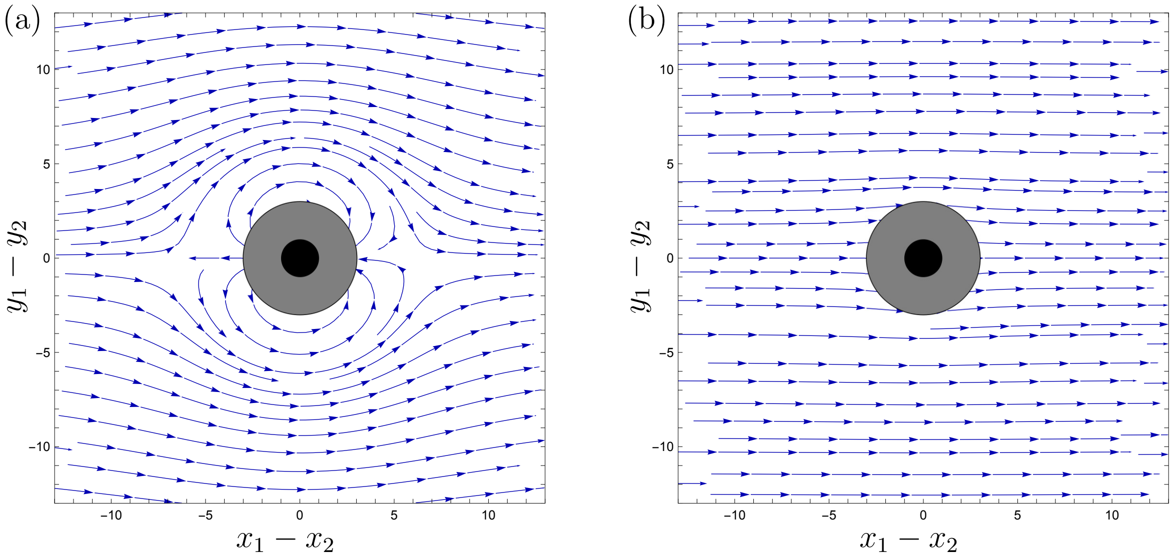

Figure 3.21: Trajectories for the two-bubble dipole dynamical system (3.60) in the frame of the smaller bubble, with $R = 2$ and (a) $\delta = 5$, (b) $\delta = 1/2$. Any trajectories entering the solid grey region $|z_1 - z_2| \leq (1 + R)$ are such that the two bubbles will collide. The solid black region $|z_1 - z_2| \leq 1$ represents the smaller bubble.

the unapproximated predictions from §3.5.2. We observe generally good agreement between the two models, although the dipole model slightly under-predicts the critical value of δ at which the stationary points occur at $s_p = 1 + R$. This is where we expect the dipole model to fall short due to the large-separation assumption becoming invalid. Otherwise, the dipole model performs exceptionally well in comparison with the full model.

We have shown in figures 3.15, 3.20–3.22 that the large-separation approximation accurately reproduces results of the full solution (3.20), even when the separation is not especially large. The utility of an approximate solution of this nature is heightened in systems of more than two bubbles where analytic solution is generally impossible. In Chapter 4 we shall use the large-separation approximation to derive a dipole model for an arbitrary number of bubbles.

3.8 Full two-bubble trajectories

Using everything developed so far in this chapter, we are now in a position to characterise the trajectories of two bubbles in a Hele-Shaw cell, with the larger of the two bubbles initially far behind. In §3.5.2 we found the existence of a critical value of $\delta = \delta_c$ above which it is impossible for the two bubbles to collide, and the larger bubble must rotate past the smaller bubble.

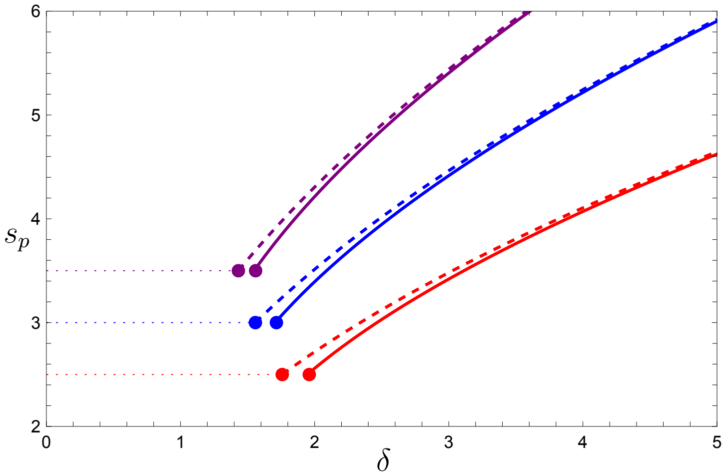

Figure 3.22: Position of the stationary point, s_p as a function of Bretherton parameter, δ, for the dipole method (3.62) (dashed) and the full problem (solid), for $R = 1.5$ (red), 2 (blue), 2.5 (purple).

We find that there are two possible cases. First, if $\delta < \delta_c$, then there exists a region $|y_1 - y_2| < b$ such that, if the trajectory starts within this region the bubbles will always collide. We call this Case 1 and show an example trajectory in figure 3.23(a). In this example, initially $x_1 - x_2 \gg 1 + R$ and $|y_1 - y_2| < b$ (see ①) so the larger bubble is far behind the smaller bubble. To begin with, each bubble behaves as if in isolation, so the larger bubble moves faster than the smaller. Eventually the larger bubble catches up with the smaller and they collide (see ②). Following our analysis in §3.6.3 we find that the bubbles rotate as a pair until the centres are aligned perpendicular to the flow ($\phi = \pi/2$); at this point the normal force between the bubbles vanishes (see ③). The bubbles then break apart and the larger bubble now overtakes the smaller bubble (see ④). From this point the larger bubble will always travel faster than the smaller and so remains ahead.

Case 2 arises when $\delta > \delta_c$ and $|y_1 - y_2| > 0$ or $\delta < \delta_c$ and $|y_1 - y_2| > b$ initially. In figure 3.23(b) we show an example trajectory. In the example, initially we have $x_1 - x_2 \gg 1 + R$ and $|y_1 - y_2| > 0$ ($|y_1 - y_2| > b$ if $\delta < \delta_c$) (see ①) so the larger bubble is far behind the smaller bubble with an offset in the y-direction. The larger bubble catches up with the smaller bubble (see ②). Now the bubble–bubble interactions are large enough that the bubbles repel each other and avoid colliding (see ③). The larger bubble then manoeuvres around the smaller bubble to the front and can now freely move faster than the smaller bubble (see ④).

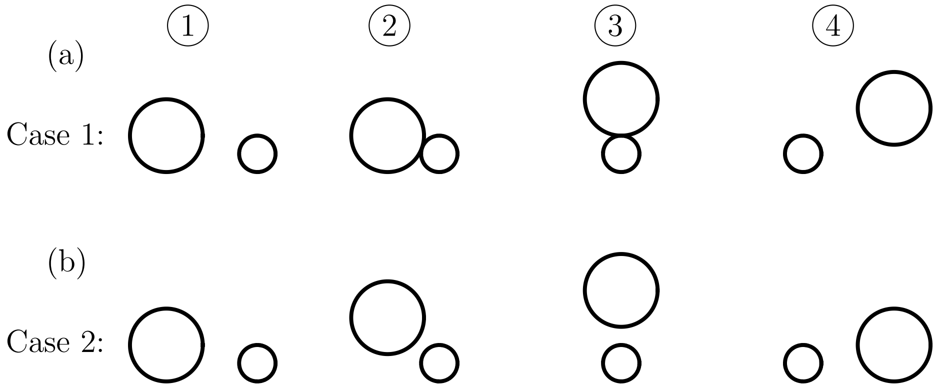

Figure 3.23: Example full trajectories for (a) Case 1 (b) Case 2, for initially far separated bubbles.

3.9 Conclusions

In this chapter, we develop a model for the motion of two circular bubbles in a Hele-Shaw cell. Through the use of complex variable methods we derive analytical expressions for the equations of motion for each bubble. In general, the instantaneous bubble velocities are obtained by solving the system of nonlinear algebraic equations (3.20).

When the two bubbles are identical they move at the same velocity and we again observe a qualitative change in behaviour depending on whether the Bretherton parameter $\delta < 1$ or $\delta > 1$. Specifically if the bubbles are aligned with the flow direction, the bubble pair travels slower than an isolated bubble for $\delta < 1$, but faster for $\delta > 1$. Conversely if the bubbles are aligned perpendicularly to the outer flow then the bubble pair travels faster for $\delta < 1$, but slower for $\delta > 1$.

For two non-identical bubbles such that the larger bubble is initially far behind the smaller bubble with a small transverse offset, there are two possible outcomes. The first is that the bubbles collide, while in the second, due to the nonlinear interactions, instead of colliding they rotate around each other. Which behaviour occurs depends on the value of the Bretherton parameter δ. For each bubble radius ratio, R, there exists a first critical Bretherton parameter, $\delta_1(R)$, above which it is impossible for two aligned bubbles to collide. Then there exists a second critical Bretherton parameter, $\delta_2(R)$, above which any trajectory with the bubbles initially far apart results in the bubbles rotating around one another, and if the bubbles are initially close with the larger bubble behind the bubbles will rotate around one another and then collide with the large one in front. We find that if $\delta \geq \delta^* \approx 3.10$ then the bubbles must always rotate around one another regardless of their radii if the smaller bubble is initially in front.

The extreme limit where the bubbles are almost touching is analysed asymptotically. The asymptotic results accurately reproduce the behaviour of the two bubbles predicted by the full numerical solutions when they are close together but the predictions quickly diverge as the separation is increased. These results confirm that the bubbles can collide in finite time.

Due to the high surface tension, we assume the bubbles do not coalesce when they touch. We thus model a touching pair of bubbles as a single entity and determine whether they stay together or separate depending on the mutual reaction force. If $\delta > \delta_2$, we find that, if the larger bubble is behind the smaller, then the pair will separate. However if the larger bubble is ahead, then the bubble pair stay together and rotate until they are aligned with the flow, with the larger bubble in front. If δ is sufficiently small then, if the smaller bubble is ahead, the bubble pair will rotate until they are perpendicular to the flow and then separate, while if the larger bubble is ahead they will always separate. Finally, there is an intermediate region where the reaction force is positive for some orientations with the larger bubble ahead and for some with the larger one behind.

Asymptotic expressions for the bubble velocities are found in the limit of large bubble separation. We find these results agree very well with the full solution even when the bubbles are quite close together. In this limit the bubbles act as though they are dipoles, and we derive a simple dynamical system that is commonly used in the literature but without justification (e.g. Beatus *et al.*, 2006; Shen *et al.*, 2014) . The dipole model here is readily generalised to an arbitrary number of bubbles and will be the subject of investigation in Chapter 4.

Finally we characterise the possible full trajectories in a two-bubble system with the larger bubble initially far behind. The first possibility is that the larger bubble catches up with the smaller bubble and they collide. The bubble pair then move together and rotate until the bubbles are aligned perpendicular to the outer flow, at which point they separate and the larger bubble is free to move faster than the smaller bubble. The other possibility is instead of colliding the bubbles rotate around one another leaving the larger bubble in front.

The results obtained here provide great insight into the interactions of bubbles in a Hele-Shaw cell. We will expand this to study the interactions of multiple bubbles in the next chapter.

Chapter 4

The motion of multiple bubbles in a Hele-Shaw cell

4.1 Introduction

In this chapter we extend the results of Chapters 2 and 3 by developing methodologies to simulate the propagation of an arbitrary number of bubbles.

We begin in §4.2 by writing down the governing equations for the motion of an arbitrary number of bubbles in a Hele-Shaw cell. Then in §4.3 we develop a numerical method to solve the equations of motion of the bubbles. We validate the numerical method by comparing with the known two-bubble solution found in Chapter 3. In this chapter, we implement finite element methods, however, the system would also lend itself to boundary element methods, which have been classically used to study Hele-Shaw problems (see e.g. DeGregoria & Schwartz, 1986; Aitchison & Howison, 1985). There has also been recent developments in the use of the level set method for Hele-Shaw flows (Morrow *et al.*, 2019).

In §4.4 we consider a train of three collinear identical bubbles moving along the centre-line of a Hele-Shaw channel. We find that the middle bubble moves either faster or slower than the outer two bubbles, depending on the physical properties of the system forming what we refer to as a "Hele-Shaw Newton's cradle". In a train of four identical bubbles, this effect can cascade down the line of bubbles leaving a pair at the front or behind, depending on the flow conditions.

In §4.5 we analyse the limit in which the bubbles are far from one another. Using matched asymptotic expansions we derive a "dipole model" for an arbitrary number of bubbles, extending the two-bubble result in §3.7. The dipole model significantly reduces the computational complexity in comparison to the numerical method proposed in §4.3, while retaining the qualitative features of the full model.

Finally, in §4.6 we derive a pairwise interaction model. Using the analytical equations of motion for a system of two bubbles derived in §3.3, we obtain approximate equations of motion for an arbitrary number of bubbles by considering the pairwise contributions. This model is exact for the propagation of two bubbles, whereas the dipole model is only exact for the propagation of an isolated bubble. We then assess the pros and cons of the dipole and pairwise approximate models, by comparing them with full numerical solutions.

4.2 General model for multiple bubbles

We begin by generalising the models derived in Chapters 2 and 3 to describe the flow of an arbitrary number of bubbles in a Hele-Shaw cell. Again we consider a dimensionless system where we scale lengths with a typical bubble radius $\hat{R}$, velocities with the background velocity $\hat{U}$, and the fluid pressure with $12\hat{\mu}\hat{U}\hat{R}/\hat{h}^2$. Then the pressure, p, satisfies the following dimensionless model

$$\nabla^2 p = 0 \qquad \text{in} \quad \Omega, \tag{4.1a}$$

$$\boldsymbol{n}\cdot\boldsymbol{\nabla}p = -\boldsymbol{U}_k\cdot\boldsymbol{n} \qquad \text{on} \quad \partial\Omega_k, \tag{4.1b}$$

$$\boldsymbol{\nabla}p \to -\boldsymbol{i} \qquad \text{as} \quad x^2+y^2\to\infty, \tag{4.1c}$$

where Ω is the fluid domain, while $\partial\Omega_k$ and $\boldsymbol{U}_k = (U_k, V_k)$ are the boundary and the *a priori* unknown velocity of the k^{th} bubble, respectively. We show the solution domain schematically in figure 4.1. In situations where there are channel walls at $y = \pm W/2$, where W is the dimensionless width of the channel, we also impose the boundary conditions

$$\frac{\partial p}{\partial y} = 0 \qquad \text{on} \quad y = \pm W/2. \tag{4.1d}$$

As in Chapter 2, there are two dimensionless parameters associated with our problem, namely the aspect ratio, $\epsilon = \hat{h}/2\hat{R}$, and the capillary number, $\text{Ca} = \hat{\mu}\hat{U}/\hat{\gamma}$, respectively, both of which are assumed to be small. Specifically, in the distinguished limit $\text{Ca} = O(\epsilon^3)$, where the viscous pressure balances the pressure drop across the menisci, both bubbles remain circular to leading order, and p is therefore fully determined by the problem (4.1) (up to an irrelevant constant) once the bubble velocities $\boldsymbol{U}_k$ are all specified. To close the system we follow Chapter 2, and perform an effective net force balance on each bubble to obtain

$$\frac{\boldsymbol{U}_k}{|\boldsymbol{U}_k|^{1/3}} = \frac{\delta}{\pi R_k}\oint_{\partial\Omega_k} -p\boldsymbol{n}\,\mathrm{d}s, \tag{4.2}$$

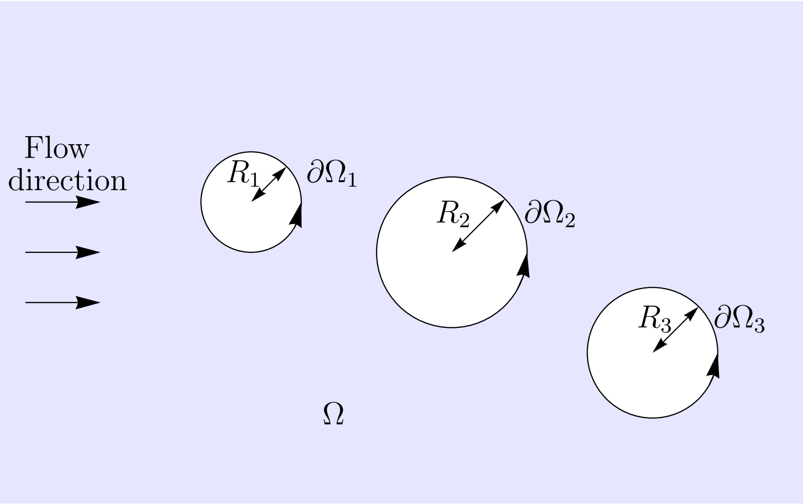

Figure 4.1: Schematic for the flow of an arbitrary number of bubbles.

where δ denotes the *Bretherton parameter*, defined by (2.13), and R_k is the dimensionless radius of the k^{th} bubble. Without loss of generality, we can set e.g., $R_1 = 1$.

We notice that $p = -x$ is a solution to the problem (4.1) if and only if all of the bubbles move at the same velocity $\boldsymbol{U}_k = \boldsymbol{i}$ for all k. The force balance (4.2) then requires $\delta R_k = 1$. Therefore it is possible for all of the bubbles to be convected at the same velocity as the outer flow, regardless of their position, only when all the bubbles are the same size and $\delta = 1$.

In this chapter we use the model (4.1)–(4.2) to analyse the effects of interactions between multiple bubbles.

4.3 Numerical solutions

4.3.1 Numerical method

For the propagation of more than two bubbles we can no longer find analytical solutions like those found in Chapters 2 and 3 and thus we rely on numerical simulations. To facilitate the numerical solution we reformulate the problem (4.1)–(4.2) in terms of the streamfunction, ψ, which satisfies the Dirichlet boundary-value problem:

$$\nabla^2\psi = 0 \qquad \text{in} \quad \Omega \tag{4.3a}$$

$$\psi(x,y) = \pm\frac{W}{2} \qquad \text{on} \quad y = \pm\frac{W}{2}, \tag{4.3b}$$

$$\psi(x,y) = q_k + U_k(y - y_k) - V_k(x - x_k) \qquad \text{on} \quad \partial\Omega_k, \tag{4.3c}$$

$$\psi(x,y) \to y \qquad \text{as} \quad x \to \pm\infty. \tag{4.3d}$$

The boundary condition (4.3c) is applied at each of the N bubble surfaces $\partial\Omega_k$, for $k \in \{1, \ldots, N\}$, and the q_k are *a priori* unknown constants, which are found by enforcing the single-valuedness of the pressure, p, by imposing

$$\oint_{\partial\Omega_k} \frac{\partial\psi}{\partial n}\,\mathrm{d}s = 0, \tag{4.4}$$

on each bubble surface. We denote the centroid of each bubble by (x_k, y_k), so $(U_k, V_k) = (\dot{x}_k, \dot{y}_k)$ where the represents the time derivative.

The force balances of on each bubble (4.2), through the use of integration by parts and the Cauchy-Riemann equations, become

$$-\frac{\delta}{\pi}\oint_{\partial\Omega_k} (x - x_k)\frac{\partial\psi}{\partial x} + (y - y_k)\frac{\partial\psi}{\partial y}\,\mathrm{d}x = \frac{R_k^2 U_k}{(U_k^2 + V_k^2)^{1/6}}, \tag{4.5a}$$

$$-\frac{\delta}{\pi}\oint_{\partial\Omega_k} (x - x_k)\frac{\partial\psi}{\partial x} + (y - y_k)\frac{\partial\psi}{\partial y}\,\mathrm{d}y = \frac{R_k^2 V_k}{(U_k^2 + V_k^2)^{1/6}}. \tag{4.5b}$$

Similarly to Chapter 2 §2.4 we decompose the streamfunction as

$$\psi = \psi^{(0)} + \sum_{k=1}^{N}\left(U_k\psi_k^{(1)} + q_k\psi_k^{(2)} - V_k\psi_k^{(3)}\right), \tag{4.6}$$

where $\psi^{(0)}$ satisfies the boundary-value problem

$$\nabla^2\psi^{(0)} = 0 \qquad \text{in} \quad \Omega, \tag{4.7a}$$

$$\psi^{(0)} = \pm\frac{W}{2} \qquad \text{on} \quad y = \pm\frac{W}{2}, \tag{4.7b}$$

$$\psi^{(0)} = 0 \qquad \text{on each} \quad \partial\Omega_k, \tag{4.7c}$$

$$\psi^{(0)} \to y \qquad \text{as} \quad x \to \pm\infty, \tag{4.7d}$$

and each $\psi_k^{(l)}$ satisfies a boundary-value problem that is independent of U_k, V_k and q_k, given by

$$\nabla^2\psi_k^{(l)} = 0 \qquad \text{in} \quad \Omega, \tag{4.8a}$$

$$\psi_k^{(l)} = 0 \qquad \text{on} \quad y = \pm\frac{W}{2}, \tag{4.8b}$$

$$\psi_k^{(l)} = \{y, 1, x\} \qquad \text{on} \quad \partial\Omega_k, \tag{4.8c}$$

$$\psi_k^{(l)} = 0 \qquad \text{on} \quad \partial\Omega_j, \ \text{for } j \neq k, \tag{4.8d}$$

$$\psi_k^{(l)} \to 0 \qquad \text{as} \quad x \to \pm\infty, \tag{4.8e}$$

where $l \in \{1, 2, 3\}$ corresponds to the position of the element chosen in (4.8c).

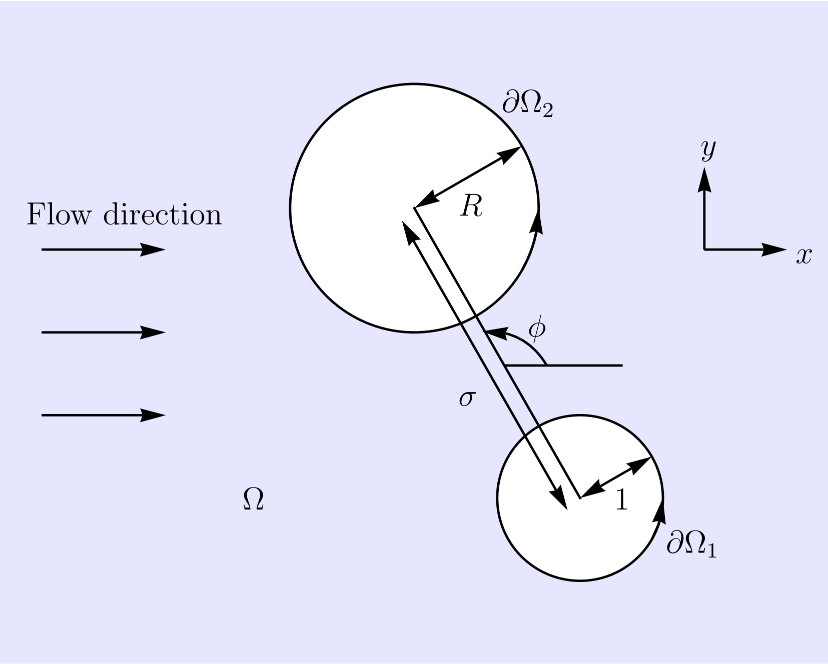

Figure 4.2: Schematic of the two-bubble problem.

The numerical solutions of $\psi^{(0)}$, and $\psi_k^{(l)}$, for $(l,k) \in \{1,2,3\} \times \{1,\ldots,N\}$, are computed using the finite element routine NDSolve in Mathematica (Wolfram Research, 2024). The finite element method requires a bounded computational domain, we use $\Omega = \{(x,y) : x_{\text{min}} - 20R_{\text{max}} \leq x \leq x_{\text{max}} + 20R_{\text{max}},\ -W/2 \leq y \leq W/2\}$, where $x_{\text{min,max}}$ are the minimum and maximum values of x_k, respectively, and R_{max} is the maximum value of R_k. Once, we have found $\psi^{(0)}$, and $\psi_k^{(l)}$, for $(l,k) \in \{1,2,3\} \times \{1,\ldots,N\}$, we use (4.5) to find U_k, V_k, and q_k, for each $k \in \{1,\ldots,N\}$.

We now validate the numerical method against the known two-bubble solution found in Chapter 3.

4.3.2 Validation of numerical method

We now compare the exact two-bubble solution (3.20) (see §3.3) with the numerical solution following the approach set out in (4.5)–(4.8). We translate the two-bubble problem into our numerical framework by setting $R_1 = 1$ and $(x_1, y_1) = (0,0)$ and $R_2 = R$ and $(x_2, y_2) = (\sigma\cos\phi, \sigma\sin\phi)$ (see figure 4.2). We set W to be large (either $W = 40$ or $W = 80$) to simulate an infinite Hele-Shaw cell for which the two-bubble solution (3.20) holds.

In figure 4.3 we plot the bubble velocities (U_k, V_k) versus angle ϕ with $R = 2$, $\sigma = 4$, and $\delta = 5$. We observe good agreement between the numerical solutions

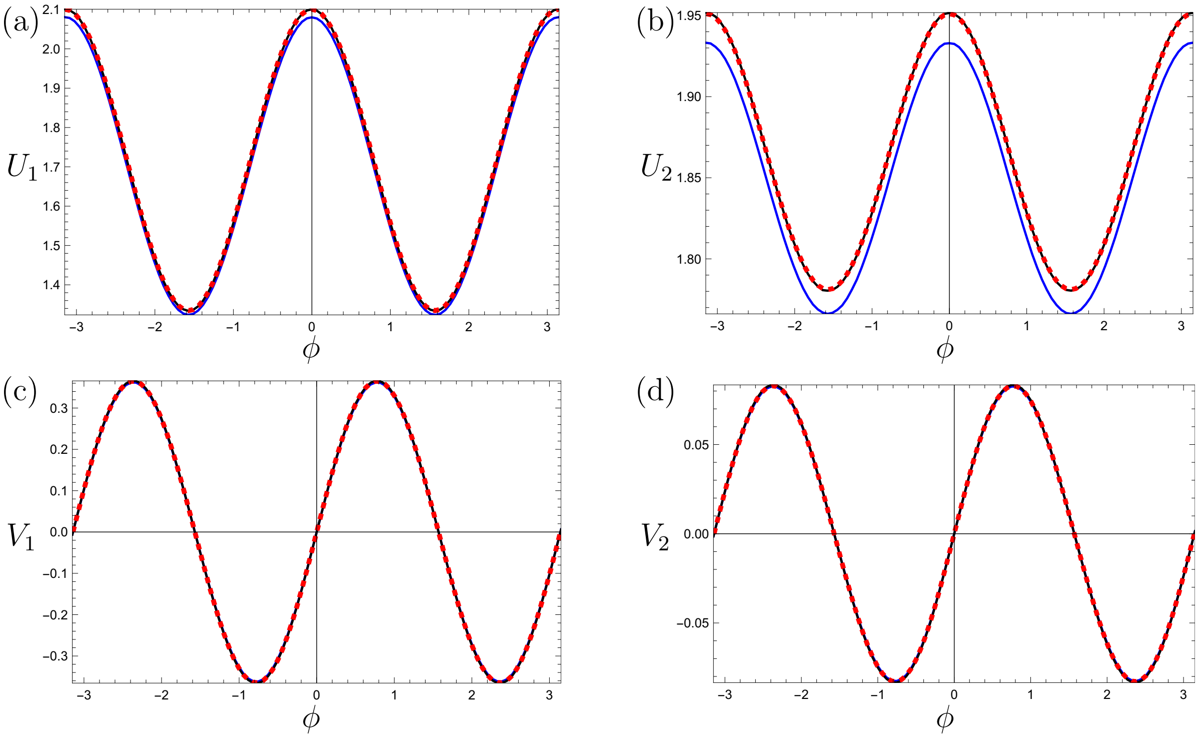

Figure 4.3: Instantaneous bubble velocity versus angle ϕ for a system of two bubbles with $R = 2$, $\sigma = 4$ and $\delta = 5$, (a, c) the smaller bubble velocity components (U_1, V_1); (b, d) the larger bubble velocity components (U_2, V_2). The analytical solution is shown by the red dashed curve and the numerical solution is shown in blue for $W = 40$, and black for $W = 80$.

of (4.5)–(4.8) and the analytical solution (3.20). The numerical solution with $W = 40$ (blue curves) closely follows the behaviour of the full solution but always under predicts the bubble velocities in the x-direction U_k. On the other hand, when $W = 80$ the numerical solution precisely matches the full solution. In figure 4.4 we plot the bubble velocities (U_k, V_k) versus separation σ with $R = 2$, $\phi = \pi/3$, $W = 80$, and $\delta = 5$. Again we observe excellent agreement between the numerical solution and the full solution, provided the truncated solution domain size is large enough.

Now that we have seen that the numerical method (4.5)–(4.8) accurately reproduces the known behaviour of the two-bubble system, in the next section we will use it to study the dynamics of three or four bubbles in a Hele-Shaw cell.

4.4 Hele-Shaw Newton's cradle

To begin we consider three identical bubbles moving along the centre-line of a channel as illustrated in figure 4.5. We will find that the bubbles in general have different

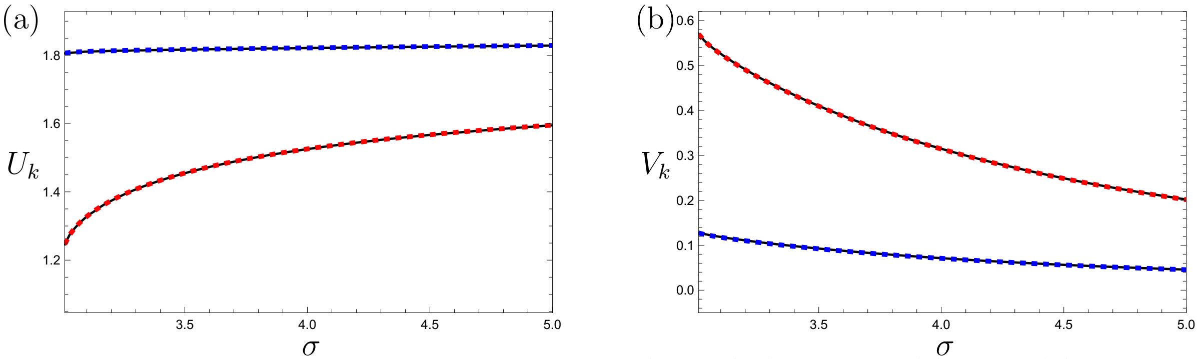

Figure 4.4: Instantaneous bubble velocity (U_k, V_k) (shown in (a), and (b), respectively) versus separation, σ, for the smaller bubble $k = 1$ (red) and the larger bubble $k = 2$ (blue), with $R = 2$, $\phi = \pi/3$, $\delta = 5$, and $W = 80$. The numerical solution is shown by the black curves and the analytical solution is shown by the dashed curves.

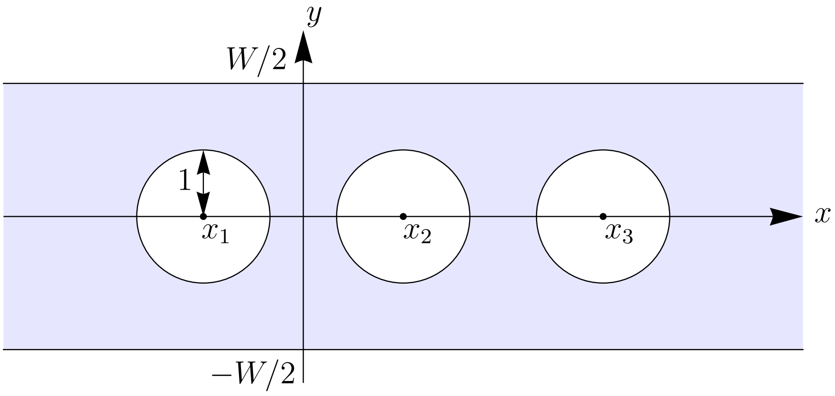

Figure 4.5: Schematic of three identical collinear bubbles.

speeds so, for the first time, we have to solve an unsteady problem when the bubbles are all identical. By symmetry, all three bubbles move in the x-direction with velocities U_k ($k = 1$, 2, 3) that are instantaneously determined by the procedure described in §4.3, allowing us to update the positions x_k. Typical solutions are shown in figure 4.6.

As for the case of two identical bubbles, we again see different behaviour depending on whether $\delta < 1$ or $\delta > 1$. At the special value $\delta = 1$, all of the bubbles move with the background flow, so the distances between them remain fixed. When $\delta < 1$, the bubbles move more slowly than the surrounding liquid. In this case, we recall from §3.4 that each bubble's speed is decreased by the presence of another bubble, with a greater decrease the closer the bubbles are together. When there are three bubbles, we find the middle one is the slowest because it is the closest to the other two bubbles. We therefore observe that the centre bubble moves backwards relative to the outer two and thus eventually becomes a pair with the rear bubble (see figure 4.6(a)). This qualitative behaviour has been observed experimentally by Shen *et al.* (2014);

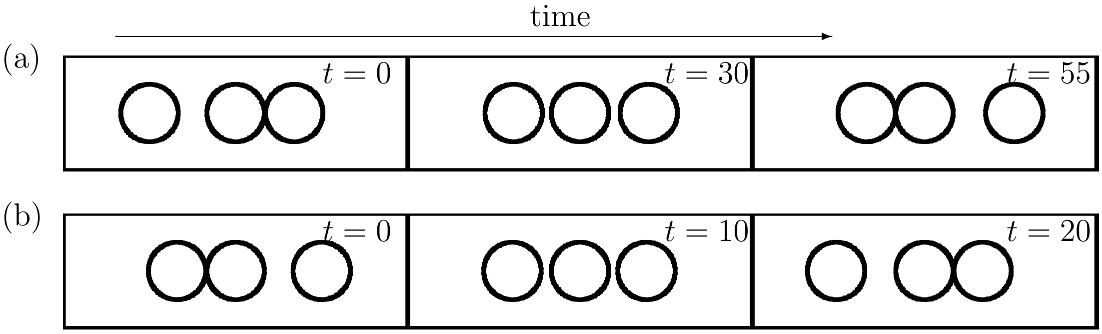

Figure 4.6: The progression of a series of three identical bubbles with $W = 4$, and (a) $\delta = 1/2$; (b) $\delta = 5$. The initial bubble separations are (a) $|x_1 - x_2| = 1$ and $|x_3 - x_2| = 0.04$, (b) $|x_1 - x_2| = 0.04$ and $|x_3 - x_2| = 1$.

however there were surfactants in their system so a quantitative comparison with our model is not possible. The opposite effect occurs when $\delta > 1$, where now the central bubble moves faster than the outer ones and so eventually joins with the front-most bubble (see figure 4.6(b)).

Figure 4.7 depicts the dependence on δ of the time T taken for the middle bubble either to be caught by the rear bubble or to catch the front bubble. The initial bubble separations are set to 1 and 0.04, as shown in figure 4.6(a) for $\delta < 1$ and figure 4.6(b) for $\delta > 1$, and we show the results for two channel widths $W = 4$ and $W = 20$. We see an asymptote at $\delta = 1$, as expected when all the bubbles travel at the same speed as the outer fluid. There is also an asymptote as $\delta \to 0$, since the bubble velocities all tend to zero in this limit. As $\delta \to \infty$, T approaches a finite non-zero value that depends on W. Furthermore, we observe that T increases as we decrease the channel width, with $T \to \infty$ as $W \to 2$ for all values of δ, again because the bubbles all move at the same speed in this limit, by conservation of mass. Even at $W = 4$, the transit time is quite large for all values of δ, indicating that the difference in speed between the bubbles is relatively small.

When there are more than three bubbles, this effect can occur multiple times, as illustrated in figure 4.8(a) for a case with four bubbles and $\delta < 1$. Initially the second bubble breaks away from the front one to form a pair with the third bubble, before that pair itself breaks up so the third and fourth bubbles can form a pair. For $\delta < 1$, we recall from §3.4 that a pair of bubbles moves more slowly than an isolated bubble, so for long times the trailing pair in figure 4.8(a) is left behind by the front two. Beatus *et al.* (2012) observed qualitatively similar longitudinal waves propagating backwards relative to the outer fluid flow in a series of bubbles on the centre-line of a Hele-Shaw channel, behaviour which they termed the peloton effect.

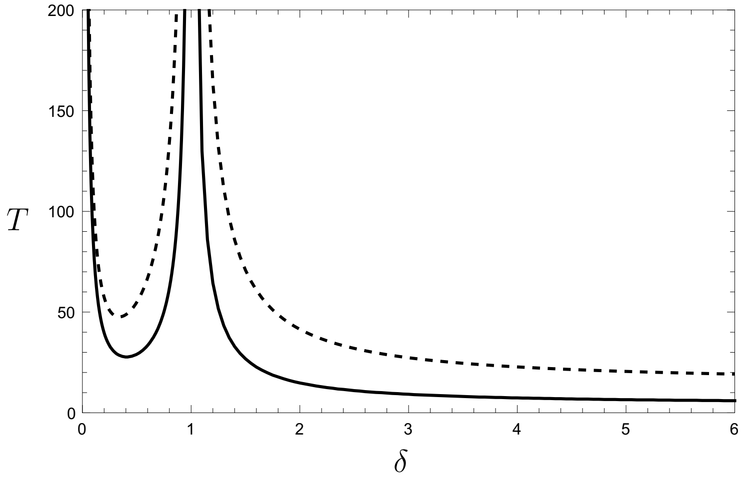

Figure 4.7: The transit time T versus Bretherton parameter δ for the system shown in figure 4.6(a) for $\delta < 1$ and figure 4.6(b) for $\delta > 1$, in a channel of width $W = 20$ (solid) and $W = 4$ (dashed). When $\delta < 1$ the computation starts with separations of 1 and 0.04 between the rear two and front two bubbles, respectively, and finishes when the separation between the rear two bubbles is 0.04; and *vice versa* when $\delta > 1$.

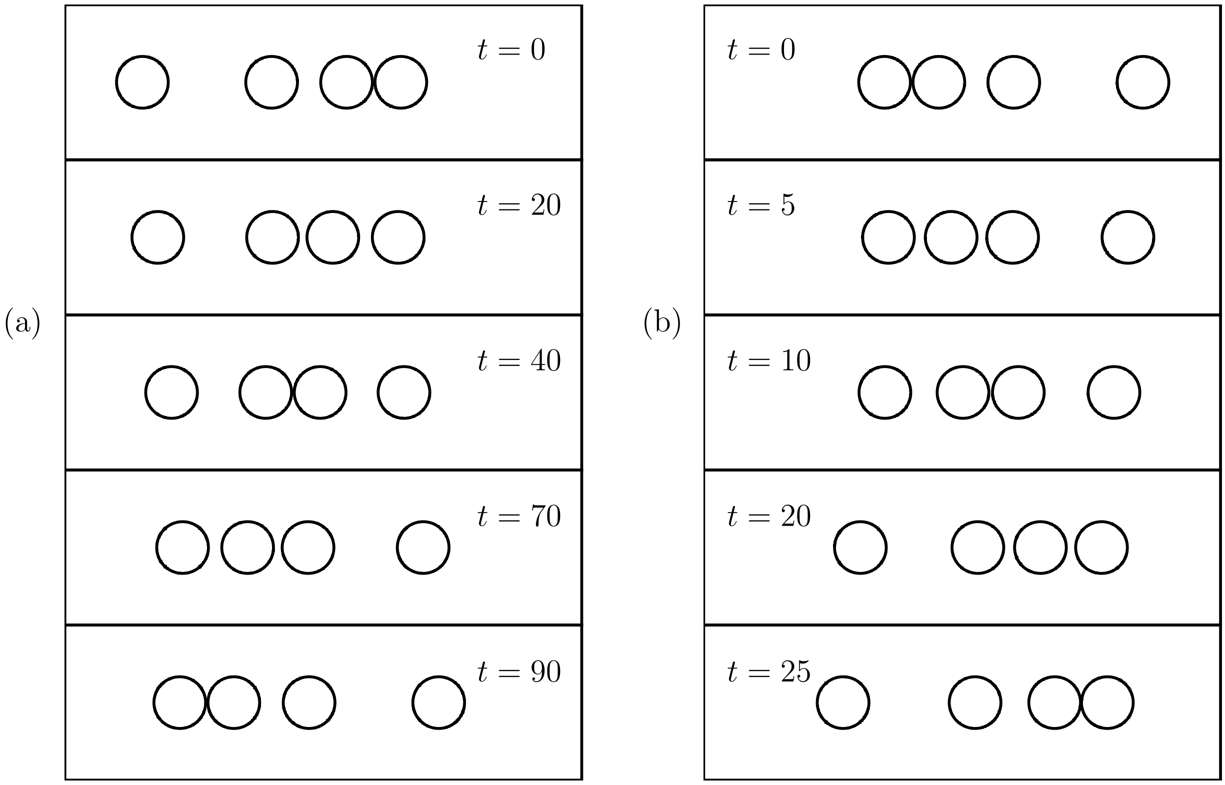

Figure 4.8: The progression of a series of four identical bubbles with $W = 6$, and (a) $\delta = 1/2$; (b) $\delta = 5$.

However we find that the wave propagation can occur in either direction, depending on whether $\delta < 1$ or $\delta > 1$. Figure 4.8(b) shows a typical case with $\delta > 1$, where the initial condition is the reverse of that in figure 4.8(a), and the observed evolutions are almost mirror images of each other. When $\delta > 1$, a pair of bubbles travels faster than an isolated bubble, so eventually the front pair breaks away and leaves behind the other two bubbles. The formation and breakup of successive bubble pairs observed in figure 4.8 is reminiscent of a Newton's cradle, even though there is no inertia in our system, and the motion arises solely due to viscous hydrodynamic interactions.

While in principle it is possible to use the methodology outlined in §4.3 to simulate an arbitrary number of bubbles, the resulting system quickly becomes unwieldy. For a general system of N bubbles, our numerical method would involve the solution of $3N + 1$ Dirichlet problems (4.7)–(4.8) and computation of $9N^2 + 3N$ force integrals (4.5) to evaluate all of the bubble velocities at each time step. In the next two sections, we derive reduced-order models to decrease the computational complexity required to study a large number of bubbles.

4.5 Dipole model

4.5.1 Model setup

In this section, we consider the propagation of N bubbles that are far away from each other and use the method of matched asymptotic expansions to derive a system of $2N$ ordinary differential equations (ODEs) to approximate the behaviour of the full system (4.1)–(4.2). We recall from Chapter 3 §3.7 for the case of two bubbles that the large-separation approximation accurately reproduces the behaviour of the full solution, even when the bubbles are not especially far apart.

The asymptotic structure of our problem is as follows. In the outer problem the bubbles act as if they are point dipoles, and the inner problem is that of an isolated bubble that experiences a uniform background flow plus the effect of the other bubbles in the far-field. In figure 4.9, we show the asymptotic structure schematically.

We begin by reformulating (4.1) using complex variables. Let $\nu \ll 1$ be the ratio of a typical bubble radius to a typical centre–centre distance. Suppose we have N bubbles of dimensionless radii R_n, at positions $(x_n, y_n) = \frac{1}{\nu}(X_n, Y_n)$. We then rescale lengths with $1/\nu$, so the rescaled distance between bubbles is $O(1)$ and the bubble radii are $O(\nu)$. Let $Z = X + \mathrm{i}Y = \nu(x + \mathrm{i}y)$, then the complex potential

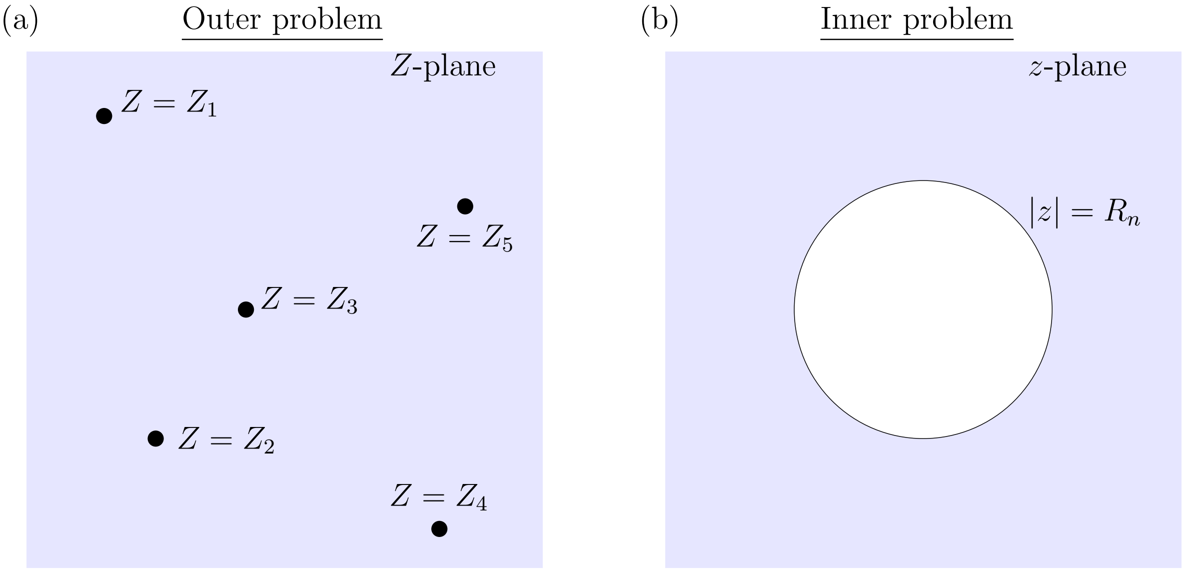

Figure 4.9: Schematic of the asymptotic structure: (a) the outer problem (b) the inner problem.

$\mathcal{W}(Z) = \nu\big(-p(X,Y) + \mathrm{i}\psi(X,Y)\big)$ is a holomorphic function that satisfies the boundary conditions

$$\mathrm{Im}[\mathcal{W}(Z)] = \nu q_n + \mathrm{Im}\left[\overline{\mathcal{U}}_n(Z - Z_n)\right] \qquad \text{on} \quad |Z - Z_n| = \nu R_n, \tag{4.9a}$$

for each $1 \leq n \leq N$, and the far field condition

$$\mathcal{W}(Z) \sim Z + o(1) \qquad \text{as} \quad Z \to \infty, \tag{4.9b}$$

where $\mathcal{U}_n = U_n + \mathrm{i}V_n$ is the complex representation of the n^{th} bubble velocity, the q_n are *a priori* unknown constants, and the over-bar denotes complex conjugation.

4.5.2 Asymptotic expansions

4.5.2.1 Outer problem

In the outer problem the bubbles act at the points $Z = Z_n$ for each $1 \leq n \leq N$ (see figure 4.9(a)). Here, we expand

$$\mathcal{W}(Z) \sim Z + \nu\mathcal{W}_1(Z) + \nu^2\mathcal{W}_2(Z) + \cdots, \tag{4.10a}$$

$$\mathcal{U}_n \sim \mathcal{U}_n^{(0)} + \nu\mathcal{U}_n^{(1)} + \nu^2\mathcal{U}_n^{(2)} + \cdots. \tag{4.10b}$$

Note that the leading-order solution is simply the far-field uniform flow and that $\mathcal{W}(Z)$ is holomorphic in $\mathbb{C}$ except at the positions of the bubbles $Z = Z_n$, for each $1 \leq n \leq N$.

4.5.2.2 Inner problem

We look at the inner region near the n^{th} bubble by scaling $(Z - Z_n) = \nu z$, and $\mathcal{W}(Z) = \nu w(z)$, where z, $w(z) = O(1)$. The inner problem is that of an isolated bubble of radius R_n centred at the origin (see figure 4.9(b)). Again, we expand our variables in powers of ν as

$$w(z) \sim w_0(z) + \nu w_1(z) + \nu^2 w_2(z) + \cdots , \tag{4.11a}$$

$$\mathcal{U}_n \sim \mathcal{U}_n^{(0)} + \nu \mathcal{U}_n^{(1)} + \nu^2 \mathcal{U}_n^{(2)} + \cdots , \tag{4.11b}$$

$$q_n \sim q_n^{(0)} + \nu q_n^{(1)} + \nu^2 q_n^{(2)} + \cdots . \tag{4.11c}$$

Here, $w(z)$ is a holomorphic function in the region $|z| > R_n$.

4.5.3 Leading-order inner solution

The leading-order inner complex potential then satisfies the boundary conditions

$$\operatorname{Im}[w_0(z)] = q_n^{(0)} + \operatorname{Im}\left[\overline{\mathcal{U}}_n^{(0)} z\right] \qquad \text{on} \quad |z| = R_n, \tag{4.12a}$$

$$w_0(z) \sim z \qquad \text{as} \quad z \to \infty, \tag{4.12b}$$

which are solved by

$$w_0(z) = z + \frac{\left(1 - \mathcal{U}_n^{(0)}\right) R_n^2}{z}, \tag{4.13}$$

with $q_n^{(0)} = 0$. This solution is equivalent to the pressure field (2.14) found in Chapter 2 §2.2 for an isolated bubble of radius R_n, as expected in the large-separation limit.

4.5.4 Correction to the outer solution

The leading-order inner solution (4.13) induces a correction to the outer solution at $O(\nu^2)$, so by Van Dyke's matching rule (Van Dyke, 1975) we find that $\mathcal{W}_1(Z) \equiv 0$ and $\mathcal{W}_2(Z)$ satisfies

$$\mathcal{W}_2(Z) \sim \frac{\left(1 - \mathcal{U}_k^{(0)}\right) R_k^2}{Z - Z_k} \qquad \text{as} \quad Z \to Z_k, \tag{4.14}$$

for each $1 \le k \le N$. Since $\mathcal{W}_2(Z) \to 0$ as $Z \to \infty$, we find that

$$\mathcal{W}_2(Z) = \sum_{k=1}^{N} \frac{\left(1 - \mathcal{U}_k^{(0)}\right) R_k^2}{Z - Z_k}. \tag{4.15}$$

4.5.5 Correction to the inner solution

4.5.5.1 $O(\nu)$

Using (4.15), we find that the $O(\nu)$ correction to the inner solution satisfies the boundary conditions

$$\operatorname{Im}[w_1(z)] = q_n^{(1)} + \operatorname{Im}\left[\overline{\mathcal{U}}_n^{(1)} z\right] \qquad \text{on} \quad |z| = R_n, \tag{4.16a}$$

$$w_1(z) \sim \sum_{\substack{k=1 \\ k\neq n}}^{N} \frac{\left(1-\mathcal{U}_k^{(0)}\right) R_k^2}{Z_n - Z_k} \qquad \text{as} \quad z \to \infty. \tag{4.16b}$$

This problem is solved by

$$w_1(z) = -\frac{\mathcal{U}_n^{(1)} R_n^2}{z} + \sum_{\substack{k=1 \\ k\neq n}}^{N} \frac{\left(1-\mathcal{U}_k^{(0)}\right) R_k^2}{Z_n - Z_k}, \tag{4.17}$$

and

$$q_n^{(1)} = \operatorname{Im}\left[\sum_{\substack{k=1 \\ k\neq n}}^{N} \frac{\left(1-\mathcal{U}_k^{(0)}\right) R_k^2}{Z_n - Z_k}\right]. \tag{4.18}$$

When computing the force balance (4.2) at the end of this section we will find that $\mathcal{U}_n^{(1)} \equiv 0$, so we must continue to $O(\nu^2)$ to find the first nonzero correction to the bubble velocity. This finding is consistent with §3.7 where our expansion (3.53) for the bubble velocity is in powers of $1/\sigma^2$, where σ is the centre–centre distance between the bubbles.

4.5.5.2 $O(\nu^2)$

Continuing to the next asymptotic order in the inner problem we find that $w_2(z)$ satisfies the boundary conditions

$$\operatorname{Im}[w_2(z)] = q_n^{(2)} + \operatorname{Im}\left[\overline{\mathcal{U}}_n^{(2)} z\right] \qquad \text{on} \quad |z| = R_n, \tag{4.19a}$$

$$w_2(z) \sim -\left(\sum_{\substack{k=1 \\ k\neq n}}^{N} \frac{\left(1-\mathcal{U}_k^{(0)}\right) R_k^2}{(Z_n - Z_k)^2}\right) z \qquad \text{as} \quad z \to \infty, \tag{4.19b}$$

which are solved by

$$w_2(z) = -\left(\sum_{\substack{k=1 \\ k\neq n}}^{N} \frac{\left(1-\mathcal{U}_k^{(0)}\right) R_k^2}{(Z_n - Z_k)^2}\right) z - \left(\mathcal{U}_n^{(2)} + \sum_{\substack{k=1 \\ k\neq n}}^{N} \frac{\left(1-\mathcal{U}_k^{(0)}\right) R_k^2}{\overline{(Z_n - Z_k)}^2}\right) \frac{R_n^2}{z}, \tag{4.20}$$

and $q_n^{(2)} = 0$.

4.5.6 Bubble velocity

Now we have solved for $w(z)$, we perform the effective force balance (4.2) on each bubble, by evaluating

$$\frac{1}{\mathrm{i}\pi}\oint_{|z|=R_n} w(z)\,\mathrm{d}z = -R_n^2\mathcal{U}_n + \frac{R_n\mathcal{U}_n}{\delta\left|\mathcal{U}_n\right|^{1/3}}. \tag{4.21}$$

Substituting our expansions (4.11) for $w(z)$ and $\mathcal{U}_n$, we find at leading order the force balance (4.21) gives

$$2\left(1-\mathcal{U}_n^{(0)}\right)R_n^2 = -R_n^2\mathcal{U}_n^{(0)} + \frac{R_n\mathcal{U}_n^{(0)}}{\delta\left|\mathcal{U}_n^{(0)}\right|^{1/3}}, \tag{4.22}$$

which is simply the equation of motion for an isolated bubble (2.16) of radius R_n. Thus, to leading order the bubbles move as if they are in isolation, so $\mathcal{U}_n^{(0)} = U_n^{(0)} \in \mathbb{R}$. Then (4.22) simplifies to

$$\frac{\left(U_n^{(0)}\right)^{2/3}}{2-U_n^{(0)}} = \delta R_n. \tag{4.23}$$

At $O(\nu)$ we find the force balance (4.21) gives

$$-2\mathcal{U}_n^{(1)} = -\mathcal{U}_n^{(1)} + \frac{1}{\delta R_n\left(U_n^{(0)}\right)^{1/3}}\left(\mathcal{U}_n^{(1)} - \frac{1}{3}\,\mathrm{Re}\left[\mathcal{U}_n^{(1)}\right]\right), \tag{4.24}$$

which is solved by $\mathcal{U}_n^{(1)} = 0$. As alluded to in §4.5.5.1 we need to advance to $O(\nu^2)$ to find the correction to the bubble velocity due to the presence of the other bubbles.

The force balance at $O(\nu^2)$ is given by

$$-2\left(\mathcal{U}_n^{(2)} + \sum_{\substack{k=1\\k\neq n}}^{N}\frac{\left(1-U_k^{(0)}\right)R_k^2}{\overline{\left(Z_n-Z_k\right)}^2}\right) = -\mathcal{U}_n^{(2)} + \frac{1}{\delta R_n\left(U_n^{(0)}\right)^{1/3}}\left(\mathcal{U}_n^{(2)} - \frac{1}{3}\,\mathrm{Re}\left[\mathcal{U}_n^{(2)}\right]\right). \tag{4.25}$$

By writing $\mathcal{U}_n^{(2)} = U_n^{(2)} + \mathrm{i}V_n^{(2)}$ and taking the real and imaginary parts of (4.25), we obtain

$$U_n^{(2)} = -\frac{6U_n^{(0)}}{4+U_n^{(0)}}\,\mathrm{Re}\left[\sum_{\substack{k=1\\k\neq n}}^{N}\frac{\left(1-U_k^{(0)}\right)R_k^2}{\overline{\left(Z_n-Z_k\right)}^2}\right], \tag{4.26a}$$

$$V_n^{(2)} = -U_n^{(0)}\,\mathrm{Im}\left[\sum_{\substack{k=1\\k\neq n}}^{N}\frac{\left(1-U_k^{(0)}\right)R_k^2}{\overline{\left(Z_n-Z_k\right)}^2}\right]. \tag{4.26b}$$

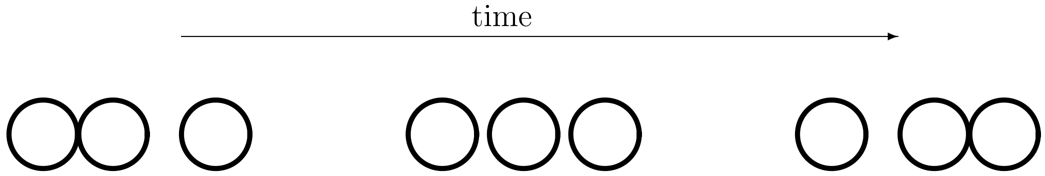

Numerical:	$t = 0$	$t = 3.22$	$t = 6.45$
Dipole:	$t = 0$	$t = 2.83$	$t = 5.66$

Figure 4.10: The progression of a series of three identical bubbles with $\delta = 5$ at time points: (i) beginning, (ii) when the bubbles are equispaced, and (iii) when the front two bubbles touch, for the numerical solution of (4.5)–(4.8) (with $W = 80$), and dipole model (4.27).

4.5.7 Dipole model

Using the results (4.22) and (4.26) we create a dynamical system for the bubble positions $z_n = x_n + \mathrm{i}y_n$ for each $1 \leq n \leq N$, namely

$$\frac{\mathrm{d}x_n}{\mathrm{d}t} = U_n^{(0)} \left(1 - \frac{6}{4 + U_n^{(0)}} \sum_{\substack{k=1 \\ k \neq n}}^{N} \frac{R_k^2 \left(1 - U_k^{(0)}\right) \left((x_n - x_k)^2 - (y_n - y_k)^2\right)}{\left((x_n - x_k)^2 + (y_n - y_k)^2\right)^2} \right), \tag{4.27a}$$

$$\frac{\mathrm{d}y_n}{\mathrm{d}t} = -2U_n^{(0)} \sum_{\substack{k=1 \\ k \neq n}}^{N} \frac{R_k^2 \left(1 - U_k^{(0)}\right) (x_n - x_k)(y_n - y_k)}{\left((x_n - x_k)^2 + (y_n - y_k)^2\right)^2}. \tag{4.27b}$$

This system is referred to as the “dipole model”, and provides a set of $2N$ real ODEs that are significantly easier to solve than the full model (4.1)–(4.2). Note that the system (4.27) reduces to (3.58) when $N = 2$, as expected.

4.5.8 Validation

In figure 4.10 we plot three snapshots of the Hele-Shaw Newton’s cradle (see §4.4), and show the dimensionless time to reach the instance, for the numerical solution (with $W = 80$) of (4.5)–(4.8) and the solution of the dipole model (4.27). Here $\delta = 5$ and the initial bubble separations are set to be 0.04 and 1. We observe the same qualitative behaviour in the dipole solution as predicted by the full numerical solution, where the central bubble moves faster than the outer bubbles and so eventually joins with the front-most bubble. There is a discrepancy in the time taken for the exchange, namely $t = 6.45$ for the numerical solution and $t = 5.66$ for the dipole solution, approximately a 12.2% difference.

4.5.9 Pairwise interactions

We expect the dipole model to break down whenever two bubbles are close or even touching. We now consider the "worst case" scenario of two identical touching bubbles, the solution for which was found in §3.6.3. In this regime, the bubbles move at the same velocity $\boldsymbol{U}_p = (U_p, V_p)$ given by (3.50), and hence the angle the vector connecting the bubble centres makes with the x-direction, ϕ, remains fixed. In figure 4.11(a) we plot the velocity of a pair of bubbles, that are perpendicular to the direction of flow ($\phi = \pi/2$), versus δ. Now we have $N = 2$, $x_1 = x_2$ and (without loss of generality) $y_2 = y_1 + 2$, and the bubbles travel parallel to the background flow at a velocity, U_p that satisfies (3.50)

$$\frac{U_p^{2/3}}{U_p + \frac{\pi^2}{3}(1 - U_p)} = \delta. \tag{4.28}$$

Then for this system the dipole method (4.27) simplifies to

$$U_p \approx \frac{U_b(11 - U_b)}{2(4 + U_b)}, \tag{4.29}$$

where U_b is the velocity of an isolated bubble, satisfying (2.16), i.e.,

$$\frac{U_b^{2/3}}{2 - U_b} = \delta. \tag{4.30}$$

In figure 4.11(a) we observe that the dipole solution under-predicts for $\delta < 1$, over-predicts for $\delta > 1$, and is exact for $\delta = 1$.

To quantify the relative error between the full solution and the dipole approximation (4.27), we define

$$E_r = \frac{|\boldsymbol{U}_p - \boldsymbol{U}_d|}{|\boldsymbol{U}_p|}, \tag{4.31}$$

where $\boldsymbol{U}_d$ is the bubble velocity predicted by the dipole method (4.27). We plot E_r versus δ for $\phi = \pi/2$ in figure 4.11(b) and observe that there is a significant relative error, especially for $\delta < 1$. In the limit as $\delta \to 0$, E_r approaches a constant value $1 - \frac{33\sqrt{3}}{2\sqrt{2\pi^3}} \approx 0.35$. We note that, although E_r may be small for large δ ($E_r \to \frac{1}{2} - \frac{9}{2\pi^2} \approx 0.044$ as $\delta \to \infty$ when $\phi = \pi/2$), this error accumulates as the bubbles are swept along the Hele-Shaw cell and thus induces large errors in the positions of the bubbles over time.

In figure 4.12 we plot U_p versus the angle, ϕ, for $\delta = 5$, again observing a significant discrepancy between the exact solution and the dipole solution. The maximum

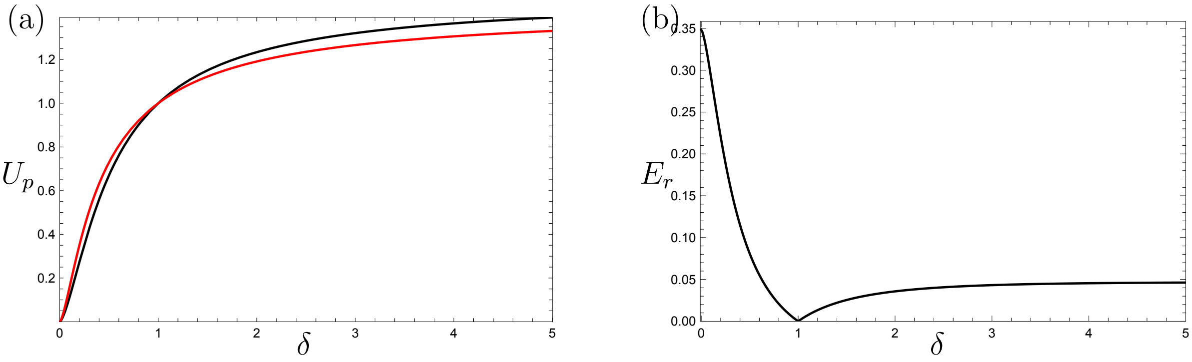

Figure 4.11: Perpendicular ($\phi = \pi/2$) bubble pair velocity, U_p, as a function of Bretherton parameter, δ, for identical touching bubbles. The analytical solution (4.28) is shown in red and the solution of the dipole model (4.29) is shown in black. (b) The relative error E_r for the velocity of a perpendicular pair of bubbles ($\phi = \pi/2$) as a function of δ.

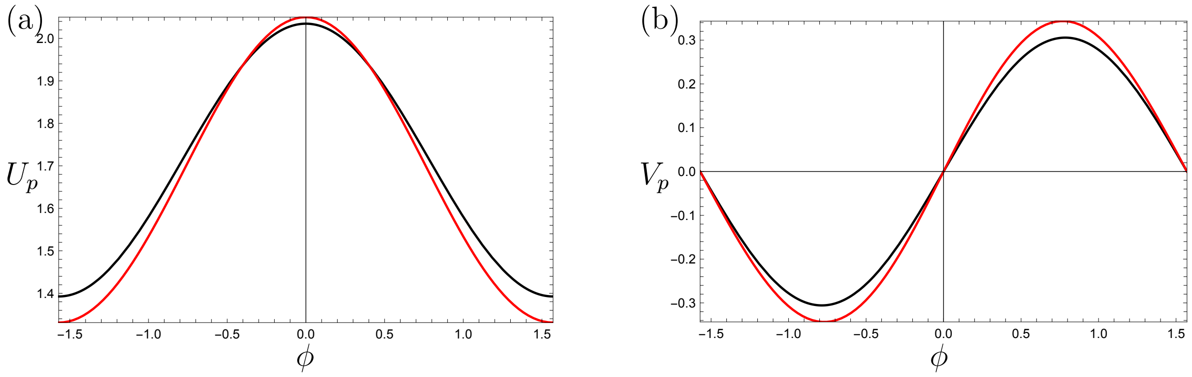

Figure 4.12: Bubble pair velocity components (U_p, V_p) (shown in (a), and (b), respectively) as a function of angle, ϕ, for identical touching bubbles with $\delta = 5$. The analytical solution (3.50) is shown in red and the solution of the dipole model (4.27) is shown in black.

discrepancy in the x-direction velocity U_p occurs for a perpendicular pair of bubbles ($\phi = \pm\pi/2$), while the error in the y-direction velocity V_p is maximised when $\phi = \pm\pi/4$.

In the next section we develop a pairwise interaction model, in which we approximate the equations of motion (4.2) by summing the pairwise contributions. This model is exact for the motion of two bubbles and so allows us to study situations in which two bubbles become close to one another, where the dipole model has been seen to generate errors.

4.6 Pairwise interaction model

4.6.1 Model setup

In §3.3 we found the analytical solution for two bubbles in a Hele-Shaw cell. Here, we use this result to develop a pairwise interaction model for the propagation of an arbitrary number of bubbles. This approach gives a significantly easier system to solve for the bubble velocity than the numerical method described in (4.5)–(4.8). While the dipole method (see §4.5) is exact for the motion of an isolated bubble, this new model will be exact for the motion of two bubbles.

Suppose we have a system of N bubbles at positions $z_n = x_n + \mathrm{i}y_n$ $(1 \leq n \leq N)$ in the complex z-plane, with dimensionless radii R_n. We then approximate the full solution (4.1)–(4.2) by considering the contribution due to the interaction between each pair of bubbles. To that end, we choose two bubbles labeled n and k, with $n \neq k$, and then the complex potential $w(z)$ for the flow due to just these two bubbles satisfies the boundary conditions

$$\begin{aligned}
\mathrm{Im}[w(z)] &= Q_n + \mathrm{Im}\left[\overline{\mathcal{U}}_n z\right] && \text{on} \quad |z - z_n| = R_n, && (4.32\text{a})\\
\mathrm{Im}[w(z)] &= Q_k + \mathrm{Im}\left[\overline{\mathcal{U}}_k z\right] && \text{on} \quad |z - z_k| = R_k, && (4.32\text{b})\\
w(z) &\sim z + o(1) && \text{as} \quad z \to \infty. && (4.32\text{c})
\end{aligned}$$

We introduce the scalings $z = R_n\tilde{z}$, and $w(z) = R_n\tilde{w}(\tilde{z})$, which transform (4.32) into

$$\begin{aligned}
\mathrm{Im}[\tilde{w}(\tilde{z})] &= q_n + \mathrm{Im}\left[\overline{\mathcal{U}}_n \tilde{z}\right] && \text{on} \quad |\tilde{z} - \tilde{z}_n| = 1, && (4.33\text{a})\\
\mathrm{Im}[\tilde{w}(\tilde{z})] &= q_k + \mathrm{Im}\left[\overline{\mathcal{U}}_k \tilde{z}\right] && \text{on} \quad |\tilde{z} - \tilde{z}_k| = R_{kn}, && (4.33\text{b})\\
\tilde{w}(\tilde{z}) &\sim \tilde{z} + o(1) && \text{as} \quad \tilde{z} \to \infty, && (4.33\text{c})
\end{aligned}$$

where $R_{kn} = R_k/R_n$, and $q_j = Q_j/R_n$. The form of (4.33) is the same as that presented in §3.2, where the centre–centre distance, and the angle that the vector connecting the bubble centres makes with the x-axis are given by

$$\sigma_{kn} = \frac{|z_n - z_k|}{R_n}, \tag{4.34a}$$

$$\phi_{kn} = \arg(z_k - z_n), \tag{4.34b}$$

respectively.

The solvability condition (4.2) can be written as

$$\oint_{|z-z_n|=R_n} w(z)\,\mathrm{d}z = -R_n^2\mathcal{U}_n + \frac{R_n\mathcal{U}_n}{\delta\left|\mathcal{U}_n\right|^{1/3}}. \tag{4.35}$$

Then the contribution to the left-hand side of (4.35) due to the interaction of bubble k on bubble n is given by

$$\begin{aligned}\oint_{|z-z_n|=R_n} w(z)\,\mathrm{d}z &= R_n^2 \oint_{|\tilde{z}-\tilde{z}_n|=1} \tilde{w}(\tilde{z})\,\mathrm{d}\tilde{z} \\ &= R_n^2\left[f_{kn}^{(1)}\left(\mathcal{U}_k-1\right)\mathrm{e}^{2\mathrm{i}\phi_{kn}} - \left(2+f_{kn}^{(2)}\right)\left(\mathcal{U}_n-1\right)\right],\end{aligned} \tag{4.36}$$

where

$$f_{kn}^{(1)} = \frac{2(1-a_{kn}^2)^2}{a_{kn}^2}\frac{\Psi'_{X_{kn}^2}(1)}{4\log^2 X_{kn}}, \tag{4.37a}$$

$$f_{kn}^{(2)} = \frac{2(1-a_{kn}^2)^2}{a_{kn}^2}\frac{\Psi'_{X_{kn}^2}\left(\frac{\log a_{kn}}{\log X_{kn}}\right)}{4\log^2 X_{kn}} - 2. \tag{4.37b}$$

Again, Ψ is the q-digamma function (Salem, 2012), and we define the quantities

$$a_{kn} = \frac{\sigma_{kn}^2 - R_{kn}^2 + 1 - \sqrt{(\sigma_{kn}^2 - R_{kn}^2+1)^2 - 4\sigma_{kn}^2}}{2\sigma_{kn}}, \tag{4.38a}$$

$$X_{kn} = a_{kn}^2 + \frac{(R_{kn}-1)a_{kn}(a_{kn}+1)(\sigma_{kn}-R_{kn}-1)}{\sigma_{kn}(\sigma_{kn}-R_{kn}-a_{kn})}. \tag{4.38b}$$

We note that in (4.36) $2(\mathcal{U}_n-1)$ is the contribution due to the interactions of the bubble with the external flow and not the influence of the other bubble. It is important not to over-count this contribution when we sum over the pairwise interactions in the next subsection.

4.6.2 Equations of motion

We now sum the pairwise terms in (4.36). For a system of N bubbles the left-hand side of (4.36) is approximated by

$$\oint_{|z-z_n|=R_n} w(z)\,\mathrm{d}z = R_n^2\left[\sum_{\substack{k=1\\k\neq n}}^{N} f_{kn}^{(1)}\left(\mathcal{U}_k-1\right)\mathrm{e}^{2\mathrm{i}\phi_{kn}} - \left(2+\sum_{\substack{k=1\\k\neq n}}^{N} f_{kn}^{(2)}\right)\left(\mathcal{U}_n-1\right)\right]. \tag{4.39}$$

Combining (4.35) and (4.39) we obtain the equations of motion for a pairwise interaction model:

$$\sum_{\substack{k=1\\k\neq n}}^{N} f_{kn}^{(1)}\left(\mathcal{U}_k - 1\right)\mathrm{e}^{2\mathrm{i}\phi_{kn}} - \left(2 + \sum_{\substack{k=1\\k\neq n}}^{N} f_{kn}^{(2)}\right)\left(\mathcal{U}_n - 1\right) = -\mathcal{U}_n + \frac{\mathcal{U}_n}{\delta R_n \left|\mathcal{U}_n\right|^{1/3}}, \tag{4.40}$$

for each $1 \leq n \leq N$. Equation (4.40) gives us N nonlinear algebraic equations for the bubble velocities, a system that is significantly easier to solve than the full problem (4.1)–(4.2). However, as we have to solve (4.40) at each time-step it is slightly more complicated than the dipole method (4.27).

We next show that the pairwise interaction model (4.40) reduces to the dipole model in the large separation limit. We then validate the model against numerical simulations.

4.6.3 Reduction to the dipole model

In the limit where the distances between bubbles are large (i.e. $\sigma_{kn} \to \infty$) we can use the expansions found in §3.7 to find that

$$f_{kn}^{(1)} \sim \frac{2R_{kn}^2}{\sigma_{kn}^2} + O\left(\frac{R_{kn}^5}{\sigma_{kn}^5}\right), \tag{4.41a}$$

$$f_{kn}^{(2)} \sim \frac{2R_{kn}^2}{\sigma_{kn}^4} + O\left(\frac{R_{kn}^5}{\sigma_{kn}^5}\right). \tag{4.41b}$$

We let $\sigma_{kn} = s_{kn}/\nu$, where $0 < \nu \ll 1$ and $s_{kn} = O(1)$, and expand

$$\mathcal{U}_n = \mathcal{U}_n^{(0)} + \nu^2 \mathcal{U}_n^{(2)} + \cdots . \tag{4.42}$$

At $O(1)$ in (4.40) we find

$$2\left(1 - \mathcal{U}_n^{(0)}\right) = -\mathcal{U}_n^{(0)} + \frac{\mathcal{U}_n^{(0)}}{\delta R_n \left|\mathcal{U}_n^{(0)}\right|^{1/3}}, \tag{4.43}$$

which is equivalent to (4.22), so we can write $\mathcal{U}_n^{(0)} = U_n^{(0)} \in \mathbb{R}$. Then at $O(\nu^2)$ we find

$$\sum_{\substack{k=1\\k\neq n}}^{N} \frac{2R_{kn}^2}{s_{kn}^2}\left(U_k^{(0)} - 1\right)\mathrm{e}^{2\mathrm{i}\phi_{kn}} - 2\mathcal{U}_n^{(2)} = -\mathcal{U}_n^{(2)} + \frac{1}{\delta R_n U_n^{1/3}}\left(\mathcal{U}_n^{(2)} - \frac{1}{3}\operatorname{Re}\left[\mathcal{U}_n^{(2)}\right]\right), \tag{4.44}$$

which is equivalent to (4.25). Thus the pairwise interaction model reduces to the dipole model in the limit where all the bubbles are far apart.

4.6.4 Comparison with full and dipole solutions

In figure 4.13 we plot three snapshots of the three-bubble Hele-Shaw Newton's cradle (see §4.4), along with the dimensionless time to reach the instance, predicted by the numerical solution (with $W = 80$) of (4.5)–(4.8), the dipole model (4.27) and the pairwise interaction model (4.40). As in figure 4.10, the initial bubble separations are set to be 0.04 and 1 and $\delta = 5$. We observe the same qualitative behaviour in the pairwise solution as in the full numerical solution: the central bubble moves faster than the outer bubbles and so eventually joins with the front-most bubble. Again there is a discrepancy in the dimensionless time taken for the exchange, $t = 6.45$ for the numerical solution and $t = 7.06$ for the pairwise interaction solution, an approximately 9.5% difference. This offers a slight improvement over the dipole method, where there was an approximately 12.4% error.

We found in §4.5.9 that the dipole method incurs large errors in the limit as the bubbles become close, with larger errors observed for small values of δ. In figure 4.14 we plot the velocity, U_2 of the middle bubble in a train of three collinear identical bubbles versus its position, x_2, with $\delta = 0.25$. We fix the position of the outer bubbles at $x_1 = -10$, and $x_3 = 2.04$. When the middle bubble is well separated from the other bubbles (see $x_2 \approx -4$ in figure 4.14) the numerical, dipole, and pairwise solutions all align, as expected in the far separation limit. In the limit $x_2 \to 0$, in which the front two bubbles are close together, the pairwise model (4.40) matches the numerical solution much more closely than the dipole model (4.27) does. The percentage error when the bubbles are close ($x_2 = 0$) for the pairwise solution is approximately 0.14%, while for the dipole model it is approximately 7.5%. Note that these are the errors for the instantaneous velocity and will accumulate as the bubbles travel along the Hele-Shaw cell. The pairwise model has a significantly greater accuracy in situations where two bubbles become close together, such as in the cascading effect observed in a collinear train of identical bubbles (see §4.3).

Hence, we find that the pairwise model offers a useful improvement over the dipole model, in situations where two bubbles become close together. However, the dipole model produces qualitatively accurate solutions for a lower computational cost even in situations where the bubbles are not especially far apart.

4.7 Conclusions

In this chapter we develop a model for the motion of an arbitrary number of approximately circular bubbles in a Hele-Shaw cell. The instantaneous bubble velocities

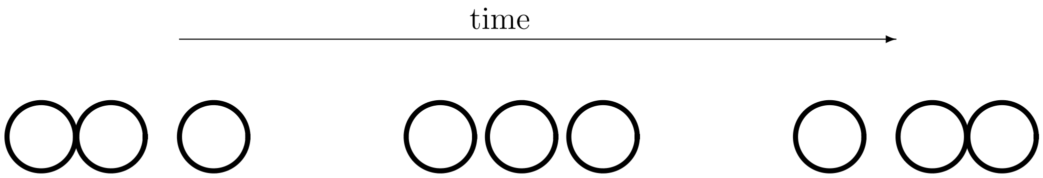

Numerical:	$t = 0$	$t = 3.22$	$t = 6.45$
Dipole:	$t = 0$	$t = 2.83$	$t = 5.66$
Pairwise:	$t = 0$	$t = 3.53$	$t = 7.06$

Figure 4.13: The progression of a series of three identical bubbles with $\delta = 5$ at time points: (i) beginning, (ii) when the bubbles are equispaced, and (iii) when the front two bubbles touch, for the numerical solution of (4.5)–(4.8) (with $W = 80$), dipole model (4.27), and pairwise model (4.40).

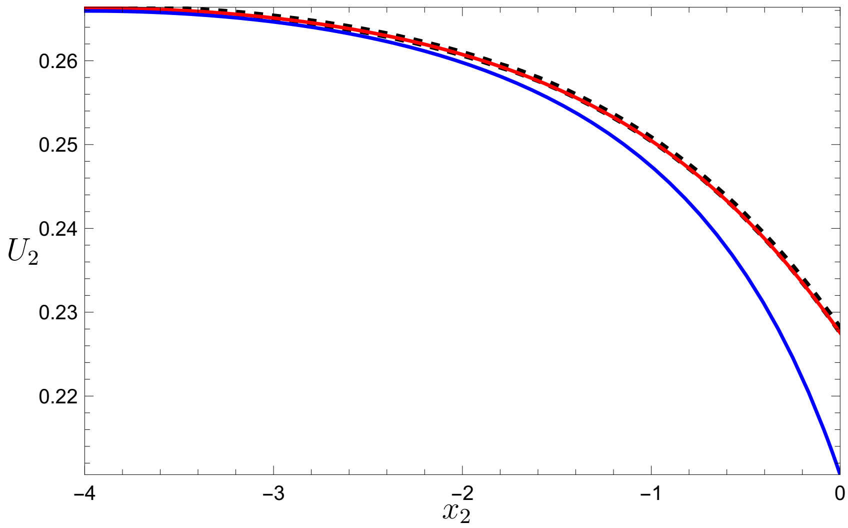

Figure 4.14: Instantaneous bubble velocity U_2 of the middle bubble versus its position, x_2, in a system of three collinear identical bubbles with $x_1 = -10$, $x_3 = 2.04$, and $\delta = 0.25$. The numerical solution of the full model (4.5)–(4.8) is shown by the black dashed curve, the pairwise interaction model solution (4.40) is shown in red and the dipole model solution (4.27) is shown in blue.

are determined by a net force balance on each bubble (4.2). We develop a numerical framework (4.5)–(4.8) to solve the full system and validate it against the known analytic equations of motion for a system of two bubbles from Chapter 3.

As in Chapters 2 and 3, we observe striking changes in the qualitative behaviour depending on whether δ is greater or less than 1. For example, in a train of three identical bubbles travelling along a Hele-Shaw channel, we find that the middle bubble either catches up with the one in front (if $\delta > 1$) or is caught by the one behind (if $\delta < 1$). In longer bubble trains, we observe bubble pairs successively forming and breaking up from the front to the back of the train if $\delta < 1$ or *vice versa* if $\delta > 1$, resembling experimental observations by Beatus *et al.* (2012), for example. Although this behaviour is reminiscent of a Newton's cradle, it arises from long-range hydrodynamic interactions rather than through momentum transfer between the bubbles.

This phenomenon suggests that it is very difficult to maintain a finite stream of equally spaced identical bubbles moving along the centre-line of a Hele-Shaw channel. The bubbles are always expected to bunch up into pairs or larger aggregates, unless we are in the special case where $\delta = 1$. We do find, though, that the relative bubble velocities are often quite small, so the clustering occurs quite slowly, and it may be minimised in experiments by reducing the channel width and by keeping δ as close to 1 as possible (see figure 4.7).

Dipole methods are commonly used in the literature without justification (see e.g. Shen *et al.*, 2014; Beatus *et al.*, 2006) to simulate the dynamics of bubbles in a Hele-Shaw cell. We systematically derive a dipole model using matched asymptotic expansions. As well as providing a theoretical underpinning, this approach allows us to incorporate the Bretherton drag law, rather than the *ad hoc* linear drag laws often used in the literature (Shen *et al.*, 2014; Sarig *et al.*, 2016; Green, 2018). The dipole model comprises a system of $2N$ ordinary differential equations (ODEs) for the propagation of N bubbles, the solution of which can be found at a much reduced computational cost as compared to the full numerical solution. Furthermore, we show that this reduced model accurately reproduces the Newton's cradle like behaviour, where the middle bubble in a train of three identical collinear bubbles moves faster or slower depending on whether $\delta > 1$ or $\delta < 1$.

In Chapter 3 we derive analytic expressions for the equations of motion of two bubbles. Here, for an arbitrary number of bubbles we derive a pairwise interaction model by summing the pairwise contributions to the equations of motion between each pair of bubbles. We obtain a system of nonlinear equations for the bubble velocities, which again can be easily solved numerically at a significantly reduced computational cost in comparison to the numerical solution proposed in §4.3. Furthermore, this method accurately models situations when two bubbles are close to each other, where the dipole method falters.

The methods we present in this chapter allow us to study the motion of an arbitrary number of bubbles in a Hele-Shaw cell. In most situations the dipole method accurately reproduces solutions to the full model and at a very cheap computational cost. However, the dipole model breaks down when bubbles are close together, in which case one can use the pairwise interaction model. Between them, the two reduced models in principle provide a framework that we can use to study an arbitrary configuration of bubbles in a Hele-Shaw cell at a low computational cost.

Chapter 5

The deformation of bubbles in a Hele-Shaw cell

5.1 Introduction

In Chapters 2, 3 and 4 we consider the distinguished limit $\mathrm{Ca} = O(\epsilon^3)$, where, ϵ, the aspect ratio and Ca, the capillary number are both small. In this limit, we find that the bubbles are circular to leading order in ϵ. In this chapter, we extend these results to find the perturbations to the bubble shape from circular.

In §5.2 we reproduce the model for an isolated bubble of arbitrary shape from §2.2. Then in §5.3 we reformulate the problem in terms of complex variables. In §5.4 we identify two distinguished limits of our problem. The first occurs when $\mathrm{Ca} = O(\epsilon^3)$, that is, when the *Bretherton parameter*, $\delta \propto \mathrm{Ca}^{1/3}/\epsilon = O(1)$. In this regime, the viscous pressure balances the pressure drop due to the thin films above and below the bubble. In the second distinguished limit, when $\mathrm{Ca} = O(\epsilon^2)$, or $\delta = O(\epsilon^{-1/3})$, the viscous pressure balances the contribution due to the curvature of the bubble boundary (in the sense of the curvature of the closed planar curve the boundary makes when viewed from above). In both limits, the bubble is a circle to leading order, and we present results for the correction to the bubble shape and velocity.

We develop a numerical framework similar to that of Green *et al.* (2017) in §5.7 to calculate solutions to our problem for general values of ϵ and Ca. We find that, for small values of δ, the bubble flattens in the direction of motion but, for large values of δ, the bubble becomes elongated. We then compare our numerical results with experimental data, collected by Katie Wu (Princeton University), in §5.8. Again, we observe a non-monotonicity in the bubble aspect ratio, with the bubble flattening for small δ and elongating for large δ. The theory and experiment agree well quantitatively for small values of δ, and qualitatively for large values of δ.

We then extend the modelling to include the effect of liquid flowing into the thin films at the front meniscus, then flowing under and above the bubble, and leaving at the rear meniscus. This flow affects the kinematic boundary condition on the bubble boundary, with a reduction in the apparent normal velocity along the front meniscus and an increase at the rear meniscus. We find this effect contributes an increase in the bubble aspect ratio for large values of δ, though not as great an increase as is observed experimentally.

Finally, in §5.10 we consider the deformation of a pair of bubbles with their centres aligned in the flow. We focus on the distinguished limit in which $\mathrm{Ca} = O(\epsilon^3)$, for which we can use leading-order solution from §3.3 and find the correction to the bubble shapes from circular. In a system of two equally sized bubbles, we find that the leading bubble flattens in the direction of motion, while the bubble behind elongates. The results of §5.7 suggest that the flattened bubble will travel more slowly than the elongated bubble, and thus lead to the bubbles colliding, Such behaviour is observed in experiments but impossible when considering only the leading-order solution.

5.2 Governing Equations

To begin we consider the flow of an isolated bubble in a Hele-Shaw cell in a uniform background flow of speed $\hat{U}$ as in §2.2. We consider a dimensionless system in which we have scaled lengths with the bubble radius $\hat{R}$, velocities with the far-field uniform flow velocity $\hat{U}$, and the fluid pressure with $12\hat{\mu}\hat{U}\hat{R}/\hat{h}^2$. Dimensionless quantities are represented without hats. Our dimensionless system is then given by (2.5), i.e.,

$$\begin{aligned}
\nabla^2 p &= 0 && \text{in} \quad \Omega, && (5.1\text{a})\\
p_b - \frac{3\mathrm{Ca}}{\epsilon} p &= 1 + \mathrm{Ca}^{2/3}\beta(U_n)U_n^{2/3} + \frac{\epsilon\pi}{4}\kappa && \text{on} \quad \partial\Omega_b, && (5.1\text{b})\\
\boldsymbol{n}\cdot\boldsymbol{\nabla} p &= -U_n && \text{on} \quad \partial\Omega_b, && (5.1\text{c})\\
p &\sim -x + o(1) && \text{as} \quad x^2+y^2 \to \infty, && (5.1\text{d})
\end{aligned}$$

where Ω is the fluid domain, $\partial\Omega_b$ is the apparent bubble–fluid boundary in the (x, y)-plane, whose normal velocity is U_n and β is the Bretherton coefficient, given by (2.4)

$$\beta(\mathrm{Ca}_n) = \begin{cases} \beta_1 \approx 3.88 & \text{when } U_n > 0, \\ \beta_2 \approx -1.13 & \text{when } U_n < 0. \end{cases} \tag{5.2}$$

One can show that the problem (5.1) has reflectional symmetry about the x-axis and thus that (in steady state) the bubble propagates in the x-direction at a speed U_b, to be determined.

5.3 Complex variable formulation

Now we reformulate the problem (5.1) using complex variables. We define a complex potential w by $w(z) + U_b z = -p(x, y) + \mathrm{i}\psi(x, y)$, where ψ is the streamfunction and $z = x + \mathrm{i}y$. This function is holomorphic on Ω and satisfies the boundary conditions

$$\mathrm{Im}[w(z)] = 0 \qquad \text{on } \partial\Omega_b, \tag{5.3a}$$

$$p_b + \frac{3\mathrm{Ca}}{\epsilon}\,\mathrm{Re}[w(z) + U_b z] = 1 + \frac{\pi\epsilon}{4}\kappa + \mathrm{Ca}^{2/3}\beta(U_n)U_n^{2/3} \qquad \text{on } \partial\Omega_b, \tag{5.3b}$$

$$w(z) \sim (1 - U_b)z + o(1) \qquad \text{as } z \to \infty. \tag{5.3c}$$

By the Riemann Mapping Theorem, there exists a conformal map $z(\zeta)$ to the fluid region Ω from the unit disk $|\zeta| < 1$, as shown schematically in figure 5.1. To fix the map uniquely, we take $z(0) = \infty$, with

$$z(\zeta) \sim \frac{a}{\zeta} \qquad \text{as} \quad \zeta \to 0, \tag{5.4}$$

where $a \in \mathbb{R}_{>0}$. We can thus let

$$z(\zeta) = \frac{a}{\zeta} + f(\zeta), \tag{5.5}$$

where $f(\zeta)$ is holomorphic in $|\zeta| < 1$ and, without loss of generality, we choose $f(0) = 0$. Note that this choice does not, in general, imply that the centroid of the bubble is at the origin, but that can be fixed *a posteriori*. The assumed symmetry about the real axis implies that f satisfies

$$f(\bar{\zeta}) = \overline{f(\zeta)}, \tag{5.6}$$

where the bar denotes complex conjugation. Equivalently, if f is expanded in the Taylor series

$$f(\zeta) = \sum_{n=1}^{\infty} c_n \zeta^n, \tag{5.7}$$

then the coefficients c_n are all real.

In the ζ-plane, the boundary conditions for $W(\zeta) = w(z(\zeta))$ can be derived from (5.3) to give

$$\mathrm{Im}[W(\zeta)] = 0 \qquad \text{on} \quad |\zeta| = 1, \tag{5.8a}$$

$$p_b + \frac{3\mathrm{Ca}}{\epsilon}\,\mathrm{Re}[W(\zeta) + U_b z(\zeta)] = \frac{\pi\epsilon}{4}\kappa + \mathrm{Ca}^{2/3}\beta(U_n)U_n^{2/3} \qquad \text{on} \quad |\zeta| = 1, \tag{5.8b}$$

$$W(\zeta) \sim \frac{a(1 - U_b)}{\zeta} + o(1) \qquad \text{as} \quad \zeta \to 0. \tag{5.8c}$$

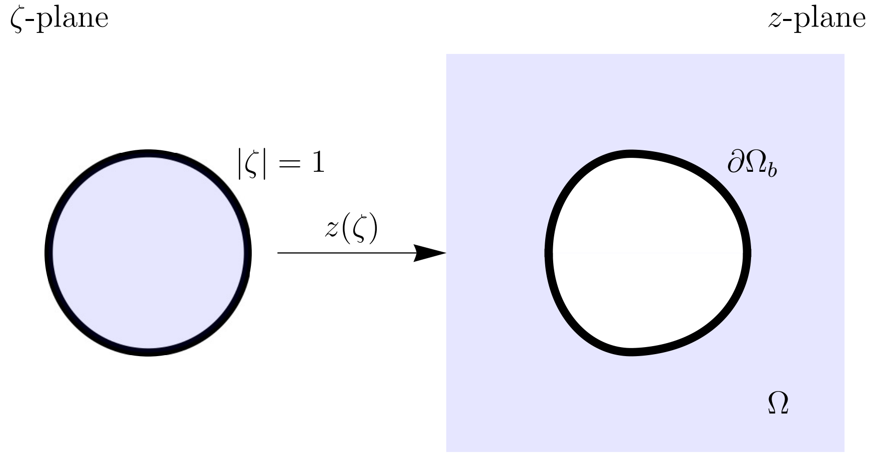

Figure 5.1: Schematic of the conformal map $z(\zeta)$ from the unit disk $|\zeta| < 1$ to the fluid region, Ω, in the z-plane.

We observe that

$$W(\zeta) = a(1 - U_b)\left(\zeta + \frac{1}{\zeta}\right) \tag{5.9}$$

satisfies (5.8a) and (5.8c). It only remains to impose the dynamic boundary condition (5.8b), which can be expressed as

$$\begin{aligned}\kappa = \frac{4}{\epsilon\pi}(p_b - 1) + \frac{12\mathrm{Ca}}{\epsilon^2\pi}\,\mathrm{Re}\left[(2 - U_b)a\zeta + U_b f(\zeta)\right]& \\ - \frac{4\mathrm{Ca}^{2/3}U_b^{2/3}}{\pi\epsilon}\beta(\boldsymbol{i}\cdot\boldsymbol{n})|\boldsymbol{i}\cdot\boldsymbol{n}|^{2/3},&\end{aligned} \tag{5.10}$$

on $|\zeta| = 1$, with

$$\kappa = -\frac{1}{|z'(\zeta)|}\left(1 + \mathrm{Re}\left[\frac{\zeta z''(\zeta)}{z'(\zeta)}\right]\right), \tag{5.11a}$$

$$\boldsymbol{i}\cdot\boldsymbol{n} = -\frac{\mathrm{Re}[\zeta z'(\zeta)]}{|z'(\zeta)|}, \tag{5.11b}$$

where $'$ denotes differentiation.

In principle, if a were known, then (5.10) would give us an ordinary differential equation for f from which we can find the bubble shape. As previously mentioned, we fix the translation by setting $f(0) = 0$. Then to close the system we impose the area constraint

$$\frac{1}{2\pi\mathrm{i}}\oint_{|\zeta|=1} z\left(\frac{1}{\zeta}\right) z'(\zeta)\,\mathrm{d}\zeta = -1, \tag{5.12}$$

which, by the use of Cauchy's Residue Theorem, reduces to

$$a = 1 + \frac{1}{2\pi\mathrm{i}}\oint_{|\zeta|=1} f\left(\frac{1}{\zeta}\right) f'(\zeta)\,\mathrm{d}\zeta, \tag{5.13}$$

or, in terms of the series expansion (5.7),

$$a = 1 + \sum_{n=1}^{\infty} n c_n^2. \tag{5.14}$$

Thus the *a priori* unknown constant a is in principle determined. The force balance (2.10) may be expressed as

$$\oint_{|\zeta|=1} \kappa z'(\zeta)\,\mathrm{d}\zeta = 0. \tag{5.15}$$

Upon substituting (5.10) this condition reduces to

$$\begin{aligned}\frac{12\mathrm{iCa}}{\epsilon^2}\big((2-U_b)a(c_1-a)+U_b(a-1-ac_1)\big)&\\ = \frac{4\mathrm{Ca}^{2/3}U_b^{2/3}}{\epsilon\pi}\oint_{|\zeta|=1}\beta(\boldsymbol{i}\cdot\boldsymbol{n})|\boldsymbol{i}\cdot\boldsymbol{n}|^{2/3}\left(-\frac{a}{\zeta^2}+f'(\zeta)\right)\mathrm{d}\zeta.&\end{aligned} \tag{5.16}$$

The right-hand side is not easily expressible in general, but (5.16) in principle determines the bubble velocity, U_b.

Finally, for any physically relevant solution the bubble boundary, $\partial\Omega_b$, is a simple closed curve, so

$$2\pi = \oint_{\partial\Omega} \kappa\,\mathrm{d}s = \oint_{|\zeta|=1} \frac{\kappa|z'(\zeta)|}{\mathrm{i}\zeta}\,\mathrm{d}\zeta, \tag{5.17}$$

which in principle determines p_b.

5.4 Distinguished limits

We return to the dynamic boundary condition (5.10), with the individual terms now labeled for clarity:

$$\begin{aligned}\overbrace{\kappa}^{①} = \overbrace{\frac{4}{\epsilon\pi}(p_b-1)}^{②} + &\overbrace{\frac{12\mathrm{Ca}}{\epsilon^2\pi}\mathrm{Re}\left[(2-U_b)a\zeta+U_b f(\zeta)\right]}^{③}\\ &\underbrace{-\frac{4\mathrm{Ca}^{2/3}U_b^{2/3}}{\pi\epsilon}\beta(\boldsymbol{i}\cdot\boldsymbol{n})|\boldsymbol{i}\cdot\boldsymbol{n}|^{2/3}}_{④}.\end{aligned} \tag{5.18}$$

The aspect ratio ϵ and capillary number Ca are both small parameters. The dominant balance in (5.18) depends on their relative sizes, and there are two distinguished limits to consider.

1. $\underline{\mathrm{Ca} = O(\epsilon^3)}$: the viscous pressure (term 3) balances the pressure drop due to the thin films (term 4).

2. $\underline{\mathrm{Ca} = O(\epsilon^2)}$: the viscous pressure (term 3) balances the contribution due to curvature (term 1).

In both distinguished limits we find that $p_b \sim 1 + O(\epsilon)$, indicating that the leading-order bubble pressure is determined by the capillary pressure jump across the meniscus.

In the following two sections, we will analyse each of these distinguished limits in detail. In each case, we will find expressions for the perturbations to the bubble shape and velocity. The asymptotic predictions will then be compared with numerical and experimental results in §§5.7 and 5.8, respectively.

5.5 Distinguished limit 1: $\mathrm{Ca} = O(\epsilon^3)$

5.5.1 Asymptotic expansions

The leading-order problem in this limit is solved in §2.2, where we define the Bretherton parameter

$$\delta = \frac{1}{\eta}\frac{\mathrm{Ca}^{1/3}}{\epsilon} = O(1) \tag{5.19}$$

as ϵ and Ca both tend to zero, where

$$\eta = \frac{(\beta_1 - \beta_2)\Gamma(4/3)}{3\sqrt{\pi}\Gamma(11/6)} \approx 0.894, \tag{5.20}$$

is a numerical constant. From (5.10) we find that the leading-order curvature is constant, so the bubble is a unit circle at leading order. It follows from (5.13) that the mapping function must take the form

$$z(\zeta) \sim \frac{1}{\zeta} + \epsilon f_1(\zeta) + O(\epsilon^2). \tag{5.21}$$

We can then calculate

$$\kappa \sim 1 + \epsilon \,\mathrm{Re}\left[(\zeta^3 f_1'(\zeta))'\right] + O(\epsilon^2), \tag{5.22a}$$

$$\boldsymbol{i}\cdot\boldsymbol{n} \sim \mathrm{Re}[\zeta] + \frac{\epsilon}{2}\mathrm{Re}[(\zeta^3 - \zeta) f_1'(\zeta)] + O(\epsilon^2). \tag{5.22b}$$

Furthermore, we expand the remaining variables in powers of ϵ as

$$\frac{4}{\epsilon\pi}(p_b - 1) \sim 1 + \frac{4\epsilon}{\pi} p_{b_2} + O(\epsilon^2), \tag{5.23a}$$

$$U_b \sim U_0 + \epsilon U_1 + O(\epsilon^2). \tag{5.23b}$$

5.5.2 Shape perturbations

The dynamic boundary condition (5.10) at $O(\epsilon)$ gives

$$\operatorname{Re}\left[(\zeta^3 f_1'(\zeta))'\right] = \frac{4}{\pi}p_{b_2} + \frac{12\delta^3\eta^3}{\pi}(2-U_0)\operatorname{Re}[\zeta] - \frac{4\delta^2\eta^2U_0^{2/3}}{\pi}\beta\left(\operatorname{Re}[\zeta]\right)|\operatorname{Re}[\zeta]|^{2/3}. \tag{5.24}$$

We can then read off

$$(\zeta^3 f_1'(\zeta))' = \frac{4}{\pi}p_{b_2} + \frac{12\delta^3\eta^3}{\pi}(2-U_0)\zeta - \frac{4\delta^2\eta^2U_0^{2/3}}{\pi}\,b(\zeta), \tag{5.25}$$

where

$$b(\zeta) = \frac{b_0}{2} + \sum_{n=1}^{\infty} b_n\zeta^n, \tag{5.26}$$

is holomorphic in $|\zeta|<1$, such that $\operatorname{Re}[b(\mathrm{e}^{\mathrm{i}\theta})] = \beta(\cos\theta)|\cos\theta|^{2/3}$. The coefficients b_n are given by

$$\begin{aligned} b_n &= \frac{1}{2\pi\mathrm{i}}\oint_{|\zeta|=1}\frac{\beta\left(\operatorname{Re}[\zeta]\right)|\operatorname{Re}[\zeta]|^{2/3}}{\zeta^{n+1}}\,\mathrm{d}\zeta, \\ &= \frac{1}{2\pi}\int_0^{2\pi}\beta(\cos\theta)|\cos\theta|^{2/3}\cos n\theta\,\mathrm{d}\theta, \\ &= \frac{\Gamma\left(\frac{5}{3}\right)\Gamma\left(\frac{n}{2}-\frac{1}{3}\right)}{4\pi 2^{2/3}\Gamma\left(\frac{n}{2}+\frac{4}{3}\right)}\Bigg[\Big((\sqrt{3}+1)\beta_1+(\sqrt{3}-1)\beta_2\Big)(-1)^{\lfloor\frac{n-1}{2}\rfloor} \\ &\qquad\qquad - \Big((\sqrt{3}-1)\beta_1+(\sqrt{3}+1)\beta_2\Big)(-1)^{\lfloor\frac{n}{2}\rfloor}\Bigg]. \end{aligned} \tag{5.27}$$

Since f_1 is holomorphic in $|\zeta|<1$ we require the linear and constant terms to vanish on the right-hand side of (5.25). We thus find that the bubble pressure perturbation p_{b_2} is given by

$$p_{b_2} = \frac{\delta^2\eta^2U_0^{2/3}b_0}{2} = \frac{\delta^2\eta^2U_0^{2/3}\Gamma(5/6)(\beta_1+\beta_2)}{2\sqrt{\pi}\Gamma(4/3)}, \tag{5.28a}$$

and the leading-order bubble velocity, U_0, satisfies

$$\frac{\delta(2-U_0)}{U_0^{2/3}} = \frac{(\beta_1-\beta_2)\Gamma(4/3)}{3\sqrt{\pi}\eta\Gamma(11/6)} = 1, \tag{5.28b}$$

which reduces to the isolated bubble velocity determined by equation (2.16). We then integrate (5.25) to find

$$f_1(\zeta) = -\frac{4\delta^2\eta^2U_0^{2/3}}{\pi}\sum_{n=1}^{\infty}\frac{b_{n+1}\zeta^n}{n(n+2)}, \tag{5.29}$$

which determines the $O(\epsilon)$ shape perturbations.

5.5.3 Asymptotics of the Bretherton integral

Next, we analyse how the shape perturbations affect the bubble velocity by expanding the force balance (5.16) up to $O(\epsilon)$. To evaluate the integral on the right-hand side, we need to understand the asymptotic behaviour of $\beta(\boldsymbol{i}\cdot\boldsymbol{n})|\boldsymbol{i}\cdot\boldsymbol{n}|^{2/3} = \mathrm{Re}[b(\mathrm{e}^{\mathrm{i}\theta})]$, where $\boldsymbol{n} = (\cos\theta, \sin\theta)$. Then we have

$$\mathrm{e}^{\mathrm{i}\theta} = -\frac{\zeta z'(\zeta)}{|z'(\zeta)|} \sim \frac{1}{\zeta}\left(1 - \epsilon\mathrm{i}\,\mathrm{Im}[\zeta^2 f_1'(\zeta)]\right) + O(\epsilon^2), \tag{5.30}$$

and thus

$$\beta(\boldsymbol{i}\cdot\boldsymbol{n})|\boldsymbol{i}\cdot\boldsymbol{n}|^{2/3} \sim \mathrm{Re}[b(\zeta)] - \epsilon\,\mathrm{Im}[\zeta^2 f_1'(\zeta)]\,\mathrm{Im}[\zeta b'(\zeta)] + O(\epsilon^2). \tag{5.31}$$

This expansion allows us to find that the asymptotic behaviour of the integral on the right-hand side of the force balance (5.16) is given by

$$\begin{aligned}
&\oint_{|\zeta|=1} \beta(\boldsymbol{i}\cdot\boldsymbol{n})|\boldsymbol{i}\cdot\boldsymbol{n}|^{2/3}\left(-\frac{a}{\zeta} + f'(\zeta)\right)\mathrm{d}\zeta \\
&\quad\sim -\oint_{|\zeta|=1} \mathrm{Re}[b(\zeta)]\frac{\mathrm{d}\zeta}{\zeta^2} + \epsilon\oint_{|\zeta|=1}\left\{\mathrm{Re}[b(\zeta)]f_1'(\zeta) + \frac{1}{\zeta^2}\mathrm{Im}[\zeta^2 f_1'(\zeta)]\,\mathrm{Im}[\zeta b'(\zeta)]\right\}\mathrm{d}\zeta. \\
&\quad\sim -\mathrm{i}\pi b_1 + \frac{\epsilon}{4}\oint_{|\zeta|=1}\Big(2\zeta b(\zeta) + (1+\zeta^2)b'(\zeta)\Big)f_1'\left(\frac{1}{\zeta}\right)\frac{\mathrm{d}\zeta}{\zeta^3},
\end{aligned} \tag{5.32}$$

by Cauchy's Residue Theorem. Finally using (5.29) and Cauchy's Residue Theorem once again we find that the integral at $O(\epsilon)$ is given by

$$\begin{aligned}
&\frac{1}{4}\oint_{|\zeta|=1}\Big(2\zeta b(\zeta) + (1+\zeta^2)b'(\zeta)\Big)f_1'\left(\frac{1}{\zeta}\right)\frac{\mathrm{d}\zeta}{\zeta^3} \\
&\qquad = -2\mathrm{i}\delta^2\eta^2 U_0^{2/3}\sum_{n=1}^{\infty} b_{n+1}(b_n + b_{n+2}) \\
&\qquad = -\mathrm{i}\left(\frac{96\Gamma(2/3)}{7\sqrt{\pi}\Gamma(1/6)} - \frac{27}{5\pi}\right)(\beta_1^2 - \beta_2^2)\delta^2\eta^2 U_0^{2/3}.
\end{aligned} \tag{5.33}$$

The last equality comes from noticing that

$$\begin{aligned}
\sum_{n=1}^{\infty} b_{n+1}(b_n + b_{n+2}) &= 2\sum_{n=0}^{\infty} b_n b_{n+1} - 2b_0 b_1 - b_1 b_2, \\
&= \frac{2}{\pi}\int_0^{2\pi}\left(\beta(\cos\theta)|\cos\theta|^{2/3}\right)^2\cos\theta\,\mathrm{d}\theta - 2b_0 b_1 - b_1 b_2.
\end{aligned} \tag{5.34}$$

5.5.4 Velocity perturbation

We are now in a position to find the velocity perturbation. We note from (5.29) that the first Taylor coefficient in f is given by

$$c_1 \sim -\frac{4\delta^2\eta^2 U_0^{2/3} b_2}{3\pi}\,\epsilon + O\left(\epsilon^2\right). \tag{5.35}$$

By using (5.32) and (5.33), we can therefore expand the force balance equation (5.16) as

$$\begin{aligned}\frac{3\eta\delta}{U_0^{2/3}}(U_0-2) + \epsilon\delta\eta\left(\frac{6(1-U_0)}{U_0^{2/3}}\,\frac{c_1}{\epsilon} + \frac{4+U_0}{U_0^{5/3}}U_1\right)&\\ \sim -b_1 - \epsilon\left(\frac{96\Gamma(2/3)\sqrt{\pi}}{7\Gamma(1/6)} - \frac{27}{5}\right)\frac{(\beta_1^2-\beta_2^2)}{\pi^2}\delta^2\eta^2 U_0^{2/3} + O(\epsilon^2).&\end{aligned} \tag{5.36}$$

At leading order we find

$$\frac{3\delta\eta(2-U_0)}{U_0^{2/3}} = b_1 = 3\eta, \tag{5.37}$$

which, as expected, reproduces (5.28b). The velocity perturbation is then found at $O(\epsilon)$ to be given by

$$\begin{aligned}U_1 = -\frac{(\beta_1^2-\beta_2^2)U_0^{7/3}}{\pi^2(4+U_0)}\Bigg\{&\left(\frac{96\Gamma(2/3)\sqrt{\pi}}{7\Gamma(1/6)} - \frac{27}{5}\right)\\ &- \frac{4\cdot 2^{2/3}\sqrt{3}(\beta_1-\beta_2)\Gamma(-2/3)\Gamma(4/3)^2}{25\pi^2}\,\frac{U_0^{2/3}(U_0-1)}{(2-U_0)^2}\Bigg\}.\end{aligned} \tag{5.38}$$

5.6 Distinguished limit 2: $\mathrm{Ca} = O(\epsilon^2)$

5.6.1 Asymptotic expansions

In this regime, we let $\mathrm{Ca} = C\epsilon^2$, where $C = O(1)$, and it follows that $\delta = O(\epsilon^{-1/3})$. The viscous pressure and curvature (terms 3 and 1, respectively, in equation (5.18)) balance at leading order. The resulting leading-order problem is well studied, and it has been shown that the only stable solution is a circular bubble that moves at twice the background flow velocity (see, for example, Lustri *et al.*, 2020). We perturb about this leading-order solution by expanding the mapping function and bubble velocity as

$$z(\zeta) \sim \frac{1}{\zeta} + \epsilon^{1/3} f_2(\zeta) + O\left(\epsilon^{2/3}\right), \qquad U_b \sim 2 + \epsilon^{1/3}\tilde{U}_1 + O\left(\epsilon^{2/3}\right). \tag{5.39a,b}$$

As in §5.5, we expand the bubble pressure as

$$\frac{4}{\epsilon\pi}(p_b - 1) \sim 1 + \frac{4\epsilon^{1/3}}{\pi} p_{b_2} + O\left(\epsilon^{2/3}\right), \tag{5.40}$$

and we can calculate

$$\kappa \sim 1 + \epsilon^{1/3}\,\mathrm{Re}\left[(\zeta^3 f_1'(\zeta))'\right] + O\left(\epsilon^{2/3}\right), \tag{5.41a}$$

$$\boldsymbol{i}\cdot\boldsymbol{n} \sim \mathrm{Re}[\zeta] + \frac{\epsilon^{1/3}}{2}\,\mathrm{Re}[(\zeta^3 - \zeta) f_1'(\zeta)] + O\left(\epsilon^{2/3}\right). \tag{5.41b}$$

5.6.2 Shape perturbations

In this limit, the dynamic boundary condition (5.10) becomes

$$\begin{aligned} 1 + \epsilon^{1/3}\,\mathrm{Re}[(\zeta^3 f_2'(\zeta))'] \sim 1 + \frac{4\epsilon^{1/3}}{\pi} p_{b_2} + \frac{12C\epsilon^{1/3}}{\pi}\,\mathrm{Re}[2f_2(\zeta) - \tilde{U}_1\zeta] \\ - \epsilon^{1/3}\frac{4C^{2/3}2^{2/3}}{\pi}\beta(\mathrm{Re}[\zeta])|\,\mathrm{Re}[\zeta]|^{2/3} + O\left(\epsilon^{2/3}\right). \end{aligned} \tag{5.42}$$

This equation is identically satisfied at leading order. At $O\left(\epsilon^{1/3}\right)$ we read off

$$(\zeta^3 f_2'(\zeta))' = \frac{4}{\pi} p_{b_2} + \frac{12C}{\pi}(2f_2(\zeta) - U_1\zeta) - \frac{4C^{2/3}2^{2/3}}{\pi} b(\zeta), \tag{5.43}$$

where $b(\zeta)$ is holomorphic in $|\zeta| < 1$ and is given by the Taylor series (5.26).

Since $f_2(\zeta)$ is holomorphic in $|\zeta| < 1$ we expand it as a Taylor series, namely

$$f_2(\zeta) = \sum_{n=1}^{\infty} d_n \zeta^n, \tag{5.44}$$

where $c_n = \epsilon^{1/3} d_n$. Substituting this series into (5.43), we find that the constant term determines the bubble pressure,

$$p_{b_2} = \frac{C^{2/3} b_0}{2^{1/3}}. \tag{5.45}$$

Then the linear term gives

$$\tilde{U}_1 = 2d_1 - \frac{2^{2/3} b_1}{3C^{1/3}}, \tag{5.46}$$

which in principle determines the velocity perturbation. Evaluating at subsequent powers of ζ we find the recurrence relation

$$d_n - \frac{\pi}{24C}(n^2 - 1) d_{n-1} = \frac{2^{2/3} b_n}{6C^{1/3}}. \tag{5.47}$$

The general solution of (5.47) for d_n grows factorially for large n, violating our assumption that the Taylor series (5.44) converges inside the unit disk. We deduce that the only acceptable solution of (5.47) is given by

$$d_n = -\frac{2^{2/3}}{6C^{1/3}}(n+1)!(n-1)!\sum_{j=0}^{\infty}\frac{b_{n+j+1}}{(n+j+2)!(n+j)!}\left(\frac{24C}{\pi}\right)^{j+1}, \tag{5.48}$$

for $n \geq 1$.

5.6.3 Velocity perturbation

The velocity perturbation is found from (5.46) and (5.48), giving

$$\tilde{U}_1 = -\frac{2^{5/3}}{3C^{1/3}}\sum_{j=0}^{\infty}\frac{b_{j+1}}{j!(j+2)!}\left(\frac{24C}{\pi}\right)^{j}, \tag{5.49}$$

where b_n is given by (5.27). Thus the velocity perturbation is determined as a function of $C = \mathrm{Ca}/\epsilon^2$.

5.7 Numerical simulations

5.7.1 Numerical formulation

In this section we calculate numerical solutions of (5.1) for general values of ϵ and Ca, following the methodology laid out in Green *et al.* (2017). We expand the bubble shape function $f(\zeta)$ as a truncated Taylor series

$$f(\zeta) \approx \sum_{n=1}^{N-1} c_n\zeta^n, \tag{5.50}$$

where we recall that the $N-1$ coefficients, c_n, are all real due to the symmetry condition (5.6). In addition to $\{c_n\}$, we have to solve for U_b, p_b, and a, so in total we need $N+2$ equations to form a closed system. We obtain the first equation by enforcement of the bubble area constraint (5.14), and the other $N+1$ equations we acquire by evaluating (5.10) at $N+1$ points along the upper half circle, namely $p_j = \mathrm{e}^{\pi j/N}$ for $0 \leq j \leq N$. Note that any physical solution will automatically satisfy the relations (5.15) and (5.17). The resulting system of $N+2$ algebraic equations is solved using Newton's method. We choose to use $N = 100$, and have checked convergence against larger values of N.

In general, we have two parameters, Ca and ϵ, which may be varied independently. We plot the results versus the Bretherton parameter, $\delta = \mathrm{Ca}^{1/3}/\eta\epsilon$, with either ϵ held constant while Ca is varied or *vice versa.*

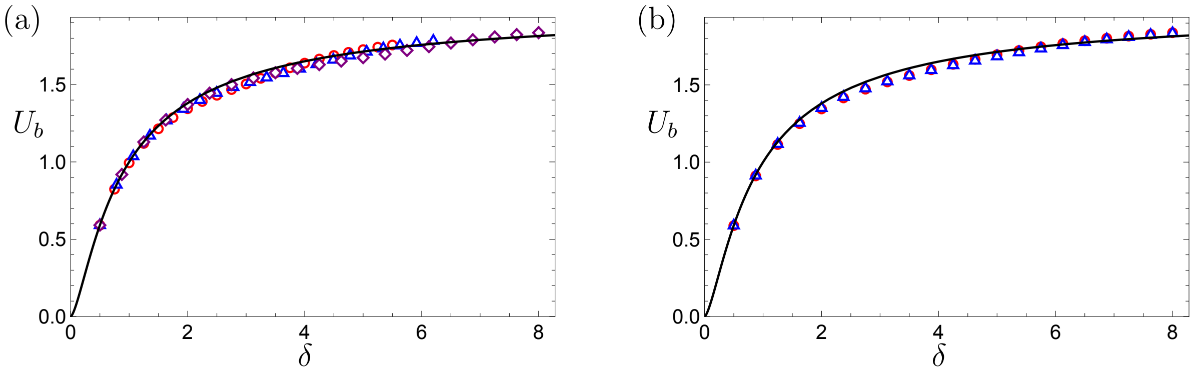

Figure 5.2: Dimensionless bubble velocity U_b versus Bretherton parameter δ. The theoretical prediction (5.28b) is shown as a black curve, and numerical simulations of (5.1) are shown as points. (a) Fixed $\epsilon = 0.05$ (red), 0.025 (blue), 0.01 (purple); (b) fixed $\mathrm{Ca} = 6.7 \times 10^{-4}$ (red), 3.3×10^{-4} (blue).

5.7.2 Results

In figure 5.2 we plot the dimensionless bubble velocity versus δ, keeping ϵ constant in figure 5.2(a), and Ca constant in figure 5.2(b). In all cases, the numerical results are observed to follow the theoretical prediction (5.28b) closely. The value of U_b is over-predicted by (5.28b) when δ is small and under-predicted for large values of δ. To see this trend more clearly we calculate

$$\Delta U_b = U_b - U_0, \tag{5.51a}$$

$$\sim \epsilon U_1 \qquad \text{when} \quad \mathrm{Ca} = O(\epsilon^3), \tag{5.51b}$$

$$\sim 2 - U_0 + \epsilon^{1/3}\tilde{U}_1 \qquad \text{when} \quad \mathrm{Ca} = O(\epsilon^2), \tag{5.51c}$$

where U_b is the numerical solution for the bubble velocity, U_0 is the leading-order approximation which satisfies equation (5.28b), and U_1 and $\tilde{U}_1$ are given by (5.38) and (5.46), respectively. We plot ΔU_b versus δ in figure 5.3, with ϵ held constant; similar qualitative behaviour is observed with Ca held constant. As $\delta \to 0$ the approximation (5.28b) becomes perfect. Then, as δ is increased, the difference transitions from (5.28b) over-predicting to under-predicting the bubble velocity.

Alongside the numerical results we plot the asymptotic results found previously in §5.4. In figure 5.3 we find that the distinguished limit where $\mathrm{Ca} = O(\epsilon^3)$ (see §5.5) accurately matches the initial over-prediction of (5.28b) for small δ, however this limit implies that the velocity difference should continue to be negative as δ increases. In the second distinguished limit (see §5.6) we observe that (5.28b) changes from over-predicting to under-predicting as seen in the numerical solutions. In figure 5.3 we observe a large difference between the asymptotic solution (5.39) in distinguished

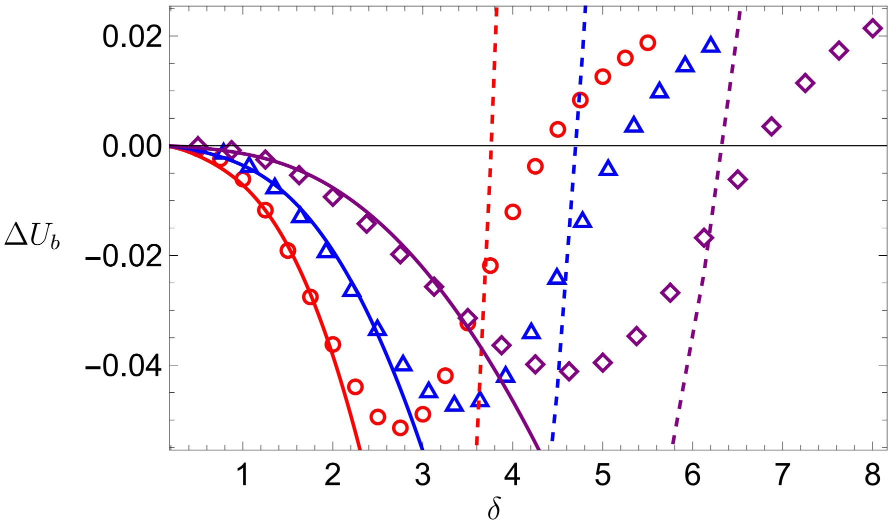

Figure 5.3: The difference ΔU_b (5.51) between the numerical solution and the prediction (5.28b) versus δ with fixed $\epsilon = 0.05$ (red circles), 0.025 (blue triangles), 0.01 (purple diamonds). Asymptotic predictions for the distinguished limits given by (5.23b) when $\mathrm{Ca} = O(\epsilon^3)$ (solid curve) and (5.39) when $\mathrm{Ca} = O(\epsilon^2)$ (dashed curve).

limit 2 (see §5.6) and the numerical solution. This discrepancy is due to the range of ϵ chosen, with the smallest being $\epsilon = 0.01$, for which $\epsilon^{1/3} \approx 0.2$. At the end of this section, we show that the asymptotic and numerical solutions converge for smaller values of ϵ.

We plot the computed bubble shapes for different values of δ in figure 5.4. For small values of δ, figure 5.4(a) illustrates that the bubble shape is flattened in the x-direction (the direction of propagation). In figure 5.4(b) it is shown that, as δ is increased, the bubble shape evolves from being flattened in the x-direction to being elongated. We plot the asymptotic bubble shapes given by $z(\zeta) \sim 1/\zeta + \epsilon f_1(\zeta)$, (5.21) in figure 5.5(a). These are observed to agree well with the numerical solutions (see figure 5.5) for small values of δ, in which we observe the bubble flattening in the direction of propagation. The bubble shapes given by $z(\zeta) \sim 1/\zeta + \epsilon^{1/3} f_2(\zeta)$, (5.39) are plotted in figure 5.6(a). There is good qualitative agreement with the numerical solutions (see figure 5.6), where, the bubble shapes are flattened in the x-direction when $C = \mathrm{Ca}/\epsilon^2$ is small and then transition to elongated as C is increased.

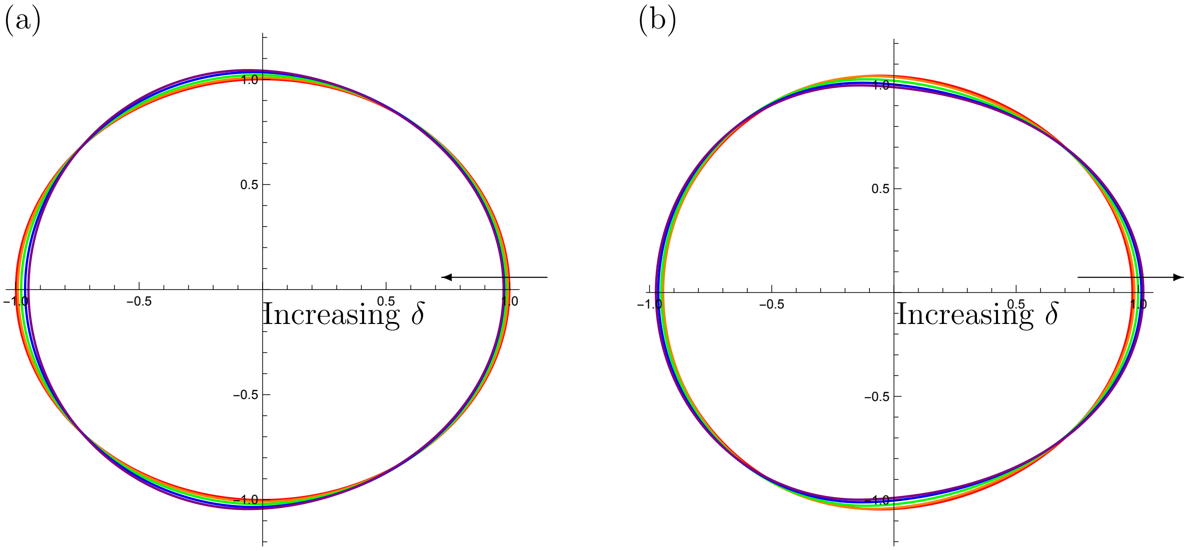

Figure 5.4: Numerical solutions for the bubble shapes with fixed $\epsilon = 0.05$. In (a), $\delta = 0.5$ (red), 1 (orange), 1.5 (green), 2 (blue), 2.5 (purple). In (b) $\delta = 2.5$ (red), 3 (orange), 3.5 (green), 4 (blue), 4.5 (purple).

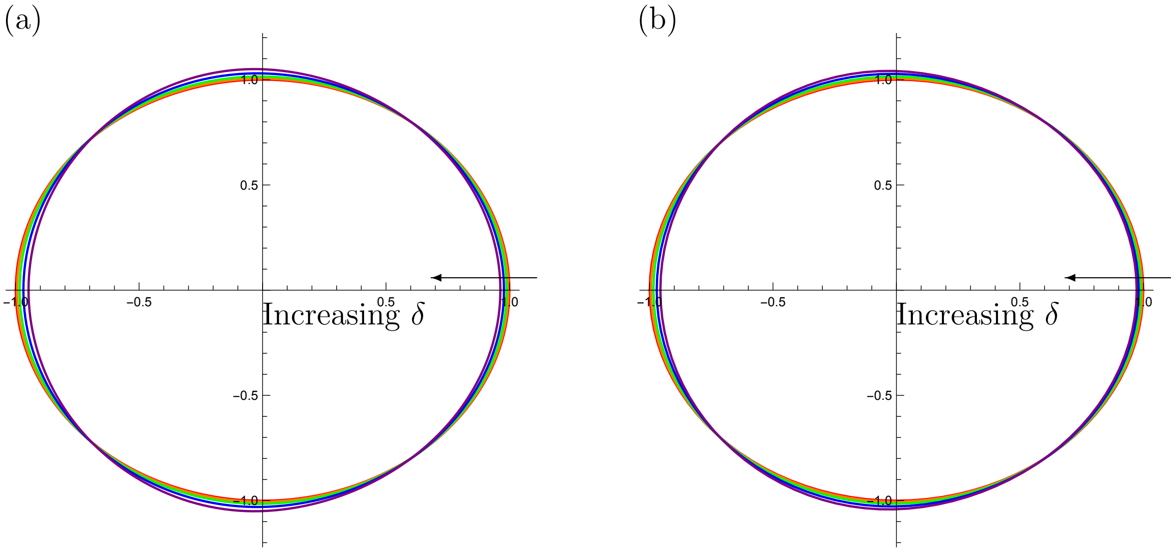

Figure 5.5: (a) Asymptotic solution, $z(\zeta) = 1/\zeta + \epsilon f_1(\zeta)$, (5.21) and (b) numerical solution for the bubble shapes where $\delta = 0.5$ (red), 1.1 (orange), 1.7 (green), 2.3 (blue), 2.9 (purple), with $\epsilon = 0.025$.

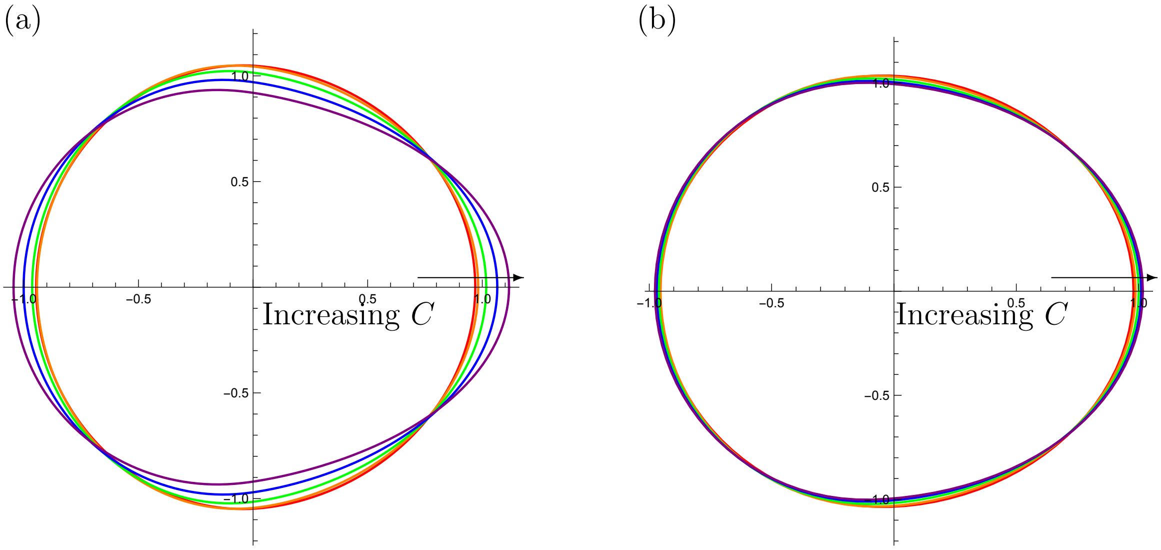

Figure 5.6: (a) Asymptotic solution, $z(\zeta) = 1/\zeta + \nu f_2(\zeta)$, (5.39) and (b) numerical solution for the bubble shapes in the regime $\mathrm{Ca} = C\epsilon^2$, where $C = 0.5$ (red), 1 (orange), 1.5 (green), 2 (blue), 2.5 (purple), with $\epsilon = 0.025$.

To quantify these results we define the aspect ratio as

$$A = \frac{z(1) - z(-1)}{2\max_{|\zeta|=1}\left\{|\operatorname{Im}[z(\zeta)]|\right\}}. \tag{5.52a}$$

$$\sim 1 - \frac{8\epsilon\delta^2\eta^2 U_0^{2/3}}{\pi}\sum_{k=1}^{\infty}\frac{b_{4k+2}}{(4k+1)(4k+3)} \qquad \text{when} \quad \mathrm{Ca} = O(\epsilon^3), \tag{5.52b}$$

$$\sim 1 + 2\epsilon^{1/3}\sum_{k=0}^{\infty} d_{4k+1} \qquad \text{when} \quad \mathrm{Ca} = O(\epsilon^2), \tag{5.52c}$$

In figure 5.7, the aspect ratio (5.52) is plotted versus δ and indeed we observe that the bubble shape changes from being flattened ($A < 1$) to elongated ($A > 1$) as δ is increased. We find that the crossover points where $A = 1$ approximately match the positions where $\Delta U_b = 0$. This suggests that the discrepancies observed in figure 5.2 can be attributed to bubble deformation, with flattened bubbles moving slower and elongated bubbles travelling faster than predicted.

Asymptotic results for the aspect ratio are also plotted in figure 5.7. In the first distinguished limit, $\mathrm{Ca} = O(\epsilon^3)$, we accurately predict that the bubble shapes initially flatten in the flow direction. In this limit we predict that the magnitude of the flattening continues to increase as δ is increased, whereas this is not seen in the numerical result or experiments (see §5.8). In the second distinguished limit $\mathrm{Ca} = O(\epsilon^2)$ we do predict the non-monotonicity of the bubble aspect ratio, with the bubbles being flattened for small values of δ, and becoming elongated for larger values of δ.

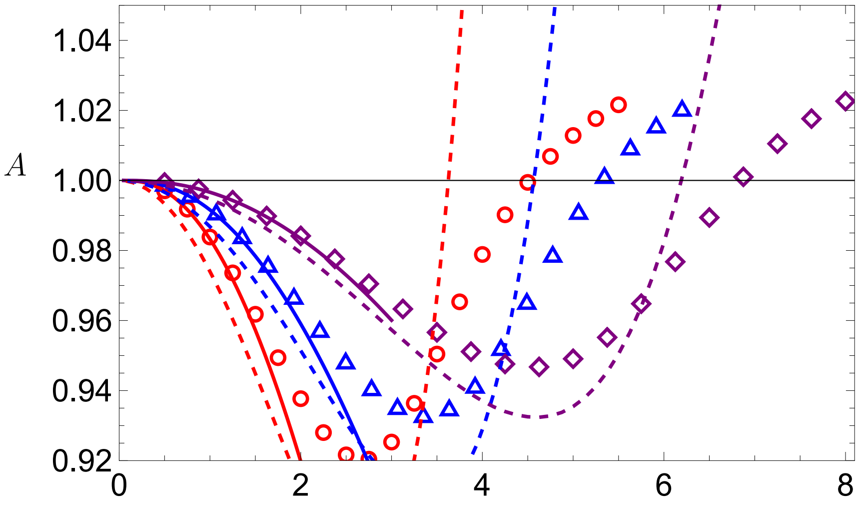

Figure 5.7: Bubble aspect ratio, A, given by (5.52) as a function of δ with fixed $\epsilon = 0.05$ (red), 0.025 (blue), 0.01 (purple). The numerical solution (points) are shown alongside asymptotic predictions for the distinguished limits: $\mathrm{Ca} = O(\epsilon^3)$ (solid curve) and $\mathrm{Ca} = O(\epsilon^2)$ (dashed curve).

In figure 5.8 we plot the velocity difference, ΔU_b, and the bubble aspect ratio, A, versus δ for $\epsilon = 5 \times 10^{-5}$, and $\epsilon = 10^{-5}$ (so $\epsilon^{1/3} \approx 0.04$ and ≈ 0.02, respectively). We observe convergence of the numerical results to the asymptotic solutions in distinguished limit 2 with decreasing ϵ, and much closer agreement than seen in figures 5.3 and 5.7.

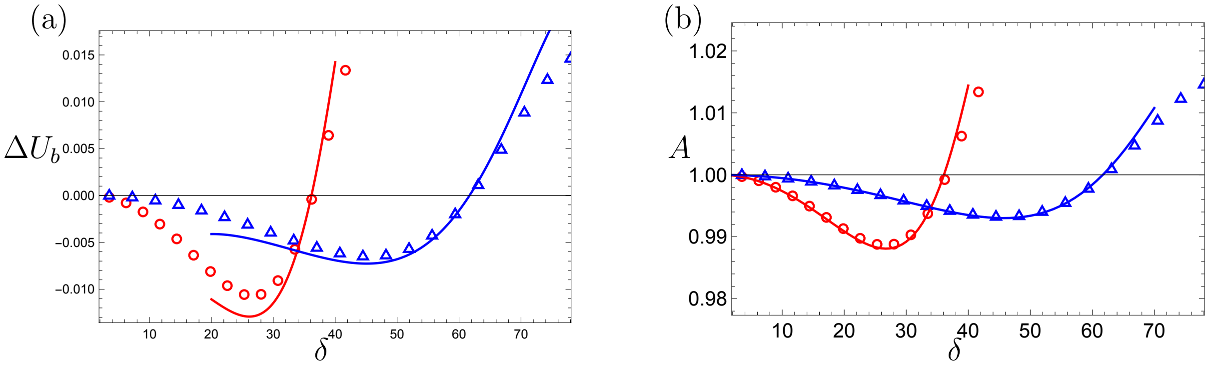

Figure 5.8: (a) The velocity difference, ΔU_b, and (b) the aspect ratio, A, plotted versus δ, with fixed $\epsilon = 5 \times 10^{-5}$ (red), 10^{-5} (blue). The points show the results of numerical computations, and the curves show the predictions of the asymptotic analysis in §5.6.

5.8 Comparison with experiments

In experiments (conducted by Katie Wu, Princeton University), the bubble boundary $\partial\Omega_b$ is captured as a set of points $\{(x_i, y_i) : i = 1, \cdots, N\}$, and the aspect ratio is then calculated using

$$A = \frac{\max|x_i - x_j|}{\max|y_i - y_j|}. \tag{5.53}$$

In figure 5.9, we plot the measured aspect ratio versus the Bretherton parameter, δ, for two fixed values of the capillary number. The corresponding numerically computed aspect ratios are plotted as solid curves. We observe good agreement for small values of δ. The experiments confirm the theoretically predicted non-monotonic behaviour of the bubble shape, and the transition from being flattened to being elongated in the direction of the flow, as δ increases. In both theoretical and experimental results, A depends only weakly on the value of Ca.

For large values of δ, the experiments document a linear increase in A, whereas the theory predicts that A saturates to a constant. In this limit, we expect the theory to start to break down, because the bubble develops a prominent fore-aft asymmetry. To account for this asymmetry, we would need to incorporate the full boundary condition found in Burgess & Foster (1990), where the value of β_2 varies along the rear meniscus as a function of $\mathrm{Ca}_n^+/\big(-\mathrm{Ca}_n^-\big)$, where $\mathrm{Ca}_n^\pm$ are the capillary numbers based on the normal velocity at corresponding points on the front and rear bubble interfaces (also see §2.2.4). We have also neglected the influence of the leakage of liquid through the thin films, which will be discussed in §5.9. Both of these effects may contribute to the much sharper rise in the aspect ratio A observed in experiments than predicted by our theory.

We show experimentally measured bubble shapes, compared with the numerical solutions at the same flow conditions, in figure 5.10. Again, we see good agreement between theory and experiments for small values of δ. As δ is increased, the theory correctly predicts the direction of deformation and the fore-aft asymmetry of the bubble shape, though the bubbles in the experiments are elongated in the flow direction more than suggested by the theory.

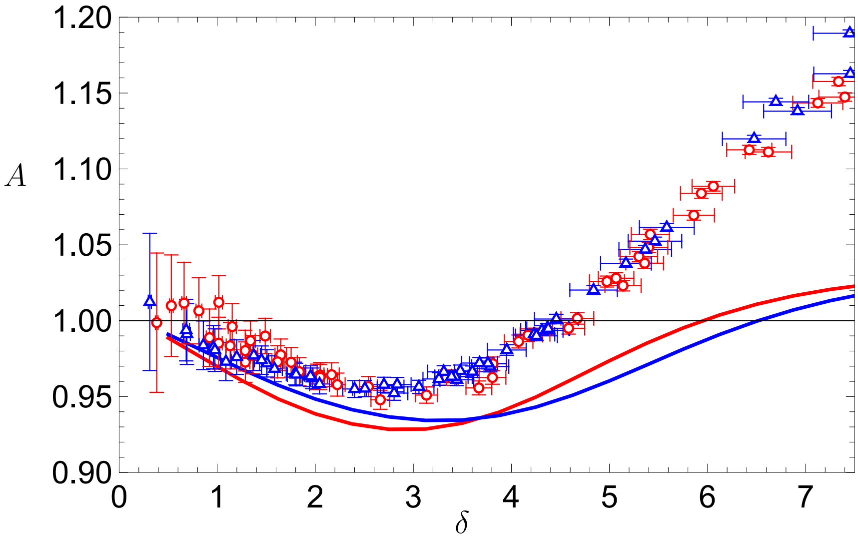

Figure 5.9: Aspect ratio, A, of the bubble, given by (5.52) (curves) and experimentally measured aspect ratio (points) versus δ. The capillary number is fixed at $\mathrm{Ca} = 6.6 \times 10^{-4}$ (red), and $\mathrm{Ca} = 3.3 \times 10^{-4}$ (blue), with ϵ in the range 0.01–0.25.

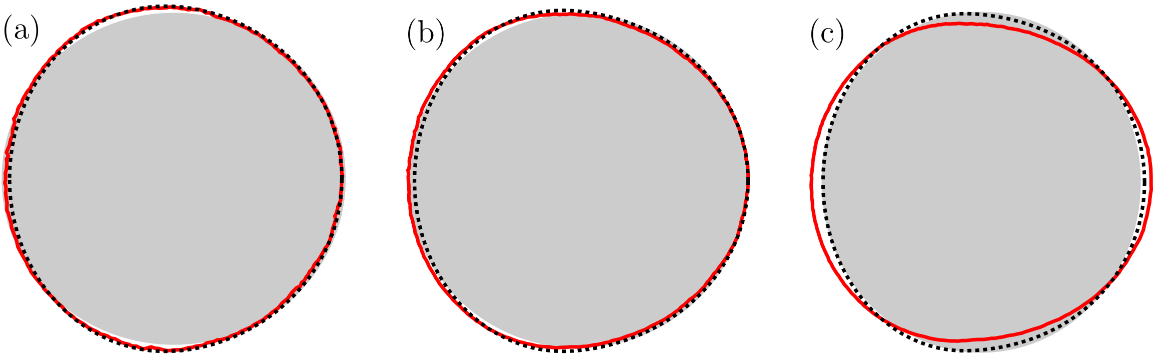

Figure 5.10: Experimental bubble shapes (red solid), numerical solution (black dashed), the unit circle (grey fill), for δ = (a) 2.66, (b) 4.67, (c) 7.12, with $\mathrm{Ca} = 6.6 \times 10^{-4}$.

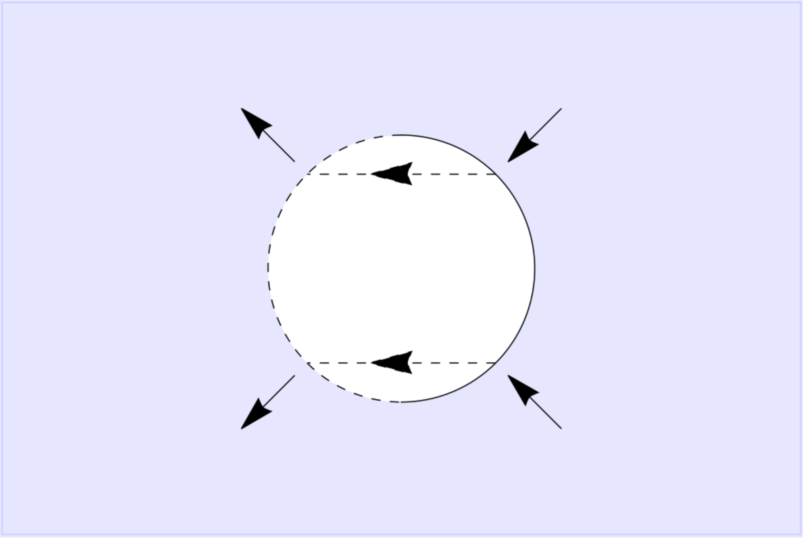

Figure 5.11: Schematic of the leakage due to the thin films. Liquid flows into the thin films at the front meniscus (shown by the solid curve). From here it flows under and above the bubble, and leaves at the rear meniscus (shown as a dashed curve).

5.9 Leakage effects

5.9.1 Governing equations

The kinematic boundary condition (5.1c) ignores the flow of liquid through the thin films above and below the bubble. As shown in Burgess & Foster (1990); Peng *et al.* (2015) one can adapt (5.1c) to include these effects, giving

$$\boldsymbol{n} \cdot \nabla p = -U_n(1 - h_0 \mathrm{Ca}_n^{2/3}) \qquad \text{on} \quad \partial\Omega_b, \tag{5.54}$$

where $h_0 \mathrm{Ca}_n^{2/3} \approx 1.337\mathrm{Ca}_n^{2/3}$ is the height of the thin films above and below the bubble (Bretherton, 1961). Physically this condition corresponds to a reduction in the average normal velocity along the advancing meniscus, because here there is fluid entering the thin film regions, and an increase in the normal velocity at the rear meniscus, where the fluid is exiting the thin film region (see figure 5.11).

To formulate our problem in complex variables we follow the model derivation in §5.3. We define a complex potential $w(z) + U_b z = -p(x, y) + \mathrm{i}\psi(x, y)$ and a mapping function f satisfying (5.4)–(5.6). In the ζ-plane, the boundary conditions (5.8) for

$W(\zeta) = w(z(\zeta))$ are modified to

$$\mathrm{Re}\left[\frac{-\zeta W'(\zeta)}{|z'(\zeta)|}\right] = -h_0 \mathrm{Ca}^{2/3} U_b^{5/3}\, \mathrm{Re}\left[\frac{-\zeta z'(\zeta)}{|z'(\zeta)|}\right]^{5/3} \quad \text{on} \quad |\zeta| = 1, \tag{5.55a}$$

$$p_b + \frac{3\mathrm{Ca}}{\epsilon}\,\mathrm{Re}[W(\zeta) + U_b z(\zeta)] = \frac{\pi\epsilon}{4}\kappa + \mathrm{Ca}^{2/3}\beta(U_n)U_n^{2/3} \quad \text{on} \quad |\zeta| = 1, \tag{5.55b}$$

$$W(\zeta) \sim \frac{(1-U_b)a}{\zeta} + o(1) \quad \text{as} \quad \zeta \to 0. \tag{5.55c}$$

Now we write

$$W(\zeta) = a(1-U_b)\left(\zeta + \frac{1}{\zeta}\right) + \mathrm{Ca}^{2/3} W_2(\zeta). \tag{5.56}$$

We note that the first term on the right-hand side of (5.56) is the solution of (5.8) without leakage. Then $W_2(\zeta)$ provides the $O(\mathrm{Ca}^{2/3})$ correction due to the leakage in the thin films. In both distinguished limits we consider in §5.4 we find that the bubble is circular to leading order, hence to simplify (5.55a) we approximate $z(\zeta) \sim 1/\zeta$, so (5.55a) becomes

$$\begin{aligned}\mathrm{Re}[\zeta W_2'(\zeta)] &= h_0 U_b^{5/3}\,\mathrm{Re}[\zeta]^{5/3},\\ &= U_b^{5/3}\,\mathrm{Re}[g(\zeta)],\end{aligned} \tag{5.57}$$

where

$$g(\zeta) = \sum_{n=0}^{\infty} g_{2n+1}\zeta^{2n+1} \tag{5.58}$$

is holomorphic in $|\zeta| < 1$, such that $\mathrm{Re}[g(\zeta)] = h_0\,\mathrm{Re}[\zeta]^{5/3}$ on $|\zeta| = 1$. The coefficients g_n are given by

$$g_n = \frac{h_0}{\pi}\int_{-\pi}^{\pi} \cos^{5/3}\theta \cos n\theta \,\mathrm{d}\theta. \tag{5.59}$$

Note that for even n this evaluates to 0, and hence only odd n appear in (5.58), with

$$g_{2n+1} = \frac{5h_0(-1)^{n+1}2^{1/3}\Gamma\left(n-\frac{1}{3}\right)}{9\Gamma\left(\frac{1}{3}\right)\Gamma\left(n+\frac{7}{3}\right)}. \tag{5.60}$$

We thus find that

$$W(\zeta) = a(1-U_b)\left(\zeta + \frac{1}{\zeta}\right) + \mathrm{Ca}^{2/3}U_b^{5/3}\sum_{n=1}^{\infty}\frac{g_{2n+1}}{2n+1}\zeta^{2n+1}, \tag{5.61}$$

satisfies the conditions (5.55c) and (5.57). It only remains to impose the dynamic boundary condition (5.55b), which can be expressed as

$$\kappa = \frac{4}{\epsilon\pi}(p_b - 1) + \frac{12\mathrm{Ca}}{\epsilon^2\pi}\,\mathrm{Re}\left[(2-U_b)a\zeta + U_b f(\zeta) + \mathrm{Ca}^{2/3}U_b^{5/3}\sum_{n=1}^{\infty}\frac{g_{2n+1}}{2n+1}\zeta^{2n+1}\right] - \frac{4\mathrm{Ca}^{2/3}U_b^{2/3}}{\pi\epsilon}\beta(\boldsymbol{i}\cdot\boldsymbol{n})|\boldsymbol{i}\cdot\boldsymbol{n}|^{2/3}, \quad (5.62)$$

on $|\zeta| = 1$, with

$$\kappa = -\frac{1}{|z'(\zeta)|}\left(1 + \mathrm{Re}\left[\frac{\zeta z''(\zeta)}{z'(\zeta)}\right]\right), \quad (5.63a)$$

$$\boldsymbol{i}\cdot\boldsymbol{n} = -\frac{\mathrm{Re}[\zeta z'(\zeta)]}{|z'(\zeta)|}. \quad (5.63b)$$

We compute numerical solutions to (5.55) in the same fashion as described in §5.7. In the next subsection we examine the effect the thin film leakage has on the shape of the bubble.

5.9.2 Results

In figure 5.12 we plot the aspect ratio, A, (5.52) versus δ, for solutions including leakage (solid curves) and not including leakage (dashed curves) with Ca fixed at the values used in experiments (see §5.8). As expected, including leakage effects contributes a small correction to the numerical solutions previously computed in §5.7. Furthermore, the correction predicts a larger increase in A for large δ than was found in §5.7. Although including leakage does not capture the magnitude of the increase in A seen in experiments (see figure 5.9), it may be a contributing factor.

5.10 The deformation of two bubbles

5.10.1 Governing equations

In this section, we extended the deformation calculation to the case of two bubbles in a Hele-Shaw cell subject to a uniform far-field velocity of unit dimensionless magnitude. Suppose we have two bubbles aligned in the direction of the flow with centres at positions $(0, 0)$ and $(\sigma, 0)$ in the (x, y)-plane, and dimensionless areas π and πR^2, respectively, with $\sigma > 1 + R$ (see figure 5.13). Using a similar approach to that taken in §5.2, one can show that the problem has reflectional symmetry about the x-axis, so the bubbles propagate in the x-direction at speeds U_1 and U_2, respectively.

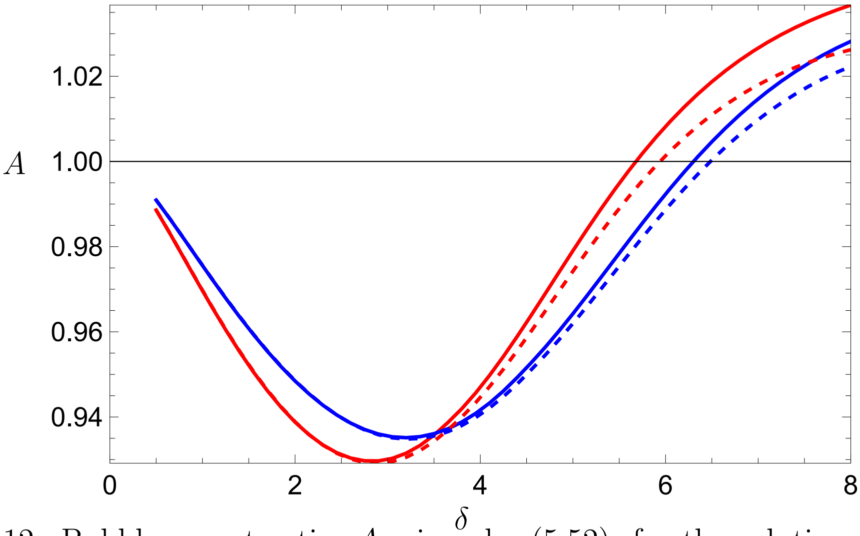

Figure 5.12: Bubble aspect ratio, A, given by (5.52), for the solution with leakage (solid) and without (dashed) as a function of δ with fixed $\mathrm{Ca} = 6.7 \times 10^{-4}$ (red), 3.3×10^{-4} (blue).

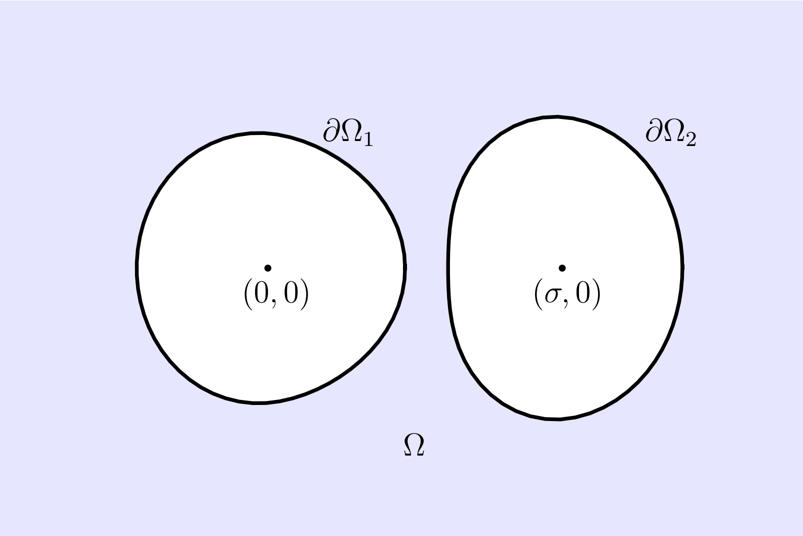

Figure 5.13: Schematic of the two-bubble deformation problem.

We assume that the deformations occur faster than the timescale, $1/|U_1 - U_2|$ for the relative motion of two bubbles, which means we can treat the deformations as quasi-steady.

Since the flow is governed by Laplace's equation we can formulate this as a problem for the complex potential $w(z) = -p + \mathrm{i}\psi$, where ψ is the streamfunction, and $z = x + \mathrm{i}y$. Then $w(z)$ is holomorphic in the region Ω outside the two bubbles and satisfies the boundary conditions

$$\begin{aligned}
\mathrm{Im}[w(z)] &= Q_1 + \mathrm{Im}[U_1 z] && \text{on} \quad \partial\Omega_1, && (5.64\text{a})\\
p_1 + \frac{3\mathrm{Ca}}{\epsilon}\mathrm{Re}[w(z)] &= 1 + \frac{\pi\epsilon}{4}\kappa_1 + \mathrm{Ca}^{2/3}U_1^{2/3}\beta(\boldsymbol{i}\cdot\boldsymbol{n})|\boldsymbol{i}\cdot\boldsymbol{n}|^{2/3} && \text{on} \quad \partial\Omega_1, && (5.64\text{b})\\
\mathrm{Im}[w(z)] &= Q_2 + \mathrm{Im}[U_2 z] && \text{on} \quad \partial\Omega_2, && (5.64\text{c})\\
p_2 + \frac{3\mathrm{Ca}}{\epsilon}\mathrm{Re}[w(z)] &= 1 + \frac{\pi\epsilon}{4}\kappa_2 + \mathrm{Ca}^{2/3}U_2^{2/3}\beta(\boldsymbol{i}\cdot\boldsymbol{n})|\boldsymbol{i}\cdot\boldsymbol{n}|^{2/3} && \text{on} \quad \partial\Omega_2, && (5.64\text{d})\\
w(z) &\sim z + o(1) && \text{as} \quad z \to \infty, && (5.64\text{e})
\end{aligned}$$

where κ_k, and p_k are the curvature and internal bubble pressure of the k^{th} bubble and the Q_k are *a priori* unknown constants. We will analyse this problem in distinguished limit 1 from §5.5, with $\mathrm{Ca} = O(\epsilon^3)$ and hence $\delta = O(1)$ as $\epsilon \to 0$.

5.10.2 Leading-order solution

The problem (5.64) was solved at leading order in ϵ in §3.2. From (5.64b) and (5.64d) we find that the leading-order curvature for each bubble is constant, so each bubble is a circle to leading order, of radius $R_1 = 1$ and $R_2 = R$, respectively. The leading-order complex potential $w(z) - z = W(\zeta)$, is given by (3.13), i.e.,

$$\begin{aligned}
W(\zeta) = \frac{(1-a^2)}{a}\sum_{n=1}^{\infty}\frac{X^n}{1-X^{2n}}\Bigg[&\left((U_1-1)\left(\frac{-a}{X}\right)^n - (U_2-1)\left(\frac{-X}{a}\right)^n\right)\zeta^n\\
&+\left((U_1-1)(-aX)^n - (U_2-1)\left(\frac{-X}{a}\right)^n\right)\zeta^{-n}\Bigg], \qquad (5.65)
\end{aligned}$$

and

$$\zeta = \frac{1-az}{z-a}, \qquad (5.66)$$

where a and X are constants given by (3.4a) and (3.4b), respectively. Then the leading-order bubble velocities are given by (3.20), i.e.,

$$f_1(U_2-1) - f_2(U_1-1) = -U_1 + \frac{U_1^{2/3}}{\delta}, \qquad (5.67\text{a})$$

$$f_1(U_1-1) - f_3(U_2-1) = -R^2U_2 + \frac{RU_2^{2/3}}{\delta}, \qquad (5.67\text{b})$$

where the f_k's are given by (3.19).

In the next subsections, we will use these results to find the corrections to the bubble shapes at $O(\epsilon)$.

5.10.3 Deformation calculation

5.10.3.1 Asymptotic expansions

We expand the curvatures and bubble pressures in powers of ϵ, as

$$\kappa_1 \sim 1 + \epsilon\kappa_{11} + \cdots\,, \tag{5.68a}$$

$$\kappa_2 \sim \frac{1}{R} + \epsilon\kappa_{21} + \cdots\,, \tag{5.68b}$$

$$p_1 \sim 1 + \frac{\pi\epsilon}{4} + \epsilon^2 p_{12}\cdots\,, \tag{5.68c}$$

$$p_2 \sim 1 + \frac{\pi\epsilon}{4R} + \epsilon^2 p_{22} + \cdots\,. \tag{5.68d}$$

Note that for completeness one should also expand the complex potential, $w(z)$, and the bubble velocities, U_1 and U_2, as asymptotic series in powers of ϵ. However, to find the first-order shape correction we only need the leading-order solutions (5.65) and (5.67) and so for ease of notation we do not include an additional subscript 0 for these variables.

5.10.4 Deformation of the first bubble

The dynamic boundary condition (5.64b) at $O(\epsilon^2)$ gives

$$\kappa_{11} = \frac{4p_{12}}{\pi} + \frac{12\delta^3\eta^3}{\pi}\,\mathrm{Re}\left[z + W\left(\frac{1-az}{z-a}\right)\right] - \frac{4\delta^2\eta^2U_1^{2/3}}{\pi}\,\mathrm{Re}[b(z)], \tag{5.69}$$

on $|z| = 1$, where b is again the function defined by (5.25)–(5.26). We define polar coordinates centred at $(0,0)$, so the bubble surface is given by $r = 1 + \epsilon g_1(\theta)$, where θ is the polar angle. The dynamic boundary condition (5.69) in polar coordinates is given by

$$-g_1'' - g_1 = \frac{4p_{12}}{\pi} + \frac{12\delta^3\eta^3}{\pi}\,\mathrm{Re}\left[\mathrm{e}^{\mathrm{i}\theta} + W\left(\frac{1-a\mathrm{e}^{\mathrm{i}\theta}}{\mathrm{e}^{\mathrm{i}\theta}-a}\right)\right] - \frac{4\delta^2\eta^2U_1^{2/3}}{\pi}\beta(\cos\theta)|\cos\theta|^{2/3}. \tag{5.70}$$

We determine p_{12} by enforcing conservation of bubble area, i.e.,

$$\int_0^{2\pi} g_1\,\mathrm{d}\theta = -\int_0^{2\pi}\kappa_{11}\,\mathrm{d}\theta = 0. \tag{5.71}$$

We solve (5.70) by expanding g_1 as the Fourier cosine series

$$g_1(\theta) = \frac{c_0}{2} + \sum_{n=1}^{\infty} c_n \cos n\theta. \tag{5.72}$$

By area conservation (5.71) we find that $c_0 = 0$. We further fix the centroid of the bubble to be at the origin, which corresponds to $c_1 = 0$. The remaining coefficients are determined by

$$c_n = \frac{1}{(n^2-1)} \int_0^{2\pi} \frac{12\delta^3\eta^3}{\pi^2} \operatorname{Re}\left[W\left(\frac{1-a\mathrm{e}^{\mathrm{i}\theta}}{\mathrm{e}^{\mathrm{i}\theta}-a}\right)\right] \cos n\theta \,\mathrm{d}\theta - \frac{4\delta^2\eta^2 U_1^{2/3} b_n}{\pi(n^2-1)}, \tag{5.73}$$

where b_n is given by (5.26). This then determines the first-order shape correction of the first bubble $\partial\Omega_1$.

5.10.5 Deformation of the second bubble

We proceed similarly with the second bubble, the dynamic boundary condition (5.64d) at $O(\epsilon^2)$ gives

$$\kappa_{21} = \frac{4p_{12}}{\pi} + \frac{12\delta^3\eta^3}{\pi} \operatorname{Re}\left[z + W\left(\frac{1-az}{z-a}\right)\right] - \frac{4\delta^2\eta^2 U_2^{2/3}}{\pi} \beta(\boldsymbol{i}\cdot\boldsymbol{n})|\boldsymbol{i}\cdot\boldsymbol{n}|^{2/3}, \tag{5.74}$$

on $|z-\sigma| = R$. Now we define polar coordinates centred at $(\sigma, 0)$, so the bubble surface is given by $r = R + \epsilon g_2(\theta)$, where g_2 is written as the Fourier cosine series

$$g_2(\theta) = \frac{d_0}{2} + \sum_{n=1}^{\infty} d_n \cos n\theta. \tag{5.75}$$

By area conservation we find that $d_0 = 0$. Again, we fix the centroid of the bubble to be at $(\sigma, 0)$, which corresponds to $d_1 = 0$. The remaining coefficients are determined by

$$d_n = \frac{R^2}{(n^2-1)} \int_0^{2\pi} \frac{12\delta^3\eta^3}{\pi^2} \operatorname{Re}\left[W\left(\frac{1-a(\sigma+R\mathrm{e}^{\mathrm{i}\theta})}{(\sigma+R\mathrm{e}^{\mathrm{i}\theta})-a}\right)\right] \cos n\theta \,\mathrm{d}\theta - \frac{4R^2\delta^2\eta^2 U_1^{2/3} b_n}{\pi(n^2-1)}. \tag{5.76}$$

This then determines the first-order shape correction of the second bubble $\partial\Omega_2$.

5.10.6 Results

5.10.6.1 Identical bubbles $R = 1$

In figure 5.14 we show example solutions for the bubble shapes, calculated using (5.72) and (5.75), with $\delta = 2.86$, and $\epsilon = 0.027$, at different separations, σ, alongside experimental images (taken by Katie Wu, Princeton University) under the same flow conditions. We observe good agreement between theory and experiments. The bubble in front flattens in the direction of motion (left to right) and the bubble behind elongates. In the theoretical plots, we use σ as a proxy for time, because we assume the deformations are quasi-steady and at present we have no theoretical prediction for the relative bubble velocity.

To quantify these results we define the aspect ratio in the same manner as (5.52), namely

$$A_k = \frac{2R_k + \epsilon(g_k(0) + g_k(\pi))}{2R_k + 2\epsilon g_k(\pi/2)} \sim 1 + \frac{\epsilon}{2R_k}(g_k(0) + g_k(\pi) - 2g_k(\pi/2)), \qquad (5.77)$$

for $k \in \{1, 2\}$. In figure 5.15 we plot the bubble aspect ratios, $A_{1,2}$, versus bubble separation, σ, for a fixed value of δ. We observe that, as the bubbles become close, the disparity in aspect ratio increases, with the bubble in front becoming more flattened, while the rear bubble has a more pronounced elongation. In the limit as $\sigma \to \infty$ both bubble aspect ratios tend to the asymptotic prediction (see §5.5) for the aspect ratio of an isolated bubble. There is good agreement between the predicted and experimentally measured aspect ratio A_2 of the front bubble, however, there is a constant offset of ≈ 0.06, which induces an $\approx$ 6–10% error between the theory and experiments. There is a discrepancy between theory and experiments for the aspect ratio A_1 of the rear bubble. In the experiments, A_1 is approximately constant, but our model predicts it to be a monotonically decreasing function, and generally under-predicts the elongation of the rear bubble. In the experiments the two bubbles become very close and, in this limit, we expect the theory may break down, because of the three-dimensional effects in the fluid flow between the two bubbles. Furthermore, we do not incorporate the full Burgess & Foster (1990) boundary condition on the bubble surface, specifically the dependence of β_2 on the ratio of $\mathrm{Ca}_n^+/\left(-\mathrm{Ca}_n^-\right)$ (see §5.8 and §2.2.4), or leakage effects due to the thin films above and below the bubbles (see §5.9).

Previously, in §3.4 we found that, if $R = 1$, the bubbles travel at the same velocity at leading order. Then in §5.8 we found that if the bubble is flattened in the direction of motion then the leading-order solution for the bubble velocity over-predicts the

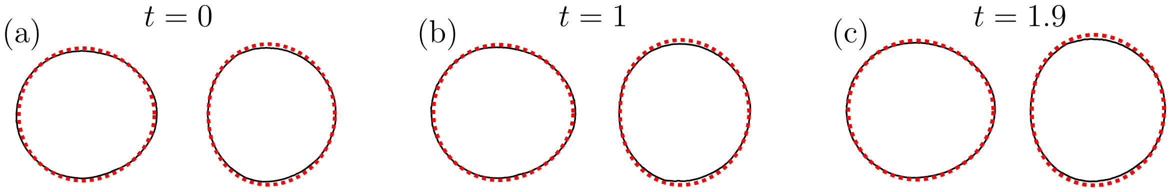

Figure 5.14: Experimental bubble shapes (black solid), asymptotic solution (5.72) and (5.75) (red dashed) dashed for $\delta = 2.86$ and $\sigma =$ (a) 2.68, (b) 2.56, (c) 2.43. The corresponding different dimensionless times $t = \hat{t}\hat{U}/\hat{R}_1$ are shown above for the experiments. The background flow is from left to right. In the experiments $\epsilon = 0.027$, and $\text{Ca} = 3.3 \times 10^{-4}$.

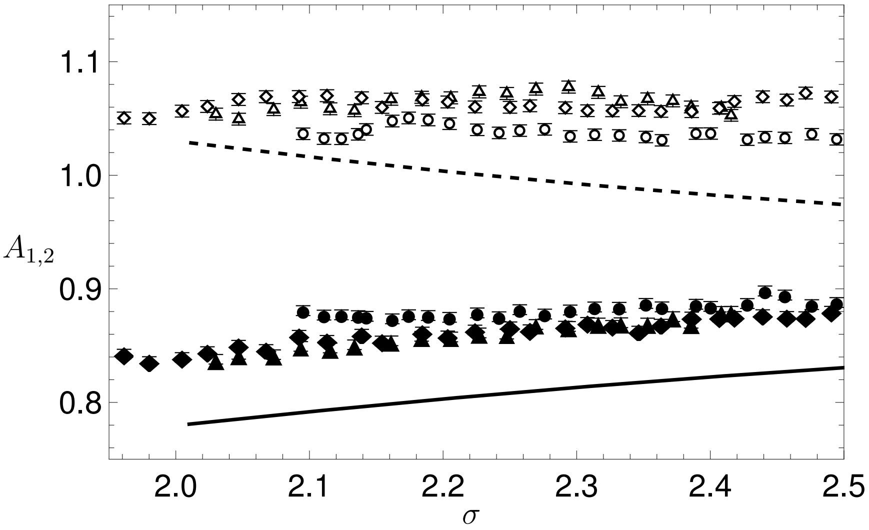

Figure 5.15: The bubble aspect ratios, $A_{1,2}$, versus separation, σ, for the front bubble (solid curve and points) and the rear bubble (dashed curve and open points), with $\delta = 2.86$ and $\epsilon = 0.027$ (red). The points show experimental measurements and the curves are the asymptotic predictions (5.52). The different marker shapes refer to different experiments. In the experiments $\epsilon = 0.027$, and $\text{Ca} = 3.3 \times 10^{-4}$.

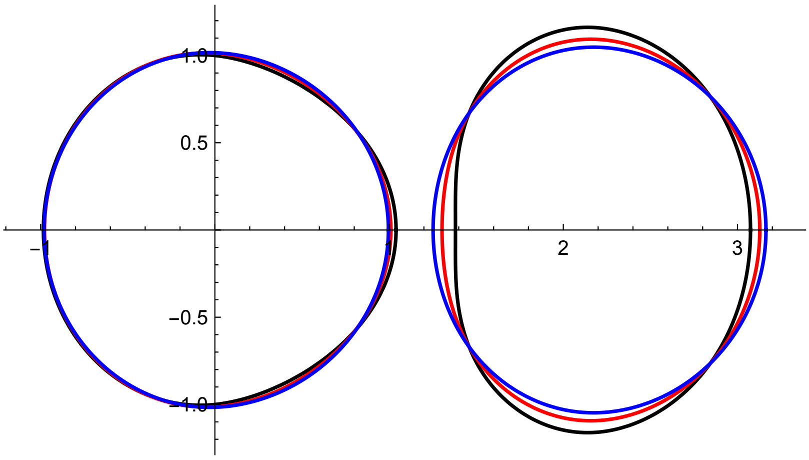

Figure 5.16: Example solutions for the bubble shapes given by (5.72) and (5.75) with, $R = 1$, $\epsilon = 0.034$, $\sigma = 2.2$ and $\delta = 2$ (blue), 2.5 (red) 3 (black).

bubble velocity and *vice versa* if the bubble is elongated. Hence, applying this rule of thought here we expect that the velocity of the bubble at the front is over-predicted by (5.67), while the velocity of the bubble behind is under-predicted by (5.67). Thus, the bubble behind travels faster than the bubble in front, which then leads to bubbles of equal sizes colliding, as is seen in the experimental observations in figure 5.14, behaviour that was not captured by the leading-order model studied in §3.4. Similar behaviour has been observed experimentally and computationally for approximately spherical bubbles rising under buoyancy (Manga & Stone, 1993). The leading bubble flattens in the direction of motion and the bubble behind elongates, allowing it to catch the bubble in front.

In figure 5.16 we plot the solutions for the bubble shapes, given by (5.72) and (5.75), for different values of δ. In agreement with figure 5.14, we observe that the bubble in front flattens in the direction of motion and the rear bubble elongates. Furthermore, we observe that the magnitude of the deformations increases as δ increases.

5.10.6.2 Bubbles of different radii

In Chapter 2 we found that larger bubbles travel faster than smaller bubbles, and in Chapter 3 we derived conditions under which two bubbles of different radii collide in finite time. Here, we present suggestions of a further mechanism where two bubbles can collide, with a smaller bubble catching a larger bubble.

We show example solutions for the bubble shapes given by (5.72) and (5.75) alongside experimental images with, $R = 1.23$ and $\delta = 2.55$ in figures 5.17(a–c) and

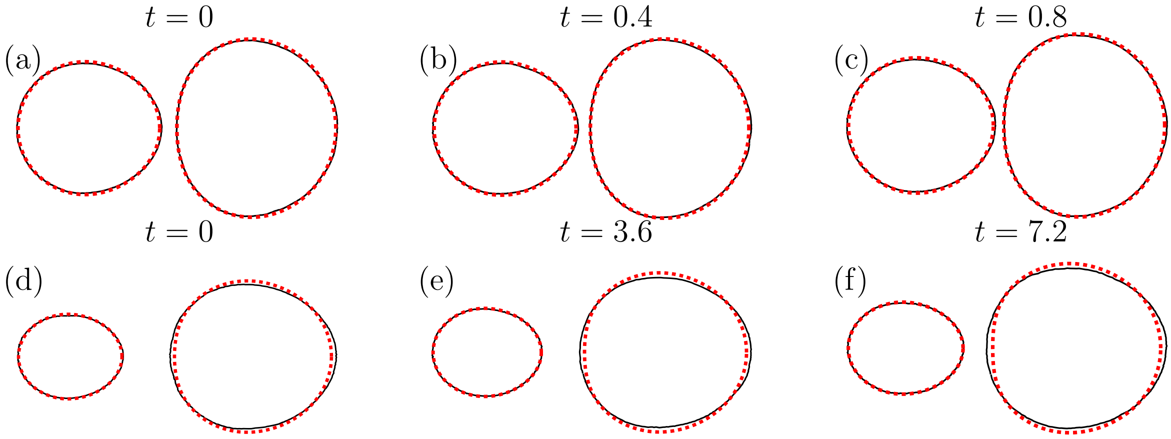

Figure 5.17: Experimental bubble shapes (black solid), asymptotic solution (5.72) and (5.75) (red dashed) for (a–c) $R = 1.23$, $\delta = 2.55$, $\epsilon = 0.03$, $\mathrm{Ca} = 3.3 \times 10^{-4}$ and $\sigma =$ (a) 2.39, (b) 2.34, (c) 2.28, (d–f) $R = 1.65$, $\delta = 1.94$, $\epsilon = 0.05$, $\mathrm{Ca} = 6.6 \times 10^{-4}$ and $\sigma =$ (d) 3.45, (e) 3.23, (f) 2.94. The corresponding different dimensionless times $t = \hat{t}\hat{U}/\hat{R}_1$ are shown above for the experiments. The background flow is from left to right.

$R = 1.65$ and $\delta = 1.94$ in figures 5.17(d–f). Similarly to the examples of the bubbles with the same leading-order radius (see figures 5.14 and 5.16) the leading bubble flattens in the direction of motion, whereas the rearmost bubble behind elongates. To quantify this observation, we plot the bubble aspect ratios $A_{1,2}$ versus separation, σ in figure 5.18. We observe good agreement between theory and experiments, in particular, we correctly predict that $A_1 > A_2$. Again, there is a discrepancy between the experimentally measured aspect ratios and theoretical predictions, which we attribute to the same reasons as discussed in §5.10.6.1. These results hint that it is possible for the smaller bubble to catch the larger one, as is observed experimentally in figure 5.17. The velocity of the larger bubble which flattens is over-predicted by (5.67), and the velocity of the smaller rearmost bubble which is elongated is under-predicted by (5.67). This could allow for a region of parameter space in which a smaller bubble can catch a larger one. To establish this result theoretically one would need to find the perturbation to the bubble speeds, for example by performing a complex variable analysis similar to §5.5. We leave such analysis for future work.

5.11 Conclusions

In this chapter, we develop a model for the flow of a bubble in a Hele-Shaw cell with a uniform background velocity and an *a priori* unknown shape. The model depends on two dimensionless parameters: the bubble aspect ratio ϵ and the capillary number Ca,

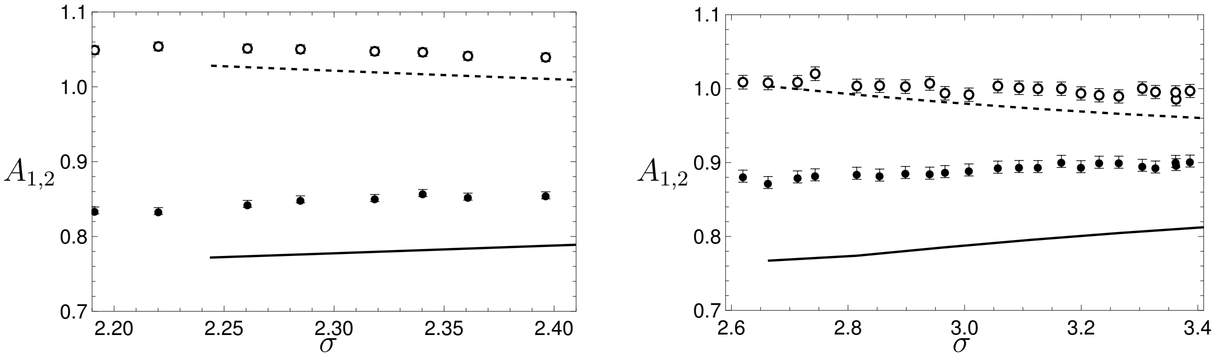

Figure 5.18: The bubble aspect ratios, $A_{1,2}$, versus separation, σ, for the front bubble (solid curve and points) and the rear bubble (dashed curve and open points), with (a) $R = 1.23$, $\delta = 2.55$ and $\epsilon = 0.03$, $\mathrm{Ca} = 3.3 \times 10^{-4}$ (b), $R = 1.65$ $\delta = 1.94$ and $\epsilon = 0.05$, $\mathrm{Ca} = 6.6 \times 10^{-4}$. The points show experimental measurements and the curves are the asymptotic predictions (5.52).

both of which are assumed to be small. We identify two asymptotic distinguished limits in which either (i) $\mathrm{Ca} = O(\epsilon^3)$ or (ii) $\mathrm{Ca} = O(\epsilon^2)$ as both ϵ and Ca tend to zero. In either case, the bubble is circular to leading order, and we obtain the first corrections to both the bubble velocity and the bubble shape. In limit (i), we reproduce the leading-order solution (2.16) found in §2.2, which determines the bubble velocity as a function of the Bretherton parameter $\delta \propto \mathrm{Ca}^{1/3}/\epsilon$, and we find that the bubble flattens in the direction of motion as δ increases from zero. In limit (ii), we find that the bubble travels at approximately twice the background flow speed, and predict that the bubble switches from being flattened to being elongated in the flow direction with increasing δ.

Numerical simulations are then shown to agree with the theoretical predictions and to reproduce the non-monotonicity seen in the experiments (see figure 5.9). The aspect ratio from the numerical simulations agrees well with the experiments for small values of δ; however, for larger values of δ the bubbles in the experiments have more pronounced deformations than the theory predicts. This is theorised to be due to not accounting for the variation of the Bretherton coefficients in (5.2) due to the variation of the normal direction at the rear meniscus or the additional leakage of fluid through the thin liquid films above or below the bubble. Extending the model to include the latter, we observe an increase in the bubble aspect ratio, A, (5.52) for large δ; the increase is still not enough to capture the experiments, but it improves the agreement, confirming that this effect may be one of the contributing factors.

Finally, we extend the deformation calculation to two aligned bubbles in a Hele-Shaw cell with a uniform background flow. We consider the distinguished limit where

$\mathrm{Ca} = O(\epsilon^3)$, in which the bubbles are circular to leading order, and the leading-order solution is found in Chapter 3. If the bubbles are the same size, we observe that the bubble in front flattens in the direction of motion, while the bubble behind elongates. In the leading-order solution found in §3.4, two bubbles of the same size travel at the same velocity, but in §5.7 we find that a flattened bubble travels slower than the leading-order prediction, and an elongated bubble travels faster. Hence, we find that the bubble behind travels faster and will collide with the bubble in front: behaviour that is impossible when considering only the leading-order solution. Furthermore, this same behaviour is seen in systems of two bubbles with a larger bubble in front, suggesting that we could see a smaller bubble catch a larger one. To establish this result theoretically requires one to find the perturbation to the bubble speeds, for example by performing an analysis similar to that in §5.5, such an analysis will be the focus of future work.

Chapter 6

The motion of a bubble in a non-uniform Hele-Shaw flow

6.1 Introduction

In all previous chapters we have only considered a uniform background flow. While this flow is common in microfluidic systems, there are many other physically relevant scenarios, such as stagnation-point flow, or flow between an injection source and sink.

We begin in §6.2 by extending the results of §2.2 to a general outer flow, again using complex variable methods. We find that the bubble goes with the flow and the centre of a bubble will travel along a streamline of the background flow. Thus the bubble acts like a tracer particle, that does not travel a the speed of the background flow. Instead, the relative speed of the bubble has the same form as that found for an isolated bubble, (2.16), when the bubble speed is measured relative to the local flow speed.

Examples of the solution are presented in §6.3, for the experimentally relevant regimes of stagnation-point flow, and flow driven by point sources and sinks. The former can be used to model flow in a T-junction and the latter to model flow between injection sources and sinks.

In §6.4 we use the methodology to derive an approximate equation of motion for a bubble in more complicated scenarios, such as those including walls or obstacles. We then compare the approximate solution with the full analytical solution in two examples. First, we explore the dynamics of a bubble near a stagnation-point on an impermeable wall. Then, we consider the flow of a bubble around a circular obstacle. In both cases, the bubble deviates noticeably from the streamlines of the background flow only when it is close very to the wall or the obstacle.

6.2 Motion of a bubble in an infinite domain

6.2.1 Governing equations

We consider a bubble that is subject to a non-uniform flow with a characteristic background velocity $\hat{U}$. We non-dimensionalise the system by scaling lengths with a typical bubble radius $\hat{R}$, velocities with $\hat{U}$, the fluid pressure $\hat{p}$ with $12\hat{\mu}\hat{U}\hat{R}/\hat{h}^2$, the pressure inside the bubble, $\hat{p}_b$ with $2\hat{\gamma}/\hat{h}$, and time, $\hat{t}$ with $\hat{R}/\hat{U}$. Dimensionless variables are denoted without hats. Again there are two dimensionless parameters associated with our problem, the aspect ratio, ϵ, and the capillary number, Ca, both of which are assumed to be small. Specifically, we consider the distinguished limit in which $\mathrm{Ca} = O(\epsilon^3)$ as $\epsilon \to 0$, so the viscous lubrication pressure balances the corrections to the pressure drop across the menisci calculated by Bretherton (1961). In this regime, the bubble remains circular to leading order (see Chapter 2).

Suppose that, without the bubble present, we have a background flow with (dimensionless) complex potential $f(z)$ where $z = x + \mathrm{i}y$. If we denote the *a priori* unknown position of the bubble centre by $z = c(t)$, then the complex representation of the bubble velocity $\mathcal{U}_b = U_b + \mathrm{i}V_b = \dot{c}$, where the dot represents differentiation with respect to t. The complex potential $w(z)$ for the flow including a bubble of unit radius at position $z = c$ therefore satisfies:

- $\mathrm{Im}[w(z)] = q + \mathrm{Im}\left[\bar{\dot{c}}(z-c)\right]$ on $|z-c| = 1,$ (6.1a)
- $w(z)$ has the same singularities as $f(z)$ in $|z-c| > 1,$ (6.1b)

where q is an arbitrary real constant and the over-bar represents complex conjugation. The first condition (6.1a) is the kinematic boundary condition on the bubble surface, while (6.1b) ensures that no external singularities are caused when we insert the bubble in the flow.

Assuming we have evaluated the complex potential $w(z)$ satisfying (6.1), we find an ordinary differential equation for $c(t)$ by performing an effective net force balance on the bubble (2.19), which leads to

$$\frac{1}{\mathrm{i}\pi}\oint_{|z-c|=1} w(z)\,\mathrm{d}z = \dot{c}\left(-1 + \frac{1}{\delta|\dot{c}|^{1/3}}\right). \tag{6.2}$$

Here, δ is the *Bretherton parameter* (2.13), defined by

$$\delta = \frac{1}{\eta}\frac{\mathrm{Ca}^{1/3}}{\epsilon} = O(1), \tag{6.3}$$

where the numerical constant $\eta \approx 0.893$ given by (5.20), incorporates the coefficients calculated by Bretherton for the pressure drops across the advancing and retreating menisci (Bretherton, 1961).

6.2.2 Equation of motion

For scenarios of interest, $f(z)$ will have no singularities in $|z-c| \leq 1$, (since we assume that the bubble cannot intersect with any external fluid sources, sinks, or obstacles). Then we can write $w(z) = f(z) + W(z)$, where

- $\mathrm{Im}[W(z)] = \mathrm{Im}\left[\bar{\dot{c}}(z-c) - f(z)\right]$ on $|z-c| = 1$, (6.4a)
- $W(z)$ is holomorphic and bounded in $|z-c| > 1$. (6.4b)

Here, without loss of generality, we have set $q = 0$, which means that $W(z)$, although bounded, does not in general tend to zero as $z \to \infty$.

Since $(z-c)(\overline{z}-\overline{c}) = 1$ on the bubble surface, we can rewrite the kinematic boundary condition (6.4a) as

$$\mathrm{Im}[W(z)] = \mathrm{Im}\left[\overline{f}\left(\overline{c} + \frac{1}{z-c}\right) - \frac{\dot{c}}{z-c}\right] \qquad \text{on} \quad |z-c| = 1, \tag{6.5}$$

where $\overline{f}(z) = \overline{f(\overline{z})}$ is the conjugate function to f. Recall that all the singularities of $f(z)$ are assumed to be in $|z-c| > 1$, so the term in the square brackets on the right-hand side of (6.5) is holomorphic in $|z-c| > 1$ and we have the solution

$$w(z) = f(z) + \overline{f}\left(\overline{c} + \frac{1}{z-c}\right) - \frac{\dot{c}}{z-c}, \tag{6.6}$$

up to an irrelevant constant.

Evaluating the force balance (2.19) gives

$$\frac{1}{\mathrm{i}\pi}\oint_{|z-c|=1}\left[f(z) + \overline{f}\left(\overline{c} + \frac{1}{z-c}\right) - \frac{\dot{c}}{z-c}\right]\mathrm{d}z = \dot{c}\left(-1 + \frac{1}{\delta|\dot{c}|^{1/3}}\right). \tag{6.7}$$

By Cauchy's Residue Theorem, the first term in the integral in (6.7) evaluates to 0, and the last term evaluates to $-2\dot{c}$. To manipulate the middle term of the integral into a suitable form for Cauchy's Residue Theorem, we take the conjugate of (6.7) to obtain

$$\frac{1}{\mathrm{i}\pi}\oint_{|z-c|=1}\frac{f(z)}{(z-c)^2}\,\mathrm{d}z = \bar{\dot{c}}\left(1 + \frac{1}{\delta|\dot{c}|^{1/3}}\right). \tag{6.8}$$

The left-hand side can now be evaluated to obtain the equation of motion

$$2\overline{f'(c)} = \dot{c}\left(1 + \frac{1}{\delta|\dot{c}|^{1/3}}\right). \tag{6.9}$$

Since the velocity of the background flow is given by $u - \mathrm{i}v = f'(z)$, equation (6.9) implies that the bubble goes with the flow, with its velocity proportional to the background velocity evaluated at the centre of the bubble. Thus, the bubble travels along a streamline of the flow that would exist if the bubble were not present. Unlike a tracer particle, however, the bubble moves at a different speed from the background flow.

By taking the absolute value of each side of (6.9), we obtain the universal relation

$$2u_f = u_b + u_b^{2/3}, \tag{6.10}$$

between $u_f = \delta^3|f'(c)|$ and $u_b = \delta^3|\dot{c}|$, which are the dimensionless speeds of the background flow and the bubble at $z = c$, respectively, when we choose the characteristic velocity $\hat{U}$ such that $\delta = 1$. We plot the prediction (6.10) for the bubble speed versus the background flow speed in figure 6.1. We observe that u_b is a monotonic increasing function of u_f. As $u_f \to 0$ we find that $u_b \sim (2u_f)^{3/2}$, while $u_b \sim 2u_f$ as $u_f \to \infty$. Thus the Taylor–Saffman prediction (Taylor & Saffman, 1959), that a circular bubble travels at twice the background flow speed, is recovered when the background flow is sufficiently fast.

If we define the relative speed of the bubble compared to the background velocity at the bubble centre as $U_{\mathrm{rel}} = u_b/u_f = |\dot{c}| \,/\, |f'(c)| > 0$, then (6.10) may be expressed in the form

$$\frac{U_{\mathrm{rel}}^{2/3}}{2 - U_{\mathrm{rel}}} = u_f^{1/3} = \delta\,|f'(c)|^{1/3} =: \Delta(c). \tag{6.11}$$

First consider the simplest non-trivial case of a uniform background flow, which can be used to describe pressure-driven flow through a Hele-Shaw channel (see, for example, Beatus *et al.*, 2006; Keeler *et al.*, 2019). The dimensionless complex potential is $f(z) = z$, so $f'(z) \equiv 1$ and (6.11) reduces to

$$\frac{U_b^{2/3}}{2 - U_b} = \delta, \tag{6.12}$$

where now $|\dot{c}| = U_b$ is the bubble speed relative to the constant background flow speed. The relation (6.12) was obtained is equivalent to (2.16) for a bubble in a uniform flow and was extensively validated experimentally. The generalised relation (6.11) is equivalent to (6.12) when the bubble velocity is measured relative to the *local* flow speed and $\Delta(c)$ is interpreted as the *local* value of the Bretherton parameter, based on the background flow velocity evaluated at the bubble centre $z = c$.

We will now apply (6.9) to two examples relevant to microfluidic devices: stagnation-point flow, and flow due to a point source.

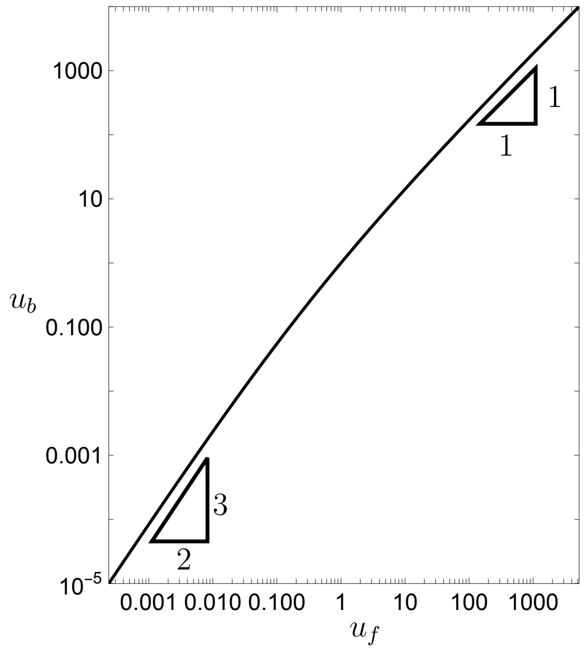

Figure 6.1: The normalised speed of the bubble, u_b, versus the normalised speed of the background flow, u_f, on log–log axes. When $u_f \to 0$, $u_b \sim (2u_f)^{3/2}$ and as $u_f \to \infty$, $u_b \sim 2u_f$.

6.3 Examples

6.3.1 Stagnation-point flow

Next, we consider stagnation-point flow, which has the complex potential $f(z) = z^2$, with appropriate non-dimensionalisation. This background velocity can be used to simulate the flow in a T-junction or a cross-junction, which are common components in microfluidic systems (see, for example, Tan *et al.*, 2008; Leshansky & Pismen, 2009; Garstecki *et al.*, 2006). In this case, (6.9) becomes

$$4\overline{c} = \dot{c}\left(1 + \frac{1}{\delta|\dot{c}|^{1/3}}\right). \tag{6.13}$$

A streamline in the positive quadrant (without loss of generality) is given by the hyperbola $xy = a^2$ for some constant $a \geq 0$. The path followed by a bubble can thus be parametrised by

$$c(t) = a\left(\mathrm{e}^{\phi(t)} + \mathrm{i}\mathrm{e}^{-\phi(t)}\right), \tag{6.14}$$

where

$$\dot{\phi}\left[1 + \frac{1}{\delta a^{1/3}|\dot{\phi}|^{1/3}(2\cosh 2\phi)^{1/6}}\right] = 4. \tag{6.15}$$

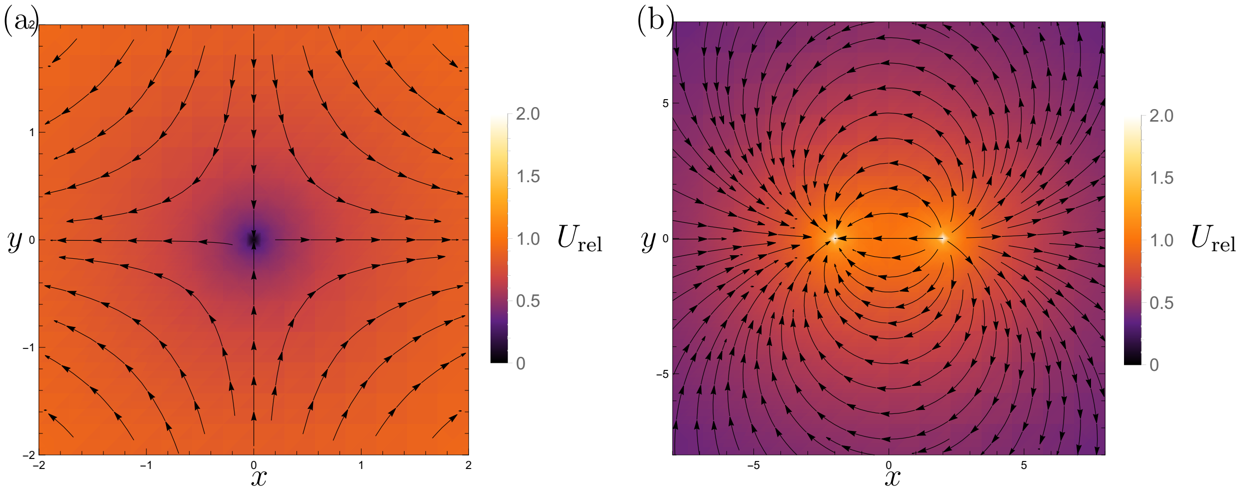

Figure 6.2: Trajectories of the bubble centre, c, in (a) a stagnation-point flow with $\delta = 0.5$, (b) flow between a point source and sink with $s = 2$ and $\delta = 1$. The colour bars show the value of U_{rel}, given by (6.11).

In figure 6.2(a) we overlay trajectories of (6.13) on a density plot of the relative bubble speed U_{rel}, given by (6.11). We observe that $U_{\mathrm{rel}} \to 2$ as $|c| \to \infty$, i.e., where the background flow is very fast, the bubble travels approximately twice as fast. On the other hand, $U_{\mathrm{rel}} \to 0$ as $|c| \to 0$, i.e., as the background flow speed approaches zero, the bubble speed decreases to zero even more rapidly. In particular, for a bubble travelling along $x = 0$, the bubble centre will approach the origin but not reach it in finite time.

6.3.2 Point source and sink

In many microfluidic devices, fluid is injected into the Hele-Shaw cell via a syringe and then removed similarly at some point downstream (Gaillard *et al.*, 2021). The resulting flow can be modelled using a point source and sink of equal strength some distance apart. Without loss of generality, we may place the singularities at $z = \pm s \in \mathbb{R}$, so the complex potential for the flow is given by

$$f(z) = \log(z - s) - \log(z + s), \tag{6.16}$$

with suitable non-dimensionalisation. For this system, (6.9) becomes

$$2\left(\frac{1}{\overline{c} - s} - \frac{1}{\overline{c} + s}\right) = \dot{c}\left(1 + \frac{1}{\delta|\dot{c}|^{1/3}}\right). \tag{6.17}$$

The streamlines are circular arcs on which

$$c(t) = h\mathrm{i} + \sqrt{h^2 + s^2}\,\mathrm{e}^{\mathrm{i}\phi(t)}, \tag{6.18}$$

for constant $h \in \mathbb{R}$, and where $\phi(t)$ satisfies

$$\frac{2s}{(h^2+s^2)(h+\sqrt{h^2+s^2}\sin\phi)} = \dot{\phi}\left[1+\frac{1}{\delta|\dot{\phi}|^{1/3}(h^2+s^2)^{1/6}}\right]. \tag{6.19}$$

In figure 6.2(b) we overlay trajectories of (6.17) on a density plot of U_{rel}. In contrast with the stagnation-point example, now the background flow velocity tends to zero far from the source–sink pair, so likewise U_{rel} tends to zero and hence the bubble velocity tails off even more rapidly in the far field. We also observe that $U_{\mathrm{rel}} \to 2$ as $c \to \pm s$, so the bubble travels faster than the background flow in a neighbourhood of the source or sink.

6.4 Flows with boundaries

6.4.1 Approximate solutions

So far, all of our solutions are for a bubble in an infinite Hele-Shaw cell. However, we can use the methodology developed in §6.2.2 to derive an approximate equation of motion for a bubble in a more complicated domain, including cell walls or obstacles. We construct the approximate solution as follows:

1. find the complex potential $f(z)$ of the flow without the bubble present;
2. use (6.9) as an approximate equation of motion for the bubble.

This approximation is equivalent to assuming that the image contributions due to the presence of the bubble are negligible, so the bubble follows but does not affect the streamlines of the background flow. Similar approximations are employed to study the dynamics of a large number of bubbles in a uniform background flow using dipole models (see, for example, Beatus *et al.*, 2006, 2012; Shen *et al.*, 2014).

The advantage of such an approximation is that one only needs to find the complex potential of the background flow once, from which the equation of motion for the bubble is found once and for all. In contrast, for the full solution, one needs to calculate the complex potential in the evolving multiply-connected domain at each time step, which is much more laborious.

In the next two subsections, we will compare the approximate solution described above with two scenarios in which we can find the full solution analytically. First, we consider a stagnation-point flow with an impermeable wall. Then we consider the flow of a bubble around a circular obstacle.

6.4.2 Bubble near a stagnation-point on a wall

6.4.2.1 Solution

Returning to the stagnation-point flow introduced in §6.3.1, we now include an impermeable wall along the real axis through the stagnation point. This setup provides a simple model for a bubble passing through a T-junction in a microfluidic device. The presence of the wall does not affect the background complex potential $f(z) = z^2$, so the approximate equation of motion for the bubble, as described in §6.4, is still given by (6.13).

To find the full solution, we seek a complex potential $w(z)$ which is a holomorphic function that satisfies the boundary conditions

$$\operatorname{Im}[w(z)] = q + \operatorname{Im}\left[\overline{\mathcal{U}}_b(z-c)\right] \qquad \text{on} \quad |z-c| = 1, \tag{6.20a}$$

$$\operatorname{Im}[w(z)] = 0 \qquad \text{on} \quad \operatorname{Im}(z) = 0, \tag{6.20b}$$

$$w(z) \sim z^2 \qquad \text{as} \quad z \to \infty, \tag{6.20c}$$

where the complex bubble velocity is again denoted by $\mathcal{U}_b = \dot{c}$. We adapt the approach used in §2.3 by conformally mapping the solution domain, Ω, onto a concentric annulus (see figure 6.3), where the problem becomes solvable with standard techniques. Following the mapping

$$\zeta = f(z) = \frac{z - \alpha - \mathrm{i}\sqrt{\beta^2 - 1}}{z - \alpha + \mathrm{i}\sqrt{\beta^2 - 1}}, \tag{6.21}$$

where $c = \alpha + \mathrm{i}\beta$, the solution domain in the ζ-plane is $A = \{\zeta : X < |\zeta| < 1\}$, where

$$X = \beta - \sqrt{\beta^2 - 1}. \tag{6.22}$$

If we write the complex potential in the form $w(z) = z^2 + W\big(f(z)\big)$, then $W(\zeta)$ is a holomorphic function on the annulus A and satisfies the boundary conditions

$$\operatorname{Im}[W(\zeta)] = 0 \qquad \text{on} \quad |\zeta| = 1, \tag{6.23a}$$

$$\operatorname{Im}[W(\zeta)] = q + \operatorname{Im}\left[\rho\left(\frac{1+\zeta}{1-\zeta}\right) + \nu\left(\frac{1+\zeta}{1-\zeta}\right)^2\right] \qquad \text{on} \quad |\zeta| = X, \tag{6.23b}$$

where $\rho = (2\alpha - \overline{\mathcal{U}}_b)\mathrm{i}\sqrt{\beta^2 - 1}$ and $\nu = \beta^2 - 1$. We expand $W(\zeta)$ as a Laurent series to obtain

$$W(\zeta) = -\sum_{n=1}^{\infty} \frac{X^{2n}}{1 - X^{2n}} \left[(4n\nu + 2\rho)\zeta^n + (4n\nu + 2\overline{\rho})\zeta^{-n}\right]. \tag{6.24}$$

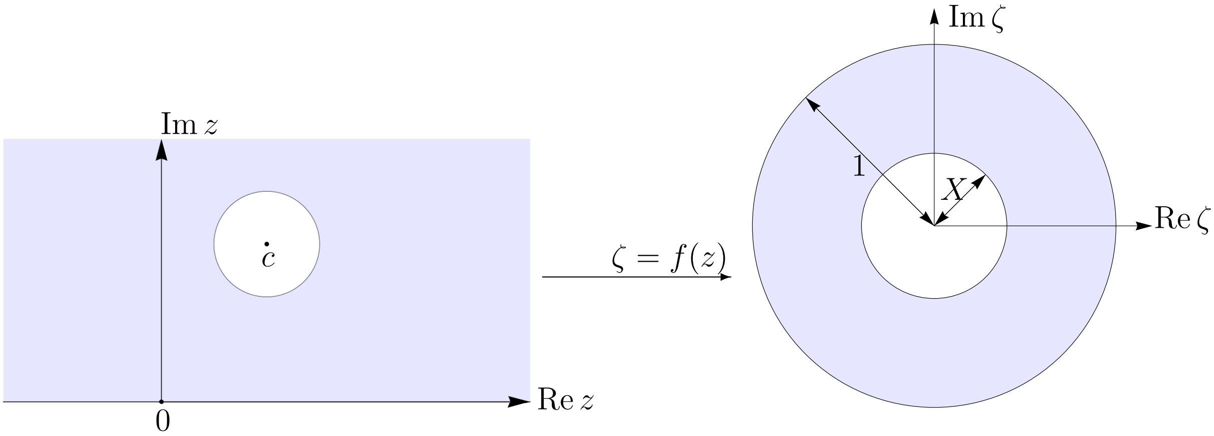

Figure 6.3: Schematic of the conformal map $\zeta = f(z)$ (2.20) from the fluid region, Ω, to the annulus $\{\zeta : X \leq |\zeta| \leq 1\}$.

Evaluating the left-hand side of the force balance (2.19) and using Cauchy's Residue Theorem we find

$$\begin{aligned}\frac{1}{\mathrm{i}\pi}\oint_{\partial\Omega_b} w(z)\,\mathrm{d}z &= -4\mathrm{i}\sqrt{\beta^2-1}\sum_{n=1}^{\infty}\frac{nX^{2n}}{1-X^{2n}}(4n\nu+2\overline{\rho}), &(6.25\text{a})\\ &= -\frac{2\sqrt{\beta^2-1}}{(\log X)^3}\Big((\beta^2-1)\mathrm{i}\Psi''_{X^2}(1)+(2\alpha-\mathcal{U}_b)\sqrt{\beta^2-1}\Psi'_{X^2}(1)\log X\Big), &(6.25\text{b})\end{aligned}$$

where we have rewritten the sums in terms of the q-digamma function, Ψ (Salem, 2012). The equation of motion (2.19) can then be written as

$$F_1(c) = \mathcal{U}_b\left(F_2(\beta) + \frac{1}{\delta|\mathcal{U}_b|^{1/3}}\right), \tag{6.26}$$

where

$$\begin{aligned}F_1(\alpha+\mathrm{i}\beta) &= -\frac{2\mathrm{i}\left(\beta^2-1\right)^{3/2}}{(\log X)^3}\,\Psi''_{X^2}(1) + \frac{4\alpha\left(\beta^2-1\right)}{(\log X)^2}\,\Psi'_{X^2}(1), &(6.27\text{a})\\ F_2(\beta) &= -1 + \frac{2\left(\beta^2-1\right)}{(\log X)^2}\Psi'_{X^2}(1). &(6.27\text{b})\end{aligned}$$

6.4.2.2 Results

One can verify that $F_1(c) \sim 4\overline{c}$ and $F_2(\beta) \to 1$ as $\mathrm{Im}[c] = \beta \to \infty$, and thus the full equation of motion (6.26) is indeed approximated by (6.13) when the bubble is sufficiently far from the wall. As demonstrated in figure 6.4, we find that the bubble trajectories continue to closely follow the streamlines of the background flow until the bubble is extremely close to the wall. Recall that the bubble has unit dimensionless

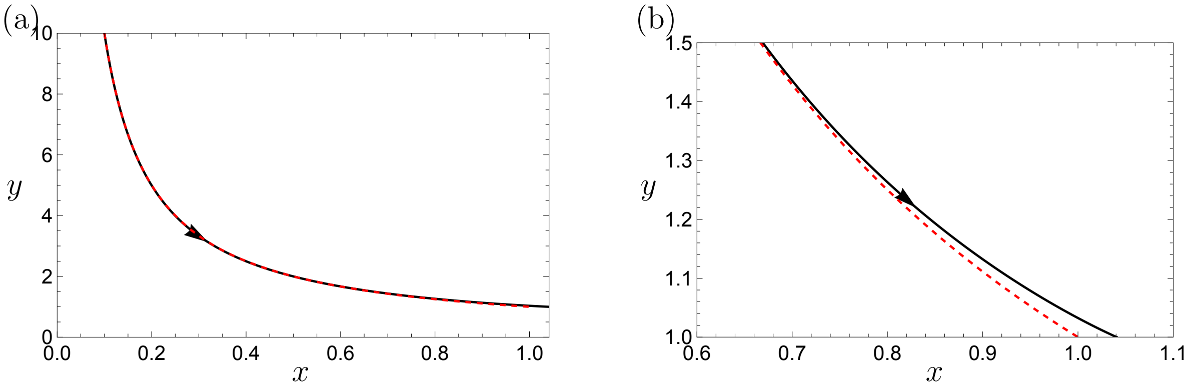

Figure 6.4: (a): A trajectory of (6.26) (black) with $\delta = 1$ and the corresponding streamline of the background flow (red, dashed). (b) The trajectory zoomed into the range $x \in [0.6, 1.1]$.

bubble radius, so the bubble intersects the wall when $\beta = 1$. The trajectory shown in figure 6.4 therefore departs noticeably from the corresponding streamline only when the bubble is less than about a quarter radius from the wall.

To distinguish between the full and approximate solutions, we denote the bubble velocities by $\mathcal{U}_b = U_b + \mathrm{i}V_b$ and $\mathcal{U}_{\text{approx}} = U_{\text{approx}} + \mathrm{i}V_{\text{approx}}$ predicted by (6.26) and by the approximate equation (6.13), respectively. We compare the directions of motion predicted by the two theories by computing the velocity ratio

$$U_{\text{ratio}} = \frac{V_b/U_b}{V_{\text{approx}}/U_{\text{approx}}} = -\frac{\alpha V_b}{\beta U_b} = \frac{\sqrt{\beta^2-1}\Psi''_{X^2}(1)}{2\beta\Psi'_{X^2}(1)\log X}. \tag{6.28}$$

This ratio is solely a function of the distance β from the wall, and is plotted in figure 6.5. It is a monotonically increasing function of β with $U_{\text{ratio}} \to 1$ as $\beta \to \infty$, and $U_{\text{ratio}} \to 6\mathcal{Z}(3)/\pi^2$ as $\beta \to 1+$, where $\mathcal{Z}(s)$ is the zeta-function. The former limit means the trajectories follow the streamlines of the background flow far away from the wall; deviations of over 5% occur only when the bubble is less than approximately 0.3 radii away from the wall. The latter limit means the bubble still has a non-zero velocity perpendicular to the wall as it approaches the wall and thus will always collide with the wall in finite time.

In figure 6.6 we plot the time for collision against δ for initial bubble positions of the form $k(0.1 + 10\mathrm{i})$ with three different values of k. In each case, the bubble starts far enough from the wall to closely follow a streamline initially, and k labels which streamline it is on. We observe that the time taken for collision decreases with δ, because the bubble speed increases with δ. We also observe that the approximate solution ignoring the wall underestimates the time taken for a collision to occur. The presence of the wall thus provides some repulsive influence on the approaching

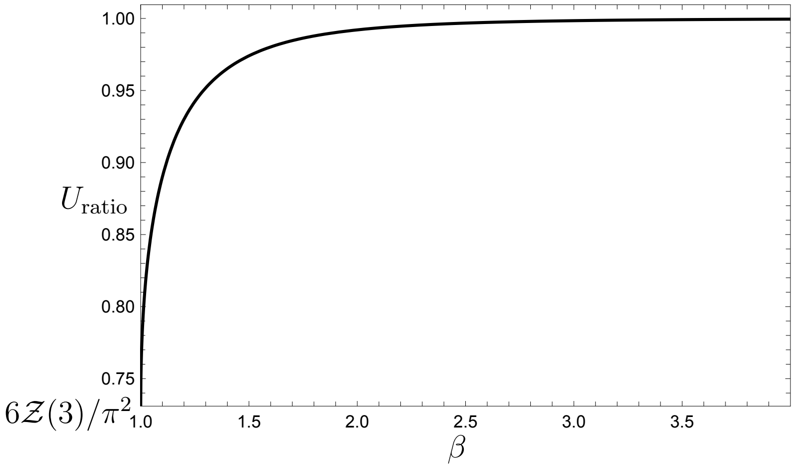

Figure 6.5: Velocity ratio U_{ratio} given by (6.28) versus distance of the bubble centre from the wall, β.

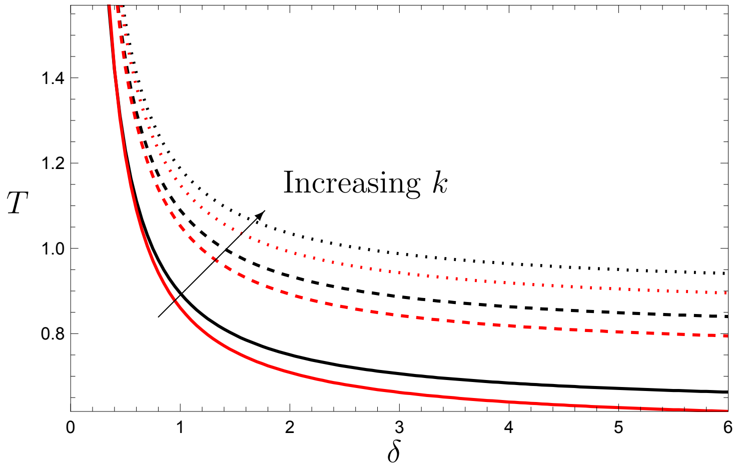

Figure 6.6: Time taken for a bubble to collide with the solid wall at $\text{Im}(z) = 0$ versus δ, for a stagnation-point flow including wall effects (black) and with no wall (red). The bubble centre is initially at $z = k(0.1 + 10\text{i})$ with $k = 1$ (solid curves), $k = 2$ (dashed curves), and $k = 3$ (dotted curves).

bubble (also indicated by the weak singularity as $\beta \to 1+$ in figure 6.5), but not strong enough to prevent finite-time collision.

To further quantify the difference between the full and approximate solutions we define the relative error as

$$\text{Error}(\beta) = \max_{\alpha \in \mathbb{R}} \frac{|\mathcal{U}_b - \mathcal{U}_{\text{approx}}|}{|\mathcal{U}_b|}. \tag{6.29}$$

We plot the error defined by (6.29) versus δ in figure 6.7, for various values of β. The maximum error is found to occur when $\beta = 1$, as expected because in this limit the bubble is touching the wall. However, as β is increased the error quickly decreases, with the error being at most 0.1 when $\beta = 2$. We find three regions of

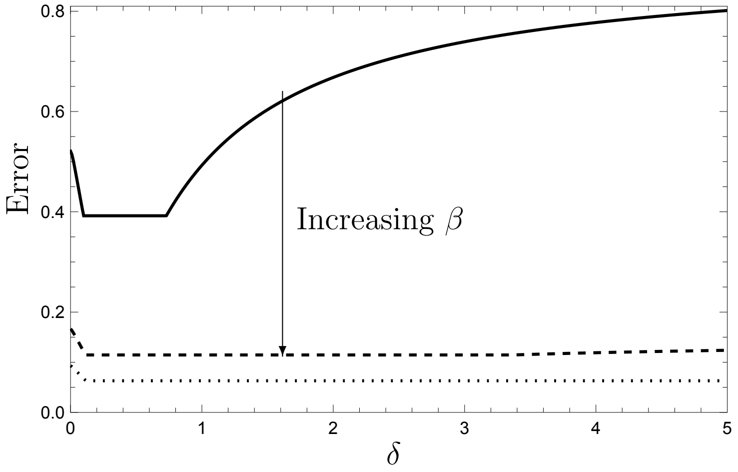

Figure 6.7: The maximum error in the bubble velocity for stagnation-point flow versus δ at fixed values of $\beta = 1$ (solid), 1.5 (dashed), 2 (dotted).

interest: as δ increases from zero, the error initially decreases, then remains constant for intermediate values of δ, before increasing again at large δ.

To explain this behaviour, in figure 6.8 we plot the bubble velocity components (U_b, V_b) and the corresponding approximations $(U_{\text{approx}}, V_{\text{approx}})$ versus α, with $\beta = 1$ and three different values of δ in each of the three regions identified above. In each case, because we keep $\beta = 1$ constant, the error is dominated by the behaviour of $|U_b - U_{\text{approx}}|$, and the errors in V_b are much smaller except near $\alpha = 0$. In the small δ regime (see figure 6.8(a)) we find that $U_{\text{approx}} < U_b$ for small values of α. However we can calculate the limit

$$\frac{U_{\text{approx}}}{U_b} \to 2 - \frac{6}{\pi^2} > 1 \qquad \text{as} \quad \alpha \to \infty, \tag{6.30}$$

so the two graphs must cross over at some value of $\alpha = \alpha^*$, say. For small values of δ, the maximum error occurs within the region $0 < \alpha < \alpha^*$. However, as δ is increased (see figure 6.8(b)), the value of α^* decreases until the maximum error occurs at $\alpha = \infty$ (and is therefore constant). Finally, as δ is further increased, α^* reaches zero so $U_b < U_{\text{approx}}$ everywhere (see figure 6.8(c)), and the largest relative error now occurs at $\alpha = 0$.

6.4.3 Motion of a bubble past a circular obstacle

6.4.3.1 Solution

In this next example, we consider the flow of a bubble past a circular obstacle in a uniform outer flow of dimensionless magnitude 1. Again suppose the bubble centre is

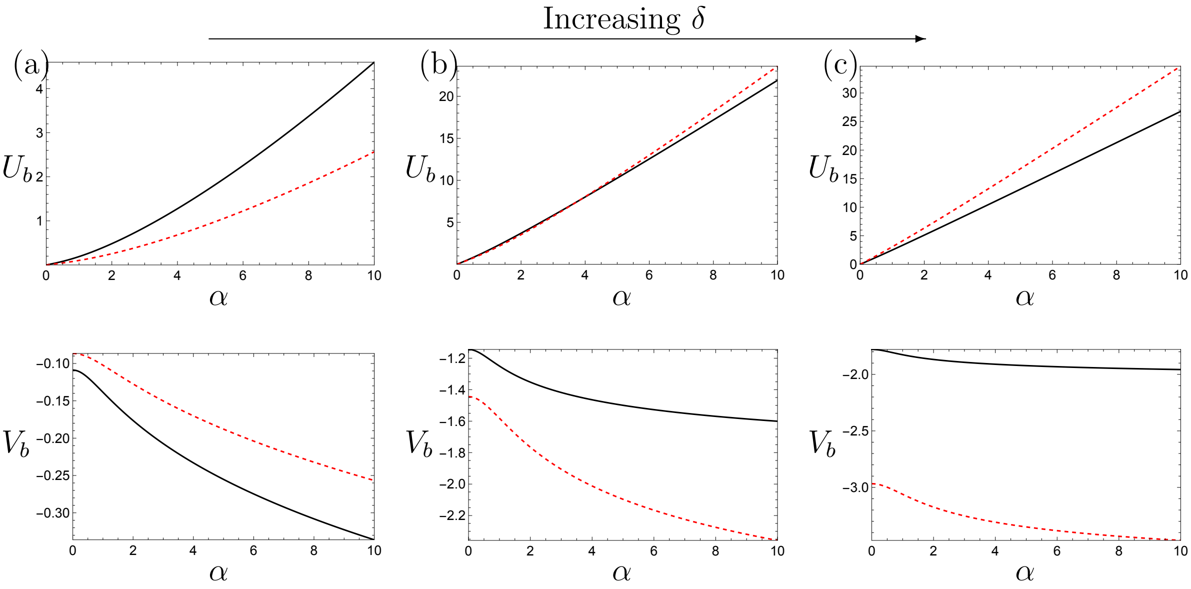

Figure 6.8: Instantaneous bubble velocity (U_b, V_b) (shown in top and bottom graphs, respectively) versus α, with $\beta = 1$, and (a) $\delta = 0.05$, (b) $\delta = 0.5$, (c) $\delta = 2$. The black solid curve shows the full solution (6.26), and the red dashed curve shows the approximate solution (6.13).

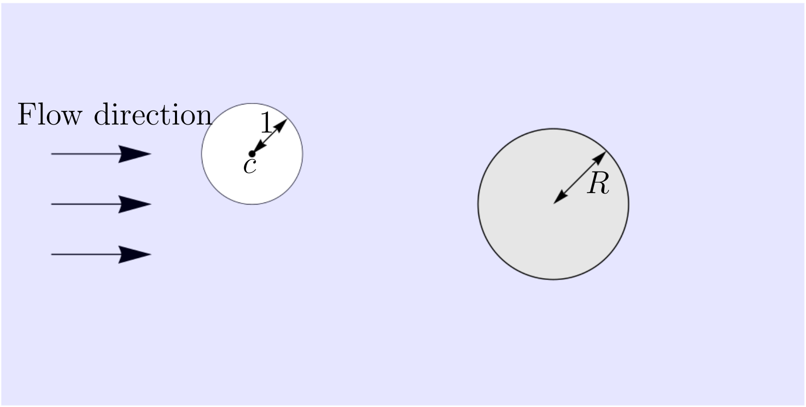

Figure 6.9: Schematic of the flow of a bubble past a circular obstacle (shown in grey).

at $c \in \mathbb{C}$ with radius 1, and the obstacle is centred at the origin with radius R. The problem setup is shown schematically in figure 6.9.

It is straightforward to construct an approximate equation of motion for the bubble using the methodology laid out in §6.4. Without the bubble present, the complex potential $f(z)$ for flow around a circular obstacle is given by

$$f(z) = z + \frac{R^2}{z}. \tag{6.31}$$

The approximate bubble velocity $\mathcal{U}_{\text{approx}}$ is then given by (6.9), i.e.,

$$2\left(1 - \frac{R^2 c^2}{|c|^4}\right) = \mathcal{U}_{\text{approx}}\left(1 + \frac{1}{\delta|\mathcal{U}_{\text{approx}}|^{1/3}}\right). \tag{6.32}$$

The complex potential $w(z)$ for the full solution is a holomorphic function in the fluid domain, Ω, and satisfies the boundary conditions

$$\begin{aligned} \operatorname{Im}[w(z)] &= q + \operatorname{Im}\left[\overline{\mathcal{U}}_b(z-c)\right] && \text{on} \quad |z-c| = 1, && (6.33\text{a})\\ \operatorname{Im}[w(z)] &= 0 && \text{on} \quad |z| = R, && (6.33\text{b})\\ w(z) &\sim z && \text{as} \quad z \to \infty. && (6.33\text{c}) \end{aligned}$$

To solve (6.33) we adapt the methodology of Chapter 3 §3.3 and conformally map from the solution domain, Ω, onto the concentric annulus $\mathcal{A} = \{\zeta : \mathcal{X} \le |\zeta| \le 1\}$ using the mapping

$$\zeta = \frac{1 - p(z-c)\mathrm{e}^{-\mathrm{i}\phi}}{(z-c)\mathrm{e}^{-\mathrm{i}\phi} - p}, \tag{6.34}$$

where $\phi = \pi + \arg(c)$ and

$$\begin{aligned} p &= \frac{|c|^2 - R^2 + 1 - \sqrt{(|c|^2 - R^2 + 1)^2 - 4|c|^2}}{2|c|}, && (6.35\text{a})\\ \mathcal{X} &= p^2 + \frac{(R-1)p(p+1)(|c| - R - 1)}{|c|(|c| - R - p)}. && (6.35\text{b}) \end{aligned}$$

We then define $w(z) = z + W(\zeta)$, so that $W(\zeta)$ is holomorphic on $\mathcal{A}$, and satisfies the boundary conditions

$$\begin{aligned} \operatorname{Im}[W(\zeta)] &= q + \operatorname{Im}\left[(\mathcal{U}_b - 1)\left(\frac{1+p\zeta}{\zeta+p}\right)\mathrm{e}^{\mathrm{i}\phi}\right] && \text{on} \quad |\zeta| = 1, && (6.36\text{a})\\ \operatorname{Im}[W(\zeta)] &= -\operatorname{Im}\left[\left(\frac{1+p\zeta}{\zeta+p}\right)\mathrm{e}^{\mathrm{i}\phi}\right] && \text{on} \quad |\zeta| = \mathcal{X}. && (6.36\text{b}) \end{aligned}$$

We expand $W(\zeta)$ as a Laurent series to obtain

$$W(\zeta) = \frac{(1-p^2)\mathrm{e}^{-\mathrm{i}\phi}}{p}\sum_{n=1}^{\infty}\frac{\mathcal{X}^n}{1-\mathcal{X}^{2n}}\left[\left((\overline{\mathcal{U}}_b-1)\left(\frac{-p}{\mathcal{X}}\right)^n - \mathrm{e}^{2\mathrm{i}\phi}\left(\frac{-\mathcal{X}}{p}\right)^n\right)\zeta^n \right.$$
$$\left. + \left((\mathcal{U}_b-1)\mathrm{e}^{2\mathrm{i}\phi}\left(-p\mathcal{X}\right)^n - \left(\frac{-\mathcal{X}}{p}\right)^n\right)\zeta^{-n}\right]. \qquad (6.37)$$

Evaluating the left-hand side of the force balance (2.19) and using Cauchy's Residue Theorem we thus find

$$\frac{1}{\mathrm{i}\pi}\oint_{|z-c|=1} w(z)\,\mathrm{d}z = \frac{2(1-p^2)^2}{p^2}\sum_{n=1}^{\infty}\frac{n\mathcal{X}^{2n}}{1-\mathcal{X}^{2n}}\left[(1-\mathcal{U}_1)\left(\frac{p}{\mathcal{X}}\right)^{2n} - \mathrm{e}^{2\mathrm{i}\phi}\right]. \qquad (6.38)$$

We can then write the equation of motion (2.19) as

$$f_2 - \frac{f_1 c^2}{|c|^2} = \mathcal{U}_b\left(f_2 - 1 + \frac{1}{\delta|\mathcal{U}_b|^{1/3}}\right), \qquad (6.39)$$

where

$$f_1 = \frac{2(1-p^2)^2}{p^2}\frac{\Psi'_{\mathcal{X}^2}(1)}{4\log^2\mathcal{X}}, \qquad (6.40\text{a})$$

$$f_2 = \frac{2(1-p^2)^2}{p^2}\frac{\Psi'_{\mathcal{X}^2}\left(\frac{\log p}{\log \mathcal{X}}\right)}{4\log^2\mathcal{X}} \qquad (6.40\text{b})$$

are functions of $|c|$ and R.

6.4.3.2 Results

One can verify that $f_1 \sim 2R^2/|c|^2$ and $f_2 \to 2$ as $|c|/R \to \infty$, and the full equation of motion (6.39) thus reduces to the approximate version (6.32) when the bubble is far from the obstacle. However, similarly to §6.4.2, the solutions to (6.33) do not precisely follow the streamlines of the background flow, as is observed in figure 6.10. Here, the bubble deviates noticeably from its initial streamline only when the bubble is very close to the obstacle (see the close-up in figure 6.10(b)).

We can quantify the deviation from a streamline by defining a velocity ratio in the same manner as (6.28), that is,

$$U_{\text{ratio}} = \frac{V_b/U_b}{V_{\text{approx}}/U_{\text{approx}}} = \mathcal{F}\,\frac{\mathrm{Re}\left[1-\frac{R^2c^2}{|c|^4}\right]}{\mathrm{Re}\left[1-\frac{f_1c^2}{f_2|c|^2}\right]}, \qquad (6.41)$$

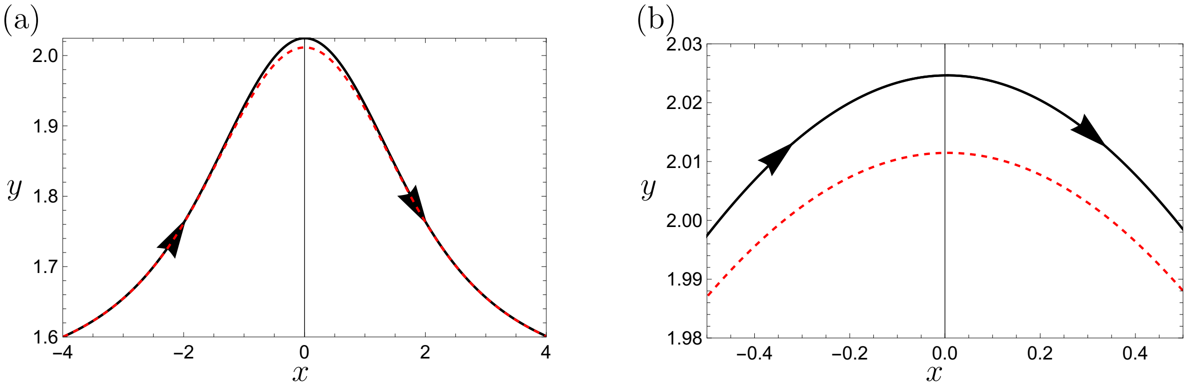

Figure 6.10: (a): A trajectory of (6.39) (black) with $\delta = 5$ and $R = 1$ and the corresponding streamline of the background flow (red, dashed). (b) The trajectory zoomed into the range $x \in [-0.5, 0.5]$.

where the prefactor is given by

$$\mathcal{F} = \frac{f_1 |c|^2}{f_2 R^2}. \tag{6.42}$$

From the above estimates for f_1 and f_2, we have that $\mathcal{F} \to 1$ and thus $U_{\text{ratio}} \to 1$ as $|c|/R \to \infty$, confirming that the bubble closely follows the streamlines of the background flow far from the obstacle. Indeed, we can use the quantity $\mathcal{F}$ as a measure of how closely the bubble follows the streamlines of the background flow, which is more useful than (6.41) because it is only a function of the distance $|c|$ (and the obstacle radius R).

We plot $\mathcal{F}$ versus $|c|$ in figure 6.11 for three different values of R. As $|c|$ decreases from $+\infty$, $\mathcal{F}$ increases from its limiting value of 1, approaching a finite limit as the bubble approaches the obstacle, namely

$$\mathcal{F} \to \frac{\pi^2 (1+R)^2}{3R^2 \mathcal{Z}\left(2, \frac{R}{1+R}\right)} > 1 \qquad \text{as} \quad |c| \to 1 + R, \tag{6.43}$$

where $\mathcal{Z}(s, b)$ is the Hurwitz zeta-function (Kanemitsu *et al.*, 2000), defined by

$$\mathcal{Z}(s, b) = \sum_{n=0}^{\infty} \frac{1}{(n+b)^s}. \tag{6.44}$$

Thus we observe significant deviations from the background flow streamlines only when the bubble is close to the obstacle, as is seen in figure 6.10(b). Furthermore, those deviations are more noticeable for smaller values of the obstacle radius R.

As in §6.3.1, we observe a mild (square root) singularity in the function $\mathcal{F}$ as the distance $|c| - R - 1$ of the bubble from the obstacle tends to zero, but this repulsive effect is too weak to prevent a finite-time collision. However, for suitably chosen

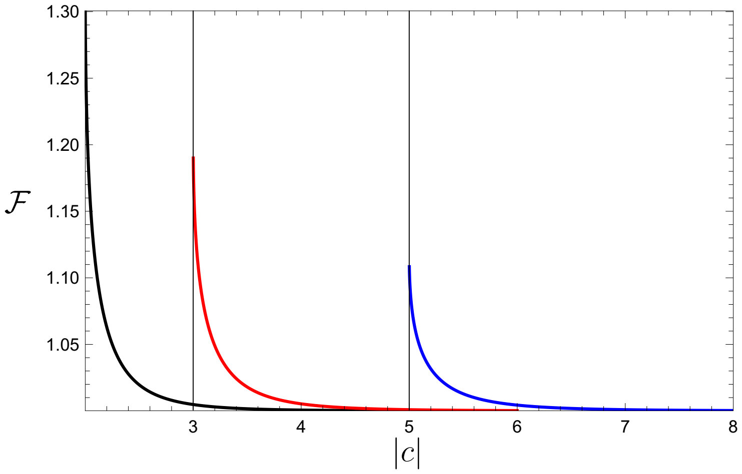

Figure 6.11: Velocity ratio function $\mathcal{F}$ versus centre–centre distance from the bubble to the obstacle, $|c|$, for $R = 1$ (black), 2 (red), 4 (blue).

initial conditions, it is possible for the bubble to safely navigate past the obstacle. In figure 6.12(a), we plot the time, T, taken for the bubble to traverse around the obstacle versus δ for two such cases. We find that T is a monotonically decreasing function of δ, as expected since the bubble speed increases with δ. Also, we observe that the approximate solution (6.32) closely matches the full solution (6.39), slightly over-predicting T for $\delta < 1$ and under-predicting for $\delta > 1$. Similar qualitative changes in behaviour as δ passes through 1 have been found throughout this thesis in Chapters 2, 3 and 4. Despite the significant deviations between the approximate and full solutions when the bubble is very close to the obstacle, the total transit time T is barely affected, because the bubble is very close to the obstacle only very briefly.

In the same manner as (6.29) we define the maximum relative error as

$$\text{Error}(|c|, R) = \max_{\arg c \in [0, 2\pi)} \frac{|\mathcal{U}_b - \mathcal{U}_{\text{approx}}|}{|\mathcal{U}_b|}. \tag{6.45}$$

We plot (6.45) versus δ, for $R = 1$ and various values of $|c|$ in figure 6.13(a) and for $|c| = 1 + R$ and various values of R in figure 6.13(b). We find that the maximum error occurs at $|c| = 1 + R$, as expected, and it quickly decreases with increasing $|c|$. Also, the error increases with the obstacle radius, R. For small values of δ, the error is a decreasing function of δ, while for large values it is an increasing function, with a non-smooth transition between the two behaviours. Similarly to §6.4.2.2, this switch in behaviour occurs when the location of the maximum error jumps from $\arg c = \pm\pi/2$ to $\arg c = 0$.

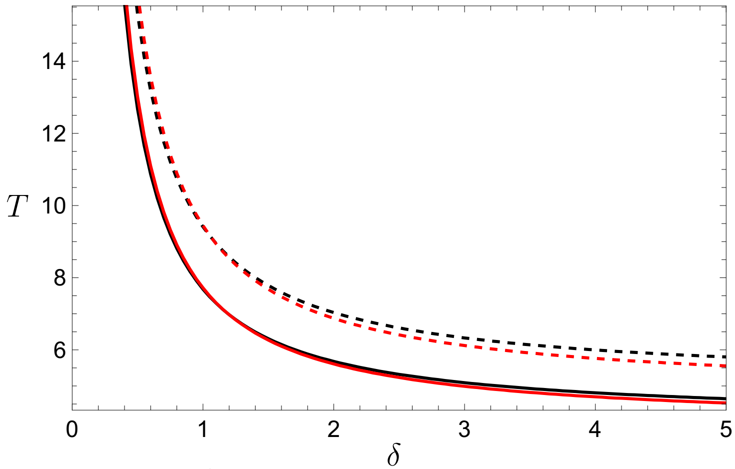

Figure 6.12: Time taken, T for the bubble to travel around the obstacle at $|z| \leq R$ for the full solution (black) and the approximate solution (red) versus δ, with (solid) $R = 1$ and the bubble centre initially at $z = -4 + 1.6\text{i}$, and ending at $z = 4 + 1.6\text{i}$, (dashed) $R = 2$ and the bubble centre initially at $z = -5 + 1.95\text{i}$, and ending at $z = 5 + 1.95\text{i}$,

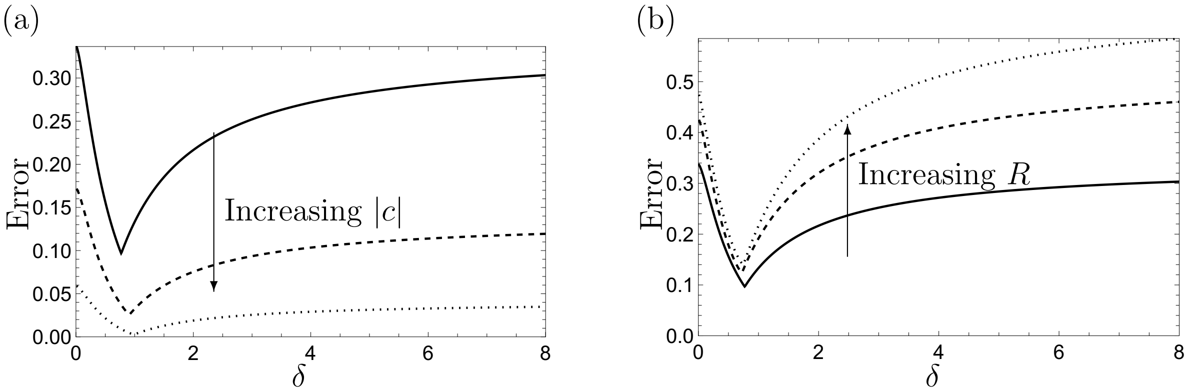

Figure 6.13: The maximum error in the bubble velocity versus δ for flow past a circular obstacle: (a) with $R = 1$ and $|c| = 2$ (solid), 2.1 (dashed), 2.5 (dotted); (b) with $|c| = 1 + R$ and $R = 1$ (solid), 2 (dashed), 4 (dotted).

6.5 Conclusions

In this chapter, we model the motion of a bubble in a non-uniform flow in a Hele-Shaw cell. We consider the distinguished limit where the bubble aspect ratio, ϵ, and the capillary number, Ca, are both small, with $\delta = \mathrm{Ca}^{1/3}/\eta\epsilon = O(1)$ (where $\eta \approx 0.893$ is a constant). In this regime, the bubble is approximately circular and its velocity is determined by a net force balance. We thus find a general equation of motion for such a bubble in an arbitrary external flow. We apply the theory to study the motion of a bubble in a stagnation-point flow, and between a source and a sink, situations that occur abundantly in microfluidic devices.

For the simplest nontrivial case of a uniform external flow, the theory reproduces the result obtained previously in §2.2: the bubble travels parallel to the background flow, and its relative speed is determined as a function of δ. We find that the same holds true for a general background flow: the bubble travels parallel to the *local* velocity, and its relative speed is determined by the same function of the *local* Bretherton parameter, which is defined using the external flow speed evaluated at the bubble centre. Hence, the bubble centre travels along a streamline of the background flow that would exist if the bubble was not present. The bubble thus acts somewhat like a tracer particle, albeit one that travels at a speed different from the background flow speed.

Next, we use the same methodology to derive an approximate equation of motion for a bubble in a more complicated domain including walls or obstacles. The strategy is to find the complex potential of the background flow without the bubble present and then simply plug this potential into our general equation of motion. This approximation ignores second-order image effects from interaction between the bubble and any boundaries present, similarly to the dipole approximations used to study the motion of bubbles in a uniform background flow (Beatus *et al.*, 2006, 2012; Shen *et al.*, 2014). In this approach, the complex potential of the background flow, and hence the equation of motion for the bubble, can be derived once and for all, whereas, in the full solution, one would need to recalculate the complex potential at each time step.

We compare the approximate solution with the full analytical solution in two test cases: a stagnation-point on a wall, and flow around a circular obstacle. In both cases, the approximate solution for the bubble velocity proves to be remarkably accurate unless the bubble is extremely close to the obstacle. Furthermore, the bubble tends to be that close to the obstacle only briefly (if at all). We can thus obtain generally good approximations for the bubble trajectories and, e.g., the time taken for the bubble either to hit or to pass by the obstacle.

The results presented in this chapter provide a framework to study the dynamics of bubbles in a wide variety of background flows found in microfluidic devices.

Chapter 7

The motion of a surfactant-laden bubble in a Hele-Shaw cell

7.1 Introduction

In the previous chapters, we studied the motion of bubbles in a Hele-Shaw cell. Looking down on the cell from above, the boundary of each bubble appears to be a closed curve in the $(\hat{x}, \hat{y})$-plane, on which we imposed the effective boundary condition (2.3b)

$$\hat{p}_b - \hat{p} = \frac{\hat{\gamma}_0}{\hat{H}} + \frac{\hat{\gamma}_0}{\hat{H}}\beta(\mathrm{Ca}_n)\mathrm{Ca}_n^{2/3} + \frac{\hat{\gamma}_0\pi}{4}\hat{\kappa}. \tag{7.1}$$

Here, $2\hat{H}$, and $\hat{p}$ are the height of the cell and the fluid pressure, respectively; $\hat{\kappa}$ is the curvature of the apparent bubble boundary, $\hat{\gamma}_0$ is the surface-tension parameter, $\hat{p}_b$ is the uniform pressure inside the bubble, $\mathrm{Ca}_n = \hat{\mu}\hat{U}_n/\hat{\gamma}_0$ is the capillary number based on the normal velocity $\hat{U}_n$, and β is the Bretherton coefficient, whose value depends on whether the meniscus is advancing or retreating (Bretherton, 1961; Halpern & Jensen, 2002; Wong *et al.*, 1995):

$$\beta(\mathrm{Ca}_n) = \begin{cases} \beta_1 \approx 3.88 & \text{when } \mathrm{Ca}_n > 0, \\ \beta_2 \approx -1.13 & \text{when } \mathrm{Ca}_n < 0. \end{cases} \tag{7.2}$$

The values taken in (7.2) are for a surfactant-free bubble. However, it is common practice in many microfluidic experiments to include surfactants (see, for example, Beatus *et al.*, 2006; Shen *et al.*, 2014; Anna, 2016) to stabilise bubbles against coalescence. In this chapter, we will analyse how surfactants alter the form of (7.2) and thus how to generalise the results of previous chapters to describe systems containing surfactants.

To that end, we consider the canonical problem of a bubble in a channel (see figure 7.1). In §7.2 we write down the dimensional governing equations for the flow around a two-dimensional bubble propagating through a viscous liquid containing surfactants. We consider the situation where the liquid contains an abundance of surfactants, which can quickly adsorb onto the surface of the bubble.

In §7.3 we describe the asymptotic structure of the front region of the bubble. We find that there are three regions of interest: the front cap, the thin film region, and the transition region, which allows for a smooth transition from the front cap into the thin film region. For each region, we derive the leading-order governing equations in the small capillary number limit. We find that, to lowest order, the front cap is a circular arc and the thin film has a constant thickness. The surfactant concentration is in equilibrium with the surrounding fluid in both the front cap and thin film regions, but can vary within the transition region.

The equations in the transition region are analysed in §7.4. Here, we find that the surfactant concentration is always less than the equilibrium concentration. Then, through matched asymptotic expansions we derive results for the thin film height and the pressure drop across the front meniscus, from which we find the surfactant-laden analogue of β_1 in (7.2).

In §7.5 we describe the asymptotic structure of the rear of the bubble. Analogously we find there are three regions of interest: the front cap, the thin film region, and the transition region. We derive leading-order equations for the rear cap and transition regions. We again find that the rear cap of the bubble is approximately a circular arc and the surfactant is in equilibrium in this region. To match the solution at the rear of the bubble with the front we ensure that the thin film height at the rear of the bubble matches the height of the thin film deposited by the front meniscus. In §7.6, the pressure drop across the rear meniscus is found through matched asymptotic expansions, from which we find the surfactant-laden analogue of β_2 in (7.2).

Finally, in §7.7 we combine the results of §§7.4 and 7.6 for β_1 and β_2 to derive the surfactant-laden analogue of (7.1), and thus investigate how the inclusion of surfactants affects the velocity of an isolated bubble in a Hele-Shaw cell. We find that we can easily generalise the results of previous chapters to include surfactant effects by updating the definition of the "Bretherton parameter" (2.13), to be

$$\delta = \frac{3\sqrt{\pi}\Gamma(11/6)}{(\beta_1 - \beta_2)\Gamma(4/3)} \frac{\mathrm{Ca}^{1/3}}{\epsilon}, \tag{7.3}$$

where now β_1 and β_2 are for a surfactant-laden bubble.

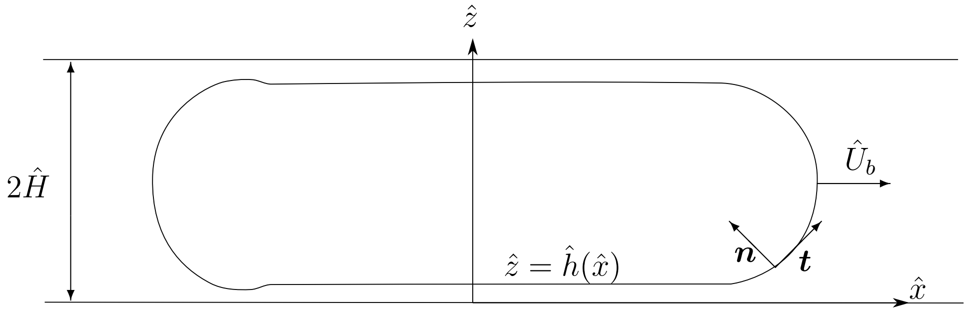

Figure 7.1: Schematic of a two-dimensional surfactant-laden bubble.

7.2 Governing Equations

7.2.1 Dimensional modelling

There is a plethora of literature studying the propagation of a bubble or a finger of air in a viscous fluid containing surfactants (see e.g. Ghadiali & Gaver, 2003; Halpern & Gaver, 2012; Park, 1992; Ratulowski & Chang, 1990; Stebe & Barthes-Biesel, 1995). Ratulowski & Chang (1990) propose five different distinguished limits based on the convective, diffusive and kinetic timescales when studying the effects of surfactants on the propagation of a bubble. In this chapter, we focus on what they term the "bulk equilibrium" model, in which there is a constant supply of surfactant in the bulk. Physically, this limit could correspond to the bulk fluid being significantly above the critical micelle concentration (CMC). This assumption allows us to focus only on the surfactant concentration along the surface of the bubble. We further assume that the surfactant quickly adsorbs or desorbs onto the surface of the bubble and thus the surfactant concentration is close to equilibrium. This implies that surfactant cannot accumulate and thus the bubble cannot rigidify, a phenomenon seen in surfactant systems without fast reactions (see e.g. Park, 1992).

We consider the steady propagation of a two-dimensional bubble inside a channel of height $2\hat{H}$ (see figure 7.1). We orient the $\hat{x}$-axis and the $\hat{z}$-axis along and perpendicular to the lower wall, respectively. We define $\boldsymbol{i}$ and $\boldsymbol{k}$ as the unit vectors in the $\hat{x}$- and $\hat{z}$-directions, respectively. We assume that buoyancy effects are negligible, so the flow is symmetric across the centre-line of the channel and we can restrict our attention to the region $0 \leq \hat{z} \leq \hat{H}$. We define the bubble surface in this region to be at $\hat{z} = \hat{h}(\hat{x})$. The normal to the liquid surface pointing into the bubble and the tangent to the bubble surface are denoted by $\boldsymbol{n}$, and $\boldsymbol{t}$, respectively and are given by

$$\boldsymbol{n} = \frac{-\hat{h}_{\hat{x}}\boldsymbol{i} + \boldsymbol{k}}{\sqrt{1+\hat{h}_{\hat{x}}^2}}, \qquad \boldsymbol{t} = \frac{\boldsymbol{i} + \hat{h}_{\hat{x}}\boldsymbol{k}}{\sqrt{1+\hat{h}_{\hat{x}}^2}}, \tag{7.4a,b}$$

where the subscript variable means partial differentiation with respect to that variable.

We assume the motion of the bubble is sufficiently slow that the flow is in the Stokes regime and we move into a frame of reference in which the bubble is stationary and the walls travel at a velocity $-\hat{U}_b\boldsymbol{i}$, where $\hat{U}_b$ is the bubble propagation speed. We denote the liquid velocity as $\hat{\boldsymbol{u}} = (\hat{u}, \hat{v})$ and the pressure as $\hat{p}$. The motion of the liquid is then governed by the Stokes equations

$$\hat{\nabla} \cdot \hat{\boldsymbol{u}} = 0, \qquad \text{in} \quad \hat{\Omega} \tag{7.5a}$$

$$\hat{\nabla}\hat{p} = \hat{\mu}\hat{\nabla}^2\hat{\boldsymbol{u}} \qquad \text{in} \quad \hat{\Omega}, \tag{7.5b}$$

where $\hat{\mu}$ is the constant liquid viscosity, $\hat{\Omega}$ denotes the liquid region, and $\hat{\nabla} = (\partial/\partial\hat{x}, \partial/\partial\hat{z})$ is the two-dimensional grad operator.

The surfactant concentration on the surface of the bubble $\hat{\Gamma}$, is governed by the reaction-advection-diffusion equation (Stone, 1990)

$$\frac{\partial}{\partial\hat{s}}\left(\hat{\Gamma}\hat{\boldsymbol{u}} \cdot \boldsymbol{t}\right) = \hat{D}\frac{\partial^2\hat{\Gamma}}{\partial\hat{s}^2} + \hat{k}_1\hat{C} - \hat{k}_2\hat{\Gamma}, \qquad \text{on} \quad \hat{z} = \hat{h}(\hat{x}), \tag{7.6}$$

where $\hat{s}$ is arclength, $\hat{D}$ is the surface diffusion coefficient, and $\hat{C}$ is the bulk concentration. We have supplemented (7.6) with a linear reaction term, with rate constants $\hat{k}_1$ and $\hat{k}_2$, to simplify the modelling and allow us to make analytical progress. There are numerous numerical studies that include nonlinear reaction kinetics, such as Fujioka & Grotberg (2005) and Muradoglu *et al.* (2019). In general one would solve a coupled convection-diffusion equation for $\hat{C}$ but, as mentioned above we focus on the "bulk equilibrium" limit in which the bulk concentration does not vary significantly, so we take $\hat{C}$ to be a known constant.

On the Hele-Shaw cell wall, we supply the no-slip boundary condition

$$\hat{\boldsymbol{u}} = -\hat{U}_b\boldsymbol{i} \qquad \text{on} \quad \hat{z} = 0. \tag{7.7a}$$

On the bubble surface, we supply a kinematic condition and normal and tangential stress balances:

$$\boldsymbol{n} \cdot \hat{\boldsymbol{u}} = 0 \qquad \text{on} \quad \hat{z} = \hat{h}(\hat{x}), \tag{7.7b}$$

$$\boldsymbol{n} \cdot \hat{\boldsymbol{\sigma}} \cdot \boldsymbol{n} = -\hat{p}_b + \hat{\gamma}\hat{\kappa} \qquad \text{on} \quad \hat{z} = \hat{h}(\hat{x}), \tag{7.7c}$$

$$\boldsymbol{t} \cdot \hat{\boldsymbol{\sigma}} \cdot \boldsymbol{n} = \frac{\partial\hat{\gamma}}{\partial\hat{s}} \qquad \text{on} \quad \hat{z} = \hat{h}(\hat{x}), \tag{7.7d}$$

where $\hat{\gamma}$ is the (no longer constant) surface tension, $\hat{\kappa}$ is the curvature, $\hat{p}_b$ is the constant pressure inside the bubble, and $\hat{\boldsymbol{\sigma}}$ is the viscous stress tensor, given by

$$\hat{\sigma}_{ij} = -\hat{p}\delta_{ij} + \hat{\mu}\left(\frac{\partial \hat{u}_i}{\partial \hat{x}_j} + \frac{\partial \hat{u}_j}{\partial \hat{x}_i}\right),$$

where δ_{ij} is the Kronecker delta, $(\hat{x}_1, \hat{x}_2) = (\hat{x}, \hat{z})$ and $(\hat{u}_1, \hat{u}_2) = (\hat{u}, \hat{v})$.

We close our model with an equation of state which relates the surface tension, $\hat{\gamma}$, to the surfactant surface concentration, $\hat{\Gamma}$. Since we are assuming linear reaction kinetics, we also supply a linear equation of state, i.e.,

$$\hat{\gamma} = \hat{\gamma}_0 + \left.\frac{\partial \hat{\gamma}}{\partial \hat{\Gamma}}\right|_{\hat{\Gamma}=\hat{\Gamma}_0} (\hat{\Gamma} - \hat{\Gamma}_0), \tag{7.8}$$

where $\hat{\Gamma}_0 = \hat{k}_1\hat{C}/\hat{k}_2$ is the equilibrium concentration of surfactant and $\hat{\gamma}_0$ is the surface tension at equilibrium.

7.2.2 Non-dimensionalisation

We non-dimensionalise the system (7.5)–(7.8) as follows (in which dimensionless variables are denoted without hats)

$$\begin{aligned} (\hat{x}, \hat{z}, \hat{s}, \hat{h}(\hat{x})) &= \hat{H}(x, z, s, h(x)), & \hat{\boldsymbol{u}} &= \hat{U}_b \boldsymbol{u}, & \hat{\gamma} &= \hat{\gamma}_0 \gamma, \\ (\hat{p}, \hat{p}_b) &= \frac{\hat{\gamma}_0}{\hat{H}}(p, p_b), & \hat{\kappa} &= \frac{\kappa}{\hat{H}}, & \hat{\Gamma} &= \hat{\Gamma}_0 \Gamma. \end{aligned} \tag{7.9}$$

The dimensionless governing equations are given by

$$\nabla \cdot \boldsymbol{u} = 0 \quad \text{in} \quad \Omega, \tag{7.10a}$$

$$\nabla p = \mathrm{Ca}\nabla^2 \boldsymbol{u} \quad \text{in} \quad \Omega, \tag{7.10b}$$

$$\frac{\partial}{\partial s}(\Gamma u_S) = \frac{1}{\mathrm{Pe}}\frac{\partial^2 \Gamma}{\partial s^2} + k(1 - \Gamma) \quad \text{on} \quad z = h(x), \tag{7.10c}$$

$$\gamma = 1 - M(\Gamma - 1) \quad \text{on} \quad z = h(x), \tag{7.10d}$$

where

$$\frac{\partial}{\partial s} = \frac{1}{\sqrt{1 + h_x^2}}\frac{\partial}{\partial x} \qquad \text{and} \qquad u_S = \frac{u + h_x v}{\sqrt{1 + h_x^2}}.$$

The model (7.10) contains the dimensionless parameters

$$\mathrm{Ca} = \frac{\hat{\mu}\hat{U}_b}{\hat{\gamma}_0}, \qquad \mathrm{Pe} = \frac{\hat{H}\hat{U}_b}{\hat{D}}, \qquad k = \frac{\hat{k}_2\hat{H}}{\hat{U}_b}, \qquad M = -\frac{\hat{\Gamma}_0}{\hat{\gamma}_0}\left.\frac{\partial \hat{\gamma}}{\partial \hat{\Gamma}}\right|_{\hat{\Gamma}=\hat{\Gamma}_0}, \tag{7.11}$$

namely the capillary number, the Péclet number, the reaction constant, and the Marangoni number.

The dimensionless boundary condition on the cell wall is given by

$$\boldsymbol{u} = -\boldsymbol{i} \qquad \text{on} \quad z = 0. \tag{7.12a}$$

On the bubble surface $z = h(x)$, the boundary conditions (7.7) become

$$\boldsymbol{n} \cdot \boldsymbol{u} = 0, \tag{7.12b}$$

$$p_b - p - \frac{2\mathrm{Ca}}{1+h_x^2}\left(\left(1-h_x^2\right)u_x + h_x(u_z+v_x)\right) = \frac{(1-M(\Gamma-1))h_{xx}}{(1+h_x^2)^{3/2}}, \tag{7.12c}$$

$$\frac{\mathrm{Ca}}{(1+h_x^2)^{1/2}}\left(-4h_x u_x + \left(1-h_x^2\right)(u_z+v_x)\right) = -M\Gamma_x. \tag{7.12d}$$

We consider slow flow in which $\mathrm{Ca} \ll 1$. Furthermore, we assume that $\mathrm{Pe} \gg 1$, and hence we take the limit $\mathrm{Pe} \to \infty$, so (7.10c) reduces to an advection-reaction equation

$$\frac{\partial}{\partial s}\left(\Gamma u_S\right) = k(1-\Gamma), \qquad \text{on} \quad z = h(x). \tag{7.13}$$

As stated by Ratulowski & Chang (1990), there are many distinguished limits which we can consider. However, here we focus specifically on the distinguished limit with

$$M = \mathcal{M}\mathrm{Ca}^{2/3}, \qquad k = \mathcal{K}\mathrm{Ca}^{-1/3}, \tag{7.14}$$

where $\mathcal{M}$ and $\mathcal{K}$ are both $O(1)$ parameters. These limits are chosen such that, in the transition region, the viscous stress balances the Marangoni stress in (7.12d), and the advection of surfactant along the surface balances the reaction kinetics in (7.13).

Note that the ratio

$$\frac{\mathcal{M}}{\mathcal{K}} = -\frac{\hat{k}_1\hat{C}}{\hat{\mu}\hat{k}_2^2\hat{H}}\frac{\partial\hat{\gamma}}{\partial\hat{\Gamma}}\bigg|_{\hat{\Gamma}=\hat{\Gamma}_0} \equiv E, \tag{7.15}$$

is independent of the bubble velocity, $\hat{U}_b$. This fact will allow us to follow the matching procedure laid out in Park & Homsy (1984) to determine how the inclusion of surfactants affects the values of β_1 and β_2 in (7.2), independently of the capillary number.

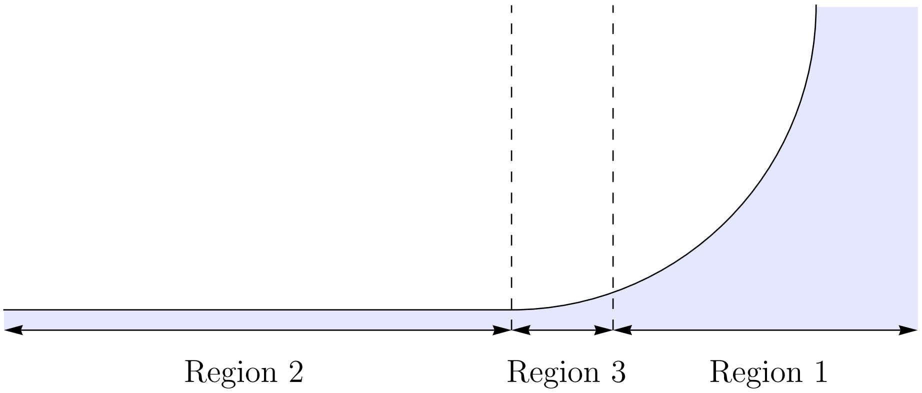

Figure 7.2: Schematic of the front of a bubble, showing the three regions of interest; (1) front cap region, (2) thin film region, (3) transition region.

7.3 The front of the bubble

7.3.1 Regions and scalings

We consider the small Ca limit and perform a perturbation expansion in powers of $\mathrm{Ca}^{1/3}$, following the analysis presented by Park & Homsy (1984), for the similar problem of a surfactant-free bubble. In the small Ca limit the problem splits into three regions of interest (see figure 7.2):

1. The front-cap region. Here the free surface is capillary static and hence, to leading order, is a circular cap.
2. The thin film region. Through a lubrication analysis, we find there is a thin liquid film of constant thickness between the channel wall and the bubble.
3. The transition region. Here both viscous and capillary forces are important, which allows us to smoothly transition from the circular cap to the thin film region.

7.3.2 Region 1: Front-cap region

In this region we expand our variables in powers of $\mathrm{Ca}^{1/3}$,

$$p(x,z) \sim p_0(x,z) + \mathrm{Ca}^{1/3} p_1(x,z) + \cdots\,, \tag{7.16a}$$

$$\boldsymbol{u}(x,z) \sim \boldsymbol{u}_0(x,z) + \mathrm{Ca}^{1/3} \boldsymbol{u}_1(x,z) + \cdots\,, \tag{7.16b}$$

$$\Gamma(x) \sim \Gamma_0(x) + \mathrm{Ca}^{1/3} \Gamma_1(x) + \cdots\,, \tag{7.16c}$$

$$h(x) \sim h_0(x) + \mathrm{Ca}^{1/3} h_1(x) + \cdots\,. \tag{7.16d}$$

At leading order the equations of motion (7.10) become

$$\nabla \cdot \boldsymbol{u}_0 = 0, \qquad \text{in} \quad \Omega, \tag{7.17a}$$

$$\nabla p_0 = \mathbf{0}, \qquad \text{in} \quad \Omega, \tag{7.17b}$$

$$\Gamma_0 = 1, \qquad \text{on} \quad z = h_0(x). \tag{7.17c}$$

Then (7.17b) implies that $p_0 =$ constant. The normal and tangential stress balances on the bubble surface (7.12c) and (7.12d) at leading order read

$$\Gamma_0' = 0 \qquad \text{on} \quad z = h_0(x), \tag{7.18a}$$

$$-\Delta p_0 = \frac{h_0''}{(1 + h_0'^2)^{3/2}} \qquad \text{on} \quad z = h_0(x), \tag{7.18b}$$

where $\Delta p_0 = p_b - p_0$ is the leading-order difference between the constant pressure inside the bubble, p_b, and the fluid pressure. These conditions alongside (7.17) imply that $\Gamma_0 = 1$ and the leading-order shape of the bubble is given by

$$h_0(x) = 1 + \frac{1}{\Delta p_0}\sqrt{1 - (\Delta p_0 x - 1)^2}, \tag{7.19}$$

where we have applied the conditions $h \to 1$ and $h' \to \infty$ at the front tip of the bubble (which we define to be at $x = 0$). It is shown in Park & Homsy (1984) through matching that $\Delta p_0 = 1$, and hence (7.19) gives a circular cap of radius 1:

$$h_0(x) = 1 - \sqrt{1 - (x+1)^2}, \qquad \text{for} \quad x \in (-1, 0). \tag{7.20}$$

Anticipating this result now will simplify the forthcoming analysis; however, one would also find it by following the matching methodology we lay out in §7.4.1.

In (7.1) we require knowledge of the pressure drop across the meniscus up to $O(\mathrm{Ca}^{2/3})$. Following Park & Homsy (1984), we find that $h_1 \equiv 0$, then at $O(\mathrm{Ca}^{2/3})$ we find

$$\beta_1 = \frac{h_2''}{(1 + h_0'^2)^{3/2}}, \tag{7.21}$$

which can be solved to give

$$h_2(x) = \beta_1 \sqrt{-x(x+2)}, \tag{7.22}$$

where β_1 is the *a priori* unknown $O(\mathrm{Ca}^{2/3})$ pressure correction.

7.3.3 Region 2: Thin film region

In the thin film region, we rescale our variables as

$$x = \tilde{x}, \qquad z = \mathrm{Ca}^{2/3}\tilde{z}, \qquad h = \mathrm{Ca}^{2/3}\tilde{h}, \qquad p = \tilde{p},$$
$$u = \tilde{u}, \qquad v = \mathrm{Ca}^{2/3}\tilde{v} \qquad \Gamma = \tilde{\Gamma}. \tag{7.23}$$

Again we expand our variables in powers of $\mathrm{Ca}^{1/3}$ as

$$\tilde{p}(\tilde{x},\tilde{z}) \sim \tilde{p}_0(\tilde{x},\tilde{z}) + \mathrm{Ca}^{1/3}\tilde{p}_1(\tilde{x},\tilde{z}) + \cdots, \tag{7.24a}$$
$$\tilde{\boldsymbol{u}}(\tilde{x},\tilde{z}) \sim \tilde{\boldsymbol{u}}_0(\tilde{x},\tilde{z}) + \mathrm{Ca}^{1/3}\tilde{\boldsymbol{u}}_1(\tilde{x},\tilde{z}) + \cdots, \tag{7.24b}$$
$$\tilde{\Gamma}(\tilde{x}) \sim \tilde{\Gamma}_0(\tilde{x}) + \mathrm{Ca}^{1/3}\tilde{\Gamma}_1(\tilde{x}) + \cdots, \tag{7.24c}$$
$$\tilde{h}(\tilde{x}) \sim \tilde{h}_0(\tilde{x}) + \mathrm{Ca}^{1/3}\tilde{h}_1(\tilde{x}) + \cdots. \tag{7.24d}$$

At leading order, the equations of motion (7.10) become

$$\tilde{u}_{0\tilde{x}} + \tilde{v}_{0\tilde{z}} = 0, \qquad \text{in} \quad 0 \le \tilde{z} \le \tilde{h}_0(\tilde{x}), \tag{7.25a}$$
$$\tilde{u}_{0\tilde{z}\tilde{z}} = 0, \qquad \text{in} \quad 0 \le \tilde{z} \le \tilde{h}_0(\tilde{x}), \tag{7.25b}$$
$$\tilde{p}_{0\tilde{z}} = 0, \qquad \text{in} \quad 0 \le \tilde{z} \le \tilde{h}_0(\tilde{x}), \tag{7.25c}$$
$$\tilde{\Gamma}_0 = 1, \qquad \text{on} \quad \tilde{z} = \tilde{h}_0(\tilde{x}). \tag{7.25d}$$

The boundary conditions (7.12a) and (7.12b) become

$$\tilde{\boldsymbol{u}}_0 = -\boldsymbol{i} \qquad \text{on} \quad \tilde{z} = 0, \tag{7.26a}$$
$$\tilde{v}_0 = \tilde{u}_0\tilde{h}_{0\tilde{x}} \qquad \text{on} \quad \tilde{z} = \tilde{h}_0(\tilde{x}), \tag{7.26b}$$

and the normal and tangential stress balances, (7.12c) and (7.12d) are given by

$$\tilde{p}_0 = 0 \qquad \text{on} \quad \tilde{z} = \tilde{h}_0(\tilde{x}), \tag{7.26c}$$
$$\tilde{u}_{0\tilde{z}} = 0 \qquad \text{on} \quad \tilde{z} = \tilde{h}_0(\tilde{x}). \tag{7.26d}$$

Hence we find that $\tilde{\Gamma}_0 \equiv 1$ and $\tilde{u}_0 \equiv -1$, and $\tilde{h}_0(\tilde{x}) = \tilde{h}_0 = \text{constant}$. Thus, region 2 has a constant (*a priori* unknown) film thickness. Next, we examine the transition region, which allows us to smoothly transition from the constant film region to the circular cap at the front of the bubble.

7.3.4 Region 3: Transition region

In the transition region, we rescale our variables as

$$\begin{aligned} x+1 &= \mathrm{Ca}^{1/3}X, \qquad z = \mathrm{Ca}^{2/3}Z, \qquad h = \mathrm{Ca}^{2/3}H, \qquad p = P,\\ u &= U, \qquad v = \mathrm{Ca}^{1/3}V, \qquad \Gamma = G, \end{aligned} \tag{7.27}$$

so $x=-1$ is the origin of the transition region. We expand our variables in powers of $\mathrm{Ca}^{1/3}$ as

$$P(X,Z) \sim P_0(X,Z) + \mathrm{Ca}^{1/3}P_1(X,Z) + \cdots , \tag{7.28a}$$

$$\boldsymbol{U}(X,Z) \sim \boldsymbol{U}_0(X,Z) + \mathrm{Ca}^{1/3}\boldsymbol{U}_1(X,Z) + \cdots , \tag{7.28b}$$

$$G(X) \sim G_0(X) + \mathrm{Ca}^{1/3}G_1(X) + \cdots , \tag{7.28c}$$

$$H(X) \sim H_0(X) + \mathrm{Ca}^{1/3}H_1(X) + \cdots \tag{7.28d}$$

The leading-order equations of motion (7.10) are given by

$$U_{0X} + V_{0Z} = 0 \qquad \text{in} \quad 0 \le Z \le H({}_0X), \tag{7.29a}$$

$$P_{0X} = U_{0ZZ} \qquad \text{in} \quad 0 \le Z \le H_0(X), \tag{7.29b}$$

$$P_{0Z} = 0 \qquad \text{in} \quad 0 \le Z \le H_0(X), \tag{7.29c}$$

$$\frac{\mathrm{d}}{\mathrm{d}X}\left(G_0U_S\right) = \mathcal{K}(1-G_0) \qquad \text{on} \quad Z = H_0(X), \tag{7.29d}$$

where $U_S = U_0(X, H(X))$. The boundary conditions (7.12a) and (7.12b) become

$$\boldsymbol{U}_0 = -\boldsymbol{i} \qquad \text{on} \quad Z = 0, \tag{7.30a}$$

$$V_0 = U_0H_{0X} \qquad \text{on} \quad Z = H_0(X), \tag{7.30b}$$

and the normal and tangential stress balances, (7.12c) and (7.12d) become

$$-P_0 = H_0'' \qquad \text{on} \quad Z = H_0(X), \tag{7.30c}$$

$$-U_{0Z} = \mathcal{M}G_0' \qquad \text{on} \quad Z = H_0(X). \tag{7.30d}$$

Using (7.29) and (7.30) we find that U_0 is given by

$$U_0 = -\frac{1}{2}H_0'''(Z^2 - 2H_0Z) - \mathcal{M}G_0'Z - 1. \tag{7.31}$$

By integrating (7.31) across the height of the transition region (from $Z=0$ to $Z=H(X)$) we find the flux of liquid in the X-direction is given by

$$Q = \frac{1}{3}H_0'''H_0^3 - \frac{1}{2}\mathcal{M}G_0'H_0^2 - H_0. \tag{7.32}$$

By conservation of mass this must be equal to the flux of liquid in the thin film region, where $Q = -\tilde{h}_0$. This then gives an equation for the height of the bubble surface in the transition region

$$H_0''' = \frac{3(H_0 - \tilde{h}_0)}{H_0^3} + \frac{3\mathcal{M}G_0'}{2H_0}. \tag{7.33}$$

Then using (7.31) and (7.33) we find that (7.29d) becomes

$$\frac{\mathrm{d}}{\mathrm{d}X}\left(\left(\frac{1}{2} - \frac{1}{4}\mathcal{M}G_0'H_0 - \frac{3\tilde{h}_0}{2H_0}\right)G_0\right) = \mathcal{K}(1 - G_0). \tag{7.34}$$

Equations (7.33) and (7.34) then form a closed system for the profile of the bubble, H_0, and the surfactant concentration along the bubble surface G_0. In addition, we enforce the matching conditions

$$H_0 \to \tilde{h}_0 \qquad \text{as} \quad X \to -\infty, \tag{7.35a}$$

$$G_0 \to 1 \qquad \text{as} \quad X \to -\infty, \tag{7.35b}$$

$$H_0(X) \sim \frac{1}{2}X^2 + \beta_1 \qquad \text{as} \quad X \to \infty, \tag{7.35c}$$

$$G_0 \to 1 \qquad \text{as} \quad X \to \infty. \tag{7.35d}$$

In the next section we analyse the problem (7.33)–(7.35).

7.4 Analysis of the transition region equations

7.4.1 Normalisation

We begin by normalising the equations (7.33) and (7.34) by scaling the variables as

$$\xi = \frac{X + \mathcal{S}}{\tilde{h}_0}, \qquad \eta(\xi) = \frac{H_0(X)}{\tilde{h}_0}, \qquad g(\xi) = G_0(X). \tag{7.36}$$

The equations (7.33) and (7.34) are translation invariant, so we introduce an arbitrary shift $\mathcal{S}$ to simplify the forthcoming analysis. Under these scaling, (7.33) and (7.34) become

$$\eta''' = \frac{3(\eta - 1)}{\eta^3} + \frac{3\mathcal{M}g'}{2\eta}, \tag{7.37a}$$

$$\frac{\mathrm{d}}{\mathrm{d}\xi}\left(\left(\frac{1}{2} - \frac{1}{4}\mathcal{M}g'\eta - \frac{3}{2\eta}\right)g\right) = \mathcal{K}(1 - g), \tag{7.37b}$$

and the boundary conditions (7.35) become

$$\eta \to 1 \qquad \text{as} \quad \xi \to -\infty, \tag{7.38a}$$

$$g \to 1 \qquad \text{as} \quad \xi \to -\infty, \tag{7.38b}$$

$$g \to 1 \qquad \text{as} \quad \xi \to \infty. \tag{7.38c}$$

The solution of (7.37a) can be shown to behave quadratically as $\xi \to \infty$ so

$$\eta \sim \frac{1}{2}a\xi^2 + b\xi + c \qquad \text{as} \quad \xi \to \infty, \tag{7.39}$$

where a, b and c are constants. Notice that the coefficients are not uniquely determined due to the arbitrary choice of origin for ξ. However, the translation-invariant groups a and $ac - \frac{1}{2}b^2$ are uniquely determined. By comparison with (7.35c), we see that they are related to the *a priori* unknown constants $\tilde{h}_0$ and β_1 by

$$a = \tilde{h}_0, \qquad ac - \frac{1}{2}b^2 = \beta_1. \tag{7.40}$$

The solution strategy is to shoot from $\xi \to -\infty$, applying the conditions (7.38a) and (7.38b), aiming to satisfy (7.38c) as $\xi \to \infty$. We can in principle read off the coefficients $\tilde{h}_0$ and β_1 from the behaviour of η as $\xi \to \infty$.

The surface velocity of the bubble is then calculated from (7.31), giving,

$$U_S = \frac{1}{2} - \frac{\mathcal{M}}{4}g'\eta - \frac{3}{2\eta}. \tag{7.41}$$

To simplify the analysis of the problem (7.37)–(7.39), we consider the extreme limit in which $\mathcal{K} \gg 1$ and $\mathcal{M} \gg 1$, but with the "elasticity parameter" $E = \mathcal{M}/\mathcal{K} = O(1)$. This regime corresponds to the fast reaction kinetics and strong Marangoni stress limits. Note that these limits are consistent with the assumptions in §§7.3.2 and 7.3.3, as long as $\mathcal{M} \ll \mathrm{Ca}^{-1/3}$.

7.4.2 Asymptotics for $\mathcal{K} \gg 1$

7.4.2.1 Asymptotic expansions

We begin by expanding our variables in powers of $1/\mathcal{K}$ as

$$\eta \sim \eta_0 + \frac{1}{\mathcal{K}}\eta_1 + \cdots, \tag{7.42a}$$

$$g \sim g_0 + \frac{1}{\mathcal{K}}g_1 + \cdots. \tag{7.42b}$$

At $O(\mathcal{K})$ in (7.37) we simply find that

$$g_0' = 0, \tag{7.43a}$$

$$-\frac{E}{4}(g_0'\eta_0'g_0)' = 1 - g_0, \tag{7.43b}$$

which imply that $g_0 \equiv 1$, so at leading order, the surfactant on the bubble is in equilibrium. Then at $O(1)$ we obtain

$$\eta_0''' = \frac{3(\eta_0 - 1)}{\eta_0^3} + \frac{3Eg_1'}{2\eta_0}, \tag{7.44a}$$

$$\frac{E}{4}(g_1'\eta_0)' = g_1 + \frac{3\eta_0'}{2\eta_0^2}, \tag{7.44b}$$

subject to

$$\eta_0 \to 1 \qquad \text{as} \quad \xi \to -\infty, \tag{7.45a}$$

$$g_1 \to 0 \qquad \text{as} \quad \xi \to -\infty, \tag{7.45b}$$

$$\eta_0 \sim \frac{1}{2}a\xi^2 + b\xi + c \qquad \text{as} \quad \xi \to \infty, \tag{7.45c}$$

$$g_1 \to 0 \qquad \text{as} \quad \xi \to \infty. \tag{7.45d}$$

This particular limiting model (7.44)–(7.45) will be the focus of the rest of this chapter. As pointed out in §7.2, there are numerous possible distinguished limits and our aim here is to pick one that includes the important physical effects but is relatively simple and amenable to numerical solution and asymptotic analysis, with the surfactant effects described by the single dimensionless elasticity parameter E.

Finally, we expand the surface velocity (7.41) as $U_S \sim U_{S0} + O(1/\mathcal{K})$. Then we find the leading-order surface velocity of the bubble is given by

$$U_{S0} = \frac{1}{2} - \frac{E}{4}g_1'\eta_0 - \frac{3}{2\eta_0}. \tag{7.46}$$

7.4.2.2 Solution

We solve (7.44) numerically by shooting from $\xi \to -\infty$. Linearising (7.44) by substituting $\eta_0 \sim 1 + \tilde{\eta}$, and $g_1 \sim \tilde{g}$, where $|\tilde{\eta}| \ll 1$ and $|\tilde{g}| \ll 1$ we find that

$$\eta_0 \sim 1 + \sum_{n=1}^{5} A_n \mathrm{e}^{\lambda_n \xi} \qquad \text{as} \quad \xi \to -\infty, \tag{7.47a}$$

$$g_1 \sim \sum_{n=1}^{5} B_n \mathrm{e}^{\lambda_n \xi} \qquad \text{as} \quad \xi \to -\infty, \tag{7.47b}$$

where the λ_n are roots of the quintic polynomial

$$\lambda^5 - \frac{4}{E}\lambda^3 - 12\lambda^2 + \frac{12}{E} = 0. \tag{7.48}$$

This equation has two real and positive roots (which we label λ_1 and λ_2), one real and negative (labelled λ_3), and a complex conjugate pair with negative real part (labelled λ_c and $\overline{\lambda}_c$). We require our solution to decay as $\xi \to -\infty$, so only the positive eigenvalues are permitted. Hence the decaying linearised solution is given by

$$\eta_0 \sim 1 + A_1 \mathrm{e}^{\lambda_1 \xi} + A_2 \mathrm{e}^{\lambda_2 \xi} \qquad \text{as} \quad \xi \to -\infty, \tag{7.49a}$$

$$g_1 \sim -\frac{6A_1\lambda_1^2}{E\lambda_1^2 - 4}\mathrm{e}^{\lambda_1 \xi} - \frac{6A_2\lambda_2^2}{E\lambda_2^2 - 4}\mathrm{e}^{\lambda_2 \xi} \qquad \text{as} \quad \xi \to -\infty, \tag{7.49b}$$

where A_1 and A_2 are *a priori* unknown constants. Due to the translation invariance we may (e.g.) set $A_1 = \pm 1$ by choice of $\mathcal{S}$ in (7.36). Note that the ± occurs because although translation allows us to set the coefficient of the exponential to be of magnitude 1, we do not know the sign of the exponential in advance. However, we always find that on the front meniscus $A_1 = 1$. We then determine A_2 via the shooting method to ensure our solution satisfies $g_1 \to 0$ as $\xi \to \infty$.

For each value of E, we use the above shooting method to solve for η_0 and g_1, then read off the coefficients in the quadratic behaviour (7.39) as $\xi \to \infty$. We then use (7.40) to determine $\tilde{h}_0$ and β_1 as functions of E. However, the shooting problem can become delicate for small or large values of E. In the next two sections, we present asymptotic results for these two limits.

7.4.3 Small E limit

7.4.3.1 Asymptotic expansions

In the limit where E is small we expand

$$\eta_0 \sim \eta_{00} + E\eta_{01} + \cdots, \tag{7.50a}$$

$$g_1 \sim g_{10} + E g_{11} + \cdots. \tag{7.50b}$$

This regime is similar to that studied by Waters & Grotberg (2002) for a surfactant-laden liquid plug and by Ginley & Radke (1989) who considered a bubble in a capillary tube. This limit is equivalent to assuming $\mathcal{M} = O(1)$, while $\mathcal{K} \gg 1$ in (7.37).

At $O(1)$ in (7.44) we find that

$$\eta_{00}''' = \frac{3(\eta_{00} - 1)}{\eta_{00}^3}, \tag{7.51a}$$

$$\frac{E}{4}(g_{10}'\eta_{00})' = g_{10} + \frac{3\eta_{00}'}{2\eta_{00}^2}. \tag{7.51b}$$

We find that the decoupled equation (7.51a) for η_{00} is the same Landau–Levich equation used by Bretherton (1961) to determine the shape of a surfactant-free bubble in the transition region. Waters & Grotberg (2002); Ginley & Radke (1989) both proceed by setting $E = 0$ in (7.51b); however, to properly analyse the surfactant equation (7.51b) one needs to perform a singular perturbation analysis due to E appearing as the coefficient of the highest derivative.

7.4.3.2 Solution for η_{00}

To find the leading-order values of $\tilde{h}_0$ and β_1 we only need to solve (7.51a) numerically using the asymptotic behaviour in the limit $\xi \to -\infty$. As in §7.4.2.2 we linearise (7.51a) by substituting $\eta_{00} \sim 1 + \tilde{\eta}$, where $|\tilde{\eta}| \ll 1$, to find that

$$\eta_{00} \sim 1 + A_1 \mathrm{e}^{\lambda_1 \xi} \qquad \text{as} \quad \xi \to -\infty, \tag{7.52}$$

where the $\lambda_1 = 3^{1/3}$ is the positive root of the equation $\lambda^3 - 3 = 0$. We can set $A_1 = 1$ by exploiting the translation invariance. The solution to (7.51a) is then determined uniquely.

The coefficients in the quadratic behaviour

$$\eta_{00} \sim \frac{1}{2} a_0 \xi^2 + b_0 \xi + c_0 \qquad \text{as} \quad \xi \to \infty, \tag{7.53a}$$

are thus also determined uniquely. In particular, we have $a_0 \approx 1.337$ and $a_0 c_0 - \frac{1}{2} b_0^2 \approx 3.88$, as found by Bretherton (1961).

7.4.3.3 Singular perturbation analysis

Once we have solved for η_{00}, if we set $E = 0$ in (7.51b) then the leading-order outer solution is given by

$$g_{10} = -\frac{3\eta_{00}'}{2\eta_{00}^2}. \tag{7.54}$$

We plot $g_{10}(\xi)$ in figure 7.3 and we notice that it already satisfies the boundary conditions (7.38), which suggests no inner region is necessary. To unequivocally show this premise is true, we scale into an inner layer by writing $\xi = \xi_0 + E\Xi$, where $\Xi = O(1)$ is our inner layer variable, and ξ_0 is the position of the inner layer, and let $N(\Xi) = \eta(\xi)$, and $G(\Xi) = g_{10}(\xi)$. At $O(1)$ in (7.44) we find

$$N''' = 0 \tag{7.55a}$$

$$\frac{1}{4}(G'N)' = \frac{3N'}{2N^2}. \tag{7.55b}$$

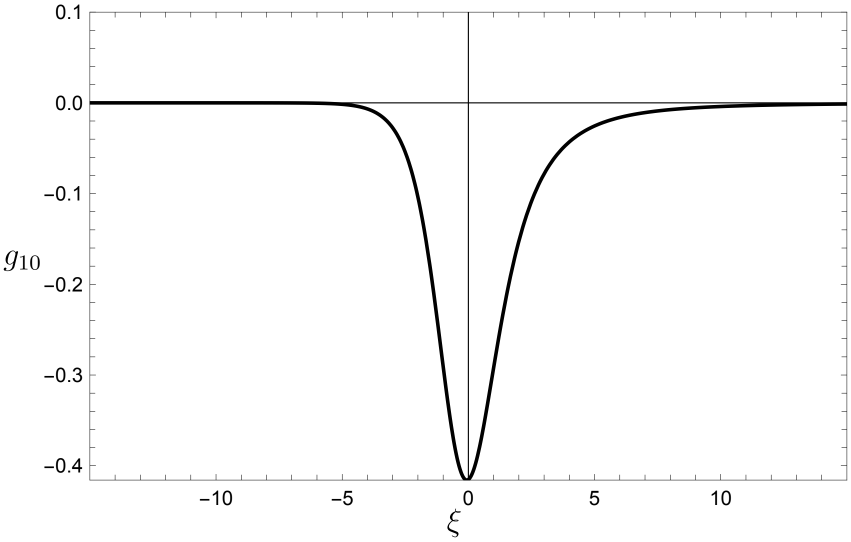

Figure 7.3: The surfactant concentration, g_{10}, given by (7.54), in the front transition region with $E \ll 1$.

The first, (7.55a) implies that $N(\Xi)$ is a quadratic; however, to match the outer solution (7.51a) we find that N = constant = $\eta_{00}(\xi_0)$. Thus, (7.55b) implies that $G(\Xi)$ is a quadratic, and thus by matching to (7.54), we find that $G(\Xi)$ = constant, and hence there is no need of an inner layer.

7.4.3.4 Solution of η_{01}

To find the correction to $\tilde{h}_0$ and β_1 due to the effect of surfactants, at first order in (7.44) we obtain the equation

$$\eta_{01}''' = \frac{12(3 - 2\eta_{00})\eta_{01} + 9(2\eta_{00}'^2 - \eta_{00}\eta_{00}'')}{4\eta_{00}^4}, \tag{7.56}$$

for the correction to the bubble surface. We then solve (7.56) in the same fashion as (7.51a) by shooting from $\xi \to -\infty$. Again the solution to (7.56) behaves quadratically for large positive ξ:

$$\eta_{01} \sim \frac{1}{2}a_1\xi^2 + b_1\xi + c_1 \qquad \text{as} \quad \xi \to \infty, \tag{7.57a}$$

where the constants a_1, b_1, c_1 are in principle determined by the solution of (7.56). In particular we find that $a_1 \approx -0.0146$, and $a_0c_1 + c_0a_1 - b_0b_1 \approx 0.58$.

7.4.3.5 Matching

Finally, following the matching methodology laid out in §7.4.2.2 we find that the thin film height and pressure drop are given by

$$\tilde{h}_0 \sim 1.337 - 0.0146E \qquad \text{as} \quad E \to 0, \tag{7.58a}$$

$$\beta_1 \sim 3.88 + 0.58E \qquad \text{as} \quad E \to 0. \tag{7.58b}$$

We note that (7.58a) and (7.58b) differ from (26) in Waters & Grotberg (2002) because they include a factor of 3 in their Ca which induces a factor of $3^{1/3}$ in the definition of E. We also note that Waters & Grotberg's expression for the pressure drop is twice ours, however, this is due to the cylindrical instead of two-dimensional geometry they are studying and it does not appear in the two-dimensional version we are considering here.

7.4.4 Large E limit

In the other extreme where E is large, we expand

$$\eta_0 \sim \eta_{00} + \frac{1}{E}\eta_{01} + \cdots, \tag{7.59a}$$

$$g_1 \sim \frac{1}{E}g_{11} + \cdots. \tag{7.59b}$$

Then at $O(1)$ in (7.44) we find

$$\eta_{00}''' = \frac{3(\eta_{00} - 1)}{\eta_{00}^3} + \frac{3g_{11}'}{2\eta_{00}}, \tag{7.60a}$$

$$\frac{1}{4}(g_{11}'\eta_{00})' = \frac{3\eta_{00}'}{2\eta_{00}^2}. \tag{7.60b}$$

We can integrate (7.60b) and substitute into (7.60a) to obtain

$$\eta_{00}''' = \frac{12(\eta_{00} - 1)}{\eta_{00}^3}, \tag{7.61a}$$

$$g_{11} = \frac{1}{2}\eta_{00}\eta_{00}'' - \frac{1}{4}\left(\eta_{00}'\right)^2 - \frac{1}{2}\beta_1. \tag{7.61b}$$

Once again, (7.61a) is the Landau-Levich equation and it is similar to the surfactant-free equation (7.51a) found by Bretherton (1961) except with an additional factor of 4 in the numerator. This additional factor of 4 induces an increase in the thin film height and correction to the pressure drop by a factor of $4^{2/3}$, i.e.,

$$\tilde{h}_0 \sim 4^{2/3} \cdot 1.337 \approx 3.369 \qquad \text{as} \quad E \to \infty, \tag{7.62a}$$

$$\beta_1 \sim 4^{2/3} \cdot 3.88 \approx 9.78 \qquad \text{as} \quad E \to \infty. \tag{7.62b}$$

This limit reproduces the large Marangoni number limit reported in many studies (see e.g. Ratulowski & Chang, 1990; Park, 1992; Stebe & Barthes-Biesel, 1995; Shen *et al.*, 2002).

In this limit, we find that the surface velocity (7.46) is given by $U_{S0} \equiv -1$, which corresponds to the bubble interface moving as a rigid body in the transition region, i.e. the bubble interface travels at the same velocity as the walls of the Hele-Shaw cell.

7.4.5 Results

We plot the correction to the surfactant concentration from equilibrium, g_1 as a function of ξ when $E \ll 1$ in figure 7.3 and when $E = 1$ in figure 7.4(a). In both cases, we observe that $g_1 < 0$ for the whole domain and so the surfactant concentration is below equilibrium in the front transition region. Similar surfactant concentration profiles were observed in the work of Stebe & Barthes-Biesel (1995), in which they consider the effect of surfactants in a system with an elevated bulk concentration. In figure 7.4(b) we plot the leading-order surface velocity, U_{S0} as a function of ξ for $E = 1$. We observe that there is a stagnation point (in the frame of the bubble) within the transition region. Its location approximately matches the minimum point of g_1 in figure 7.4(a), this is because the flow is directed out of the stagnation point and thus advects surfactant away, creating a reduction in surfactant concentration near the stagnation point. The presence of a stagnation point along the front of the bubble is a generic feature of surfactant-laden gas bubbles in a Hele-Shaw cell or capillary tube, even in systems with more complicated surfactant dynamics, and non-zero Reynolds number (Fujioka & Grotberg, 2005; Zheng *et al.*, 2007).

The normalised height of the thin film $\tilde{h}_0$ is plotted as a function of the elasticity parameter E in figure 7.5. As $E \to 0$, surfactant effects become negligible and the thin film height approaches 1.337, discovered by Bretherton (1961) for a surfactant-free bubble. At the other extreme, when E is large, $\tilde{h}_0$ approaches 3.369 which is larger by a factor of $4^{2/3}$. Interestingly, (7.58a) predicts a decrease in the thin film height for small E (see figure 7.5(b)). However, figure 7.5(b) shows that the asymptotic result (7.58a) is misleading and quickly becomes redundant and the thin film height, $\tilde{h}_0$, increases quickly thereafter.

The correction to the pressure drop across the front meniscus, β_1, is plotted as a function of E in figure 7.6. Again when E is small we recover the Bretherton (1961) result that $\beta_1 \approx 3.88$. We observe that β_1 is a monotonic increasing function and when E is large β_1 approaches the predicted value 9.78. In the numerical simulation

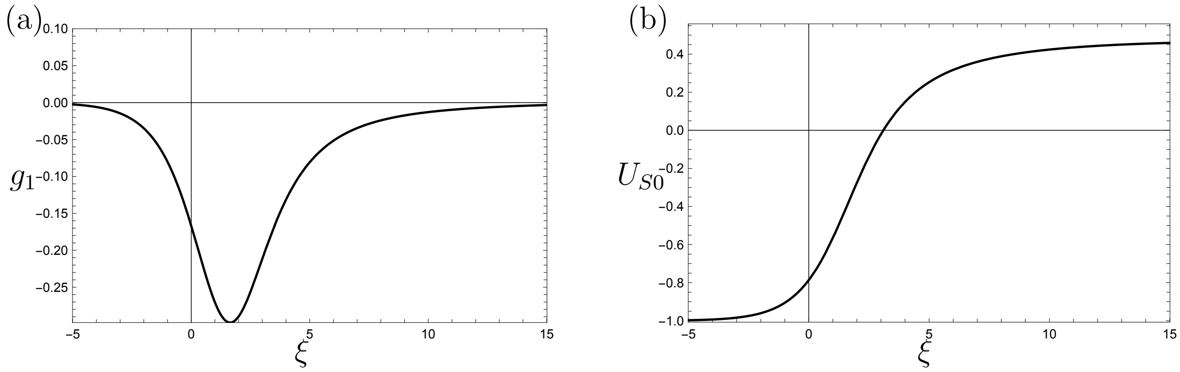

Figure 7.4: (a)The surfactant concentration, g_1, and (b) the surface velocity, U_{S0}, in the front transition region with $E = 1$.

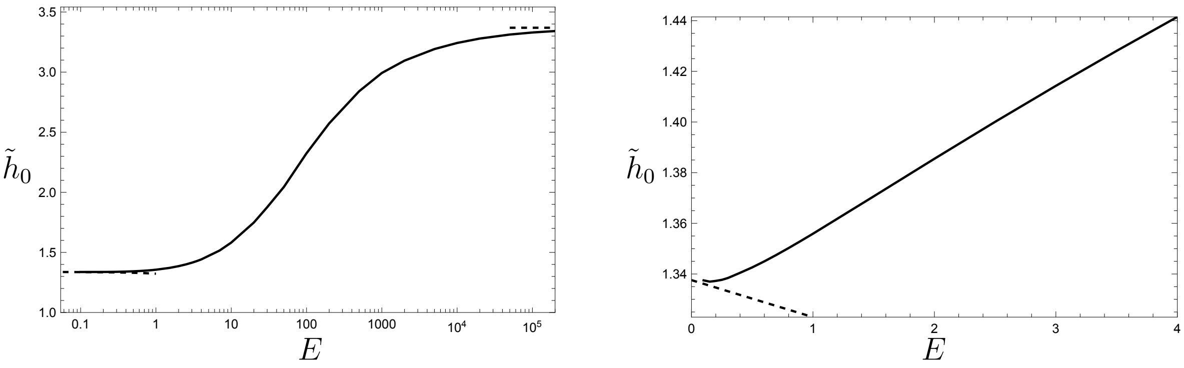

Figure 7.5: The thin film height $\tilde{h}_0$ versus elasticity parameter E. The solid curve is from the numerical solution of (7.44), and dashed curves are the asymptotic predictions: (7.58a) for small E and (7.62a) for large E. (a) A log–linear plot to show the full range of E. (b) The solution for $0 \leq E \leq 4$.

of (7.44) sufficient convergence for the value of β_1 could not be attained for values of $E < 0.2$ due to the sensitivity of the numerical shooting method, caused by the singular nature of (7.44) as $E \to 0$. This was not an issue in figure 7.5(b) since to find $\tilde{h}_0$, truncating the endpoint at $\xi = 50$ is sufficient, but the truncation needs to be done at a much larger value (at least $\xi = 100$) for sufficient convergence of $ac - \frac{1}{2}b^2$.

7.5 Rear of the bubble

7.5.1 Regions

Similar to the front meniscus in the small Ca limit the problem at the rear of the bubble splits into three regions of interest (see figure 7.7). In particular, at the rear of the bubble, we can follow the same analysis as in §7.3.2 and find that the leading-order

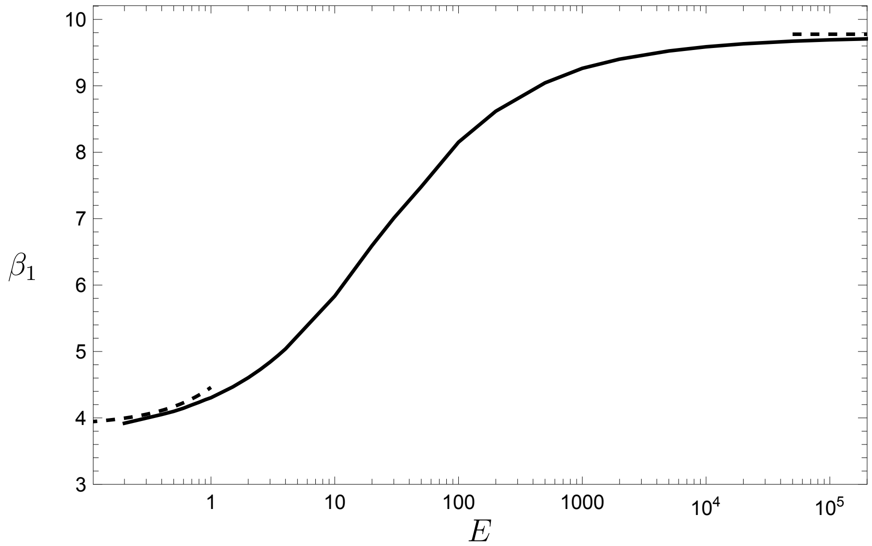

Figure 7.6: The correction to the pressure drop across the front meniscus β_1 versus elasticity parameter E. The solid curve is from the numerical solution of (7.44), and dashed curves are the asymptotic predictions: (7.58b) for small E and (7.62b) for large E.

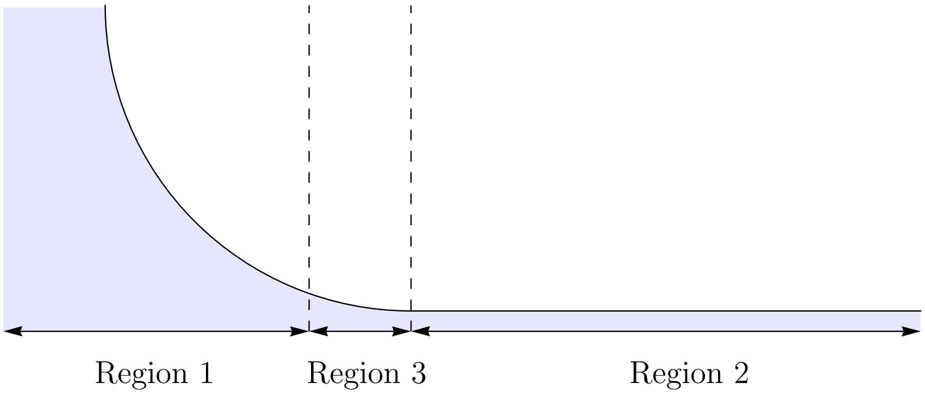

Figure 7.7: Schematic of the rear of a bubble, showing the three regions of interest; (1) Front cap region, (2) Thin film region, (3) Transition region.

shape and surfactant concentration are given by

$$h_0(x) = 1 - \sqrt{1-(l-1+x)^2}, \tag{7.63a}$$

$$h_2(x) = \beta_2\sqrt{(x+l)(2-l-x)}, \tag{7.63b}$$

$$\Gamma_0(x) = 1. \tag{7.63c}$$

where l is the dimensionless length of the bubble, and β_2 is the *a priori* unknown $O(\mathrm{Ca}^{2/3})$ correction to the pressure drop across the rear meniscus.

Similarly to §7.3.3, in the thin film region (region 2), the thin film height $\tilde{h}_0$ is constant.

7.5.2 Transition region

It therefore just remains to analyse the rear transition region. As in §7.3.4, we focus on the distinguished limit where $\mathcal{K} \gg 1$ and $E = \mathcal{M}/\mathcal{K} = O(1)$.

7.6 Analysis of the rear transition region equations

7.6.1 Normalisation

We again normalise by scaling the variables as

$$\xi = \frac{X+\mathcal{S}}{\tilde{h}_0}, \qquad \eta(\xi) = \frac{H_0(X)}{\tilde{h}_0}, \qquad g(\xi) = G_0(X), \tag{7.64}$$

where $\mathcal{S}$ is an arbitrary shift of our coordinates. We then expand our variables in powers of $1/\mathcal{K}$ as

$$\eta \sim \eta_0 + \frac{1}{\mathcal{K}}\eta_1 + \cdots, \tag{7.65a}$$

$$g \sim 1 + \frac{1}{\mathcal{K}}g_1 + \cdots, \tag{7.65b}$$

and obtain exactly the same equations (7.44) as the front transition region, i.e.,

$$\eta_0''' = \frac{3(\eta_0-1)}{\eta_0^3} + \frac{3Eg_1'}{2\eta_0}, \tag{7.66a}$$

$$\frac{E}{4}(g_1'\eta_0)' = g_1 + \frac{3\eta_0'}{2\eta_0^2}. \tag{7.66b}$$

Again, the leading-order surface velocity, U_{S0} is given by (7.46).

We solve (7.66) numerically now by shooting from $\xi \to \infty$. We find that the decaying linearised solution is given by

$$\eta_0 \sim 1 \pm \mathrm{e}^{\lambda_3 \xi} + S\mathrm{e}^{\lambda_R \xi}\cos(\lambda_I \xi - q) \tag{7.67a}$$

$$g_1 \sim \pm\frac{6\lambda_3}{E\lambda_3^2 - 4}\mathrm{e}^{\lambda_3 \xi} - S\Lambda_c(\lambda_R, \lambda_I)\mathrm{e}^{\lambda_R \xi}\cos(\lambda_I \xi - q) - S\Lambda_s(\lambda_R, \lambda_I)\mathrm{e}^{\lambda_R \xi}\sin(\lambda_I \xi - q), \tag{7.67b}$$

as $\xi \to \infty$. Here, S and q are *a priori* unknown parameters which we fix via the shooting method, λ_3 is the real negative solution of (7.48), and $\lambda_c = \lambda_R + \mathrm{i}\lambda_I$ is the complex root with positive imaginary part. The coefficients are given by

$$\Lambda_c(\lambda_R, \lambda_I) = \frac{6\lambda_R(-4 + E(\lambda_R^2 + \lambda_I^2))}{16 + 8E(\lambda_I^2 - \lambda_R^2) + E^2(\lambda_R^2 + \lambda_I^2)^2}, \tag{7.68a}$$

$$\Lambda_s(\lambda_R, \lambda_I) = \frac{6\lambda_I(4 + E(\lambda_R^2 + \lambda_I^2))}{16 + 8E(\lambda_I^2 - \lambda_R^2) + E^2(\lambda_R^2 + \lambda_I^2)^2}. \tag{7.68b}$$

Note again that the ± occurs in (7.67) because although translation allows us to set the coefficient of the exponential to be of magnitude 1, in this case we do not know the sign of the exponential in advance. Finally, we still have that η_0 behaves quadratically for large negative ξ, i.e.,

$$\eta_0 \sim \frac{1}{2}A\xi^2 + B\xi + C \qquad \text{as} \quad \xi \to -\infty. \tag{7.69}$$

To solve (7.66), for each value of E we apply a shooting method with two unknown parameters S and q, which are fixed by ensuring $g_1 \to 0$ and $\eta_0'' \to \tilde{h}_0$ as $\xi \to -\infty$, where $\tilde{h}_0(E)$ is as shown in figure 7.5. The first condition corresponds to matching the surfactant concentration in the thin film to the equilibrium concentration in the rear cap (see §7.5.1), and the second ensures that the thin film height at the rear meniscus matches the height of the thin film deposited at the front meniscus. Following the matching procedure laid out in §7.4.1, we then obtain the $O(\mathrm{Ca}^{2/3})$ correction to the pressure drop across the rear meniscus as

$$\beta_2 = AC - \frac{1}{2}B^2. \tag{7.70}$$

This two-parameter shooting problem can be extremely sensitive, so we examine the limiting cases using asymptotic analysis.

7.6.2 Small E limit

In the extreme where E is small we expand

$$\eta_0 \sim \eta_{00} + E\eta_{01} + \cdots , \tag{7.71a}$$

$$g_1 \sim g_{10} + Eg_{11} + \cdots . \tag{7.71b}$$

Then at $O(1)$ in (7.66) we find that

$$\eta_{00}''' = \frac{3(\eta_{00} - 1)}{\eta_{00}^3}, \tag{7.72a}$$

$$\frac{E}{4}(g_{10}'\eta_{00})' = g_{10} + \frac{3\eta_{00}'}{2\eta_{00}^2}. \tag{7.72b}$$

We note that (7.72b) is singular in the limit $E \to 0$, however, for the same reasons as presented in §7.4.3.3 there is no inner layer and the outer solution of (7.72b) (obtained by setting $E = 0$) satisfies the relevant boundary conditions.

The equation (7.72a) for η_{00} decouples and we solve it numerically using boundary conditions from the asymptotic behaviour in the limit $\xi \to \infty$. Linearising (7.72a) we find that the solution which decays as $\xi \to \infty$ is given by

$$\eta_0 \sim 1 + \mathrm{e}^{\lambda_R \xi}\cos(\lambda_I \xi - q) \qquad \text{as} \quad \xi \to \infty, \tag{7.73}$$

where $\lambda_c = \lambda_R \pm \mathrm{i}\lambda_I = \frac{3^{1/3}}{2}(-1 \pm \mathrm{i}\sqrt{3})$ are the complex roots of the equation $\lambda^3 - 3 = 0$, and q is an *a priori* unknown parameter. Note that we set the coefficient of the exponential to be 1 by exploiting the translation invariance. Following Bretherton (1961) we find q via the shooting method to ensure that the thin film height at the rear of the bubble matches the thin film height at the front of the bubble, i.e., we choose q such that

$$\lim_{\xi \to -\infty} \eta_{00}'' = a_0 \approx 1.337, \tag{7.74}$$

where a_0 is given by (7.53). We then find that $\eta_{00}\eta_{00}'' - \frac{1}{2}(\eta_{00}')^2 \to A_0 C_0 - \frac{1}{2}B_0^2 \approx -1.13$ as $\xi \to -\infty$, which is Bretherton's result for β_2 in the absence of surfactant.

At first order in (7.66) we obtain the equation

$$\eta_{01}''' = \frac{12(3 - 2\eta_{00})\eta_{01} + 9(2\eta_{00}'^2 - \eta_{00}\eta_{00}'')}{4\eta_{00}^4}, \tag{7.75}$$

for the correction to the bubble surface. We then solve (7.75) in the same fashion as (7.72a) by shooting from $\xi \to \infty$.

Finally, following the matching methodology laid out in §7.4.1 we find that $O(\mathrm{Ca}^{2/3})$ correction to the pressure drop is given by

$$\beta_2 \sim -1.13 - 0.97E \qquad \text{as} \quad E \to 0. \tag{7.76}$$

7.6.3 Large E limit

In this limit we follow the same methodology as in §7.4.4 to obtain

$$\eta_{00}''' = \frac{12(\eta_{00} - 1)}{\eta_{00}^3}. \tag{7.77}$$

Matching with the rear cap solutions (7.63) we find that the correction to the pressure drop is then given by

$$\beta_2 \sim -4^{2/3} \cdot 1.13 \approx -2.85 \qquad \text{as} \quad E \to \infty. \tag{7.78}$$

Again this is a factor of $4^{2/3}$ larger than the original Bretherton (1961) result. This extends the large Marangoni number limit reported in many studies (see e.g. Ratulowski & Chang, 1990; Park, 1992) to the rear meniscus.

7.6.4 Results

In figures 7.8(a) and (b) we show example solutions for the correction to the surfactant concentration, $g_1(\xi)$, for $E = 1$ and $E = 4$, respectively. In figure 7.8(a) we observe that the surfactant concentration can be both above and below the equilibrium concentration in the rear transition region, in contrast to the front transition region, where the concentration is always below equilibrium. For these specific solutions, we find that $\beta_2 \approx -1.50$ for $E = 1$ and $\beta_2 \approx -2.33$ for $E = 4$, which are greater in magnitude than the pressure drop $\beta_2 \approx -1.13$ for a surfactant-free bubble found by Bretherton (1961). In figures 7.8(c) and (d) we plot the corresponding surface velocities, U_{S0} for the specific solutions with $E = 1$ and $E = 4$. Similarly to the front meniscus, we observe a stagnation point (in the frame of the bubble) in the transition region. However, here the flow is directed into the stagnation point, resulting in an increase in the surfactant concentration near the stagnation point.

One could perform a parameter sweep to find the full behaviour of β_2 as a function of E. However, it is computationally challenging due to the sensitivity of the two-parameter shooting problem, so we leave this as future work.

7.7 Application to the motion of bubbles in a Hele-Shaw cell

7.7.1 Force balance

We are now in a position to generalise the model presented in Chapter 2 to include the effect of surfactants on the motion of a bubble in a Hele-Shaw cell.

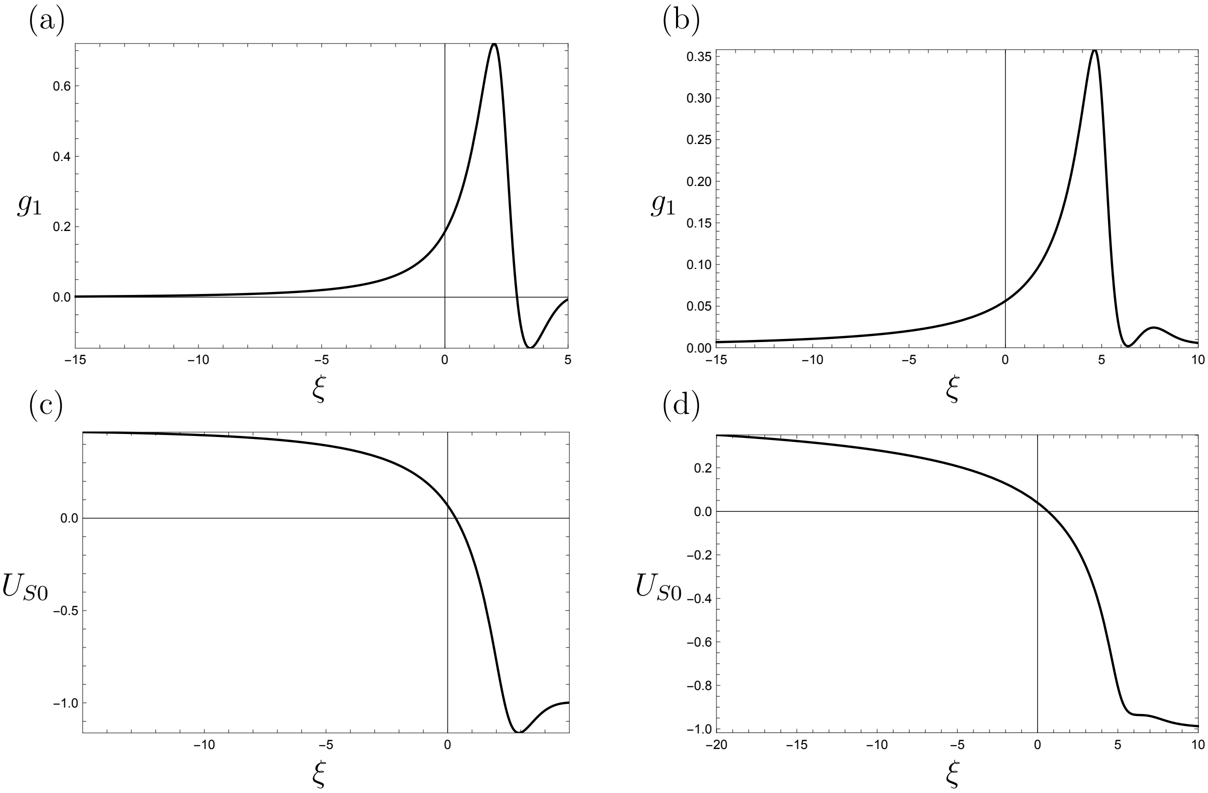

Figure 7.8: (a and b) The surfactant concentration, g_1, and (c and d) the surface velocity, U_{S0}, in the rear transition region with (a and c) $E = 1$, (b and d) $E = 4$.

In Chapter 2 we find that the dimensionless velocity of a bubble in a Hele-Shaw cell with a uniform background flow is given by the force balance (2.12):

$$\frac{\boldsymbol{U}_b}{|\boldsymbol{U}_b|^{1/3}} = \frac{\delta}{\pi} \oint_{r=1} -p\boldsymbol{n}\,\mathrm{d}s, \tag{7.79}$$

where we define the *Bretherton parameter*

$$\delta = \frac{3\sqrt{\pi}\Gamma(11/6)}{(\beta_1 - \beta_2)\Gamma(4/3)} \frac{\mathrm{Ca}^{1/3}}{\epsilon}, \tag{7.80}$$

and, for a surfactant-free bubble, β_1 and β_2 are given by (7.2). This result is now easily generalised for a surfactant-laden bubble by using the expressions for $\beta_1(E)$ and $\beta_2(E)$ found in §§7.4 and 7.6, respectively. Crucially, we recall that the elasticity parameter E, given by (7.15), is independent of the capillary number, so the values of β_1 and β_2 are constant for given surfactant properties and concentrations.

For an isolated bubble from (7.79) we find the velocity of the bubble is given by $\boldsymbol{U}_b = U_b\boldsymbol{i}$, where U_b is given by (2.16):

$$\frac{U_b^{2/3}}{2 - U_b} = \delta = \left(\frac{\beta_1(0) - \beta_2(0)}{\beta_1(E) - \beta_2(E)}\right)\delta_B, \tag{7.81}$$

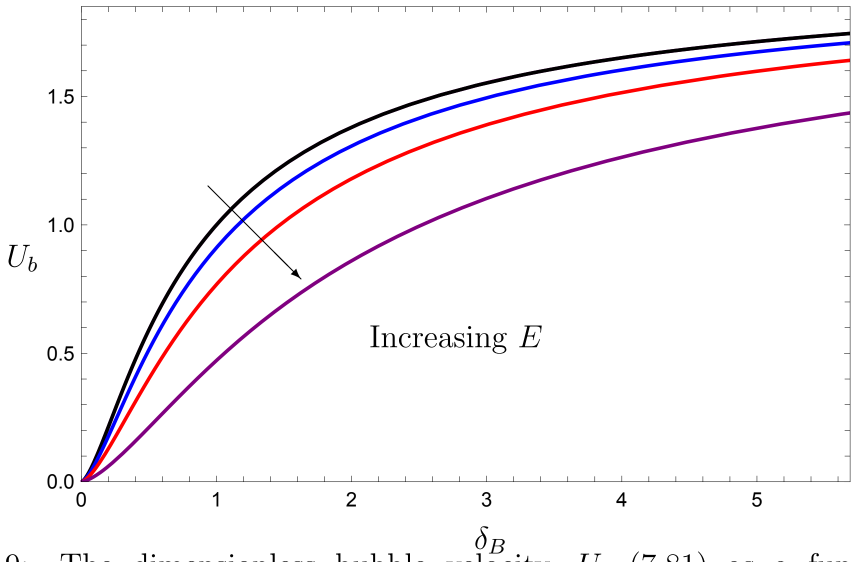

Figure 7.9: The dimensionless bubble velocity, U_b (7.81) as a function of the surfactant-free Bretherton parameter, δ_B (7.82) for a range of values of $E = 0$ (black), $E = 1$ (blue), $E = 4$ (red), $E = \infty$ (purple), with β_1 and β_2 given by (7.40) and (7.70), respectively.

where we define the surfactant-free Bretherton parameter

$$\delta_B = \frac{3\sqrt{\pi}\Gamma(11/6)}{(\beta_1(0) - \beta_2(0))\Gamma(4/3)} \frac{\mathrm{Ca}^{1/3}}{\epsilon} \approx 1.12\frac{\mathrm{Ca}^{1/3}}{\epsilon}, \tag{7.82}$$

as before.

7.7.2 Results

In figure 7.9 we plot U_b versus δ_B, for a range of values of E. Note that if we plotted versus the Bretherton parameter, δ given by (7.80), all the curves would collapse. Plotting U_b versus δ_B allows us to analyse the effect surfactants have on the bubble velocity in comparison with a surfactant-free bubble experiencing the same flow conditions. We observe that the velocity of a surfactant-laden bubble ($E > 0$) at each δ_B is less than that of a surfactant-free bubble ($E = 0$) at the same value of δ_B. This trend continues as we increase E, up to when $\delta = 4^{2/3}\delta_B$, the maximum value that δ can take for a fixed δ_B. Hence, we always find that a surfactant-laden bubble travels slower than a surfactant-free bubble under the same flow conditions.

The methodology presented in this section is easily generalisable to the flow of an arbitrary number of bubbles. We simply adapt the Bretherton parameter as in (7.80) to include the correction to the pressure drop in the presence of surfactants and then proceed as in Chapters 3 and 4.

7.8 Conclusions

In this chapter, we develop a model for the propagation of a two-dimensional surfactant-laden bubble in a channel. Through the method of matched asymptotic expansions, we derive results for the correction to the pressure drop across the front and rear menisci of the bubble. Using these results we generalise the methodology laid out in previous chapters to include the effect of surfactants on the motion of bubbles in a Hele-Shaw cell.

We analyse the motion of a bubble in what is termed the bulk equilibrium model (Ratulowski & Chang, 1990) in which we assume there is an abundance of surfactants in the liquid; physically this limit could correspond to the liquid being significantly above the CMC. In this regime, we derive the dimensionless system (7.6). The asymptotic structure of these equations is broken down into three regions of interest: the front cap region, the thin film region and the transition region. The full solution is then found by matching the solution in the transition region into the front cap and the thin film regions.

Through analysis of the transition region equations, we derive expressions for the thin film height, $\tilde{h}_0\mathrm{Ca}^{2/3}$, and the additional pressure drop across the front meniscus, β_1. We consider the fast-reaction-kinetics and strong Marangoni stress limits, $\mathcal{K} \gg 1$ and $\mathcal{M} \gg 1$, and the distinguished limit in which $E = \mathcal{M}/\mathcal{K} = O(1)$, where $\mathcal{K}$ is a reaction rate constant, and $\mathcal{M}$ is a Marangoni number (see (7.14)). In this particular distinguished limit the surfactant effects are described by a sinlge dimensionless "elasticity parameter" E, which allows us to interpolate between the cases of no surfactant ($E = 0$) and saturated with surfactant ($E = \infty$). When E is small, $\tilde{h}_0$ approaches 1.337 and β_1 approaches 3.88; these are the same values discovered by Bretherton (1961) for a surfactant-free bubble. In the extreme when E is large, $\tilde{h}_0$ approaches 3.369 and β_1 approaches 9.78, both of which are a factor of $4^{2/3}$ larger than their small-E-limit counterpart. We observe that $\tilde{h}_0$ has a non-monotonic increase between the two extremes as there is an initial decrease in the thin film height for small E (see figure 7.5(b)). Conversely, the additional pressure drop β_1 is observed to monotonically increase between the two extremes.

At the rear of the bubble, we find a similar asymptotic structure as in the front of the bubble. However, now we have the additional constraint that the thin film height at the rear of the bubble must match the height of the thin film deposited at the front of the bubble. Again we find that the additional pressure jump across the rear meniscus, β_2, depends on the elasticity parameter E. In the small-E limit, we find that β_2 approaches -1.13, which again reproduces the result by Bretherton (1961) for a surfactant-free bubble. Then in the other extreme, when E is large we find $\beta_2 \approx -2.85$, which again is a factor of $4^{2/3}$ larger than the small E limit. For intermediate values of E, we present solutions for $E = 1$ and $E = 4$ and find a greater pressure drop across the rear meniscus than that for a surfactant-free bubble.

Finally, we show how to generalise the results in previous chapters for the motion of a bubble in a Hele-Shaw cell to include the effects of surfactants. This is achieved by simply altering the definition of the *Bretherton parameter*, δ (7.80) to include the surfactant-laden versions of β_1 and β_2 found in §§7.4 and 7.6, respectively. The bubble velocity is then found via the usual force balance (7.79). We find that for the same flow conditions, an isolated surfactant-laden bubble will travel slower than an isolated surfactant-free bubble. The model generalises to an arbitrary number of bubbles by changing the definition of δ in the same fashion.

While the work presented in this chapter is focused on the motion of a bubble in a Hele-Shaw cell, the methodology presented here can be adapted to study the propagation of a liquid plug and film coating. This problem thus has applications to the transport of fluid in the lung (see Waters & Grotberg, 2002; Halpern & Gaver, 2012; Shemilt *et al.*, 2023), and in fibre coating (see Shen *et al.*, 2002; Delacotte *et al.*, 2012).

Chapter 8

Conclusions and further work

8.1 Summary of results

In this thesis, we present and analyse models for the motion of bubbles in a Hele-Shaw cell. Our work has many applications to microfluidic experiments and devices that involve generating bubbles and propagating them along a microfluidic channel. In these applications the bubbles are often large enough to be pancake-shaped (flattened against the top and bottom walls of the Hele-Shaw cell), but small enough to be approximately circular in plan view, with thin liquid films separating the bubble from the cell walls. It is the motion of such bubbles that form the focus of our study.

We begin in Chapter 2 by developing a model for the motion of a single bubble in a Hele-Shaw cell in a uniform flow. We consider the distinguished limit where the typical bubble aspect ratio ϵ and capillary number Ca are both small and satisfy $\mathrm{Ca} = O(\epsilon^3)$. In this limit, the pressure drop due to the thin liquid films is of the same order as the Hele-Shaw viscous pressure. In this regime the bubble is circular to leading order and its velocity is determined by a net force balance. We find that the qualitative behaviour depends on the dimensionless *Bretherton parameter* $\delta \propto \mathrm{Ca}^{1/3}/\epsilon$: the bubble travels faster than the outer fluid speed for $\delta > 1$, slower for $\delta < 1$, and exactly at the fluid speed for $\delta = 1$. This theoretical prediction agrees well with experimental data. The inclusion of cell walls is found to increase the bubble velocity (from that of an isolated bubble) for $\delta < 1$, but to decrease it for $\delta > 1$. The change in behaviour as δ is varied across $\delta = 1$ resonates throughout this thesis.

In Chapter 3 we consider the motion of two approximately circular bubbles in a Hele-Shaw cell with a uniform background flow. We formulate the problem in complex variables and present analytical equations of motion for each bubble. When the bubbles are identical we again observe a qualitative change in behaviour as δ is varied across $\delta = 1$. When the bubbles are aligned in the flow direction, the bubble pair travels slower than an isolated bubble for $\delta < 1$, but faster for $\delta > 1$. If the bubbles are aligned perpendicular to the background flow direction, however, then the opposite occurs.

In a system of two non-identical bubbles with the larger bubble initially far behind, the larger bubble can catch up with the smaller one. In some cases the bubbles rotate around each other, leaving the larger in front, while in other cases the bubbles collide. Which behaviour occurs depends on the value of δ. For each bubble radius ratio, R, we derive conditions on the fluid parameters such that it is impossible for the bubbles to collide.

We examine the extreme limit where the bubbles are almost touching to prove that two bubbles can collide in finite time. When they do so, we assume that the bubbles do not coalesce, due to their high surface tension. We thus model the touching pair of bubbles as a single entity and determine whether they stay together or separate depending on the mutual reaction force.

In the other extreme where the two bubbles are far apart, we find that the bubbles act like dipoles and thus derive a simple dynamical system to describe their motion. We find that the two-bubble dipole model agrees well with the full solution even when the bubbles are quite close together, where the model should break down.

In Chapter 4 we derive the equations of motion for an arbitrary number of approximately circular bubbles. To solve the model we develop and validate a numerical method. Again, we observe striking changes in the qualitative behaviour depending on whether δ is greater or less than 1. For example, in a train of three identical bubbles travelling along a Hele-Shaw channel, we find that the middle bubble either catches up with the one in front (if $\delta > 1$) or is caught by the one behind (if $\delta < 1$). In longer bubble chains we observe bubble pairs successively forming and breaking up, cascading from the back of the train to the front if $\delta > 1$ and *vice versa* for $\delta < 1$. We refer to this behaviour as the “Hele-Shaw Newton’s cradle”, though we note that this is due to hydrodynamic interactions and not the transfer of momentum.

Dipole methods are commonly used in the literature without justification (see e.g. Shen *et al.*, 2014; Beatus *et al.*, 2006) to simulate the dynamics of a large number of bubbles in a Hele-Shaw cell. We systematically derive a dipole model using matched asymptotic expansions. As well as providing a theoretical underpinning, this approach allows us to incorporate the Bretherton drag law, rather than the *ad hoc* linear drag laws often used in the literature (Shen *et al.*, 2014; Sarig *et al.*, 2016; Green, 2018). The dipole model comprises a system of $2N$ ordinary differential equations for the motion of N bubbles, the solution of which can be found at a much reduced computational cost as compared to the full numerical solution.

To improve upon the dipole model we use the analytic expressions for the equations of motion of two bubbles to derive a pairwise interaction model. Here, we approximate the equations of motion for an arbitrary number of bubbles by summing the pairwise contributions between each pair of bubbles. We obtain a system of nonlinear equations for the bubble velocities, which again can be easily solved numerically at a significantly reduced computational cost in comparison to the full numerical solution. Furthermore, this method accurately models situations when two bubbles are close to each other, where the dipole method breaks down.

In Chapter 5 we develop a model for the motion of a bubble in a Hele-Shaw cell with a uniform background velocity and an *a priori* unknown shape. We identify two distinguished limits in which either (i) the viscous pressure balances the pressure drop across due to the thin films or (ii) the viscous pressure balances the contribution due to the in-plane curvature of the bubble. In either case, the bubble is circular to leading order in ϵ, and we obtain the first-order corrections to both the bubble velocity and the bubble shape. In limit (i), we find that the bubble flattens in the direction of motion as δ increases. In limit (ii), we find that the bubble travels at approximately twice the background flow speed, and predict that the bubble switches from being flattened to being elongated in the flow direction with increasing δ. The theoretically predicted bubble aspect ratio agrees well with experimental observations for small δ, while for large δ the bubble in the experiments have more pronounced deformations.

Next, we extend the deformation calculation to two aligned bubbles in a Hele-Shaw cell with a uniform background flow. In the leading-order solution two bubbles of the same size travel at the same velocity. However, we observe that the bubble in front slightly flattens in the direction of motion, while the bubble behind elongates. Since a flattened bubble travels slower than an elongated bubble, we predict that the bubble behind and will eventually collide with the bubble in front. This effect is sufficiently pronounced that we could even see a smaller bubble catching a larger one.

In Chapter 6, we consider a bubble in a non-uniform background flow. Again the bubble's velocity is determined by a net force balance. We find that the bubble centre travels along a streamline of the background flow although, unlike a tracer particle, the bubble does not travel at the same speed as the background flow. In the simplest nontrivial case of a uniform background flow, the theory reproduces the result of Chapter 2 for an isolated bubble. We find that the same relation for the relative speed holds true for a general background flow: the bubble travels parallel to the local velocity, and its relative speed is determined by the same function of the local Bretherton parameter, which is defined using the external flow speed evaluated at the bubble centre. We then apply the model to common microfluidic components, such as a T-junction and injection sources and sinks.

Next, we use the same methodology to derive an approximate equation of motion for a bubble in a more complicated domain including walls or obstacles. For this solution, we find the complex potential of the background flow without the bubble present from which the equation of motion for the bubble can be found once and for all, whereas, for the full solution, one would need to recalculate the complex potential of the complicated domain with the bubble at each time step. We validate the approximate approach with two test cases in which we can find the full solution analytically. First, we consider the effect of an impermeable wall on a bubble in a stagnation-point flow. Second, we consider the motion of a bubble around a circular obstacle. In both cases, the approximate solution for the bubble velocity is remarkably accurate unless it is very close to the wall or the obstacle. However, the bubble tends to be close to the obstacle only briefly, thus we can obtain good estimates for the bubble trajectories.

Surfactants are widely used in microfluidic devices (see e.g. Anna, 2016) to stabilise bubbles against coalescence. We start by considering the side view of a surfactant-laden bubble in a channel. Focusing on a particular distinguished limit, we derive results for the additional pressure drops across the front and rear menisci due to the thin films above and below the bubble. Using these results we generalise the methodology of our previous chapters to include the effect of surfactants on the motion of a bubble in a Hele-Shaw cell.

We find that, in the small capillary number limit, we can consider the front and rear of the bubbles separately. At the front of the bubble, there are three regions of interest: the front cap, the thin film region, and a transition region that allows for a smooth transition between the other two regions. Through matched asymptotic expansions we derive results for the thin film height and the pressure drop across the front meniscus. In the transition region, the surfactant effects are described by a single parameter, which allows us to interpolate between the cases of no surfactant and saturated with surfactant. We find that the pressure drop across the front meniscus of a surfactant-laden bubble is always larger than that of a surfactant-free bubble, by a factor of up to $4^{2/3}$. A similar analysis is conducted at the rear meniscus. Again, we find that the pressure drop across the rear meniscus of a surfactant-laden bubble is always larger in magnitude than for a surfactant-free bubble, again up to a maximum factor of $4^{2/3}$.

To apply these results to the motion of a bubble in a Hele-Shaw cell, we adapt the definition of the Bretherton parameter, δ, to include the surfactant-modified pressure drop across the menisci. We then find that, for the same flow conditions, an isolated surfactant-laden bubble will travel slower than an isolated surfactant-free bubble.

8.2 Future work

In §2.2.4 we discuss how the dynamic boundary condition (2.5b) changes for a non-circular bubble. To describe highly deformed bubbles, we would need to incorporate the full boundary condition found in Burgess & Foster (1990). The Bretherton drag coefficient is given by $\beta(\mathrm{Ca}_n) = \mathcal{F}\big(\mathrm{Ca}_n^+/\big(-\mathrm{Ca}_n^-\big)\big)$ when $\mathrm{Ca}_n < 0$, where $\mathrm{Ca}_n^\pm$ are the capillary numbers based on the normal velocity at corresponding points on the front and rear bubble interfaces. Including this into the solution of the fluid pressure (2.5) would require developing new numerical techniques, in which one tracks the front meniscus and the corresponding point on the rear meniscus. Such solutions may provide insight into the large increase in aspect ratio of the bubble seen experimentally for large values of δ (see §5.8).

Another extension proposed in §2.2.4 is the inclusion of a time-dependent background flow. For a circular bubble in a time-dependent uniform background flow of dimensionless velocity $V(t)$, we denote the position of the bubble centre by $x(t)$, so the bubble velocity is given by $U_b(t) = \dot{x}(t)$. The force balance (2.10) then produces the fascinating integro-differential equation

$$\pi(2V(t) - \dot{x}(t)) = \frac{\epsilon}{3\mathrm{Ca}^{1/3}}\dot{x}(t)^{2/3}\int_{-\pi/2}^{\pi/2}\left(\beta_1 - \mathcal{F}\left(\frac{\dot{x}(t_f(t,\theta))}{\dot{x}(t)}\right)\right)\cos^{5/3}\theta\,\mathrm{d}\theta, \tag{8.1}$$

where $t_f(t,\theta) = x^{-1}(x(t) - 2\cos\theta)$ is the time at which the thin film was deposited by the corresponding point on the front meniscus. An interesting question that arises is: can a time-dependent background flow generate instabilities in the motion of the bubble?

Some experiments include bubbles that grow or shrink as they are propagated along a Hele-Shaw cell (see e.g. Gnyawali *et al.*, 2017). It would be mathematically and practically interesting to understand how the growing/shrinking affects the propagation dynamics of the bubbles. For a circular bubble, incorporating growth affects

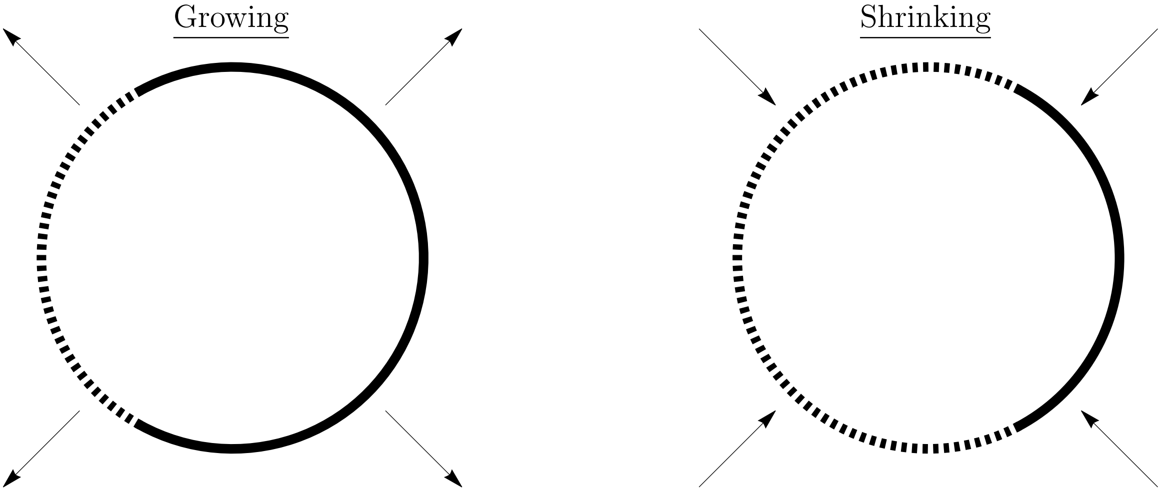

Figure 8.1: Advancing (solid) and retreating (dashed) menisci for (a) a growing bubble, (b) a shrinking bubble.

where the bubble surface is advancing ($U_n > 0$, where $U_n = \boldsymbol{U}_b \cdot \boldsymbol{n} + \mathrm{d}R/\mathrm{d}t$ is the normal velocity of the bubble surface, $r = R(t)$) or retreating ($U_n < 0$). For a growing bubble ($\mathrm{d}R/\mathrm{d}t > 0$), the advancing meniscus will constitute a larger proportion of the bubble surface, whereas, for a shrinking bubble, the rear meniscus will be larger (see figure 8.1).

It is found in §5.10 that, for two aligned bubbles, the bubble in front flattens in the direction of motion and the rear bubble elongates. This observation suggests that the rear bubble should travel faster than the one in front, leading to a collision. This phenomenon is impossible when considering only the leading-order solution, since the bubbles travel at the same leading-order velocity. To confirm this hypothesis, one would need to find the correction to the bubble velocities due to the shape change. This could be achieved either in a complex variable analysis similar to that presented in §5.3 or by using the shape change calculations in §5.10 and then computing the correction to the pressure field around the two bubbles.

Finally, in §7.6 we present two specific solutions of the rear transition region equations (7.66). Our current method to solve the equations (7.66) numerically involves an extremely sensitive two-parameter shooting problem, so an improved bespoke numerical method would need to be designed to perform a complete parameter sweep.

Appendix A

q-digamma function

There are various instances in this thesis, for example (2.34), where an infinite sum is evaluated as a q-digamma function (Salem, 2012). Here we will show how these sums can be written in terms of the q-digamma function and its derivatives. Firstly the q-digamma function is given by

$$\Psi_q(z) = -\log(1-q) + \log(q) \sum_{k=0}^{\infty} \frac{q^{k+z}}{1-q^{k+z}}. \tag{A.1}$$

We can then define the series

$$\begin{aligned} S_0(X,Z) &= \sum_{n=1}^{\infty} \frac{Z^{2n}}{1-X^{2n}}, \\ &= \sum_{k=0}^{\infty} \frac{Z^2 X^{2k}}{1-Z^2 X^{2k}}, \\ &= \frac{1}{2\log(X)} \left[\Psi_{X^2}\left(\frac{\log(Z)}{\log(X)}\right) + \log\left(1-X^2\right) \right]. \end{aligned} \tag{A.2}$$

Then we can compute the series

$$\begin{aligned} S_1(X,Z) &= \sum_{n=1}^{\infty} \frac{nZ^{2n}}{1-X^{2n}}, \\ &= \frac{Z}{2} \frac{\partial}{\partial Z} S_0(X,Z), \\ &= \frac{1}{4\log(X)^2} \Psi'_{X^2}\left(\frac{\log(Z)}{\log(X)}\right). \end{aligned} \tag{A.3}$$

This series is used to evaluate the infinite sum (2.33). Furthermore, we can compute

$$\begin{aligned} S_2(X,Z) &= \sum_{n=1}^{\infty} \frac{n^2 Z^{2n}}{1-X^{2n}}, \\ &= \frac{Z}{2} \frac{\partial}{\partial Z} S_1(X,Z), \\ &= \frac{1}{8\log(X)^3} \Psi''_{X^2}\left(\frac{\log(Z)}{\log(X)}\right), \end{aligned} \tag{A.4}$$

which is used in the evaluation of (6.25a).

Appendix B

The motion of a buoyancy-driven bubble in a Hele-Shaw cell

B.1 Rising isolated bubble

Many Hele-Shaw experiments study the rise of a bubble due to buoyancy, such as those presented in Maxworthy (1986) and Monnet *et al.* (2022). We start by deriving a model for an isolated bubble in a pressure- and buoyancy-driven flow, generalising the model presented in §2.2. We then analyse the effect of side walls on the dynamics of the bubble in §B.2.

B.1.1 Model setup

We consider a bubble propagating in a Hele-Shaw cell of thickness $\hat{h}$ parallel to the $(\hat{x}, \hat{y})$-plane, inclined at an angle α to the horizontal (see figure B.1). Under the lubrication approximation, in the limit where $\hat{h}$ is much smaller than the radius of the bubble, the flow away from the bubble is still governed by the Hele-Shaw equations

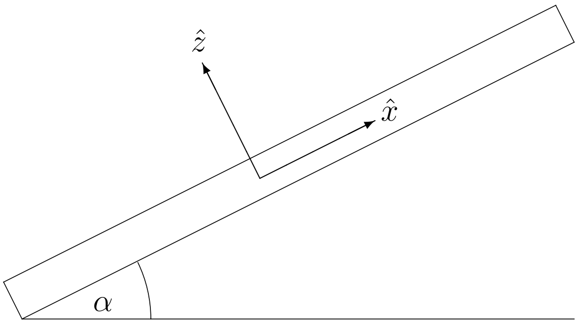

Figure B.1: Side view of a Hele-Shaw cell inclined at an angle α to the horizontal.

(2.1), where now $\hat{p}(\hat{x},\hat{y})$ is the modified pressure such that

$$\hat{p}(\hat{x},\hat{y}) = \hat{P}(\hat{x},\hat{y}) + \hat{\rho}\hat{g}\hat{x}\sin\alpha, \tag{B.1}$$

where $\hat{P}$ is the fluid pressure, and $\hat{\rho}$ and $\hat{g}$ are the fluid density and acceleration due to gravity, respectively.

B.1.2 Dimensionless problem

After incorporating buoyancy into (2.1)–(2.3), we non-dimensionalise as follows (in which dimensionless variables are denoted without hats),

$$\begin{aligned}(\hat{x},\hat{y}) &= \hat{R}(x,y), \quad (\hat{\boldsymbol{u}},\hat{U}_n) = \left(\hat{U} + \frac{\hat{\rho}\hat{g}\hat{h}^2\sin\alpha}{24\hat{\mu}}\right)(\boldsymbol{u},U_n),\\ (\hat{p},\hat{P}) &= \frac{12\hat{\mu}\hat{R}}{\hat{h}^2}\left(\hat{U} + \frac{\hat{\rho}\hat{g}\hat{h}^2\sin\alpha}{24\hat{\mu}}\right)(p,P), \quad \hat{p}_b = \frac{2\hat{\gamma}}{\hat{h}}p_b, \quad \hat{\kappa} = \frac{1}{\hat{R}}\kappa.\end{aligned} \tag{B.2}$$

The choice of this particular normalisation is not obvious in advance but we will see in due course that it simplifies the derived equation of motion for an isolated bubble. We note that (B.2) reduces to the non-dimensionalisation used in §2.2 when $\alpha = 0$ and $\hat{U} > 0$, and that we also recover the other extreme in which bubbles are purely buoyancy driven when $\hat{U} = 0$ and $\alpha > 0$.

We obtain the following dimensionless system:

$$\begin{aligned} \nabla^2 p &= 0 && \text{in} \quad \Omega, && \text{(B.3a)}\\ p &= P + 2(1-B)x && \text{in} \quad \Omega, && \text{(B.3b)}\\ p_b - \frac{3\mathrm{Ca}}{\epsilon}P &= 1 + \mathrm{Ca}^{2/3}\beta(U_n)U_n^{2/3} + \frac{\epsilon\pi}{4}\kappa && \text{on} \quad \partial\Omega_b, && \text{(B.3c)}\\ \boldsymbol{n}\cdot\boldsymbol{\nabla}p &= -U_n && \text{on} \quad \partial\Omega_b, && \text{(B.3d)}\\ p &\sim -Bx + o(1) && \text{as} \quad x^2+y^2\to\infty. && \text{(B.3e)} \end{aligned}$$

The problem (B.3) contains three dimensionless parameters: the aspect ratio, capillary number and velocity ratio, defined by

$$\epsilon = \frac{\hat{h}}{2\hat{R}}, \quad \mathrm{Ca} = \frac{\hat{\mu}\hat{U}}{\hat{\gamma}B} = \frac{\hat{\mu}}{\hat{\gamma}}\left(\hat{U} + \frac{\hat{\rho}\hat{g}\hat{h}^2\sin\alpha}{24\hat{\mu}}\right), \quad B = \frac{\hat{U}}{\hat{U} + \hat{\rho}\hat{g}\hat{h}^2\sin\alpha/24\hat{\mu}}, \tag{B.4a–c}$$

respectively. The velocity ratio $B \in [0,1]$ allows us to interpolate between the limiting cases of a horizontal cell ($B = 1$) and a purely buoyancy-driven bubble ($B = 0$). As in §2.2, for the boundary-value problem (B.3) to be valid, both ϵ and Ca must be small, and the dominant balance in the boundary condition (B.3c), depends on the relative size of these two small parameters.

By integrating (B.3c) around the bubble contour $\partial\Omega_b$ we derive the solvability condition

$$\oint_{\partial\Omega_b} -P\boldsymbol{n}\,\mathrm{d}s = \frac{\epsilon}{3\mathrm{Ca}^{1/3}} \oint_{\partial\Omega_b} \beta(U_n)U_n^{2/3}\boldsymbol{n}\,\mathrm{d}s, \tag{B.5}$$

which corresponds to (2.10) and, again, may be interpreted as a force balance on the bubble. As in §2.2, it can be shown by symmetry that the bubble moves in the x-direction, with *a priori* unknown velocity U_b, say, and thus $U_n = U_b\boldsymbol{i}\cdot\boldsymbol{n}$.

B.1.3 Leading-order solution

In the distinguished limit where $\mathrm{Ca} = O(\epsilon^3)$, from (B.3c) we find that the leading-order curvature is constant, so the bubble boundary is a unit circle to leading order. By defining polar coordinates (r, θ) based on the bubble centre, the leading-order problem can be solved using standard techniques to give

$$P = \left(\frac{U_b}{r} - 2r\right)\cos\theta - B\left(\frac{1}{r} - r\right)\cos\theta. \tag{B.6}$$

The bubble velocity is then determined by the solvability condition (B.5). Since the term in which(B.6) involving B is identically zero on the leading-order bubble boundary $r = 1$, the bubble velocity is independent of B and satisfies the algebraic equation

$$\frac{U_b^{2/3}}{2 - U_b} = \delta. \tag{B.7}$$

By our choice of normalisation, U_b satisfies the same equation (2.16) as for a purely pressure-driven bubble, regardless of the value of B. As $\delta \to 0$, the Bretherton drag term dominates and $U_b \sim (2\delta)^{3/2}$. In the other extreme we find that $U_b \to 2$, as $\delta \to \infty$. In the purely buoyancy-driven case $(B = 0)$ reverting whichback to dimensional quantities the bubble velocity is given by

$$\hat{U}_b = \frac{\hat{h}^2\hat{\rho}\hat{g}\sin\alpha}{12\hat{\mu}}, \tag{B.8}$$

which is the prediction Maxworthy (1986) made for a rising circular bubble in the absence of surface tension.

In figure B.2 we plot the normalised velocity U_b of a buoyancy-driven bubble versus the Bretherton parameter δ. Data from our collaborator, Katie Wu's (Princeton

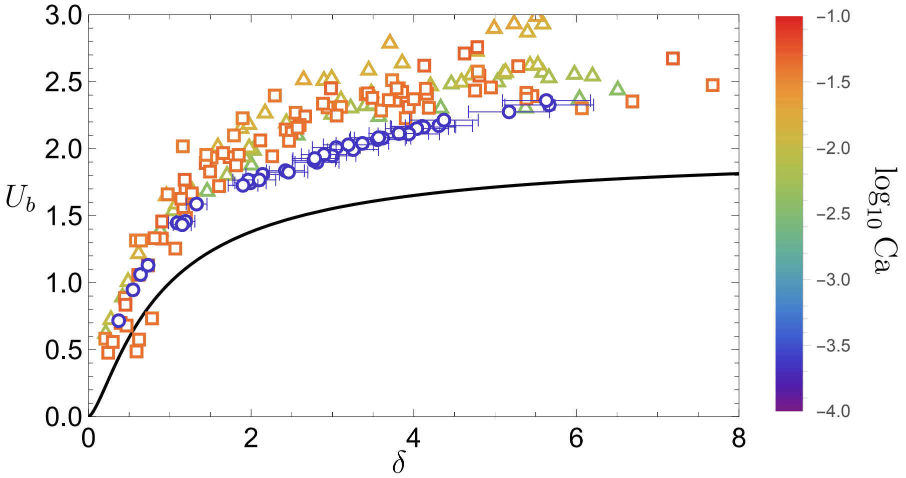

Figure B.2: Relative bubble velocity U_b as a function of Bretherton parameter, δ. Experimental data are shown from experiments by Katie Wu (Princeton University), (circle), from Maxworthy (1986) (triangle), and from Monnet *et al.* (2022) (square). The model prediction (B.7) is represented by a black curve. The color bar shows $\log_{10}$ Ca.

University) experiments are shown alongside rescaled data from Maxworthy (1986) and Monnet *et al.* (2022). The three datasets, which collectively span a wide range of heights $\hat{h}$, inclination angles α, and capillary numbers Ca, collapse under the scalings that we have presented in this study, in particular when plotted against the dimensionless group

$$\delta \propto \left(\frac{\hat{\rho}\hat{g}\hat{R}^3 \sin\alpha}{\hat{\gamma}\hat{h}} \right)^{1/3}. \tag{B.9}$$

It is especially notable that the data collapse across such a large range of capillary numbers, suggesting that the model for the Bretherton pressure drop, which assumes $\mathrm{Ca}^{1/3} \ll 1$, is sufficiently accurate up to $\mathrm{Ca} = O(10^{-1})$ or possibly greater.

Although the collapse of the experimental results is encouraging, we find that the theoretical prediction (B.7) (shown as a black curve) significantly under-predicts the bubble velocity (though the qualitative behaviour is similar). This observation is in contrast with the pressure-driven case shown in figure 2.2. The nature of this discrepancy suggests that the rise velocity is underestimated by Maxworthy's prediction $U_b = 2$ for a circular bubble (attained in the limit $\delta \to \infty$ in our theory). Both Maxworthy (1986) and Monnet *et al.* (2022) argue that elongated bubbles should travel faster than circular bubbles and accordingly multiply by the aspect ratio to adapt the expected rise velocity for an elliptical bubble shape. Such adjustments to the bubble rise velocity based on the bubble shape are not included in the simple model (B.7). Nonetheless, our model helps to explain the observed behaviour, including the monotonic increase up to an approximately constant rise velocity as δ becomes large and the associated deviation from Maxworthy's prediction $U_b = 2$ for smaller δ.

The discrepancies between the predictions of our model and experimental measurements could be attributed to a number of other factors. For example, we have neglected gravitational effects on the capillary-static meniscus at the bubble boundary. Suresh & Grotberg (2005) show that, at $O(1)$ values of the Bond number $\mathrm{Bo} = 24\mathrm{Ca}/\sin\alpha$, gravitational effects modify the Bretherton coefficients $\beta_{1,2}$ (see (2.4)).

B.2 Rising bubble near a wall

Next, we consider the pressure- and buoyancy-driven flow of a bubble near a wall. Following the methodology in §2.3, we formulate our problem using complex variables to find a holomorphic complex potential $w(z) = -p + \mathrm{i}\psi$, the complex potential that satisfies the boundary conditions

$$\begin{aligned} \mathrm{Im}[w(z)] &= 0 && \text{on} \quad \mathrm{Im}(z) = 0, && \text{(B.10a)}\\ \mathrm{Im}[w(z)] &= q + \mathrm{Im}\left[\overline{\mathcal{U}}_b z\right] && \text{on} \quad |z - a\mathrm{i}| = 1, && \text{(B.10b)}\\ w(z) &\sim Bz && \text{as} \quad z \to \infty, && \text{(B.10c)} \end{aligned}$$

where $\mathcal{U}_b$, the bubble velocity and the real constant q are *a priori* unknown. We then impose the solvability condition (B.5) to obtain

$$\frac{1}{\mathrm{i}\pi}\oint_{\partial\Omega_b} w(z)\,\mathrm{d}z = -\mathcal{U}_b - 2(1-B) + \frac{\mathcal{U}_b}{\delta\,|\mathcal{U}_b|^{1/3}}. \tag{B.11}$$

Writing the complex potential in the form $w(z) = Bz + W(f(z))$, where $f(z)$ is the conformal map (2.20), we find that $W(\zeta)$ is holomorphic on the annulus, $A = \{\zeta : X < |\zeta| < 1\}$ and satisfies the boundary conditions

$$\begin{aligned} \mathrm{Im}[W(\zeta)] &= 0 && \text{on} \quad |\zeta| = 1, && \text{(B.12a)}\\ \mathrm{Im}[W(\zeta)] &= q - \mathrm{Im}\left[\alpha\left(\frac{1+\zeta}{1-\zeta}\right)\right] && \text{on} \quad |\zeta| = X, && \text{(B.12b)} \end{aligned}$$

where $\alpha = \left(B - \overline{\mathcal{U}}_b\right)\mathrm{i}\sqrt{a^2-1}$. We know that the solution to this problem is given by (2.31). Using (B.11), we thus find that the equation of motion for the bubble is given by

$$(B - \mathcal{U}_b)F(a) = -\mathcal{U}_b - 2(1-B) + \frac{\mathcal{U}_b}{\delta\,|\mathcal{U}_b|^{1/3}}, \tag{B.13}$$

where $F(a)$ is given by (2.34). By taking the imaginary part of (B.13) we find that $V_b = 0$, so the bubble moves parallel to the wall at a velocity U_b given by

$$\frac{U_b^{2/3}}{(B - U_b)F(a) + U_b + 2(1 - B)} = \delta. \tag{B.14}$$

Note that now the bubble velocity does in general depend on B. Nevertheless, once again, if we choose $B = 1$ we recover the solely pressure-driven Hele-Shaw result (2.36).

In the purely buoyancy-driven regime ($B = 0$) (B.14) reduces to

$$\frac{U_b^{2/3}}{(1 - F(a))U_b + 2} = \delta, \tag{B.15}$$

which may be compared with (2.36). For the extreme values of the Bretherton parameter, δ, we now find

$$U_b \to \frac{2}{F(a) - 2} \qquad \text{as} \quad \delta \to \infty, \tag{B.16a}$$

$$U_b \sim (2\delta)^{3/2} \qquad \text{as} \quad \delta \to 0. \tag{B.16b}$$

Then taking the derivative of (B.15) with respect to δ we find

$$\frac{\partial U_b}{\partial \delta} = \frac{3U_b}{\delta(3\delta F(a)U_b^{1/3} + 2)} > 0, \tag{B.17}$$

thus U_b is an increasing function of δ. In the limit $a \to \infty$ we find that $F(a) \to 2$, so in this limit (B.15) reduces to (B.7), by design, through our choice of non-dimensionalisation. Furthermore we can calculate

$$\frac{\partial U_b}{\partial a} = \frac{-\delta F'(a)U_b}{((F(a) - 1)\delta + \frac{2}{3}U_b^{-1/3}} > 0. \tag{B.18}$$

It follows that U_b is always an increasing function of distance to the wall a. This is in contrast to §2.3 where we observed a change in behaviour based on the sign of $\delta - 1$.

Similarly to (2.41) we can rewrite the force balance (B.11) as

$$\oint_{\partial\Omega_b} u \, \mathrm{d}s = U_b\left(1 + \frac{1}{\delta U_b^{1/3}}\right) - 2, \tag{B.19}$$

and we calculate the average flow between the bubble and the wall in a similar manner to (2.42) to find

$$\frac{1}{a-1}\int_0^{a-1} (u - U_b)\, \mathrm{d}y = \frac{q}{a-1} = -U_b\sqrt{\frac{a+1}{a-1}} < 0. \tag{B.20}$$

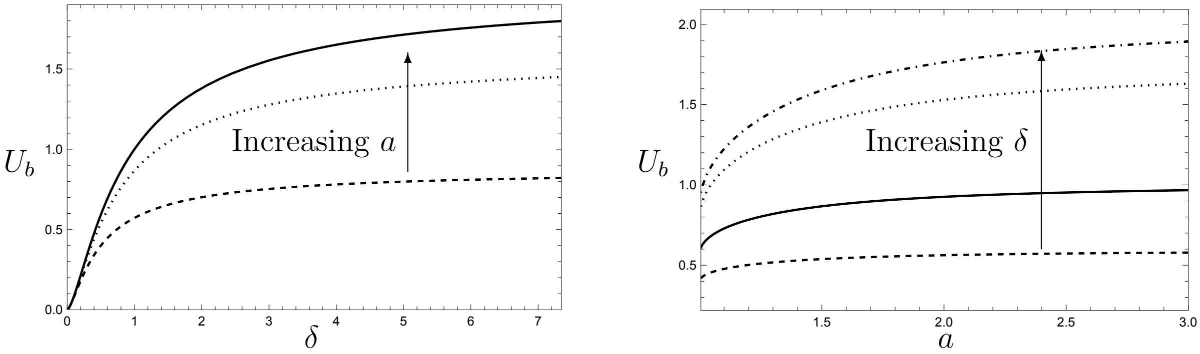

Figure B.3: (a) Buoyancy-driven bubble velocity U_b versus Bretherton parameter δ for $a = 1$ (dashed), 1.5 (dotted) and ∞ (solid). (b) Buoyancy-driven bubble velocity U_b versus distance a from the wall for Bretherton parameter $\delta = 1/2$ (dotted), 1 (solid), 5 (dashed), $\delta = \infty$ (dot-dashed).

This means that the flux of the liquid between the bubble and the wall is always negative and increases as the separation $a - 1$ increases. We then find that the average velocity on the surface of the bubble increases as $a - 1$ increases and by (B.19) we observe that the bubble velocity increases. This argument is analogous to the argument for $\delta > 1$ presented for a bubble in solely pressure-driven flow in §2.3, because in both cases the bubble is travelling faster than the outer fluid speed.

In figure B.3 the dimensionless bubble velocity U_b is plotted versus δ and a. Matching our physical argument, we observe that the presence of a wall always decreases the bubble velocity, with the effect becoming stronger the closer the bubble is to the wall.

Appendix C

Computation of δ_1 and δ_2

C.1 Introduction

In §3.5.2 we find two conditions, one necessary and one sufficient, for the dividing trajectory to completely enclose circle $\sigma = 1 + R$ and thus prevent collision between two initially separated bubbles. For each condition we find a value of $\delta = \delta_k$, for $k \in \{1, 2\}$, at which condition k is first satisfied (see §3.5.2). We will show how to calculate the values of δ_k's in the sections below.

C.2 Computation of δ_1

To find the value of δ_1 at which the stationary points exist on the surface $|z_1 - z_2| = 1 + R$, using the behaviour of f_k (3.32)–(3.35) in the limit $\sigma \to 1 + R$ we look to solve the system

$$\frac{2R^2}{(1+R)^2}\left(\frac{\pi^2}{6} - \mathcal{Z}\left(2, \frac{R}{1+R}\right)\right)(U-1) = -U + \frac{U^{2/3}}{\delta_1}, \tag{C.1a}$$

$$\frac{2R^2}{(1+R)^2}\left(\frac{\pi^2}{6} - \mathcal{Z}\left(2, \frac{1}{1+R}\right)\right)(U-1) = -R^2U + \frac{RU^{2/3}}{\delta_1}, \tag{C.1b}$$

where $\mathcal{Z}(s, b)$ is the Hurwitz zeta-function (Kanemitsu *et al.*, 2000) given by

$$\mathcal{Z}(s, b) = \sum_{n=0}^{\infty} \frac{1}{(n+b)^s}. \tag{C.2}$$

We can easily eliminate δ_1 from the (C.1) by multiplying (C.1a) by R and subtracting (C.1b), which leaves a linear equation for U. The solution for U is then substituted back into one of the equations to solve for δ_1.

We observe that as $R \to 1^+$, δ_1 tends to a finite constant. To find the value of this constant we have to be particularly careful because when $R = 1$ the equations have a one-parameter family of solutions, because the bubbles travel at the same velocity. To find the limiting value we suppose $R = 1 + \epsilon$, where $\epsilon \ll 1$ is a small parameter and expand $U \sim U^{(0)} + \epsilon U^{(1)} + \cdots$ and $\delta_1 \sim \delta_1^{(0)} + \epsilon \delta_1^{(1)} + \cdots$. At $O(1)$ both equations in (C.1) give

$$\frac{\pi^2}{6}\left(1 - U^{(0)}\right) = -U^{(0)} + \frac{\left(U^{(0)}\right)^{2/3}}{\delta_1^{(0)}}, \tag{C.3}$$

which gives us a one-parameter family of solutions. To find the relevant solution we need to find a solvability condition. To that end we subtract (C.1b) from (C.1a) and divide by $R - 1$ and then expand as above, doing so we obtain

$$\frac{7}{2}\mathcal{Z}(3)\left(1 - U^{(0)}\right) + 2U^{(0)} = \frac{\left(U^{(0)}\right)^{2/3}}{\delta_1^{(0)}}, \tag{C.4}$$

where $\mathcal{Z}(s) = \mathcal{Z}(s, 1)$ is the usual zeta-function.

Solving this in conjunction with (C.3) gives $U^{(0)} \approx 1.64$ and $\delta_1^{(0)} \approx 2.37$.

C.3 Computation of δ_2

To find the value δ_2 we need to determine when $\partial U_n/\partial\phi = 0$ at $\sigma = 1 + R$, $\phi = \pi/2$, this can be written as

$$\frac{\partial V_1}{\partial\phi} - \frac{\partial V_2}{\partial\phi} + U_2 - U_1 = 0. \tag{C.5a}$$

Then from (3.38) we obtain

$$\frac{2R^2}{(1+R)^2}\left(\frac{\pi^2}{6}(U_2 - 1) + \mathcal{Z}\left(2, \frac{R}{1+R}\right)(U_1 - 1)\right) = U_1 - \frac{U_1^{2/3}}{\delta_2}, \tag{C.5b}$$

$$\frac{2R^2}{(1+R)^2}\left(\frac{\pi^2}{6}(U_1 - 1) + \mathcal{Z}\left(2, \frac{1}{1+R}\right)(U_2 - 1)\right) = R^2 U_2 - \frac{R U_2^{2/3}}{\delta_2}. \tag{C.5c}$$

By taking the derivative of (3.38) and taking the imaginary part we obtain

$$\frac{2R^2}{(1+R)^2}\left(\frac{\pi^2}{6}\left(\frac{\partial V_2}{\partial\phi} - 2(U_2 - 1)\right) - \mathcal{Z}\left(2, \frac{R}{1+R}\right)\frac{\partial V_1}{\partial\phi}\right) = -\frac{\partial V_1}{\partial\phi}\left(1 - \frac{1}{\delta_2 U_1^{1/3}}\right), \tag{C.5d}$$

$$\frac{2R^2}{(1+R)^2}\left(\frac{\pi^2}{6}\left(\frac{\partial V_1}{\partial\phi} - 2(U_1 - 1)\right) - \mathcal{Z}\left(2, \frac{1}{1+R}\right)\frac{\partial V_2}{\partial\phi}\right) = -\frac{\partial V_2}{\partial\phi}\left(R^2 - \frac{R}{\delta_2 U_2^{1/3}}\right). \tag{C.5e}$$

These equations (C.5) form a closed system of five nonlinear equations for five unknowns $\{\delta_2, U_1, U_2, \partial V_1/\partial\phi, \partial V_2/\partial\phi\}$ which can be solved numerically via for example Newton's method.

References

Abramowitz, M. & Stegun, I.A. 1968 *Handbook of mathematical functions*. US Government printing office.

Acheson, D.J. 1990 *Elementary fluid dynamics*. Oxford University Press.

Aitchison, J.M. & Howison, S.D. 1985 Computation of Hele-Shaw flows with free boundaries. *J. Comp. Phys.* **60** (3), 376–390.

Anna, S.L. 2016 Droplets and bubbles in microfluidic devices. *Ann. Rev. Fluid Mech.* **48**, 285–309.

Anselmo, T., Nelson, R., Carneiro da Cunha, B. & Crowdy, D.G. 2018 Accessory parameters in conformal mapping: exploiting the isomonodromic tau function for Painlevé VI. *Proc. R. Soc. London, Ser. A* **474** (2216), 20180080.

Askey, R. 1978 The q-gamma and q-beta functions. *Appl. Anal.* **8** (2), 125–141.

Beatus, T., Bar-Ziv, R.H. & Tlusty, T. 2012 The physics of 2D microfluidic droplet ensembles. *Phys. Rep.* **516** (3), 103–145.

Beatus, T., Tlusty, T. & Bar-Ziv, R.H 2006 Phonons in a one-dimensional microfluidic crystal. *Nat. Phys.* **2** (11), 743–748.

Booth, D.J., Griffiths, I.M. & Howell, P.D. 2023 Circular bubbles in a Hele-Shaw channel: a Hele-Shaw Newton's cradle. *J. Fluid Mech.* **954**, A21.

Bretherton, F. 1961 The motion of long bubbles in tubes. *J. Fluid Mech.* **10** (2), 166–188.

Burgess, D. & Foster, M.R. 1990 Analysis of the boundary conditions for a Hele-Shaw bubble. *Phys. Fluids A* **2** (7), 1105–1117.

Chauhan, S. & Kumar, P. 2020 Approach and breakup of taylor bubble and taylor drop in a hele-shaw cell. *Phys. Fluids* **32** (8), 082104.

Crabtree, J.R. & Bridgwater, J. 1971 Bubble coalescence in viscous liquids. *Chem. Eng. Sci.* **26** (6), 839–851.

Crowdy, D.G. 2009 Multiple steady bubbles in a Hele-Shaw cell. *Proc. R. Soc. Lond. A* **465** (2102), 421–435.

Crowdy, D.G. 2016 Uniform flow past a periodic array of cylinders. *Eur. J. Mech. B. Fluids* **56**, 120–129.

Cummings, L.J., Howison, S.D. & King, J.R. 1999 Two-dimensional stokes and Hele-Shaw flows with free surfaces. *Eur. J. Appl. Math.* **10** (6), 635–680.

DeGregoria, A.J. & Schwartz, L.W. 1986 A boundary-integral method for two-phase displacement in Hele-Shaw cells. *J Fluid Mech.* **164**, 383–400.

Delacotte, J., Montel, L., Restagno, F., Scheid, B., Dollet, B., Stone, H.A., Langevin, D. & Rio, E. 2012 Plate coating: influence of concentrated surfactants on the film thickness. *Langmuir* **28** (8), 3821–3830.

Franco-Gómez, A., Thompson, A.B., Hazel, A.L. & Juel, A. 2018 Bubble propagation in Hele-Shaw channels with centred constrictions. *Fluid Dyn. Res.* **50** (2), 021403.

Fujioka, H. & Grotberg, J.B. 2005 The steady propagation of a surfactant-laden liquid plug in a two-dimensional channel. *Phys. Fluids* **17** (8), 082102.

Gaillard, A., Keeler, J.S., Le Lay, G., Lemoult, G., Thompson, A.B., Hazel, A.L. & Juel, A. 2021 The life and fate of a bubble in a geometrically perturbed Hele-Shaw channel. *J. Fluid Mech.* **914**, A34.

Garstecki, P., Fuerstman, M.J., Stone, H.A. & Whitesides, G.M. 2006 Formation of droplets and bubbles in a microfluidic T-junction—scaling and mechanism of break-up. *Lab Chip* **6** (3), 437–446.

Garstecki, P., Gitlin, I., DiLuzio, W., Whitesides, G.M., Kumacheva, E. & Stone, H.A. 2004 Formation of monodisperse bubbles in a microfluidic flow-focusing device. *Appl. Phys. Lett* **85** (13), 2649–2651.

Ghadiali, S.N. & Gaver, D.P. 2003 The influence of non-equilibrium surfactant dynamics on the flow of a semi-infinite bubble in a rigid cylindrical capillary tube. *J. Fluid Mech.* **478**, 165–196.

Ginley, G.M. & Radke, C.J. 1989 Influence of soluble surfactants on the flow of long bubbles through a cylindrical capillary. *ACS Symp. Ser.* **396**, 480–501.

Gnyawali, V., Moon, B.U., Kieda, J., Karshafian, R., Kolios, M.C. & Tsai, S.S.H. 2017 Honey, I shrunk the bubbles: microfluidic vacuum shrinkage of lipid-stabilized microbubbles. *Soft Matter* **13** (22), 4011–4016.

Green, C.C., Lustri, C.J. & McCue, S.W. 2017 The effect of surface tension on steadily translating bubbles in an unbounded Hele-Shaw cell. *Proc. R. Soc. Lond. A* **473** (2201), 20170050.

Green, Y. 2018 Approximate solutions to droplet dynamics in Hele-Shaw flows. *J. Fluid Mech.* **853**, 253–270.

Gustafsson, B. & Vasil'ev, A. 2006 *Conformal and potential analysis in Hele-Shaw cells*. Springer Science & Business Media.

Halpern, D. & Gaver, D.P. 2012 The influence of surfactant on the propagation of a semi-infinite bubble through a liquid-filled compliant channel. *J. Fluid Mech.* **698**, 125–159.

Halpern, D. & Jensen, O.E. 2002 A semi-infinite bubble advancing into a planar tapered channel. *Phys. Fluids* **14** (2), 431–442.

Howison, S.D. 1986 Fingering in Hele-Shaw cells. *J. Fluid Mech.* **167**, 439–453.

Howison, S.D. 1992 Complex variable methods in Hele-Shaw moving boundary problems. *Eur. J. Appl. Math.* **3** (3), 209–224.

Huerre, A., Miralles, V. & Jullien, M.-C. 2014 Bubbles and foams in microfluidics. *Soft Matter* **10** (36), 6888–6902.

Kanemitsu, S., Katsurada, M. & Yoshimoto, M. 2000 On the Hurwitz—Lerch zeta-function. *Aequ. Math.* **59** (1), 1–19.

Keeler, J.S., Gaillard, A., Lawless, J., Thompson, A.B., Juel, A. & Hazel, A.L. 2022 The interaction of multiple bubbles in a Hele-Shaw channel. *J. Fluid Mech.* **946**, A40.

Keeler, J.S., Thompson, A.B., Lemoult, G., Juel, A. & Hazel, A.L. 2019 The influence of invariant solutions on the transient behaviour of an air bubble in a Hele-Shaw channel. *Proc. R. Soc. Lond. A* **475** (2232), 20190434.

Kopf-Sill, A.R. & Homsy, G.M. 1988 Bubble motion in a Hele-Shaw cell. *Phys. Fluids* **31** (1), 18–26.

Kreyszig, E. 1959 *Differential Geometry*. University of Toronto Press.

Leshansky, A.M. & Pismen, L.M. 2009 Breakup of drops in a microfluidic T junction. *Phys. Fluids* **21** (2).

Love, A.E.H. 1938 Electrostatic problems related to a perforated strip. *Q. J. Math.* (1), 246–258.

Lustri, C.J., Green, C.C. & McCue, S.W. 2020 Selection of a Hele-Shaw bubble via exponential asymptotics. *SIAM J. Appl. Math.* **80** (1), 289–311.

Manga, M. & Stone, H.A. 1993 Buoyancy-driven interactions between two deformable viscous drops. *J. Fluid Mech.* **256**, 647–683.

Maruvada, S.R.K. & Park, C.-W. 1996 Retarded motion of bubbles in Hele-Shaw cells. *Phys. Fluids* **8** (12), 3229–3233.

Maxworthy, T. 1986 Bubble formation, motion and interaction in a Hele-Shaw cell. *J. Fluid Mech.* **173**, 95–114.

Meiburg, E. 1989 Bubbles in a Hele-Shaw cell: Numerical simulation of three-dimensional effects. *Phys. Fluids A* **1** (6), 938–946.

Monnet, B., Madec, C., Vidal, V., Joubaud, S. & Jerome, J.J.S. 2022 Bubble rise in a Hele-Shaw cell: bridging the gap between viscous and inertial regimes. *J. Fluid Mech.* **942**, R3.

Morrow, L.C., Moroney, T.J. & McCue, S.W. 2019 Numerical investigation of controlling interfacial instabilities in non-standard Hele-Shaw configurations. *J. Fluid Mech.* **877**, 1063–1097.

Muradoglu, M., Romanò, F., Fujioka, H. & Grotberg, J.B. 2019 Effects of surfactant on propagation and rupture of a liquid plug in a tube. *J. Fluid Mech.* **872**, 407–437.

Park, C.-W. 1992 Influence of soluble surfactants on the motion of a finite bubble in a capillary tube. *Phys. Fluids A* **4** (11), 2335–2347.

Park, C.-W. & Homsy, G.M. 1984 Two-phase displacement in Hele-Shaw cells: theory. *J. Fluid Mech.* **139**, 291–308.

Park, C.-W., Maruvada, S.R.K. & Yoon, D.-Y. 1994 The influence of surfactant on the bubble motion in Hele-Shaw cells. *Phys. Fluids* **6** (10), 3267–3275.

Peng, G.G., Pihler-Puzović, D., Juel, A., Heil, M. & Lister, J.R. 2015 Displacement flows under elastic membranes. Part 2. Analysis of interfacial effects. *J. Fluid Mech.* **784**, 512–547.

Ratulowski, J. & Chang, H.-C. 1990 Marangoni effects of trace impurities on the motion of long gas bubbles in capillaries. *J. Fluid Mech.* **210**, 303–328.

Reichert, B., Cantat, I. & Jullien, M.-C. 2019 Predicting droplet velocity in a Hele-Shaw cell. *Phys. Rev. Fluids* **4** (11), 113602.

Reichert, B., Huerre, A, Theodoly, O., Valignat, M.-P., Cantat, I. & Jullien, M.-C. 2018 Topography of the lubrication film under a pancake droplet travelling in a Hele-Shaw cell. *J. Fluid Mech.* **850**, 708–732.

Reinelt, D.A. 1987 Interface conditions for two-phase displacement in Hele-Shaw cells. *J. Fluid Mech.* **183**, 219–234.

Reyssat, E. 2014 Drops and bubbles in wedges. *J. Fluid Mech.* **748**, 641–662.

Saffman, P.G. 1959 Exact solutions for the growth of fingers from a flat interface between two fluids in a porous medium or hele-shaw cell. *Q. J. Mech. Appl. Math.* **12** (2), 146–150.

Salem, A. 2012 A completely monotonic function involving q-gamma and q-digamma functions. *J. Approx. Theory* **164** (7), 971–980.

Sarig, I., Starosvetsky, Y. & Gat, A.D. 2016 Interaction forces between microfluidic droplets in a Hele-Shaw cell. *J. Fluid Mech.* **800**, 264–277.

Shemilt, J.D., Horsley, A., Jensen, O.E., Thompson, A.B. & Whitfield, C.A. 2023 Surfactant amplifies yield-stress effects in the capillary instability of a film coating a tube. *J. Fluid Mech.* **971**, A24.

Shen, A.Q., Gleason, B., McKinley, G.H. & Stone, H.A. 2002 Fiber coating with surfactant solutions. *Phys. Fluids* **14** (11), 4055–4068.

Shen, B., Leman, M., Reyssat, M. & Tabeling, P. 2014 Dynamics of a small number of droplets in microfluidic Hele-Shaw cells. *Exp. Fluids* **55** (5), 1–10.

Stebe, K.J. & Barthes-Biesel, D. 1995 Marangoni effects of adsorption—desorption controlled surfactants on the leading end of an infinitely long bubble in a capillary. *J. Fluid Mech.* **286**, 25–48.

Stone, H.A. 1990 A simple derivation of the time-dependent convective-diffusion equation for surfactant transport along a deforming interface. *Phys. Fluids A* **2** (1), 111–112.

Suresh, V. & Grotberg, J.B. 2005 The effect of gravity on liquid plug propagation in a two-dimensional channel. *Phys. Fluids* **17** (3).

Tan, J., Xu, J.H., Li, S.W. & Luo, G.S. 2008 Drop dispenser in a cross-junction microfluidic device: Scaling and mechanism of break-up. *Chem. Eng. J.* **136** (2-3), 306–311.

Tanveer, S. 1986 The effect of surface tension on the shape of a Hele-Shaw cell bubble. *Phys. Fluids* **29** (11), 3537–3548.

Taylor, G. & Saffman, P.G. 1959 A note on the motion of bubbles in a Hele-Shaw cell and porous medium. *Q. J. Mech. Appl. Math.* **12** (3), 265–279.

Van Dyke, M. 1975 Perturbation methods in fluid mechanics. *NASA STI/Recon Technical Report A* **75**, 46926.

Vasconcelos, G.L. 1994 Multiple bubbles in a Hele-Shaw cell. *Phys. Rev. E* **50** (5), R3306.

Waters, S.L. & Grotberg, J.B. 2002 The propagation of a surfactant laden liquid plug in a capillary tube. *Phys. Fluids* **14** (2), 471–480.

Wolfram Research, Inc. 2024 Mathematica, Version 13.0. Champaign, IL, 2024.

Wong, H., Radke, C.J. & Morris, S. 1995 The motion of long bubbles in polygonal capillaries. Part 2. Drag, fluid pressure and fluid flow. *J. Fluid Mech.* **292**, 95–110.

Zheng, Y., Fujioka, H. & Grotberg, J. B. 2007 Effects of gravity, inertia, and surfactant on steady plug propagation in a two-dimensional channel. *Phys. Fluids* **19** (8).

Zhu, L. & Gallaire, F. 2016 A pancake droplet translating in a Hele-Shaw cell: lubrication film and flow field. *J. Fluid Mech.* **798**, 955–969.